Ultrafast pulsed laser plasma fabrication of erbium doped thin film sensors

Tarun Kakkar

School of Chemical and Process Engineering

University of Leeds

A thesis submitted for the degree of

Doctor of Philosophy

September,2017

This thesis is dedicated to my dear parents Shri Bhim Sain Kakkar
and Shrimati Manju Kakkar.

The candidate confirms that the work submitted is his own, except where work, which has formed part of jointly authored publications, has been included. The contribution of the candidate and the other authors to this work has been explicitly indicated below. The candidate confirms that appropriate credit has been given within the thesis where reference has been made to the work of others.

Conference journals and paper

Chapter 4

1. Kakkar, T., Bamiedakis, N., Fernandez, T. T., zhao, Z., irannejad, M., steenson, P., Jha, A., Penty, R., White, I. & Jose, G. 2014. Glass–polymer superlattice for integrated optics. Optical engineering, 53, 071818-071818.

Chapter 7

2. Kakkar, T., Richards, B., Ajjan, R., Saha, S., Grant, P. & Jose, G. Blood glucose sensing through skin by non-invasive finger touch meter. Diabetes technology & therapeutics, 2016. Mary ann liebert, inc 140 huguenot street, 3rd fl, New Rochelle, NY 10801 USA, a40-a40.

3. Kakkar, T., Richards, B., Jha, A., Saha, S., Ajjan, R., Grant, P. & Jose, G. Glucosense: photonic chip based non-invasive glucose monitor. Diabetes technology & therapeutics, 2015. Mary ann liebert, inc 140 huguenot street, 3rd fl, New Rochelle, NY 10801 USA, a82-a83.

All the works contained in papers 7 are directly attributable to Tarun Kakkar under the guidance of academic supervisors Prof. G. Jose, Prof. P. J. Grant and Dr. Sikha Saha, Dr Ramzi Ajjan. Papers 1 includes the research work done in research group under Prof. G. Jose, where my work was also included. Chapter 4 do not include the co-author work from paper 1.

Acknowledgements

First and foremost, I would like to extend my utmost gratitude and deepest appreciation to Prof. Gin Jose for providing me with the opportunity to work on this project and previous job roles held under his guidance. I am very grateful for his patience, motivation, enthusiasm, immense knowledge, which he had shared with me. His friendly nature and continuous support guided me throughout my research career up till now in Leeds. In addition, he has always been accessible and willing to help me during my research. I am deeply indebted for all his contributions of time, ideas, and funding to make my PhD experience productive and stimulating. In every sense, none of this work would have been possible without him. Thank you for the experiences that I will carry with me throughout my life.

I am also grateful to my co-supervisors Dr Sikha Saha, Prof. Peter Grant and Dr Ramzi Ajjan for their outstanding assistance and continuous support throughout my research. Their excellence, perception and personal experiences with the project had a great impact on my dissertation. I would sincerely like to thank them for their valuable support, logical inputs and proper guidance to make my goals achievable.

In addition, I wish to acknowledge my former guide, Dr Ashish K Rehni and Prof Animesh Jha for providing their kind assistance and continuous support in my scientific career.

My sincere thanks to my colleague and dear friend, Dr Matthew Murray for providing me with a wonderful support throughout my tenure. My special thanks goes to Dr Toney Teddy Fernandez for helping me in my early days in the lab.

I am thankful to Dr Patricia Miranda Azpiazu for helping in improving my lab skills, training me in cell culture and for providing her

valuable insights. I would also like to thank Dr Billy Richards for training me in the lab. It had been a great experience working with you. I would sincerely like to thank you for reviewing my thesis.
Furthermore, I would like to thank my dearest office and lab mates Eduardo Santos, Brindusa Mironov, Jayakrishnan Chandrappan, Antonio Salix, Oluwatoyin Jegede, Sabah Khan, Thomas Mann, Fangyuan Zhu, Suraya Ahmad Kamil, Yothin Chimupala for being there throughout my time in Leeds.
I also thank Rahul Sharma for his helpful suggestions and treating me like his younger brother.
I would also like to acknowledge my dear friends Vasudha Malhotra, Mohit goyal, Chetan Arora, Sakshi Verma, Prabhnoor Singh Hayer, Mayank Kumar, Sidharth Puri, Siddharth dhone back home and in there respective countries who were just a "phone-call away" at any odd hour of time for their concerns, and understanding that has always given me strength.
I would also like to thank Sonal Gupta for helping me, bearing my every reasonable, unreasonable questions and great support at odd times during my PhD.
Lastly, I owe the deepest gratitude to my parents, my brother and my sister in law for their undivided love and support. I would not be the person I am today, without their basic lessons of life.

Abstract

Erbium (Er^{3+}) ions have been extensively used in the field of integrated photonics due to it's characteristic fluorescence properties which can be used to amplify the optical signal in fibre based optical communication systems. In this study, novel materials were developed by doping Er^{3+} ions in glass polymer (GP) superlattice coated on a silicon substrate to investigate its application as an infrared (IR) sensor. The conventional IR detectors are classified as thermal detector and photonic detectors. The conventional photonic detector has better sensing capabilities however, they are required to be cooled down to 77 K for sensing IR radiations. Thus the current requirement is to develop uncooled IR detector which can sense minute changes in the temperature. The initial studies show that GP superlattice coated tipless cantilevers are able to sense changes in temperature with a resolution of 2 mK per nm deflection of the cantilever.

The second part of the study was to dope Er^{3+} ions with or without Ytterbium (Yb^{3+}) ions as a co-dopant in fused silica for glucose sensing. The fabrication was done using the pulsed laser deposition method which is a well established technique for manufacturing nano-engineered thin films. The parameters for fabrication of optical glucose sensor were altered to assess the impact of different parameters such as chamber oxygen pressure, deposition time, Er^{3+} and Yb^{3+} ions concentrations on structural and fluorescence characteristics of thin films. The spectroscopic characterisation revealed that the low doping (0.25 mol %) concentration of Er^{3+} ions in the thin films results in longer fluorescence lifetime of up to 12.4 ms while the doping of Er^{3+} ion in fused silica has been achieved to 2.4 μm depth. The fabricated

thin films were also characterized using techniques such as absorption spectroscopy, fluorescence spectroscopy, prism coupling, energy dispersive x-ray mapping using transmission electron microscopy. The thin films with longer fluorescence lifetime were selected for glucose monitoring device development.

Poor management of diabetes mellitus can result in various complications such as cardiovascular disease, retinopathy, neuropathy and limb amputations. Diabetes control and complication trial highlighted that, with better glycaemic control resulted in reduced complications due to diabetes. The current techniques available to measure glucose levels are invasive in nature. Presently there is a desperate need for non-invasive sensing technology which is considered as holy grail for glycaemic control. The glucose sensing capabilities of the Er^{3+} ions doped fused silica was tested using *in-vitro* glucose measurement in aqueous solutions, blood samples, and intralipids solution. A laboratory bench prototype was developed for a pilot clinical study on people with type 1 diabetes. The change in fluorescence lifetime due to change in glucose concentrations was analysed. The calibrated values were then correlated with the actual glucose reading from finger prick handheld glucose meter and invasive continuous glucose monitor (ICGM). The results were analysed using clarke error grid (CEG) analysis which is a standard statistical analysis tool to assess the accuracy of the device. The next stage of the development includes fabricating a new batch of the photonics chips which has shown the glucose sensing capabilities and thereafter carrying out in-vitro testing as well as carry out the second stage of clinical trials.

Abbreviations

α	Alpha
AFM	Atomic force microscope
AUC	Area under curve
β	Beta
CDT	Cluster of differentiation T cells
CE	Coulombs explosion
CLSM	Confocal laser scanning microscope
CPA	Chirped pulse amplification
cps	Counts per second
CVD	Chemical vapour deposition
DIC	Differential interface contrast
DMEM	Dulbecco's modification of eagle's minimum essential medium
DMSO	Dimethyl sulfoxide
EDTA	Ethylene diamine tetraacetic acid
EDX	Energy disperve X ray
Er	Erbium
FCS	Feotal Calf Serum
FDA	Food and Drug Administration
FIB	Focused ion beam
FL	Fluorescence lifetime
fs	Femtosecond
FWHM	Full width half mximum
GaAs	Gallium aresenic
γ	Gamma
GP	Glass superlattice
HLA	Human leukocyte antigen
HOMO	Higher occupied molecular orbital

Hz	Hertz
λ	lambda
ICGM	Invasive continuous glucose monitor
IR	Infrared
ISC	Inter system crossing
K	Kelvin
kHz	kilo hertz
km	kilo meter
LIFT	Laser Induced Forward Transfer
LUMO	Lower unoccupied molecular orbital
MARD	Mean absolute relative difference
MEM	eagle's minimum essential medium
MCT	Mercury cadmium tellurium
MPI	Mutiphoton ionization
ms	millisecond
MTT	3-(4,5-dimethylthiazol-2-yl)-2,5-diphenyltetrazolium bromide
NBCS	New born calf serum
NFTGM	Non invasive finger touch glucose meter
NGM	Non invasive glucose monitor
NIR	Near infrared
NR	Neutral Red
ns	nanosecond
OCP	Oral contraceptives
PBS	Phosphate saline buffer
PCI	Peripheral Component Interconnect
PDMS	Poly dimethyl siloxane
PLD	Pulsed laser deposition
PMT	Photo multiplier tube
PT	Phospho tellurite
PVD	Physical vapour desposition
QD	Quantum dots
SEM	Scanning electron microscopy
SMBG	Self monitoring of blood glucose
SPR	Surface plasmon resonance
SPW	Surface plasmon wave
τ	Fluorescence lifetime
TE	Transverse electric
TEM	Transmission electron microscopy

TM	Transverse magnetic
TZN	Tellurium zinc sodium
UFPLD	Ultrafast pulsed laser deposition
UV	Ultra violet
XRR	X-ray Reflectometry
Yb	Ytterbium

Contents

List of Figures

List of Tables

Chapter 1

Introduction and literature review

1.1 Introduction

In the field of photonics, there has been a growing demand for nano-engineered thin films with wide-ranging applications in bio-sensing, bio-imaging, therapeutics, chemical sensing, data transfer, and optical signal processing. The development of lasers has revolutionized the thin films fabrication techniques. Rare earth metals ions are becoming very popular in development of thin film sensors as they have characteristic optical properties. Erbium (Er^{3+}) is one of the very extensively used rare earth metal ions mainly in optical communication systems to amplify the signal. The inception of pulsed laser deposition has led to the technological revolution in the field of photonics because it can fabricate more customised thin films. It has a potential to override the current conventional thin film device fabrication techniques such as sol-gel, chemical vapour deposition (CVD). There has been extensive research taking place in the present century to develop nano engineered thin films which offer better sensitivity, ease of fabrication, reproducibility, and longevity.

1.1.1 Aims

The aim of this study is to exploit the optical properties of Er^{3+} in development of novel glucose biosensors and infrared (IR) sensors. The use of femtosecond pulsed laser deposition (fs-PLD) in fabricating nano-structured thin films doped with Er^{3+} ions with different fabrication parameters will be assessed in this study. The proof of concept of non-invasive sensing of glucose will be examined using Er^{3+} doped thin films on fused silica using in-vitro and in-vivo testing. The potential of ytterbium ions (Yb^{3+}) will be investigated as a co-dopant with Er^{3+} ions to improve overall optical gain from the medium. Thereafter, structural and spectroscopic characterisation will be carried out for Er^{3+} & Yb^{3+} ions doped thin film sensors. The multi-target nanosecond pulsed laser deposition (ns-PLD) was done on the silicon substrate to develop Er^{3+} ions doped glass polymer (GP) superlattice for IR sensing. The structural characterisation and proof of concept of Er^{3+} ions doped GP superlattice will also be examined in this study.

1.1.2 Objectives

The objective of this study are outlined below:

1. To fabricate the target glass doped with different concentrations of Er^{3+} and Yb^{3+} ions in the tellurite glass.
2. To fabricate Er^{3+} and Yb^{3+} ions doped in fused silica using different fs-PLD parameters.
3. To carry out the structural and spectroscopic characterization to find out the set of potential thin film sensors for glucose sensing.
4. To carry out biological safety testing of the thin films doped with different concentrations of Er^{3+} and Yb^{3+} ions in fused silica.
5. To assess glucose sensing of thin films by in-vitro testing using the different biological mediums.
6. To examine the proof of concept study of glucose sensing by conducting clinical trials on people with type-1 diabetes.
7. To carry out the fabrication of Er^{3+} ions doped in glass polymer (GP) superlattice using multi target ns-PLD on silicon substrates.
8. To analyse the structural and spectroscopic characterisation of the GP superlattice.
9. To assess the IR sensing capabilities of the GP superlattice.

1.1.3 Chronological order of study

To test IR sensing capability of the GP superlattice, the samples were fabricated by multi-target ns-PLD. Thereafter structural and spectroscopic characterisations were carried out. The IR sensing proof of concept study was carried out thereafter. The Er^{3+} and Yb^{3+} ions doped thin films on fused silica has been called as photonic chips in this study. Two batches of the photonic chips were fabricated using fs-PLD. The first set of photonic chips fabricated with fs-PLD has been

named as G series and next batch prepared has been named as T series. The structural and spectroscopic characterisations of the G series batch was carried out at the start of the study. Then, the in-vitro sensing of glucose using the photonic chips was carried for G series batch. The laboratory benchtop prototype was developed housing the photonic chip with longest achievable fluorescence lifetime from G series. The early stage pilot clinical study was carried out. The next stage was to identify experimental parameters for the fabrication of photonic chips (T series batch) on fused silica by fs- PLD and carry out spectroscopic and structural characterisation of the samples. The biological safety testing of the T series batch photonic chips was carried out to assess there cytotoxicity The in-vitro sensing of the glucose using T series batch was assessed afterwards.

1.1.4 Thesis outline

Chapter 1 details the literature review of the optical sensors and challenges faced in sensing. It also includes the previous studies reported for the fabrication of thin films. The current challenges in non-invasive glucose sensing and why is it the holy grail of glucose diagnostics in diabetes has also been discussed. The optical characteristics of Er^{3+} ions has also been reported in this chapter. The IR sensing challenges has also been discussed.

Chapter 2 discusses the theoretical aspects of the pulsed laser deposition (PLD) and laser ablation in this chapter. The experimental parameters of fabrication of Er^{3+} and Yb^{3+} ions doped in tellurite glass and photonic chips are detailed.

Chapter 3 the structural and spectroscopic characterisation of the fabricated photonic chips in G and T series batch has been discussed.

Chapter 4 the experimental setup for the fabrication of the GP superlattice has been detailed. Thereafter results from characterisation of the GP polymer superlattice is detailed in this chapter.

Chapter 5 the bio-compatibility of the photonic chip using T series batch was carried out to test cytotoxicity based on ISO 10993 guidelines.

Chapter 6 the experimental setup of the optical device which is called as non invasive finger touch glucose monitor (NFTGM) in this study has been discussed

and also the in-vitro glucose sensing was analysed.
Chapter 7 the in-vivo glucose sensing of the photonic chip was assessed by carrying out the clinical trials on people with type 1 diabetes as a proof of concept study.
Chapter 8 then concludes the thesis and probable future work has been discussed.

1.2 Literature review

1.2.1 Thin film optical sensors

The silica or silicon based integrated photonics has become an essential part of sensing, data transfer and optical communication systems. The key requirement for optical amplifiers is to identify the functional materials and there fabrications techniques which can provide a better optical gain. The current approaches used for multi ions fabrication are expensive and its large scale production is very challenging. The functional materials with rare earth metals for thin film fabrication requires basic laser based fabrication techniques which has a standard protocol and easy to implement large scale production (Bradley, 2017). It is important to comprehend the application requirements of thin film optical sensors for light based activation of the functional material used in the fabrication of the thin films (Prasad, 2004). The applications of the thin film optical sensors have been enlisted below:

- Developing the compact ultrafast lasers with ease of use and also for more sensitive optical detectors.
- Developing optoelectronic device for cosmetics and therapeutics applications.
- Bioimaging of the labelled probes conjugated with biomarkers related to chronic diseases such as cancer, arthritis, cardiovascular disease.
- Nano-engineered structures for the tissue engineering.

- Sensitive thin films for the detection of bandwidth of electromagnetic spectrum.
- Biological safety study of the implant and nano probes.
- Non invasive label free detection of respective biomarkers present in chronic and acute diseases.
- Chemical and thermal sensing using thin films.

1.2.2 Biosensors

Biosensor provides the information from the living organism and the information transmitted should be accurate enough to define the medical state of the living system in contact. The biosensor faces various challenges as it should not interfere with the local functioning of an organism. Biosensors are used to detect concentration levels of a biological component or biomolecules. The key concept is to exploit the chemical or physical properties of a matter to specifically measure qualitatively or quantitatively to provide a portable and simple tool. Its application ranges from food inspection, targeted drug discovery, healthcare sensing, environmental monitoring, security and defence purposes. The inception of biosensors can be dated back to 1962 when Clark (Clark & Lyons, 1962) and his team gave an inquisitive approach for the measurement of the blood glucose by using platinum electrode coated with an immobilised enzyme–glucose oxidase. This enzyme helps in the breaking down glucose molecule yielding hydrogen peroxide (H_2O_2) which change the net voltage applied across the electrodes. This technique led to an acceleration in the invention of more state of the art and portable technique for medical diagnostics instrumentation. The electrochemical detection has become a standard module in medical diagnostics, with advancement in manufacturing caused a shift of biomedical instrument from laboratory use to home based applications. This leap forward in technology resulted in US $13 billion turnover of world leading diagnostics companies annually. Whilst the electrochemical detection has found greater niche in the diagnostic world, optical diagnostics technique have been the focus of research (Turner, 2013).

The future of biosensing lies in the label free detection of the biomolecules as it doesn't require any organic or inorganic dye which has some toxic effect on the human body. The biosensor developed using optical waveguides are considered as better than electrochemical or mechanical sensors as they can be reused, are very sensitive in nature and have a better signal to noise ratio. The optical biosensors has quick response and can be used for the real time measurements of the biomolecules which is specific to that sensor (Ciminelli *et al.*, 2013). The label free detection mainly uses the concept of evanescent wave detection by exploiting the electromagnetic properties of a biomolecule to develop an optical sensor for measuring its concentration levels. The key development in this type of sensing is surface plasmon sensors (SPR) where a certain radiation from the electromagnetic spectrum is used to excite the free electrons of a metal present in the dielectric interface. This results in the emission of electromagnetic radiation which can interact with the adjacent media and sensing is done by assessing the decay in evanescent optical waves (Estevez *et al.*, 2014). However, it has some limitations as the evanescent waves emitted from the metal ions can travel to few micrometers of the neighbouring media. Thus it has more sensitivity in the lower concentrations while becoming inefficient in measuring higher concentrations of the analyte (Homola, 2008).

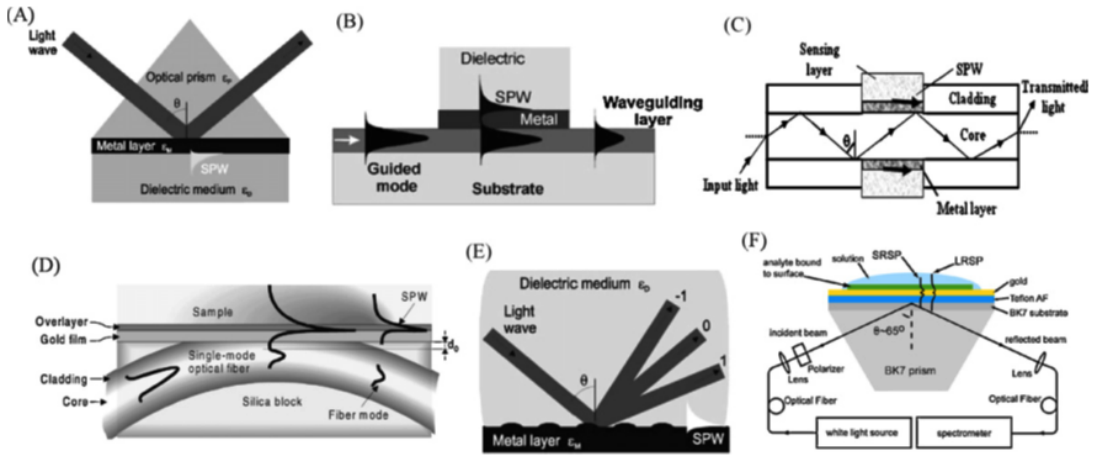

Figure 1.1: Plasmon optical sensor configurations (a) Prism coupling, (b) Thin film coated optical waveguides,(c) Metal doped fibre optics (d) Edge coupling using optical fibres (e) Grating coupling (f) Surface plasmon coupling (Fan *et al.*, 2008).

The plasmon sensors were first developed in 1983 for biosensing by Leidburg *et al* (Liedberg *et al.*, 1983). In the prism coupling biosensors (fig 1.1 (a)) the prism is kept in conjunction with the metal ion layer and the light with a specific excitation wavelength is applied from one side of the prism which causes emission of evanescent light waves from the metal layer. At a certain angle, the propagation constant matches to the surface plasmon wave (SPW) thus coupling the photons in SPW based on the equation:

$$\frac{2\pi}{\lambda} n_p \sin\theta = \beta_{sp} \tag{1.1}$$

where λ is excitation wavelength, β_{sp} propagation constant of SPW, θ angle of incidence, n_p refractive index of the prism. The limitation of this sensing technique is that the prism integration is required which makes the sensor bulky. The next upgrade from the prism coupling has been resolved by the invention of optical waveguides. They are easy to fabricate, has better integration with other opto-electrical components. The principle of sensing is similar to the prism coupling where the light travels in the waveguide and then excites the metal layer to emit the evanescent wave. In the fibre coupling method, a small part of the optical fibre is stripped and then a thin film of metal is coated on the surface and the principle is when the light travels through the higher refractive index core of the optical fibres it couples with the metal layer thus emitting an evanescent wave (Jorgenson & Yee, 1993; Piliarik *et al.*, 2003). Another method is by using a metallic grating and in which the light is applied at an incident angle at which the diffracted radiation causes the coupling into SPW. This can be mainly used in case of a medium which is required to be sensed, has a good optical transmittance. Final method in the discussion is surface plasmon coupling, where the metal layer is kept in between two dielectric layers thus providing an advantage in interpreting the refractive index change in the surface based SPW and background refractive index (Guo *et al.*, 2008). In these types of plasmon optical sensor the light emitted is detected by CCD camera or avalanche photodiodes (Fan *et al.*, 2008).

The thin film biosensor offers various advantages over thick films as it is manufactured using ultra-fast laser deposition technique known as pulsed laser deposition (PLD). It offers monolayers to multilayer fabrication based on characteristics required for sensing. The thin film technology is also advantageous as

it can precisely maintain the consistency and reproducibility with low variability (Neuman *et al.*, 1994).

1.2.3 Infrared detectors

The development of the Infrared (IR) detectors dates back to the late 20 century. Presently, IR detection is required for many applications such as defence, chemical sensing, meteorology, climatology. The IR radiation was first discovered by William Herschel in the 1800s (Karim & Andersson, 2013). However, the better understanding of the IR waves has been provided by the plank's law developed in the 1900s which is still applicable in quantum physics. The IR radiation ranges from 0.76 μm to 1000 μm. The IR sensing has been used a lot in astronomy to provide vital information about universe (Beletic *et al.*, 2008; Gehrz *et al.*, 2009). The IR detectors are classified into thermal detectors and photonic based detectors. The sensing principle for thermal sensors is based on the change in material characteristics such as electrical resistance with a change in the temperature. Thermal detection is done through the thermocouples, bolometers and thermopile. In the bolometers, the electrical resistance changes due to change in temperature while absorbing the IR radiation. In the photonic sensors, the IR radiation causes the absorption or emission of IR waves from the sensing material. The photonic sensors can be based on the IR conduction or change in the voltage potential of the materials due to IR absorption One of the first photonic based IR sensor developed were lead sulphide (PbS) for the detection in mid IR range ≈ 3 μm (Corsi, 2010). The mercury cadmium tellurium (MCT) based photonic sensor can cover the whole range of IR spectrum (Lawson *et al.*, 1959). The photonic detector needs to be cooled down to 77 K or more depending on the detector material used. The new technology of IR detectors is based on quantum dots (QDs) or thin film super-lattice with different thermal expansion constants. In the QD photonic sensor, the quantum dots are deposited on the GaAs substrate while in case superlattice can be two or more materials with different thermal expansion coefficients are deposited as layers on the surface of the substrate. The latter has an advantage as it can be customised for the detection of the specific bandwidth of IR spectrum. The glass has poor thermal expansion coefficient and

can be doped with the material that has an absorption in IR spectrum. While the polymers expand linearly with the increase in temperature thus mismatch in the thermal expansion coefficients causes the innate stress in the superlattice producing a very sensitive optical sensor (Karim & Andersson, 2013).

1.2.4 Optical waveguides: Fabrication techniques

The optical waveguides can be either dielectrics or semiconductor system in which the electromagnetic waves travel from one end point to another. The optical waveguides are fabricated by doping metal ions which alters the refractive index of the thin films to aid light propagation. Waveguides can be either single mode or multimode depends on the thickness and the refractive index of the material. The amorphous silica (SiO_2) has become a standard material in the optical communications mainly in optical amplifiers (Miller, 1969). Currently, glass remains as the primary dielectric material for optical integrated circuits due to low production cost, resistant to chemical damage, relatively high optical transmission (based on type of glass used), and a wide range of refractive index to choose and mainly the option of doping active metal oxides and other functional materials. Thus fabrication methods of different glass waveguides will be discussed in this section. The fabrication of optical waveguides should offer reproducibility, ability to fabricate/dope the intended material, low cost of production and high yield. The fabrication techniques for optical waveguides are classified as shown in figure 1.2. The optical waveguide must have a layer with higher refractive index than the substrate, and two ways to fabricate is either thin film deposition or surface modification of the material locally (Righini & Chiappini, 2014).

The fabrication of optical waveguides was first developed through the sol-gel chemistry in the 1970s. In this method, the hydrolysis of the metallic alkoxide to replace the alkoxide group with the hydroxyl groups, followed by the condensation to form the amorphous material and with the release of H_2O and C_2H_5OH (fig 1.2). The chemical reaction used in the fabrication by sol-gel method is carried out by either oxidation or reduction of material used. This method is very complex and final material formed is a colloidal solution which can be deposited as a thin film by spray coating method or dipping the glass substrate in the sol-gel

preform. This process of fabrication is very tedious and requires a lot of time for preparation. The stress is induced in the coated thin film with thickness > 200 nm, therefore it cannot be deposited in one step. Glass waveguides have low optical losses, better integration of the different range of materials (polymers, ferroelectrics, glasses) than monolithic materials such as silicon.

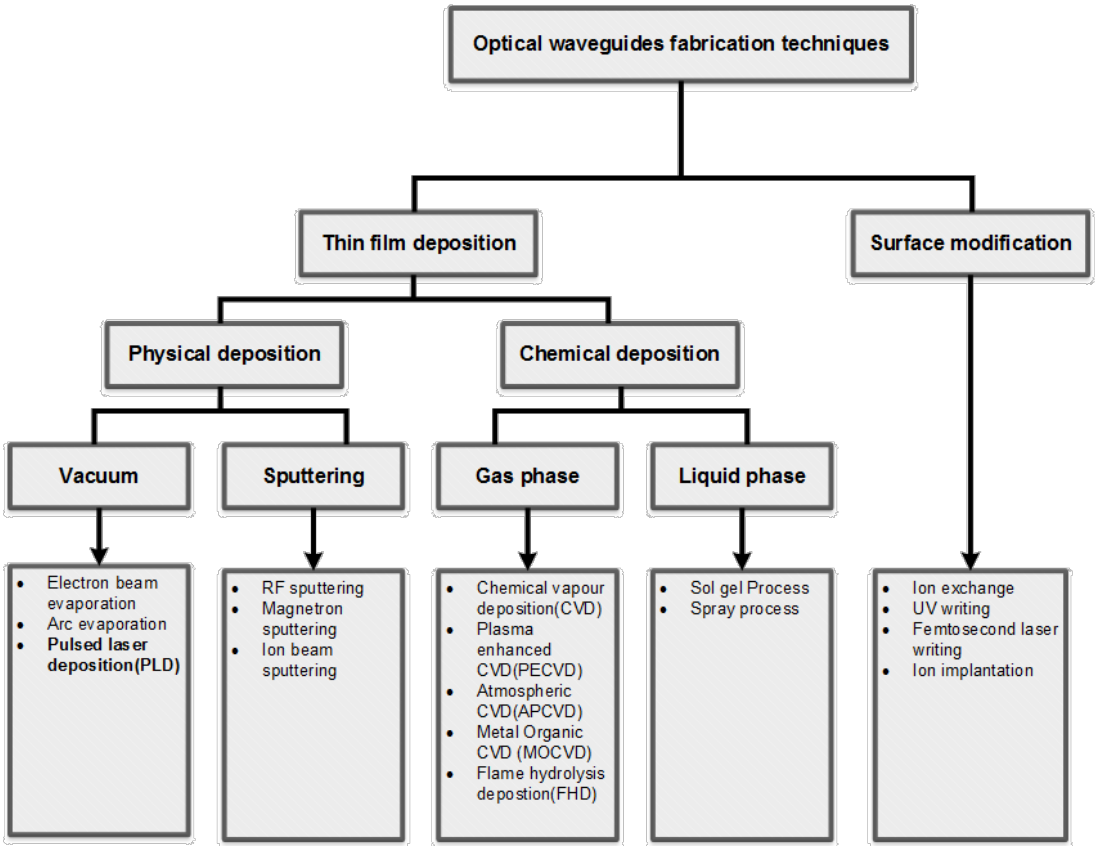

Figure 1.2: Fabrication techniques of optical waveguides mainly divided into thin film deposition and refractive index modification (Righini & Chiappini, 2014).

The thin film deposition can be done by physical vapour deposition method which carried out in vacuum by using radio frequency or magnetron sputtering process or chemical vapour deposition (CVD) by vaporising the material and depositing as liquid phase (Righini & Chiappini, 2014). In the femtosecond laser deposition, the ions are released without any mass destruction to the target material. It is also easy to scale up the operation and less target material is wasted

(Gamaly *et al.*, 2002). The aim of the laser deposition process is to formulate a continuous manufacturing process (Eason, 2007). Previously, the pulsed laser deposition techniques have been used in the thin film coating of the substrate by using low repetition nanosecond (ns) laser. This fabrication process yields a poor quality and non uniform films (Chrisey & Hubler, 1994; Haglund *et al.*, 1997). The deposition techniques have evolved significantly with time, the ablation energy required has dropped from joules to microjoules. Pulsed laser durations have reduced from nanoseconds ($10^{-9}s$) to femtosecond ($10^{-15}s$) region and with high repetition rate of $\approx$ 1 KHz . This method of deposition is called as high intensity ultra-fast pulsed laser deposition. Laser with high repetition rate and short pulse durations yields fewer fragments of atoms ($10^{11} - 10^{12}/s$) resulting in better deposition of material in the substrate (Perry *et al.*, 1999; Rode *et al.*, 1999).

The key advantage of planar waveguides is that, other materials present in the waveguides are nonresponsive to emission wavelength as well as excitation wavelength of a fluorescent ion doped inthe thin film. Due to better transparency, the loss of light is minimum therefore it produces high optical gain waveguides. (Kik, 2001).

1.2.5 Fused silica

Fused silica is an amorphous form of silicon dioxide commonly knows as vitreous silica or silica glass. Silica occurs naturally in crystalline form as quartz, tridymite and cristobalite (Hart, 1927; Kitamura *et al.*, 2007; Sosman, 1965).The material in interest is silica glass due to its low thermal expansion coefficient and able to withstand very high temperatures to about 1000 ^oC which makes it ideal for fabrication process. The silica glass can be fabricated as follows:

1. Type I: It is fabricated by melting quartz crystal in induction furnace carried out at very low pressure in presence of an inert gas. This type of glass has metallic traces present in the SiO_2 network. The key example of this type of glass is Infrasil, pursil, GE 105.

2. Type II: This type of glass is manufactured by Verneuil process in which the quartz powder is melted while oxygen and hydrogen are combusted at about 2000^oC. The brand name available for this glass are herosil, homosil, vitrasil, KU.

3. Type III: The Type 3 fused silica is synthetic in nature and fabricated by flame fusion process (verneuil process) by melting $SiCl_4$ which hydrolyses the latter. Type 3 silica glass have high water content thus have strong absorption bands between 2200 nm and 2700 nm (Davis *et al.*, 1996). They have very high transparency in ultraviolet region and also in near infrared (NIR) region. The common example of Type III are spectrosil, corning 7940, KV, Suprasil.

4. Type IV: This is produced by melting $SiCl_4$ in hydrogen and oxygen free environment by using plasma flame. Type IV has low water content, thus a better IR transmission. Common examples are suprasil W, spectrosil WF and corning 7943. Type IV also features better ultraviolet transmission than the Type 1.

The Type III and IV which are synthetic in nature are known as fused silica whilst Type I silica is called as fused quartz (Brückner, 1970; Hetherington *et al.*, 1965). An optical fibre made with silica are commercially used because of low optical loss and scattering (Keiser, 2003; Senior & Jamro, 2009). Silica glass was chosen as the substrate for the manufacturing of the biosensor. Silica glass is used in optical telecommunications, photo mask because of its intrinsic properties i.e. excellent transparency, low optical loss across the broadband range of wavelength between the ultraviolet light and near infrared region. It has a high glass transition temperature which is 1300 ^oC making it ideal for fabrication of waveguides at high temperatures.

1.2.6 Optical characteristics of Erbium ions

Rare earth metals ions are known to have a characteristic fluorescence emission, one such rare earth metal ions from lanthanide series i.e. erbium has been selected for glucose sensing. Erbium ions exits in glass hosts in the trivalent state

with electronic configuration [Xe]-$4f^{11}$. Due to the incomplete 4f shell, Er^{3+} has different electronic configurations (Razavi & Shapiro, 2003). When Er^{3+} ions is present in the solid material, its 4f wave function is influenced by neighbouring molecules. Er^{3+} kept in the host material induces stark splitting at different energy levels due to which it produces a broad peak emission at 1.54 μm when excited at 980 nm (fig 1.3).

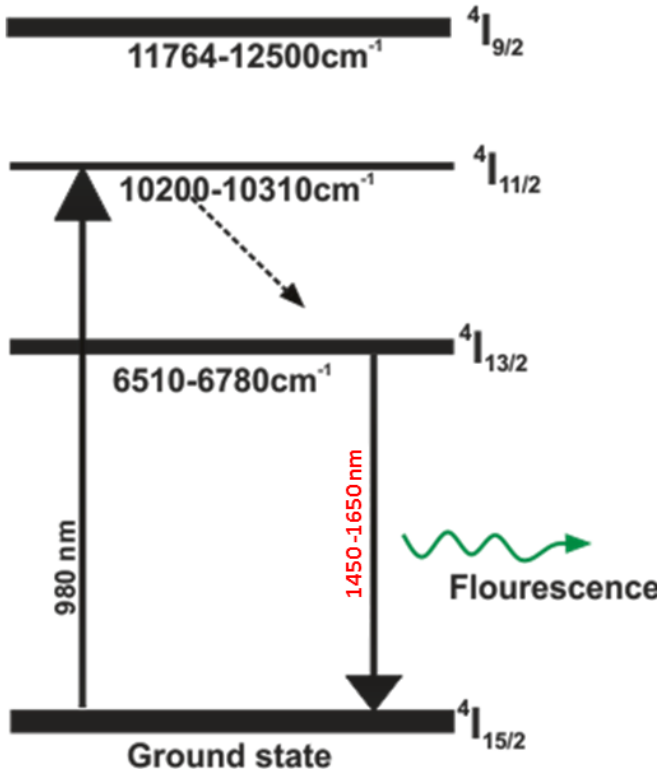

Figure 1.3: Energy level diagram of Er^{3+} ions. The 980 nm excitation of Er^{3+} ion causes the transfer of electrons to $^4I_{11/2}$ energy level from the ground state, $^4I_{15/2}$. While the electron relaxation process is going on, the intersystem crossing of electrons takes place from $^4I_{11/2}$ to $^4I_{13/2}$ with multi phonon emission. The energy release from $^4I_{13/2}$ excited state to ground state $^4I_{15/2}$ results in fluorescence at 1535 nm (Razavi & Shapiro, 2003)

.

While the time taken for optical excitation state and emission is small, its radiative lifetime is long which ranges up to few milliseconds. When an Er^{3+}

ion is excited from ground state to higher energy state, the electrons are rapidly transferred back to lower energy levels with multiphonon emission. An exception to this pattern is when electrons are transferred from first excited state to ground state it causes the release of lower energy thus the multiphonon emission is forbidden resulting in broadband emission with the peak at 1535 nm (Kik, 2001). Er^{3+} ion doped optical fibre is widely used in long distance optical fibre communication because of signal amplification due to electrical transitions of Er^{3+} ion at 1535 nm. A similar concept is being used in Er^{3+} doped planar waveguides fabricated in silica glass for glucose sensing and glass-polymer superlattice for IR sensing.

1.2.7 Fluorescence

When a molecule which has an absorption energy band in the ultraviolet, visible or near infrared region it causes the transfer of electrons from the ground state to the excited state based on the excitation wavelength used. When the excited electrons come back to the ground state, the energy is released as non-radiative emission as heat energy or by radiative emission in visible or IR region (see fig 1.4). The radiative emission is known as fluorescence (Albani, 2008).

The emission pathways after the molecule absorb energy as certain wavelength can be described as following using Jablonski diagram:

1. **Radiative emission** takes place when the electrons are transferred from S_1 to S_0 release of photons corresponding to energy band gap takes place. It is also known as fluorescence. The rate constant is $k_f \leq 10^9\ s^{-1}$.

2. **Non-radiative emission** takes place with multiphonon emission from S_1 to S_0. Rate constant is k_{nf}.

3. **Inter system non radiative emission** when the electron are transferred from S_1 to T_1 by intersystem crossing (ISC) no radiation is released, the electron spin change occurs and decay process takes longer when the heavier element is not present in the surrouding medium. Rate constant is k_{isc}

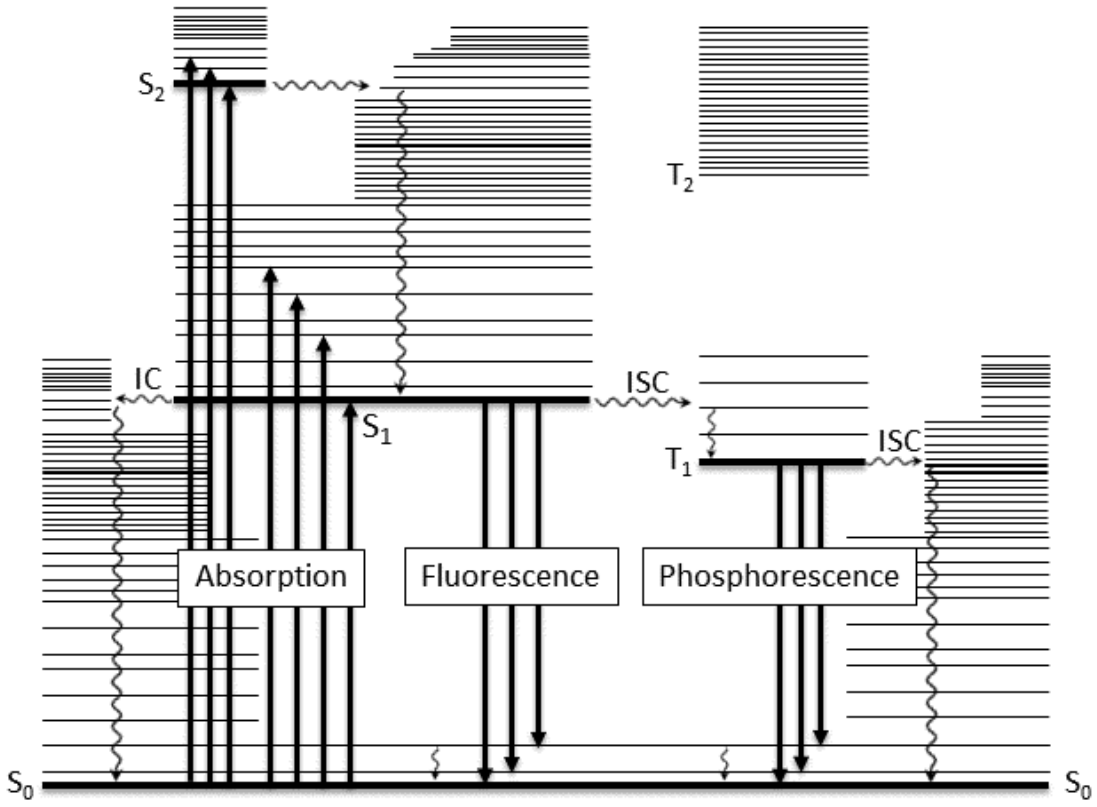

Figure 1.4: Perrin-Jablosnki diagram demonstrating absorption and emission pathways (Sauer *et al.*, 2010).

4. **Photoreactive channel** occurs in case of biomolecular reactions, which involves ISC when a molecule has reached triplet state T_1. The rate constant is k_r.

5. **Phosphorescence** the spin of the electrons changes when the molecule reaches triplet state, the transition of electron spin from T_1 to S_0 is forbidden thus the rate constant (k_p) is slow i.e. 10^{-1} to 10^{0} s^{-1}.

6. **Inter system non radiative emission** occur sometimes with non radiative emission from T_1 to S_0 with rate constant k_{nrT}.

7. **Photoreactive emission T1** If a biomolecular reaction takes place from T_1 when a is in singlet state. Rate constant k_{rT} (Albani, 2008).

1.2.8 Fluorescence decay

The excited electrons can return to the ground state with the release of the certain fluorescence intensity. The rate by which they do so can be calculated as a function of time after excitation. The exponential decay rate of the total excited population can be given by:

$$k_f + k_{nf} + k_{isc} + k_r = k_f + k_{nf} = 1/\tau \tag{1.2}$$

The rate constants k_{nf}, k_{isc}, k_r are the processes that do not release radiative energy. The exponential fluorescence decay, τ is time taken to reach the measured fluorescence to $1/e$ of the initial value (fig 1.5)

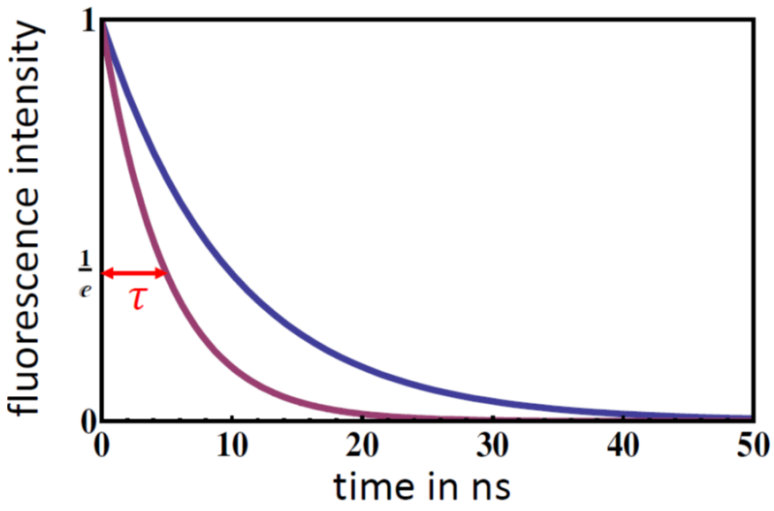

Figure 1.5: The exponential fluorescence decay of a molecule after pulsed excitation (Albani, 2008).

To obtain information about the molecule which influences the fluorescence decay Stern Volmer method can be used. The change in decay process can take place due to fluorescence quenching by an acceptor ion, Q. This can be helpful is assessing the concentration of the acceptor ion, Q. If we do not consider the photo-reactive emission the change in fluorescence of the excited molecule M^* can be affected as given in table 1.1.

Table 1.1: The process affecting the fluorescence of molecule,M (Albani, 2008)

Photoexcitation	$M- > M^*$	$k_{abs}[M]$
Fluorescence	$M^*- > M^*$	$k_f[M^*]$
Non radiative relaxation	$M^*- > M^*$	$k_{nf}[M^*]$
Quenching	$M^* + Q- > M + QorQ^*$	$k_q[M^*][Q]$

The initial rate of absorption when the quencher molecule is influencing the fluorescence of molecule, M can be given by $I_{abs} = k_{abs}[M]$ the differential equation for the excited population state can be given by

$$\frac{d[M^*]}{dt} = I_{abs} - (k_f + k_{nf} + k_q[Q])[M^*] \tag{1.3}$$

if the quencher molecules are not present then equation becomes:

$$\frac{d[M^*]}{dt} = I_{abs} - (k_f + k_{nf})[M^*] \tag{1.4}$$

also if the excitation of the molecule, M takes place continuously, the equation becomes:

$$\frac{d[M^*]}{dt} = 0 \tag{1.5}$$

considering the fluorescence quantum yield, Φ which can be calculated by the following equation:

$$\phi = \frac{number\,of\,released\,photons}{number\,of\,absorbed\,photons} = \frac{rate\,of\,emission}{rate\,of\,absorption} \tag{1.6}$$

The substituting the equation 1.3 and 1.4 in 1.6 for the equation influenced by the florescence quenching by an acceptor molecule, Q we get:

$$\phi_Q = \frac{k_f}{k_f + k_{nf} + k_q[Q]} \tag{1.7}$$

and the quantum yield, when $Q = 0$,

$$\phi_0 = \frac{k_f}{k_f + k_{nf}} \tag{1.8}$$

and ratio of fluorescence quantum yield equation 1.7 and 1.8 gives the ,

$$\frac{I_0}{I_Q} = \frac{\phi_0}{\phi_Q} = \frac{k_f + k_{nf} + k_q[Q]}{k_f + k_{nf}} = 1 + \frac{k_q[Q]}{k_f + k_{nf}} \tag{1.9}$$

Inserting the eq 1.2 in eq 1.9 the net absorption of the molecule becomes:

$$\frac{I_0}{I_Q} = 1 + \tau k_q[Q] \tag{1.10}$$

which is also known as Stern-Volmer equation. It helps in determining the change in lifetime due to the acceptor molecule,Q. It also signifies the dependence of the fluorescence lifetime on the acceptor molecule concentration. This is only permissible when the fluorescence emission overlaps with the absorption band of the acceptor molecules (Albani, 2008).

1.2.9 Diabetes

Diabetes mellitus is a chronic disease in which the endocrine system is unable to regulate the level of glucose present in the blood. Recently, it was suggested that the considerable part of global diabetes susceptibility is acquired during neonatal programming via epigenetic phenomena i.e. these individuals are more susceptible to develop the disease than others. Therefore prevention strategies at an early stage of life are quite essential so as to adequately tackle this disease. Pathogenesis of diabetes is initiated by either destruction of islet β cells present in the pancreas gland or reduced adipose tissue responses to the surplus glucose thus limiting its absorption. This results in the nutrient spill over, insulin resistance, metabolic stress (Nolan *et al.*, 2011).

Diabetes mellitus (DM) is subdivided into two types:

1. **Insulin dependent diabetes mellitus** Type 1 diabetes is the medical condition in which pancreatic gland stops producing insulin. Insulin is a hormone synthesized by the pancreas to regulate the blood glucose levels. Thus rapid changes in blood glucose levels are not controlled.

2. **Non-insulin dependent diabetes mellitus** Type 2 diabetes is the chronic abnormality in which insulin is still produced bythe pancreas. However, skeletal muscle and liver develop insulin resistance due to which glucose is not absorbed by tissue and level of blood glucose fluctuates rapidly (DeFronzo, 1988, 1997; Yki-Järvinen, 1994).

In a healthy individual, blood glucose is rigorously maintained by the body within the narrow range of 4 to 7 mmol/l blood glucose. The average glucose variation in type 2 diabetes generally stays similar to non-diabetic subjects. The key variation is in the post prandial (after the meal) concentrations (Holman & Turner, 1979). In case of subjects with type 1 diabetes blood glucose level is unpredictable because they do not have any internal homeostasis over the blood glucose concentration. Blood glucose concentration fluctuates rapidly, therefore one glucose measurement a day doesn't comprehend to the overall glucose fluctuations (Gonen *et al.*, 1977; McCance *et al.*, 1988). It is vital to maintain blood glucose level as its poor management in people with diabetes can cause hyperglycaemia (higher blood glucose levels) and hypoglycaemia (lower blood glucose levels). Both the states are associated with acute and long term implication in the body. Central nervous system is critically dependent upon glucose concentration to run its normal functions (Cryer *et al.*, 2003; McAulay *et al.*, 2001; Zammitt & Frier, 2005). The lower level of blood glucose can possibly cause cessation of brain functioning which leads to prolonged unconsciousness in principle known as comatoseness (Briscoe & Davis, 2006). It is responsible for 2-4 percent deaths of people with type-1 diabetes. Hyperglycaemia is characterized by high blood glucose levels which have a deleterious effect on the fluid balance and cause a reduction in immune function (Bistrian, 2001; McCowen *et al.*, 2001; McMahon & Bistrian, 1995). During hyperglycaemia, the antagonistic effect on leukocytes is observed which is instigated by increasing granular adhesion, free radicals generation, and disruption in respiration thus inhibiting cell function and collaboratively leading to inflammation. Since the hyperglycaemia is present mostly in peripheral blood, glucose inflammation occurs mainly in highly vascularised muscles. Any organ with higher vasculature has a probable risk of developing abnormality e.g. brain, eye, heart, blood vessels (McMahon & Bistrian, 1995).

1.2.10 Pathogenesis of diabetes mellitus

The equilibrium of blood glucose is maintained by negative feedback inhibition mechanism in the body. In this mechanism the hormone which promotes the synthesis of their intended biomolecules are inhibited when that molecule is in optimum concentration. This phenomenon is used in glucose metabolism in the human body (fig 1.6). During an event of high blood sugar pancreas directs the release of insulin which stimulates glucose conversion to glycogen and facilitates the absorption of blood glucose into tissues, thus maintaining overall glucose concentration in blood. If the blood glucose falls below the normal level, glucagon is released to assist the gluconeogenesis from the stored glycogen (Fox, 2009).

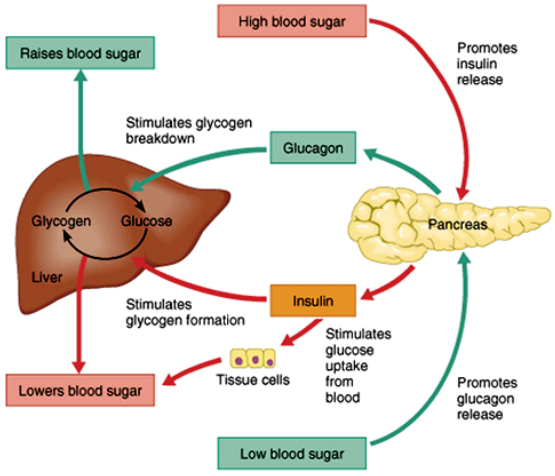

Figure 1.6: A diagrammatic view of glucose metabolism in human body (Fox, 2009)

.

Diabetes mellitus as mentioned before is of two types; Type 1 and Type 2 diabetes.

1. Type-1 diabetes also known as insulin dependent diabetes mellitus(IDDM) is an autoimmune disorder, where selective annihilation of islet β cells present in the pancreatic gland. Islet β cells are responsible for the secretion of insulin hormone. This selective destruction of β cells is initiated by the CD4 T-cell facilitated immune response. During the onset of pathogenesis, the antigen presenting cells which are transferred through pancreatic lymph

nodes gets attached to auto reactive CD4-T cells. The complex starts its self-cloning and hence selectively destroying β cells (Gepts, 1965). The significant role in damaging islet β cells is caused by "human leukocyte antigen (HLA) class II immune response genes" (fig 1.7). It is estimated that 5-10 percent individuals diagnosed with the type 2 diabetes eventually develop type 1 diabetes. The initial symptoms are generally noticed in few months to year time, when the insulin secretion is lowered to such a level that it is unable to control the glucose surfeit. The symptoms are generally polydipsia (excessive thirst), polyuria (excessive production of urine), confused state, loss of weight (Pickup & Williams, 1997). Young adults mainly below 20 years are more prone to this type of infection (Gepts, 1965).

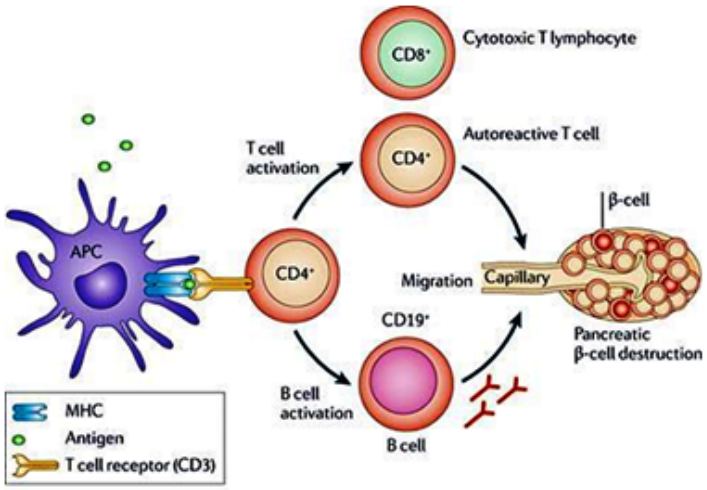

Figure 1.7: Pathogenesis of Type-1 Diabetes (Waldron-Lynch & Herold, 2011)

.

2. Type-2 diabetes also known as non-insulin dependent diabetes mellitus (NIDDM) is heterogeneous in nature and mainly alters the carbohydrate and fat metabolism. The key difference from type-1 is that disruption of β cell is a secondary feature in this medical condition. It is more characterised by increased insulin resistance of liver, muscle, adipose tissue, as well as pancreas (Scheen, 2003; Scheen & Lefebvre, 1992). This causes the impaired absorption of the glucose by muscle and adipose tissue as well

disturbance of negative feedback mechanism which the results in release of hepatic glucose in blood stream (DeFronzo, 1997). The susceptibility of this disease is more related to genetic predisposition as well environmental condition such as obesity. Type 2 symptoms are similar to the type 1 i.e. anorexia, polyuria, polydipsia, fatigue, tremors, however are less occurring (Pickup & Williams, 1997).

1.2.11 Complications

The individuals with either Type-1 or Type-2 diabetes are prone to the serious risk of developing retinopathy, neuropathy, nephropathy, cardiovascular disease. The acute complications related to diabetes are ketosis, ketoacidosis, hypoglycaemic episodes, hyperglycaemic crisis, and infections (Nathan, 1993).

The high fluctuation in glycaemic levels especially hyperglycaemia is associated with retinopathy. The various late complications associated with diabetes are following:

1. **Retinopathy** occurs in almost all patients with diabetes. It produces micro-aneurysms (bubble like formation in the localised area) which are induced due to substantial haemorrhages induced in retinal vessels. The ischemic condition (presence of less oxygen leading to poor respiration) induced due to haemorrhages leads to neovascularization. The new vessels are fragile in nature and tend to bleed into vitreous humour (fluid present inside eye) (Group *et al.*, 1978).

2. **Nephropathy** or end stage renal failure is often associated with rise in hypertension due to acute complications. It is leading cause of mortality in patients with type 1 diabetes. Neuropathy is also the most recurrent chronic medical complication of diabetes. Prolonged diabetic stress can lead to impotence, also can cause the amputation if postural low blood pressure is not controlled for a long time. This condition can be fatal if it affects limb region.

3. **Cardiovascular disease**, this type of disease is multifarious in origin. It mainly occurs in Type 2 diabetes than in Type 1 where hyperglycaemia is

more prevalent. Other factors such as hypertension, high cholesterol levels, poor physical activity contribute to the manifestation of this disease (Group *et al.*, 1988).

1.2.12 Self-management of diabetes

Poor management of diabetes is caused due to various factors which includes poor knowledge of self-management, invasive technologies with a poor user interface, improper dose regimen. The better glycaemic control assists reduction of chronic complications associated with diabetes e.g. 21 percent reduction in deaths were reported, 14 percent in myocardial infarctions, 37 percent in microvascular complications (Adler *et al.*, 2000).

The blood glucose is measured by following methods:

1. **Handheld glucose meters**: These type of meters are used for home based self-monitoring of blood glucose (SMBG). Their accuracy level ranges from 80 – 95 percent of gold standard measurement for blood glucose. They require lancet to prick fingertip, thereafter the blood is squeezed out from the fingertip which is applied to the test strip which measures the blood glucose. It is a painful task and is prone to infections (Douglas & Teaney, 1988).

2. **Continuous glucose monitors:** In this kind of glucose monitoring the needle is inserted/implanted into the skin in mainly upper arm/ abdomen from which realtime change in blood glucose is measured. The life of the sensor is usually 5-7 days. This device requires frequent calibration by obtaining corresponding blood glucose levels from an other device like handheld meter (Vidhya *et al.*, 2004).

3. **Biochemical analysers:** These are the laboratory based glucose measuring systems. They require a large amount of blood to be withdrawn to measure the blood glucose. They are recognised as the gold standards of the blood glucose measurement (Astles *et al.*, 1996).

4. **Non-invasive glucose monitors:** They are considered as the holy grail of blood glucose monitoring. Measurement of blood glucose without extracting blood from the subject is the main feature of non-invasive blood glucose monitors (Müller *et al.*, 1997).

1.2.13 Invasive Glucose monitors

The current biosensors in glucose sensing offers both *in-vitro* and *in-vivo* sensing. The *in-vitro* sensors require a blood specimen to carry out the measurement whilst the *in-vivo* sensor requires the sensor to be implanted subcutaneously in the human body for the measurement. The conventional blood glucose monitoring is the *in-vitro* type of glucose sensing. It was first portable and home based glucose measuring method offering improved glycaemic control, if used regularly. It is used regularly by a patient with type 1 and high risk patient with type 2 diabetes to check blood glucose levels. The current development in glucose sensing is introduction of invasive continuous glucose monitors (ICGM) which gives better usability compared to conventional finger prick method. The key objective for the development of invasive continuous glucose monitor (ICGM) was to measure real time glucose value which can used then in administration of insulin like an artificial pancreas. Currently, implantable glucose sensors are being used to continuously monitor glucose levels. They are advantageous over the conventional system as it doesn't require the user to be active while taking a measurement which is an essential requirement as it monitors glucose across the time period of the sensor being implanted (Newman & Turner, 2005; Wang, 2008).

1.2.14 Non invasive glucose monitors (NGM)

The non-invasive glucose monitors are represented as future of glucose sensing and "holy grail" to issues faced by current ICGM techniques. It is the only method to obtain a pain free long acting glucose monitor. Various routes of development have been followed for the development of non-invasive glucose monitor (NGM) techniques which has been discussed below.

Multiple sensing monitor

GlucoTrack^{TM} is a NGM technique which combines three sensing techniques; ultrasonic, electromagnetic, and heat capacity. This is a non-optical technique and it doesn't measure the glucose intrinsically instead it measures the parameters which are related to change in glucose concentration (Alexeeva, 2011). It is predicted to show better acceptability in clinical trials as it combines various techniques therefore reducing error margin. It measures the glucose from the ear lobe and the sensor is clipped to it. It requires individual calibration using glucose references from the candidate which is valid for one month. It obtained CE marking on June 2013 and it is yet to announce anything about FDA approval. The major hurdle with GlucoTrack is its intended replacement is for intermittent glucose measurement as each time the sensor has to be clipped to measure glucose and that clip cannot have wireless connectivity to the readout device. Therefore the user has to be active to take a measurement (Harman-Boehm *et al.*, 2009).

Near infrared occlusion spectroscopy

Near infrared occlusion spectroscopy is a direct method of measuring blood glucose. It is based on the absorption by glucose in near infrared region which is more specific to blood glucose than other metabolites present in the blood. It is shown to measure glucose, haemoglobin and oxygen saturation. This measurement requires temporary cessation of blood in the finger to take one measurement. The device based on this technique was developed by OrSense Ltd, Isreal. It has obtained CE marking and is portable. Its key drawback is the finger has to be occluded to make a measurement (Vashist, 2012).

Transdermal patch monitor

SpectRx blood glucose monitor employed an *"Altea Micropor laser"* which creates very tiny micropores in the stratum corneum, which is the outermost layer of the skin. The interstitial fluid oozes out of the tissue which is then collected in an external patch which is then measured by the conventional glucose sensor. It claims the use of low energy laser and it only affects the outermost layer without causing any deleterious effect to the internal organs. It is able to measure glucose

from 60 - 400 mg/dl blood glucose level. The device is calibrated with the help of conventional blood glucose monitor and technology was licensed to Abbott laboratories Ltd. Symphony is a continuous NGM technique invented by Sontra Medical Corporation, which uses conventional glucose sensor in conjugation with transdermal permeation system known as prelude skin prep. Symphony requires a short warm up period which is similar to the time required by GlucoWatch before it starts measuring blood glucose levels. The results are transmitted wirelessly to the readout device. The clinical trials conducted in 2011 presented very accurate results. There is no clarity on which the development stage of the device is, as there has not been any announcement for CE marking or timeline for intended product launch (Vashist, 2012).

Raman spectroscopy

This was another major development in the field of NGM sensing. So as to measure blood glucose, high power laser is used with a customized portable raman spectroscopy to measure the amount of vibrations from glucose molecules and water. After a comparison between differences in intensity of Raman signal from water and glucose peak the concentration is determined. To obtain single glucose value it requires 3 mins measurement time. The device was developed by C8 medisensors known as HG1-c. They obtained CE marking in 2012. However, no further information is available for the development stage of this technique (Vashist, 2012).

Reverse iontophoresis spectroscopy

Iontophoresis has been implied in the transdermal patches to deliver drugs across the skin. The reverse iontophoresis method was used to extract glucose from the skin. The extracted glucose was measured by the conventional glucose sensor (Potts *et al.*, 2002). GlucoWatch G2 biographer was the first NGM device from this technique to obtain CE marking and FDA approval. It was launched in the market in 2002 to measure glucose continuously from GlucoWatch which requires initial 2-3 hrs warm up period. Another issue with GlucoWatch was, it has 15 mins lag period from actual blood glucose levels. Some individuals found

this process very uncomfortable due to skin irritation and sometimes painful as well. The study conducted by University College of London, highlighted that participant observed discrepancies in the glucose values. Half of the alarms for hypoglycemic and hyperglycemic were incorrect. Due to regular problems with GlucoWatch it was discontinued in 2007 (Tierney *et al.*, 2000).

Bio-impedance Spectroscopy

This is a non-optical technique which measures the dielectric component of tissue by varying the alternating currents of known intensity. It measures varying Na^+ and K^+ ions concentration which is influenced by the changes in blood glucose levels (Hillier *et al.*, 1999). It is an indirect glucose measurement technique. It is packaged as an open resonant circuit in Pendra tape which was kept in the contact with the surface of the skin from which it carries out the measurement. The resistance can be measured 4 times per minute with glucose error bar of 20–60 mg/dl glucose per ohm. The regular use of the device during the clinical investigation revealed its poor performance with the constant requirement for calibration with blood glucose. It requires individual patient calibration and could be used for only 2-3 days after the calibration has been completed (Wentholt *et al.*, 2005). The Pendra tape was replaced after every 24 hrs of use and the new tape has to be kept at the same position of calibration. The correlation between the commercial handheld glucose meters and Pendra was 35.1 percent. Another limitation of this technique was that it can only be applied to those skin which has very less change in resonance frequency of device (Hillier *et al.*, 1999).

1.2.15 Near infrared (NIR) sensing of glucose

Near infrared spectroscopy is the key area under investigation for about 20 years up till now for the development of NGM techniques. Two main features of this technique are that human skin has better transparency in this region and absorptivity of glucose is substantially higher than other metabolites present in blood in this region. The molar absorptivity of glucose in the broadband region of 1500-1625 nm is higher than lactate, urea, ascorbate, alanine and triacetin which are common components of the blood (Amerov *et al.*, 2004). The glucose molecule

interacts with near infrared photons by two phenomena i.e. absorption of NIR photons and scattering induced due to change in glucose concentration. NIR glucose sensing method was proposed by Maier *et al.* (1994) based on the change in scattering of light due to varying glucose concentration in blood. When the near infrared light is transmitted through the varying regions of the skin, interstitial fluid and then to the blood, it experiences the misalliance in the refractive index due to which scattering effect is observed. The increase in refractive index of blood is due to increasing concentration of glucose the mismatch in the overall refractive index of tissue and blood is reduced. This implicates that overall coherent scattering is reduced. Thus the fluorescence lifetime of single NIR photon travelling longer path follows Strickler-Berg relationship. It states that change in refractive index is inversely proportional to the fluorescence lifetime (Strickler & Berg, 1962).

The glucose molecules have higher absorptivity in the near infrared region of 1500-1600 nm. Figure 1.8 (left) shows the comparison of the glucose absorptivity with that of a water molecule, the glucose has higher absorptivity in 1520-1804 nm than other metabolites present in blood. Thus, the absorption of more photons will take place with increasing glucose concentration, only if total molecules of water are either same or less than their initial concentration. The main barriers to the non-invasive glucose measurement are water and skin. The optical window for skin lies in the region of 250 nm to 3000 nm varying with the penetration depth and depends on the wavelength range used. In this case the ions with infrared emission has more chance of penetration in skin. This approach has already been used for the measurement of the level of melanin, oxygenation, haemoglobin but its accuracy levels varies.

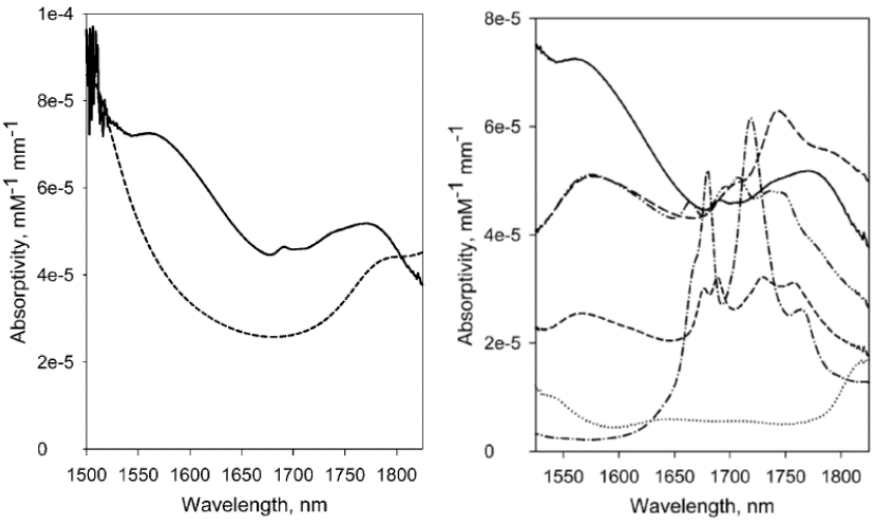

Figure 1.8: (Left) The Absorptivity of the glucose (solid) compared with the absorptivity of the water molecules from 1500-1800 nm. (Right) The molar absorptivity of the glucose (solid) compared with other biomolecules present in blood alanine (dash-dot-dot), ascorbate (medium dash), lactate (short dash), urea (dotted), triacetin (dash-dot) in the near infra-red spectrum (Amerov *et al.*, 2004).

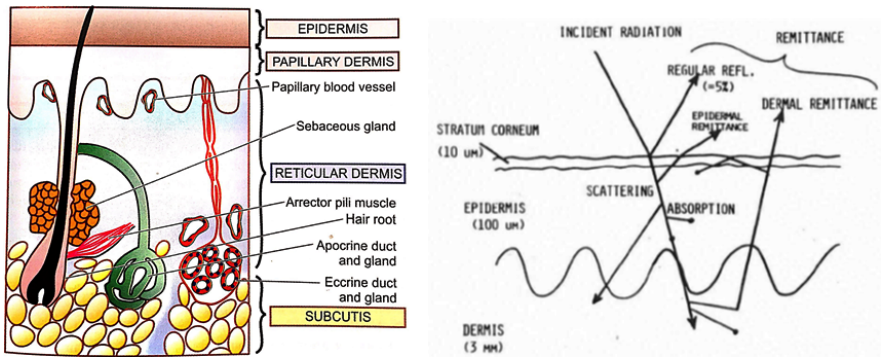

Figure 1.9: Structural cross section of the skin (left) (Mohan, 2005), optical pathway of the transmitted radiation in the cross section of skin (right) (Anderson & Parrish, 1981).

The structure of the skin is given in fig 1.9. The skin is made of three basic layers, **Stratum corneum** which is the top layer with 10 μm thickness, it

made of eosinophilic layers of keratin. **Epidermis** which is the next layer with 100 μm thickness. It mainly contains melanocytes which define the colour of the skin. The **dermis** layer is present below epidermis which contain blood vessels , lymphatic and excretory glands. The glucose molecules are present in the blood and interstitial fluid released from blood capillaries (Mohan, 2005). The transmittance of photons into the skin depends on the optical window of the skin. The transmission measurement (fig 1.10) done on the excised porcine layer shows the net transmittance of $\approx$ 30 % in the optical window II.

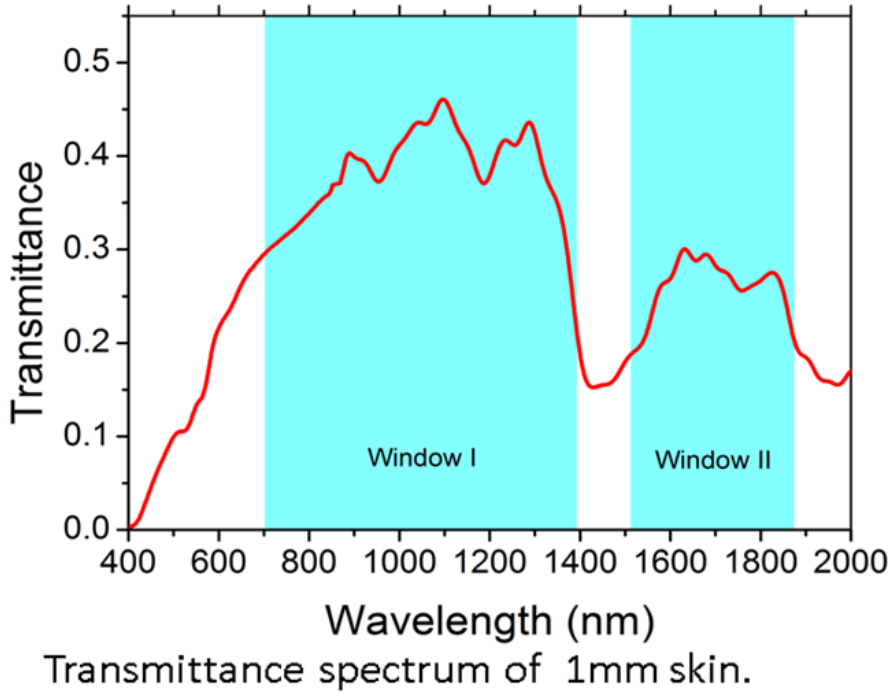

Figure 1.10: The transmittance spectrum of a porcine skin of thickness 1 mm.

The Er^{3+} ions emission from the energy level $^4I_{13/2}$ to ground state $^4I_{15/2}$ is the broadband emission between the 1450-1650 nm with an emission peak at 1535 nm.The broadband emission (1535 nm) of the Er^{3+} ions overlaps with the glucose absorption band thus making it feasible for sensing of glucose (fig 1.11). This emission is overlapping with the glucose absorptivity in the near infrared region (Amerov *et al.*, 2004). This provides a perfect opportunity to investigate the effect of a change in glucose concentration with Er^{3+} ion emission. However,

the basic mechanism will be more complex than just the absorption effect as the light scatter (93-96 %) as it travels through the skin (fig 1.9 (right)). The scattered photon can either return to the doped Er^{3+} ion layer or be lost/absorbed in the medium. The scattering light is dependent on the size of molecules present in the medium: size of molecule < wavelength of the radiation will cause lower scattering , mainly isotropic in nature whilst the molecule size of the order of the wavelength will cause much stronger scattering. The molecules size larger than the wavelength used causes Mie scattering, where scattering is weak and highly diffused (Anderson & Parrish, 1981).

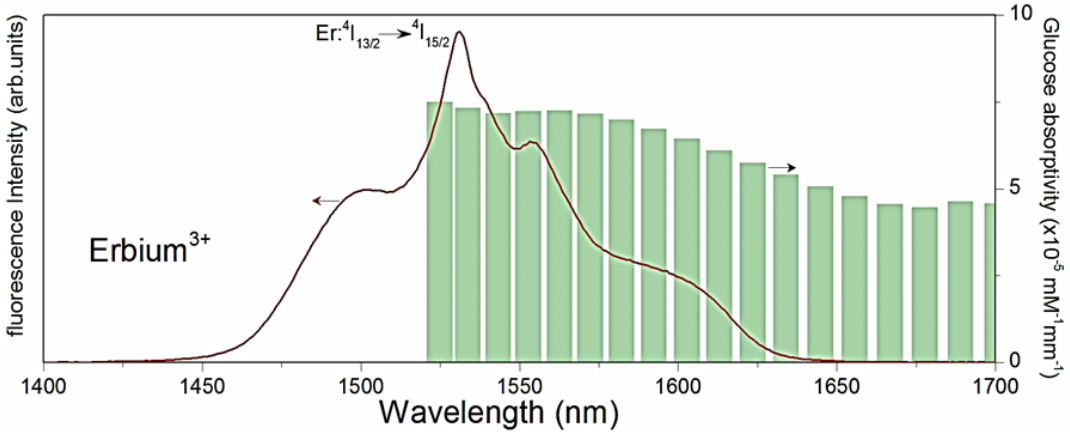

Figure 1.11: Overlap of absorption bands of glucose (column graph) in the NIR wavelength range with typical fluorescence spectrum of Er^{3+}ions.

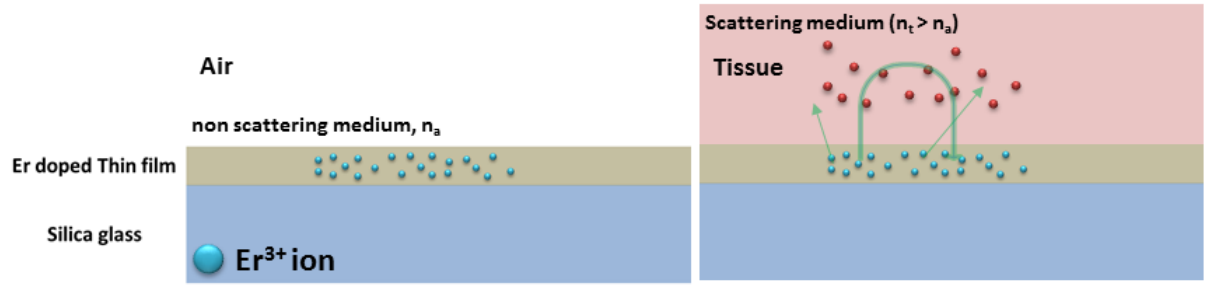

Figure 1.12: The experimental model of the proposed photonic chip configuration and the influence of the scattering medium on the emitted photons from the Er^{3+} ions.

The amount of photon scattered is dependent on the change in refractive index from one medium to another. Assuming that the low proportion of Er^{3+} ions are excited when pump laser of 980 nm is used, the emitted photons are either reabsorbed by Er^{3+} ions at the ground state. This process continues until the photons are released finally resulting in increase the overall lifetime. The emitted photons can also be reabsorbed by the excited Er^{3+} ions causing the stimulated emission resulting in a shorter lifetime. When a scattering medium such as tissue ($n_t > n_a$) is brought in contact with the Er^{3+} ions doped surface of the photonic chip (fig 1.12), back-scattered photons can travel through the medium and gets absorbed by the glucose molecules. Internal reflections of photons lead to an increase of the overall absorption coefficient by increasing the optical path length within the cells. Thus the fraction of backscattered photons returning to the film is related to the glucose concentration (Maier *et al.*, 1994). The key requirement here is the refractive index of the doped layer must have higher refractive index than that of the silica glass.

1.3 Conclusion

In this section, the two key aspects were discussed i.e. development of the thin film superlattice for the IR sensing, and erbium ion doped fused silica for glucose sensing. The key requirement for the IR detector is to sense changes in temperature without the need to cool down the system to decrease the overall background noise. The aim of this part of the study was to use materials in the superlattice with different thermal expansion coefficients, and thus a change in temperature can induce the stress in the thin film. The structural and microscopic characterisation of the superlattice is necessary to assess the overall stress induced in the thin film. The superlattice is doped with erbium ions which absorbs NIR radiation with peak absorbance at 980 nm. The absorbed IR radiation can cause an increase in overall temperature of the superlattice. The hypothesis here is that when the superlattice is heated the thermal expansion coefficient mismatch can change the induced stress in the thin film. This can be measured using the optical microscope and quantified using AFM.

In the second part of the study, erbium is doped into the fused silica for its application in glucose sensing. As discussed earlier in section 1.2.15, the key component of this study remains the interaction of photons emitted from erbium ions and their interaction with glucose molecules present in the biological medium, as well as the change in fluorescence properties of erbium ions with varying altering glucose concentrations. The glucose biosensor will be subjected to thorough structural and spectroscopic characterisation. Thereafter the material will be tested for the biocompatibility as it needs to be in contact with the skin. It is important to establish whether a sensor is safe to be used for longer periods of glucose sensing. The in-vitro and in-vivo sensing of glucose by the erbium-doped thin films will be assessed. The glucose biosensor was also co-doped with Ytterbium ions in a few samples, to check whether it can enhance the signal to noise ratio by improving the overall fluorescence emitted from erbium ions. The next chapter discusses the theory of the laser ablation and depostion process. It also details the fabrication parameters and samples fabricated using PLD.

Chapter 2

Fabrication of Photonic chip

2.1 Introduction

The exploration in the field of biosensors using optical waveguides has been very significant in the past decade. The application of pulsed laser based fabrication in stoichiometric transfer of ions on the substrates has been investigated so as to achieve better performance. It enables the growth of multiple elements with varied ionising properties in thin films. This requires precise stoichiometry to deliver an optimum composition of the thin film. The pulsed laser deposition is carried out under vacuum in which the laser is focused on the target material to be deposited on or in the substrate. The ablated ions strike the susbtrate with high kinetic energy. The ablation process has features of molecular beam epitaxy and sputter deposition. The ions permeate into the silica structure and gets embedded to a depth of 2-3 microns into the substrate. The phenomenon is under investigation. However, it is hypothesized that acceleration of ion momenta due to multi-photon-emission which is created by high electrostatic field (Gamaly *et al.*, 2002) leads to dense plasma of free ions moving at the rate of km/s. The primary requirement for the ablation of target material is that the laser fluence focused on the spot is sufficient to create a plasma plume. It is also dependent on the pulse repetition rate, energy and deposition wavelength of the pulsed laser beam, as well as the temperature of the substrate, pressure of the chamber and background gas. The chamber pressure range required in the experiment ranged from 65 mTorr to 95 mTorr (Eason, 2007)

The aim of this chapter is to identify and standardise the fabrication method of thin films and also to understand the underlying mechanism of the doping process to assess theoretical and experimental aspects of ablation of dielectrics using short $10^{-11}s$ pulses from high-repetition-rate ($500 - 1000$ Hz) lasers, and thereafter analysing the deposition process of ions into a fused silica layer. The parameters of the laser determine the ablation process i.e. the repetition rate, energy required, and duration of each pulse of the laser beam. It has been observed that high repetition rate, ultra short dwell time has the synergistic effect on plasma production yielding high quality thin films.

Pulsed laser deposition (PLD) method used in the $1990s$ had low repetition rate with nanosecond laser pulses (Chrisey & Hubler, 1994; Miller, 1998) which

produce poor quality films with less control over the particle size deposited deposited. The literature on PLD predicts the inferior quality of the film was a result of pulse parameters which cause the release of large particles of material from the target surface thus causing more damage to the target material (Gamaly *et al.*, 1999; Rode *et al.*, 1999). The plasma plume formed by expansion of the ions removed from the target material causes an increase in thermal energy and vaporisation. The droplets of materials released expand into the vacuum, thereafter condensing onto the substrate forming relatively inconsistent thin film (Eason, 2007).

The release of materials in an ionic form requires more understanding of the mechanism of the laser ablation process. The operating criteria for the pulsed laser can supersede the droplets formation. It has been estimated that reduction in laser energy i.e. from joules to microjoules coupled with the reduction in pulse duration from nanosecond to femtosecond and higher repetition rate (500–1000 Hz rather than 10 Hz) results in the production of fewer (10^{11}–10^{12}) atoms per pulse. This process is known as high repetition ultra-fast pulsed laser deposition (UF-PLD) (Perry *et al.*, 1999; Rode *et al.*, 1999). Gamaly *et al* proposed "Top hat"intensity distribution in the ablation process over the focal area on target material used for near perfect surface silicon films by using femtosecond pulsed laser (Gamaly *et al.*, 2004).

The symmetric distribution of materials is dependent on $\cos^n(\theta)$ where n can vary from $\sim 4 - 30$. The raster scanning of the target materials plays a critical role in the uniform distribution of the ions on the substrate. The pulsed laser deposition technique has been used to fabricate biosensors as coated thin films on the substrate. This fabrication offers more precise orientation of the molecules and reproducibility which is a significant improvement over thick film fabrication in which the substrate deforms and losses its lattice strength during the fabrication. This manufacturing technique offers deposition onto the substrate and thus there is a risk of wearing off the material over time (Gamaly *et al.*, 2002). The characteristics of the film are quite dependent on the focus of the laser on the target, pressure of the chamber and temperature of the substrate. Despite the complex arrangement, ionic distribution in the plume, alteration of isotopic content in the plasma, metastable nature of the ion deposited in the

film, femtosecond laser ablation has proven to be a better alternative for thin film production for various materials (Millon *et al.*, 2003; Pronko *et al.*, 1999).

The deposition of carbon films (Banks *et al.*, 1999), metal oxides (Okoshi *et al.*, 2000; Perriere *et al.*, 2002; Pronko & Pan, 2001), nitrides (Ristoscu *et al.*, 2003; Zhang *et al.*, 2000) and optical waveguides have been fabricated using the UFPLD technique. Femtosecond laser etching has been used to embed microstructures using a technique called Laser Induced Forward Transfer (LIFT) to prepare specific holograms and diffractive material structures (Mailis *et al.*, 1999; Zergioti *et al.*, 1999, 2003). They demonstrated that this etching technique produced high quality printing which was a significant improvement over the standard method which used excimer lasers. The pulsed laser deposition technique has been used previously to fabricate various biosensors including an in-vitro glucose sensing biosensor with deposition of cerium oxide. It aids in immobilisation of the glucose oxidase enzyme which is used in glucose hand held meters (Saha *et al.*, 2009).

2.2 Laser ablation

Femto-second laser ablation of dielectrics or semiconductors takes place through multiple physical processes i.e. non linear absorption, and difference in balance of equilibrium in electronic and vibrational excitations. This is further escalated by avalanche breakdown, producing thick, intense electron hole plasma while the laser is targeted on the material. The key feature of this ablation process is structural and physical changes in the optical characteristics from the pellucid and light transmitting surface to a metallic state. This state develops in a localised area as the electronic thermal conductivity takes place in a high density region (Phipps, 2007). In metals, the thickness of the layer due to electrothermal conduction is much smaller than the area of the focal spot due to which it is considered as a one-dimensional formulation (Von der Linde & Sokolowski-Tinten, 2000). Whilst in dielectrics, the ablation process is a complex mechanism. Two possible scenarios of ablation are considered to be coloumb or phase explosion.

The etching process can be of two types:

1. **Moderate ablation** occurs where the material released from the target is of the order of a few nanometres per pulse when the laser energy is marginally above the threshold ablation level, and the frequency of the laser pulse is low.

2. **Severe ablation** is observed when the ablation rate is magnitude higher i.e. significantly higher laser energy pulses compared to the moderate ablation case, exhibiting the process of phase explosion.

Laser ablation with pulse duration of 100 fs requires power density $I_p \sim 10^{13}$- $- 10^{14}$ W/cm^2 which is much higher than what is required in nanosecond laser ablation which is around $\sim 10^8 - 10^9$ W/cm^2 (Perry *et al.*, 1999). This implies that power density is inversely proportional to pulse duration required for ablation. The degree of ionization of the material varies from gentle to strong ablation. In moderate ablation, the plume is mainly made up of ions which are non thermal in nature and exhibit a high velocity of 2 x 10^4 m/s as well as narrow angular velocity distribution directed normal to the surface. Whilst in the severe ablation process the ion velocity is lower 1.2 x 10^4 m/s accompanied by thermal dependent plasma ions with broader ionic distribution of the plume.

2.2.1 Coulomb Explosion

Coulomb explosion (CE) takes place when the intense beam of photons is targeted on the surface, ions gain high positive charge which causes an increase in phonon system. This leads to repulsion between ions which exceeds the binding strength, leading to germination and release of materials. The intriguing part of CE is that after the process is completed it leaves a smooth surface. The probability of occurrence of coulomb explosion and hence genesis of high ion kinetic energies and ionic removal of materials has been observed in dielectrics. However, to ascertain the dynamics of coulomb explosion and parameters influencing the process, it is critical to establish the criterion for the occurrence of the coulomb explosion. The electric field generated due to irradiation of the target material is strong

enough to cause breakdown of atomic bonds and release of ions from the surface. The threshold electric field for CE should emit electrostatic charge density/atom higher than the sublimation energy/atom. The threshold electric field is given by

$$E_{th} \mid_{x=0} = \sqrt{2\lambda_{at} n_0 / \varepsilon\varepsilon_0} \tag{2.1}$$

where λ_{at} is the enthalpy of sublimation per atom, n_0 is the lattice atomic density, and ε is the dielectric permittivity. The threshold electric field will change when the frequency is high or pulse width is longer in duration. So as to compensate the thermal reduction process during the strong ablation, the threshold electric field will given by

$$E_{th} \mid_{x=0} = \sqrt{(2\lambda_{at} - 3kT_l) n_0 / \varepsilon\varepsilon_0} \tag{2.2}$$

2.2.2 Phase explosion

When the power intensity (I_p) is lower than 10^{13} W/cm^2, (Sokolowski-Tinten *et al.*, 1998; Von der Linde & Schüler, 1996) the process changes from coulomb to phase explosion, where localized heating increases the temperature rapidly forming metastable regions. This takes place when the power density is between $10^8 - 10^9$ W/cm^2 with an upper limit pulse duration of about $10^{-11}s$. The phase explosion process is non isochoric and non adiabatic in nature (Lorazo *et al.*, 2003).

2.2.3 Dynamics of laser ablation

The theoretical mechanism of the laser ablation and carrier transport from dielectrics is required to understand the wide spectrum of the inter-related process. The steps involved in the ablation process start with irradiation of the target leading to photoionization. The photon energy should be sufficient to meet the threshold requirement of the material band gap energy i.e. the entropy difference between lower occupied energy levels and highest occupied energy levels also known as Fermi energy, E_f. The excited electrons which are present in the conduction band can absorb more energy and generate secondary electrons. This

alters the reaction from the dielectric materials. At the initiation of an explosion, the absorption and reflection process modifies considerably. As avalanche dictates the separation of superficial layers of the target surface, the collisional multiplication of secondary electron seizes, thus regulating the irradiation by leveraging the free electron density. In addition to this, multi photo-emission alters the charge neutrality of plasma, thus creating a positive charge on the surface of target leading to an ambipolar electric field. The electromagnetic field drives the excited electron to the ground state in order to balance the positive charge. At intensities above 10^{14} W/cm^2, the dielectric ionized in few femtoseconds, mainly shorter than the pulse duration of 100 fs. The electrons released during the ionization process then dominates the absorption mechanism as free carriers in metals. The properties of the laser-matter interactions are then independent of the early state of the target glass. Due to which the resonance absorption and phenomenon of the inverse bremsstrahlung play the major role in absorption characteristics of both metals and dielectrics. The relationship in the dielectric function ε and refractive index k of the target glass can be illustrated by the equaztion (Landau *et al.*, 2013):

$$\varepsilon^{'} \approx \frac{\omega^2}{\omega_{pe}^2}, \varepsilon^{''} \approx \frac{\omega_{pe}}{\omega}\left(1+\frac{\omega^2}{\omega_{pe}^2}\right)^{-1}, n \approx k = \left(\frac{\varepsilon''}{2}\right)^{1/2} \tag{2.3}$$

Where ω_{pe} is electron plasma frequency, ω is the laser frequency. The absorption coefficient A thereafter follows from the Fresnel formulas:

$$A = 1 - R \approx \frac{4n}{(n+1)^2 + n^2} \tag{2.4}$$

and the depth of absorption (skin depth) l_s is given by :

$$l_s = \frac{c}{\omega k} \approx \left(\frac{2c^2}{\omega\omega_{pe}}\right)^{1/2}\left(1+\frac{\omega^2}{\omega_{pe}^2}\right)^{1/2} \tag{2.5}$$

The ratio of the absorption coefficient to the skin depth (Luther-Davies & Gamaliĭ; Rozmus & Tikhonchuk, 1990) becomes

$$\frac{A}{l_s} \approx \frac{2\omega}{c}\left(1+\frac{1}{n}+\frac{1}{2n^2}\right)^{-1} \tag{2.6}$$

2.2.4 Unified approach

In the ultrafast laser ablation process, the laser induced metallic nature has been investigated using unified approach.

1. The equation used for the formation of laser induced charged electrons :

$$\frac{\partial n_x}{\partial t} + e^{-1}\frac{\partial J_x}{\partial x} = S_x + L_x \tag{2.7}$$

   where S_x and L_x are source and loss terms explaining the free carrier population, n_x is the carrier density with x, i depicting the electrons and ions respectively.

2. The electron current density J_x includes drift and diffusion terms, it can be denoted as an equation of motion (Mendes *et al.*, 1998):

$$J_x = \mid e \mid n_x \mu_x E - eD_x \nabla n_x \tag{2.8}$$

   where D_x is the diffusion coefficient according to Einstein's relation $D_x = kT_x\mu_x/e$, T_x is the carrier temperature, k is Boltzmann's constant and μ_x is the carrier mobility. The assumption made here is that the alteration of quasi neutrality takes place both above and below the target surface.

3. The Poisson equation was used to estimate the electric field produced due to alteration of the charge in plasma:

$$\frac{\partial E}{\partial x} = \frac{e}{\varepsilon\varepsilon_0}\left(n_i - n_e\right) \tag{2.9}$$

4. The final consideration is the conservation of energy which explains the heating of the phonon subsystem in the target surface. The understanding of the energy in this case has been depicted by two temperature models:

$$C_e\left(\frac{\partial T_e}{\partial t} + \frac{J}{en_e}\frac{\partial T_e}{\partial x}\right) = \frac{\partial}{\partial x}K_e\frac{\partial T_e}{\partial x} - g(T_e - T_l) + \Sigma(x,t) \tag{2.10}$$

$$(C_l + L_m\delta\left(T_l - T_m\right))\frac{\partial T_l}{\partial t} = \frac{\partial}{\partial x}K_l\frac{\partial T_l}{\partial x} + g(T_e - T_l) \tag{2.11}$$

The values of T_e and T_i can be considered as the average energies of the electrons and lattice. The terms e, l in above equation refers to the electron and lattice parameters. C, K represents the heat capacity and thermal conductivity respectively. $\Sigma(x,t)$ is the energy source term. The term $L_m\delta\left(T_l - T_m\right)$ denotes the calculation of liquid solid surface, where T_m is the temperature and L_m is the latent heat of fusion. These energy equations represent both the thermal conductivity and carrier transport in vacuum.

2.2.5 Multiphoton ionization (MPI)

The target material studied in this thesis is tellurite glass doped with erbium ions which is dielectric in nature. The process starts with multi-photon ionization coupled with generation of secondary electrons. The source in loss terms for electrons are:

$$S_e = (W_{mph} + Q_{av})\frac{n_a}{n_a + n_i} \tag{2.12}$$

$$L_e = -R_e - PE \tag{2.13}$$

W_{mph} is the photon ionization process, n_a is the density of neutral atom. $Q_a v$ is the avalanche term, R_e represents the decay term and PE denotes the photo-electron emission. The loss of the photon-emission in the tellurite glass can be estimated by Fresnel formulae based on free electron release and optical response related to the plume. The localized intensity is based on the superposition of the direct photo-emission and back scattered light:

$$\frac{\partial}{\partial x}I(x,t) = -W_{mph}\frac{n_a}{(n_a + n_i)}\omega n_{ph} - a_{ab}(x,t)I(x,t) \tag{2.14}$$

where n_{ph} is the electron involved in the multiphoton emission process while the absorption coefficient of the free electron process, given by a_{ab}, is estimated from the dielectric response (Stuart *et al.*, 1996). To quantitatively estimate the photoemission, the key assumption made here is that the free electron motion in the broad bandgap of the target glass, in case where vacuum level is closer to the minimum conduction band, the electrons which are closer to movement

of the electrons which are normal to the surface can escape into the vacuum. Another estimation made is that at least 50% of the electrons are released in multiphoton emission and thus the avalanche process takes place on the surface of dielectric medium. The photons are emitted mainly from the surface which decreases exponentially with increasing depth into the target from the surface irradiated by the laser (Bulgakova *et al.*, 2004), and is described by:

$$PE(x,t) = \frac{1}{2}\left(W_{mph} + Q_{av}\right)\frac{n_a}{n_a + n_i} exp\left(\frac{-x}{l_{PE}}\right) \tag{2.15}$$

where l_{PE} is the electron escape depth

2.2.6 Avalanche displacement

The binding energy required to displace ions from a dielectric is significantly higher than the photon energy of the laser at low intensities. The process of displacement is driven by multi photon-ionization, in which the gain in energy of the free electron is accelerated when it strikes bound electrons. The multiple collisions of free electrons can lead to an increase in its kinetic energy to a level such that it can exceed the ionisation potential, thus resulting in the release of more free electrons. When this event advances, there can be an exponential increase in the number of free electrons, resulting in an avalanche. It is estimated that the avalanche displacement plays a major role in laser ablation by femtosecond laser pulses further after the MPI has been initiated.(Du *et al.*, 1994; Pronko *et al.*, 1998).

2.2.7 Skin effect

Due to ultra-short laser interaction with dielectric materials it is important to note that the plasma only lasts for a short duration with very high ionic density. The key feature of MPI and avalanche displacement is the release of ions with densities above the critical density n_c, thus producing an opaque plasma with an angular frequency of ω

$$n_c = \frac{m_e \omega^2}{4\pi e^2}\varepsilon_o \tag{2.16}$$

where e and m_e are the charge and mass of an electron, respectively. The plasma density > critical density are highly reflective in nature, it is localized as a standing wave just above the target creating an evanescent field. The evanescent wave entering the highly dense plasma is dependent on the electromagnetic field according to:

$$E(x) = E_0 exp\left(\frac{-x}{l_s}\right) \tag{2.17}$$

E_0 and E_x are the electric field at the boundary of plasma to vacuum. This phenomenon is called the skin effect.

2.3 Deposition process

Silica glass has been explored for possible high gain in optical waveguides. The key advantage of the technique is that structural modification in fused silica can be used to improve performance for certain tasks in optical communication, computation, and measurement. It modifies the refractive index of the doped layer. The multi-ion process of doping/implantation is complex in nature. The tellurite glasses offer structural sites for rare earth ions resulting in the possibility of large doping concentrations. However, tellurite glasses are chemically reactive in nature, also it is a soft glass limiting its use for optical applications. The transfer of Er^{3+} ions from tellurite glass to fused silica can however improve upon the low doping limits of the silica glass while improving on the inferior mechanical and thermal properties of the tellurite glass. The oxygen rich environment in silica provides the required stability to the structure. The deposition process is carried out at 700 $^{\circ}C$ and the doping depths up to several microns is achieved with a homogeneous distribution of the Er^{3+} ions, with refractive index increase from 1.45 to 1.61 in the doped layer. For solid dielectrics, including glasses, it is frequently assumed that dn/dT depends directly upon the temperature-induced change in density, ρ , but not on temperature itself. In fact,

$$\frac{dn}{dT} = \left(\frac{\partial n}{\partial T}\right)_{\rho} + \left(\frac{\partial n}{\partial \rho}\right)_{T}\left(\frac{\partial \rho}{\partial T}\right) \tag{2.18}$$

or

$$\frac{dn}{dT} = \left(\frac{\partial n}{\partial T}\right)_{\rho} - \left(\frac{\rho \partial n}{\partial \rho}\right)(\gamma) \tag{2.19}$$

where γ is the coefficient of volume expansion. Different pressures in the chamber have been used for the fabrication of optical waveguides. With increasing temperature of the substrate, a refractive index change has been reported indicating structural modification of the fused silica substrate. In order for the ions to penetrate the surface of the substrate, the kinetic energies of the ions must range from a few eV to hundreds of eVs. It has been reported that the compressive stress which is introduced by the continuous collision of ions causes surface damage. The coefficient of linear expansion is high at $\approx 700\ ^oC$ thus both of these processes provide a synergistic effect for doping of the ions on the subsurface layer.

Typical displacement energies of atoms in metals are in the order of 20 eV. With increasing ion energy, ε above the displacement energy threshold, ions penetrate increasingly deeply into the substrate. At $\varepsilon > 30$ eV (the so-called critical energy of subplantation), the maximum of the projectile distribution moves beneath the free surface of the substrate. The penetration of incoming film particles beneath the surface of the substrate reduces their mobility and contributes to the reduction of the grain size and porosity through the permanent grain renucleation. The marked decrease in the crystallite size occurs at ion energies <100 eV. The ion-induced collapse of unstable clusters on the surface of the growing film and voids beneath the surface as well as sputtering of loosely bound adatoms removes the protruding spikes and roughness. On the other hand, the growth of the outer surface roughness via surface diffusion and coalescence of adatoms in islands is suppressed due to a greatly reduced bulk diffusion in the sub-plantational growth mode. Atomic mixing processes induced by deposition and implantation of energetic particles seem to be responsible for the better film homogeneity (Eason, 2007).

2.4 Target glass

The tellurium oxide glasses have been used as target glass mainly because of there high solubility i.e. 10 to 50 time higher than the silica glass. Furthermore, they exhibit better absorption and lower phonon energy compared to the silica glass (Berneschi *et al.*, 2007; Shen *et al.*, 2006; Zhao *et al.*, 2011). The use of tellurite glass thus helps in increasing the solubility of erbium ions in the thin films implanted into the silica glass network. The target glass was fabricated in the glass fabrication laboratory in the University of Leeds. The glass samples were fabricated using the conventional melting and quenching process (Rivera *et al.*, 2007). The puratronic (99.9995% purity) powder samples of tellurium oxide, zinc oxide, sodium oxide, erbium oxide, ytterbium oxide were obtained from Alfa Aesar. The samples were then mixed in the proportions of the mole percent of each sample required in the target glass. The mortar-pestle was used to pulverise the mixture into homogeneous particle size which helps in uniform mixing during the melting process. In each batch, the mixture samples were then carefully transferred to a clean gold crucible. The crucible with powder sample were then placed in quartz cradle and heated to 850 ^oC for the sample without ytterbium oxide for about 3 hours. The mixture samples were heated to the 950 ^oC for the mixture with ytterbium oxide as the desired homogeneity for molten glass was not obtained at 850 ^oC. The mould was heated to 300 ^oC and then molten glass was filled into the mould. The annealing process was carried for about 4 hours at 300 ^oC to reduce internal stress and stressed induced by thermal shock. The composition of target glass is given in table 2.1.

Table 2.1: The composition of target glass used for the fabrication of photonic chip

Sample	Tellurium oxide	Zinc oxide	Sodium oxide	Erbium Oxide	Ytterbium Oxide
1	79.75	10	10	0.25	0
2	79.25	10	10	0.25	0.5
3	79.5	10	10	0.5	0
4	79	10	10	0.5	0.5
5	79.25	10	10	0.75	0
6	77.5	10	10	0.75	1.5

2.5 Pulsed laser deposition(PLD)

The material processing technique used in this project is femtosecond-laser plasma doping to obtain functional surfaces in dielectric substrates. The photonic chip is fabricated by a novel fabrication method of multi ion diffusion into silica glass. For the multi ion deposition, PLD exhibits a high intensity plasma plume with efficient yields around 70 %. The kinetic energy of the plasma plume can range from tens to hundreds of electron volts. Tight control over the plasma plume generation is necessary as more kinetic ions can lead to structural defects on the substrate of glass. This introduces compressive stress in the substrate. The impinging effect of energetic species leads to doping of metal ions into the amorphous substrate. The thermal control of the substrate is also necessary so as to aid the metal ions to enter the top surface of the substrate. The 3-D network of silica ions is bonded by strong covalent bonds with interstitial voids with a concentration of 10^{-22} cm^3. The metals ions tellurium (Te^{3+}), zinc (Zn^{2+}) and sodium (Na^{+}) and erbium, (Er^{3+}) were implanted using the femtosecond pulsed laser ablation and deposition method. The process is initiated by pumping down and maintaining the chamber at a pressure between 65-95 mTorr of oxygen. The substrate is maintained at a temperature of 700 ^oC during the process of the deposition. The ablation of the target glass was done using a pulse width of 100 fs and a repetition frequency of 500 Hz. It produces a plasma plume enriched with metal ions removed from the surface of the target glass. These highly energetic

particles ejected from the plasma plume, embed into the substrate's silica glass network.

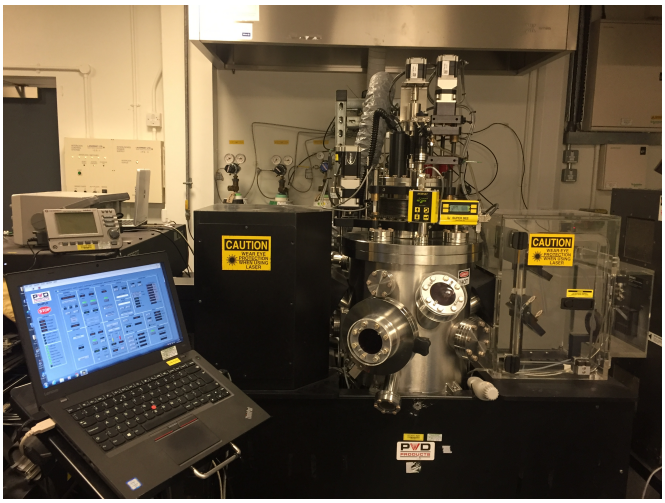

Figure 2.1: Pulsed laser deposition system

2.5.1 Construction of pulsed laser depostion

1. **Libra amplifier system:** The Libra ultrafast amplifier laser system was obtained from Coherent Inc. The Libra is Class IV laser and is enclosed in the protective housing to prevent human access to radiation. The housing has safety interlocks to make sure the laser is not illuminated whilst the top cover is open. This laser system has been constructed to amplify pulses to produce the energy up to 1 mJ at 1 kHz with linear horizontal polarization. The repetition rate can be altered from 0.25 kHz to 1 kHz with an average power of < 1 W at 1 kHz and pulse duration of approximately 100 femtoseconds with wavelength output, 800 nm. The Libra system employs a chirped pulse amplification (CPA) method in which the combination of diffracting Nd:YLF amplifier system is used to amplify the pulse to terawatt levels (fig 2.2) (Maine *et al.*, 1988).

Figure 2.2: Libra ultra fast laser amplifier system

2. **Lens Focussing assembly:** It consist of adjustable focus, mirror, step motor. The laser beam passes through the polariser to focusing lens assembly to adjust the spot size and position of laser on the target. The step motor is used to adjust the position by moving back or forward direction. The beam then passes through the Quartz window onto the target material.

3. **Target manipulator:** It consist of 6 target holder and is used to provide a dual axis rotation to efficiently ablate the target from each side. Target-holder is rotated clockwise during the manufacturing process and relative speed of target mount is set to specific number of rounds per minute. It can be used for multiple target deposition on a single substrate as well.

4. **Heater:** Its is equipped with silicon nitride heater to heat the substrate and is protected by quartz window as shown in figure 2.3. The temperature

can go up to 800 ^oC with ramp rate of maximum of 50 ^oC $/mins$. Heater is remotely controlled through eurotherm tab in the PLD software which allows you to setup the temperature range over the deposition period. Substrate holder hangs below the quartz window and rotates in anti-clockwise direction.

5. **Vacuum pump:** The pressure in the chamber is controlled by the Pfeiffer Hi pace 700 turbo pump supported by dry pump. Turbo pump works only when the pressure is below 1 mTorr and can bring down the chamber pressure to 10^{-7} $Torr$. So as to reach very low pressure to activate the turbo pump, dry pump is connected to bring down pressure to 1 mTorr.

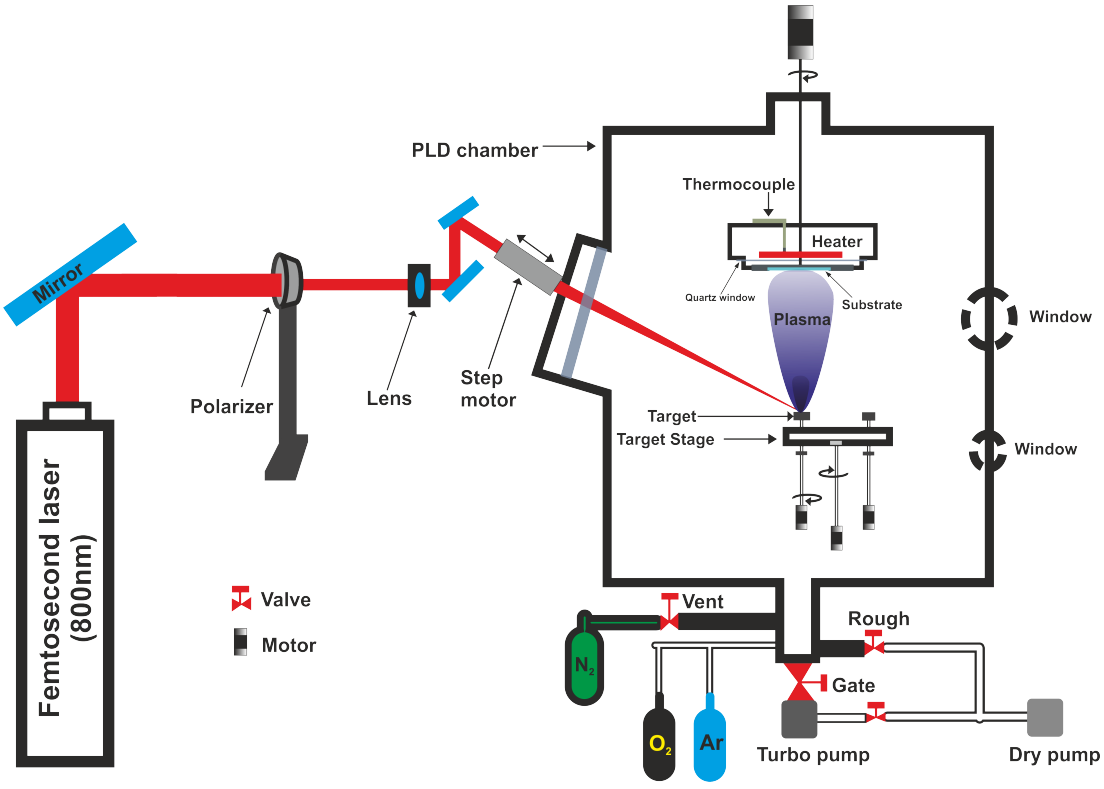

Figure 2.3: Pulsed laser deposition setup

6. **Valves:** The valve is an integral part of the chamber which helps in maintaining the chamber pressure and also remotely controlled. The VAT gate

valve is used for maintaining ultra high vacuum. The valves are also used to allow nitrogen gas to vent the PLD chamber to bring to atmospheric pressure (760 Torr).

7. **Pressure gauges:** The pressure gauge is important for monitoring pressure. During deposition, gas specific to experiment is introduced in the chamber and certain pressure. The gauge helps in monitoring pressure levels. Instrutech IGM401 Hornet, Hot cathode ion gauge is attached with the chamber. It has the capability to measure pressure range between $1e^{-09}$ to $5e^{-02}$ Torr. The ion current changes with a density of the gas in chamber thus it directly proportional to the pressure. When the chamber is purged, the ion currents drops hence the low pressure reading.

8. **Chiller:** Since the turbo pump rotates at 49,000 rpm lot of heat is produced and it is essential to maintain the temperature for the flange to work properly. The chiller is used to maintain the temperature of the turbo pump.

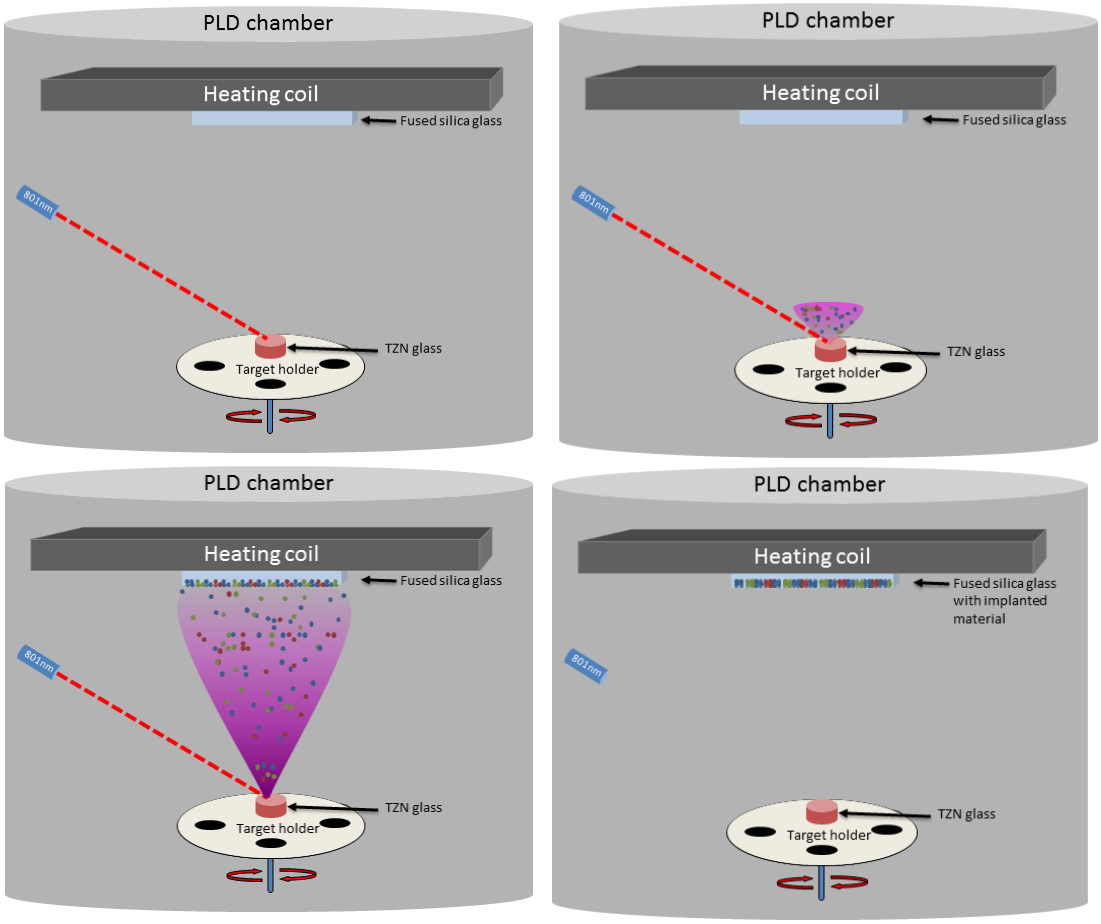

Figure 2.4: Fabrication process of photonic chip using Ultrafast Laser Plasma Implantation (ULPI)

2.6 Ultrafast laser plasma doping process

The PLD chamber is the steel frame integrated with lens assembly to focus the laser onto the target surface (fig 2.3). The pressure is monitored by VAT closed loop Gate valve with an ability to change the pressure from 1 to 500 mTorr. The target is polished to obtain a smooth surface to avoid the larger particle formation due to thermal shock caused by super-heating during the ablation process. A smooth surface of the target glass is also necessary to maintain vertical direction of the plasma to substrate which might be altered due to formation of ridges and curves on the target surface. The photonic chip is fabricated by a novel fabrication

by multi ion diffusion of ions into silica glass. The 3-D network of silica ions are bonded by strong covalent bonds with interstitial voids $10^{-22}cm^3$ (Sato *et al.*, 2011). The erbium doped tellurite glass in molar percent concentration in a ration of $(80 - xEr_2O_3)TeO_2 - 10ZnO - 10Na_2O - xEr_2O_3$. The erbium ion concentration was varied from 0.25-0.75 mol percent. Another target prepared was $(80 - (xEr_2O_3 + yYb_2O_3))TeO_2 - 10ZnO - 10Na_2O - xEr_2O_3 - yYb_2O_3$, this has Yb_2O_3 either in equal amount as erbium oxide or double the amount. The two set of photonic chips were fabricated using i.e. G series and T series and their parameters are detailed in Table 2.2 and 2.3 respectively. The metals ions such as Tellurium (Te^{3+}), (Zn^{2+}), (Na^{+}) doped with erbium ion (Er^{3+}) and co-doped in few samples with Yb^{3+} ion were implanted using pulsed femtosecond laser ablation and deposition method. The Ti-sapphire femtosecond laser with given operating conditions were used to manufacture photonic chips. The process starts by pumping down and maintaining the chamber at a low chamber pressure of oxygen. The temperature of the substrate is raised to 700 ^oC. The ablation of target glass was done by pulsed $\approx$ 100 fs laser with a frequency of 500 Hz. It produces a plasma plume of the ion released from the surface of the target glass. These highly energetic particles are ejected from the plasma plume embeds themselves into silica glass network. The femtosecond pulsed implantation creates a layer of nanometres to micron thick structural layer.

Table 2.2: The photonic chips fabricated with 0.5 mol percent erbium doped TZN glass, with oxygen chamber pressure of 70 mTorr, substrate temperature of 700 ^oC, 500 Hz trigger frequency whilst changing the femtosecond laser energy as mentioned in the table below. The substrate used is spectrosil 2000 fused silica.

Sample ID	Femtosecond Laser energy (μJ)
Ga	40
Gb	50
Gc	60
Gd	70
Ge	80
Gf	90

Table 2.3: Fabrication parameters for the photonic chip for second set of experiments with each photonic chip fabricated at 700 ^oC with altering oxygen chamber pressure, substrate temperature, altering Er^{3+}, Yb^{2+} ions in the target glass.

Sample id	Erbium concentration (mol %)	Ytterbium concentration (mol %)	Deposition Time (hours)	Chamber Pressure (mTorr)
T2	0.25	0	8	95
T3	0.25	0	8	95
T4	0.75	1.5	4	65
T5	0.25	0	4	65
T6	0.75	1.5	8	95
T7	0.75	0	4	95
T8	0.25	0.5	8	65
T10	0.5	0.5	6	80
T11	0.5	0.5	6	80
T14	0.75	0	8	65
T15	0.25	0.5	4	95
T16	0.5	0.5	6	80
T20	0.75	1.5	8	65
T21	0.25	0	4	95
T22	0.25	0.5	8	95
T23	0.5	0.5	6	80
T24	0.25	0	8	65
T25	0.75	1.5	4	95
T26	0.75	0	8	95
T27	0.75	0	4	65
T28	0.25	0.5	4	65
T29	0.5	0.5	6	80
T30	0.5	0.5	6	80

2.7 Conclusion

Photonic chips have been fabricated in two batches i.e. G series batch given in table 2.2 and T series batch given in table 2.3. The key difference between the two batches is that only the laser energy of the femtosecond laser was varied in the first batch whilst the laser energy was kept constant during the fabrication of the second batch. Table 2.1 gives the composition of target glass used in the fabrication of the photonic chips in the T series batch. The chamber pressure and duration of deposition was also varied in the T series batch. In the next section, characterisation of the photonic chips fabricated for the glucose sensing is discussed in detail.

Chapter 3

Characterisation of Photonic chip

3.1 Introduction

To standardize the manufacturing parameters of the photonic chip it is important to understand the variables which influences fluorescence lifetime (FL) decay and intensity. The FL decay of the erbium doped bulk glass lies between 3-5 ms. However, the FL decay can be increased by changing thin film deposition parameters to around 10 ms. The sensitivity of the biosensor i.e. photonic chip depends significantly on the manufacturing parameters and measures taken to optimize the light scattering to promote absorption by biomarkers. The control variables are fabrication parameters used in PLD which might have direct or indirect effects on the response variables. The primary objective of the fabrication process is to yield a photonic chip with a maximum possible linear response of changing fluorescence lifetime with increasing concentration of the glucose. The experiment conducted was in two blocks, the resolution of experiments is shortened to decrease the number of runs required. It is not necessary that all the factors will influence the linear response of the photonic chip. Therefore, the high order interaction i.e. response from all the factors is unlikely.

Table 3.1: The theoretical estimation of the variables that alter the photonic chip's chemical and optical properties (Wu *et al.*, 2003)

Control variable	**Range**	**Precision**	**Theoretical prediction**
Erbium Concentration (mol %)	0.25-0.75	1 %	Lower conc. gives a longer time decay
Yb^{3+} Concentration (mol %)	0.5-1.5	1 %	Increase in pump absorption giving higher intensity of fluorescence
Deposition Time (hours)	2-8	1 min	Longer deposition gives a thicker layer and larger fluorescence intensity
Chamber pressure (mTorr)	65-95	5	Alter refractive index

Table 3.2: The fabricated samples listed below are grouped based on similar target glass compositions but varying duration of deposition and chamber pressure. All the photonic chips have been fabricated at 65 μJ laser energy and substrate temperature of 700 ^oC.

Sample ID	Er^{3+} concentration (mol %)	Yb^{3+} concentration (mol %)	Duration of deposition (hours)	Chamber pressure (mTorr)
T1	0.25	0	8	95
T2	0.25	0	8	95
T5	0.25	0	4	65
T21	0.25	0	4	95
T24	0.25	0	8	65
T8	0.25	0.5	8	65
T15	0.25	0.5	4	95
T22	0.25	0.5	8	95
T28	0.25	0.5	4	65
T3	0.5	0	6	80
T9	0.5	0	6	80
T18	0.5	0	6	70
T19	0.5	0	6	70
T10	0.5	0.5	6	80
T11	0.5	0.5	6	80
T16	0.5	0.5	6	80
T23	0.5	0.5	6	80
T29	0.5	0.5	6	80
T7	0.75	0	4	95
T17	0.75	0	8	65
T26	0.75	0	8	95
T27	0.75	0	4	65
T4	0.75	1.5	4	65
T6	0.75	1.5	8	95
T12	0.75	1.5	1	80
T25	0.75	1.5	4	95

3.1.1 Methodology

1. The fabricated photonic chip have been grouped according to the concentration of Er^{3+} and Yb^{3+} ions in the target glass used in the deposition process as shown in the table 3.2.

2. The thin film glass samples mentioned in Table 2.2 and 2.3 were then characterised using absorption, emission spectroscopy, prism coupler, optical microscopy technique.

3.2 Structural characterization

The photonic chip as mentioned earlier has implanted thin film layer doped with Er^{3+} ions and Yb^{3+} ions. To understand how various parameters play role in defining the structural characteristic of the layer it is important to determine the thickness, refractive index, surface topography and chemical composition of the doped layer present in the substrate. So as to assess the influence of various parameters changed in the photonic chip, following techniques were used in this study.

3.2.1 Differential interface contrast (DIC) microscopy

Differential interface contrast(DIC) microscopy is a variant of the polarized light microscope in which the two wollaston/nomarski prisms are added, one on the front focal plane and one on the rear focal plane of the microscope. This aids in observing the very thin components of the sample which are otherwise invisible using a polarized microscope. The path of light is modified in a manner that the distinct objects alters the path difference between the waves crossing the sample.This helps in eliminating the halo artefacts (the edge of sample with higher refractive index shows more illuminated fringe on the outside and dark fringe on the inside of the sample). DIC measures the amplitude of optical path length which is then visible in the final image. The optical path difference of the sample is measured by multiplying the difference of the refractive index i.e. between the sample and its surrounding medium and the distance travelled by the light

between two distinct points on the optical path. The images generated by DIC have an area with clear, dark and varied colour appearance even on relatively transparent specimen. This can be misinterpreted as pseudo 3D images and misjudged as an actual topographical feature of the sample (Lang, 1982). The key feature of DIC is optical staining of the objects in the specimen thus its shows the optical shear and its direction, dense or lighter areas of the specimen (Allen & David, 1969; Hayashi, 1990).

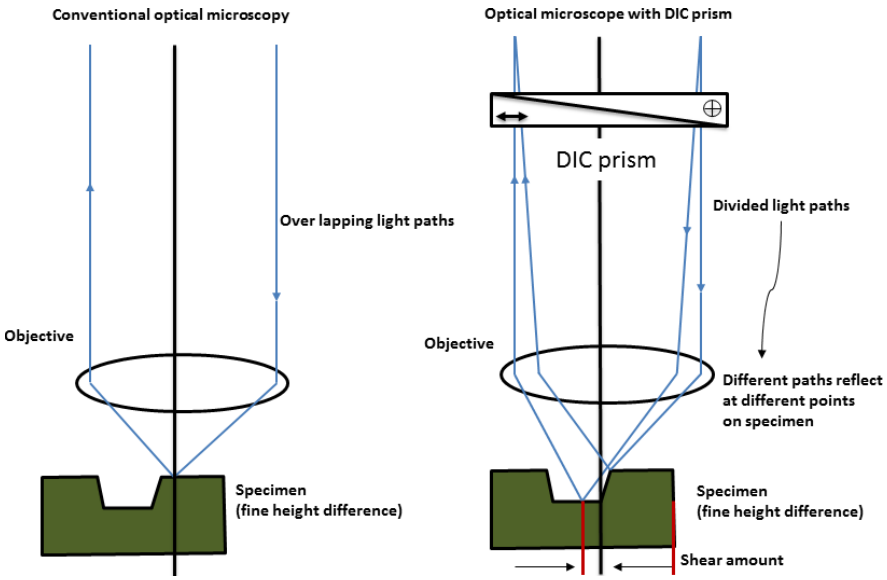

Figure 3.1: Understanding shear amount in differential interface contrast microscopy(Corporation, 2017b)

The light paths bisected by the prism and in the manner they are reflected from different regions of the specimen reveal a qualitative estimation of shear in the specimen . The optical path difference when the two light rays are bounced back passes through an objective lens and overlaps in the prism increasing the contrast of the region equal to the spatial difference of the light paths as shown in figure 3.1 (Corporation, 2017b)]. Thus the contrast of the image increase with the rise in the path difference of the light. The resolution of the image is dependant on shear amount of the specimen i.e. larger the shear amount lesser will be the resolution and vice versa (Allen & David, 1969; Corporation, 2017b). There-

fore, DIC is an essential tool for estimating the isotropy or anisotropy of optical performance of the photonic chips because shear amount determines the homogeneity of refractive index in the waveguide (Huang, 2003). The photo-elasticity or photo elastic effect is the result of the anisotropy of refractive index. This helps in determining the stress distribution in the optical waveguide. This effect is based on the birefringence which states that, when the light passes through certain optical materials they might have two refractive indices causing double refraction (Solehmainen *et al.*, 2004).

3.2.2 3D Confocal laser scanning microscopy(CLSM)

The Olympus OLS 4100 microscope is the high resolution 3D confocal laser scanning microscopy which is capable of carrying out non contact 3D surface observation of the specimen. This microscope is integrated with 405 nm laser and wavelength selection devices and z plane scanning assembly. The microscope is based on the basic epi-fluorescence principle i.e. when the polarized light is emitted from the laser system and traverses through the specimen after passing through a pinhole aperture, it crosses thereafter through a second pinhole aperture in the front of the detector. The polarized beam is reflected from a dichromatic mirror and scanned through the specific area of sample, fluorescence emitted from the sample travel through the dichromatic mirror and converged as confocal point on the detector. Since the light is only detected on the pinhole aperture detector, the background or out of focus light is not detected thus providing a better image (Claxton *et al.*, 2006; Pawley, 2006; Stelzer, 2000). This technique was used to measure the surface roughness of the photonic chip and get an estimate about the thickness and how the layer is diffused in the fused silica glass network as it doesn't show the definite boundary between doped silica layer and undoped layer.The parameters for surface roughness as recommended in ISO 4827 for thin films are as follows:

1. R_a: Arithmetical average roughness (R_a) and is measured in μm. The surface of the thin film is not an optically flat surface but more like irregular

waviness which is based on the surface quality of glass as shown in figure 3.2. The part of the example specimen shown has R_a is given by:

$$R_a = \frac{1}{L}\int_0^L |y(x)|\, dx \tag{3.1}$$

It is a measure of the area under curve above and below the central line between a sampling length, L. The roughness curve is given by $|y| = f(x)$ with x axis extending in the direction of centre line.

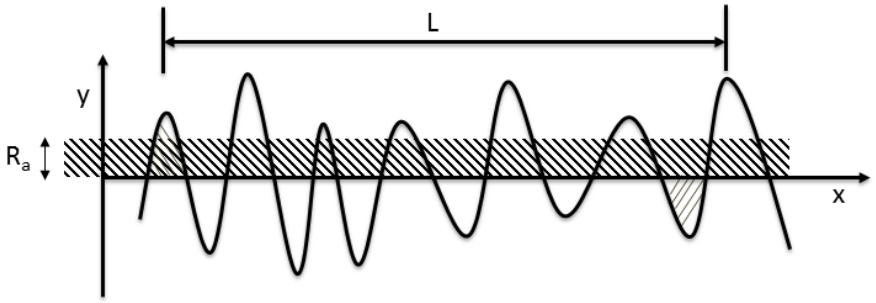

Figure 3.2: The diagrammatic representation of the specimen with y axis representing the magnitude and x axis the measuring the length of portion of the sample. Shaded pattern representing the arithmetical average surface roughness, R_a (Gadelmawla *et al.*, 2002)

2. R_y: It is the maximum height between the peak above reference line and valley of the specimen as shown in figure 3.3.

$$R_y = R_p + R_v \tag{3.2}$$

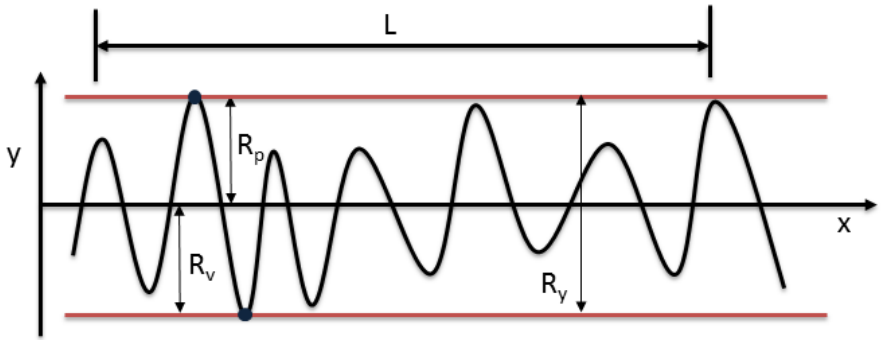

Figure 3.3: The diagrammatic representation of the specimen with y axis representing the magnitude and x axis measuring the length of portion of the sample. The maximum height (R_y) between the highest peak and lowest valley along y direction (Gadelmawla *et al.*, 2002)

3. R_z: It is the ten point average height of the surface. Considering a central line along the x axis as the reference line on the roughness curve, five highest heights above and below the reference line are measured in the given length, L. The absolute average height from these is then measured using the following equation and represented in fig 3.4:

$$R_z = \frac{(R_1 + R_3 + R_5 + R_7 + R_9) + (R_2 + R_4 + R_6 + R_8 + R_{10})}{5} \tag{3.3}$$

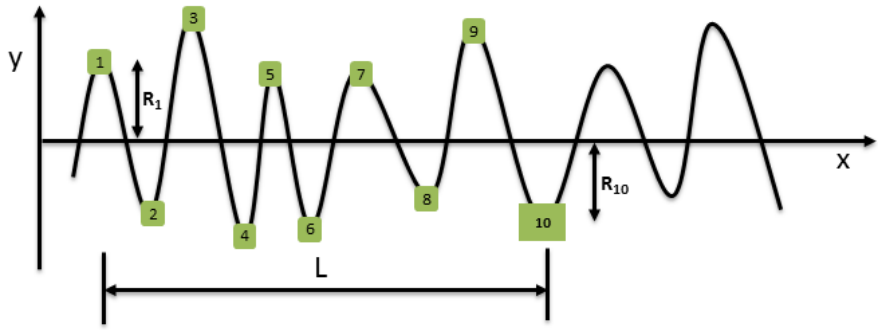

Figure 3.4: The diagrammatic representation of the specimen with y axis representing the magnitude and x axis measuring the length of portion of the sample. The ten points given on the specimen are the selected 5 highest peak points and 5 lowest valley points with central line as reference line selected to calculate the average height of the surface (Gadelmawla *et al.*, 2002)

3.2.3 Scanning electron microscopy (SEM)

Scanning electron microscope provides the high resolution surface topographical images. In SEM, an electron gun emits the electrons with energy ranging from 2-40keV. It uses field emission guns also known as cold cathode emitters which apply very high electric fields producing a brighter beam. The secondary electron beam imaging is used to detect surface topology as it is capable of detecting low energy electrons released from the top layer of the specimen (Cheney, 2007; Vernon-Parry, 2000). It is important to analyse the surface of the photonic chip to understand the level of damage or surface modification caused by the fabrication process (Murray, 2013). The sample is attached to a stainless steel stub using conductive graphite paint. This helps in keeping the specimen attached to stub and assist dissipation of the charge produced by the field emission gun. This will help in providing important information regarding characteristics of the fabrication process. The SEM used here is a Zeiss (LEO) 1530 FEG Scanning Electron Microscope (SEM) for surface imaging.

3.2.4 Transmission electron microscopy (TEM) with EDX analysis

So as to confirm the metal ions from the target glass are implanted in the fused silica glass and also to analyse the general composition of the thin layer compared to the fused silica substrate TEM equipped with energy eispersive X-ray (EDX) analysis was used. The cross section of the photonic chip which had the longest lifetime was performed using focussed ion beam sectioning. The cross section was then analysed using transmittance electron microscopy to assess the thickness of the implanted layer in the silica substrate. The energy dispersive X-ray spectroscopy was used to investigate the ions present in the implanted layer and pristine silica.

Focused ion beam cross sectioning (FIB)

The focused ion beam (FIB) uses the highly and precisely focused ion beam to prepare the cross section of a sample in nanometer to micron range. The system used here was a FEI nova 200 nanolab for the sample preparation. Before the cross sectioning process, the top surface is coated with the platinum layer in order to mask any effect produced by energized gallium ion beam on the sample. During FIB cross sectioning, a 30 keV Ga^+ ion beam is used to mill the sample in a manner that mills a thin block of sample. This sample is collected b a micromanipulator arm and transferred to a TEM grid where is it further milled to produce the desired dimensions of the specimen (Giannuzzi *et al.*, 2006; Gierak *et al.*, 2001; Latif, 2000).

Transmission electron microscopoy (TEM)

Transmission electron microscope employs an electron gun and multiple magnetic lenses to focus the beam of electrons onto the sample. It consists of the illumination system where the electron gun emits the eletcrons which is then traversed through the vertical stack of condenser lenses to focus the electrons onto the specific point of the sample. In the specimen stage the sample is either kept stationary or moved across if required, in order to provide better spatial resolution of the specimen. The imaging system of the TEM is equipped with at least three

magnetic lenses to produce a highly magnified image of the sample on the CCD detector (Egerton, 2005; Ma *et al.*, 2006). The system used here is FEI Tecnai TF20 Field emission gun TEM with Oxford Instruments INCA 350 EDX system.

Energy dispervse Xray analysis (EDX)

Energy dispersive X-ray analysis is used to carry out elemental mapping of the cross section of the photonic chip. The EDX analysis was done using an Oxford Instruments INCA 350 EDX system. In the EDX system, the high energy X-rays are focused on the sample. At the ground state the electrons are present in specific energy levels, whilst the beam focused on the sample the electron from the inner most shell is released causing an electron hole pair. The transfers of electrons from the outer shell takes the place causing an energy imbalance which causes release of x-rays. The energy of the beam is recorded by the spectrometer which corresponds to the specific element's atomic structure. This helps in revealing the element and its approximate quantity in the specimen (Van Grieken & Markowicz, 2001).

3.2.5 Prism coupler

Metricon model 2010 prism coupler, an optical waveguiding method was used to measure the thickness, optical modes, refractive index of dielectric layers i.e. thin films. The prism coupler consist of a coupling head and prism which can measure a specific range of refractive indices (Adams *et al.*, 1979; Liu *et al.*, 2008). The sample is kept in between the coupling head and prism(fig 3.5). There is a small air gap between the prism and the thin film. The laser beam is introduced from one side of the prism and refracted in a manner such that it strikes the detector under normal conditions. However, as the stage is rotated, at certain incident angle the laser beam enters the thin film causing a drop in intensity which is known as the mode angles. At these incident angles, photons from the beam enter an optical prorogation mode, which determines the refractive index of the thin film (Kersten, 1975). There can be multiple intensity drops when the laser beam couples into the thin films and finally with substrate which indicates the number of modes present in the thin films. The discrete incident angles at which

the different modes are found determines the thickness of the thin film in the photonic chip.

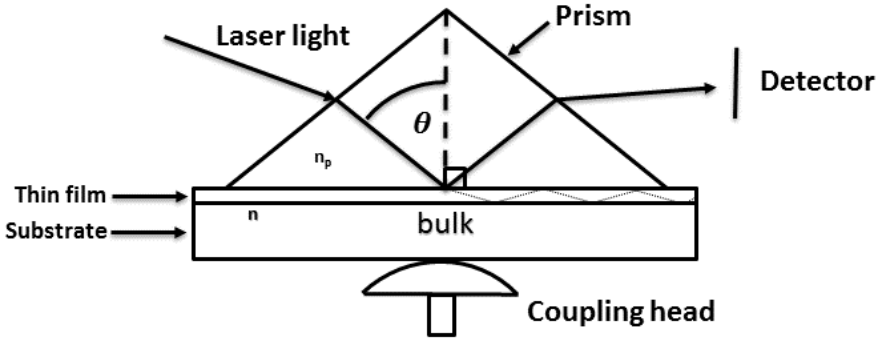

Figure 3.5: Principle of prism coupler (Ibrahim *et al.*, 2006)

The angle θ of incident angle of laser beam on the prism determines the coupling of the light into the thin film. The angle θ measures the phase velocity of the beam which is given by:

$$\upsilon^{(i)} = \frac{c}{n_p} sin\theta \tag{3.4}$$

where n_p is the refractive index of the prism, $\upsilon^{(i)}$ is the phase velocity and c is the speed of light. When incident phase velocity i.e. $\upsilon^{(i)}$ equals the phase velocity υ_m of the propagation mode at certain discrete angle the coupling of light occurs. The polarization of the laser beam ρ, can be either transverse-electric (TE) where $\rho = 0$ or transverse magnetic (TM) where $\rho = 1$, which follows different propagation constants. Hence, by analysing the strongest angle of coupling the specific propagation constant can be calculated which is given by

$$\tilde{N}_m = \frac{c}{\upsilon_m} = n_p sin\theta_m \tag{3.5}$$

This technique has a key advantage that it is quite convenient to measure the thickness and refractive index of the thin film with precision. However the film must be sufficiently thick so that at least two modes are supported by the medium, which is required to determine the thickness of the medium. If only one mode is found either refractive index or thickness of the thin film can be

calculated (Corporation, 2017a; Tien, 1971; Ulrich & Torge, 1973). The value of the refractive index and thickness is given by the dispersion equation, for instance if we consider TE polarization, the dispersion of three layers will be (Ibrahim *et al.*, 2004a) :

$$\tan k_{2x}d = \frac{k_{2x}(\gamma_1 + \gamma_3)}{k_{2x}^2 - \gamma_1\gamma_3} \tag{3.6}$$

where:

k_{2x}: transverse polarization constant for thin film layer

γ_1: transverse polarization constant for prism

γ_3: transverse polarization constant for substrate

d: Guide layer thickness

The parameters can be further extended to

$$\tan(k_o d\sqrt{n_2^2 - n_{eff}^2}) = \frac{k_o\sqrt{n_2^2 - n_{eff}^2}\left[\left(k_o\sqrt{n_{eff}^2 - n_1^2}\right)\left(k_o\sqrt{n_{eff}^2 - n_3^2}\right)\right]}{k_o^2\sqrt{n_2^2 - n_{eff}^2} - \left[\left(k_o\sqrt{n_{eff}^2 - n_{e1}^2}\right)\left(k_o^2\sqrt{n_{eff}^2 - n_3^2}\right)\right]} \tag{3.7}$$

where k_o is the propagation constant. From equation 3.7, the refractive index of the guiding layer can be calculated according to the reference refractive index of the substrate at a given wavelength, λ. Only limitation of this technique is that it requires a minimum of two modes to calculate the refractive index, n_2. Further the thickness, d of the thin film is calculated (Ibrahim *et al.*, 2004a, 2006).

3.3 Molecular spectroscopic characterization

3.3.1 UV-Vis-IR absorption spectroscopy

The absorption/transmission measurement were carried out using the Perkin Elmer Lambda 950 UV/Vis/NIR spectrophotometer. It is base on the principle that when electromagnetic radiation of a certain wavelength is transmitted through a material under investigation, part of light is absorbed/reflected back by the material and rest of the emitted light is received by the detector. This

technique is based on the Beer-Lambert law which states that when monochromatic radiation of specific energy is passed perpendicularly through an absorbing medium with length b (solid, liquid, gas) above the threshold intensity I_o, the photons are captured by the ions/molecules/atoms media and resultant energy obtained on the other side of the medium is reduced to intensity, I.

$$A = log\frac{I_o}{I} = \epsilon bc = -logT \tag{3.8}$$

Considering the cross section of the sample S with thickness dx. Assuming that this surface contains particles which will cause photon capture and photon will be instantly absorbed while passing through this medium. The area where the absorption occurs is dS and ratio to the whole capture area will be dS/S which denotes the chance of photon to be absorbed by the medium. The intensity absorbed is dI_x compared to the initial intensity i.e. I_x which is directly proportional to the porbablity of photon captutred by the medium (eq 3.9).

$$-\frac{dI_x}{I_x} = \frac{dS}{S} \tag{3.9}$$

Now, as mentioned earlier dS denotes the infinitesimal capture medium of the total project area , thus it will be proportional to the number of molecules/ions present in that medium.

$$dS = adn \tag{3.10}$$

where dn represents the number of ions and a is the constant of capture cross section. Integrating equation 3.2 and 3.3 between 0 to n we obtain,

$$\int_{I_0}^{I} \frac{dI_x}{I_x} = \int_0^n \frac{adn}{S} \tag{3.11}$$

which after integration gives

$$-ln\frac{I}{I_0} = \frac{an}{2.303S} \tag{3.12}$$

where n is the total number of particles. For the cross section S with volume V and length b yields the equation,

$$S = \frac{V}{b} \tag{3.13}$$

and combining wih equation 3.12 and 3.13 gives,

$$-ln\frac{I}{I_0} = \frac{anb}{2.303V} \tag{3.14}$$

Volume in this case will be represented as cubic centimetre or litres and n is number of moles of particles inside the medium. Thus n/V will be the overall concentration of the medium i.e c and, ϵ gives the equation :

$$log\frac{I_o}{I} = \epsilon bc = A \tag{3.15}$$

Instrumentation

The Perkin Elmer Lambda 950 is dual beam spectrometer in which the light from the source i.e. deuterium/tungsten lamp is splitted into two beams by a V shaped mirror. One beam passes through the reference and other beam crosses the sample to a photomultiplier detector. The output signal is then amplified and the ratio from reference to sample is displayed on the readout device.

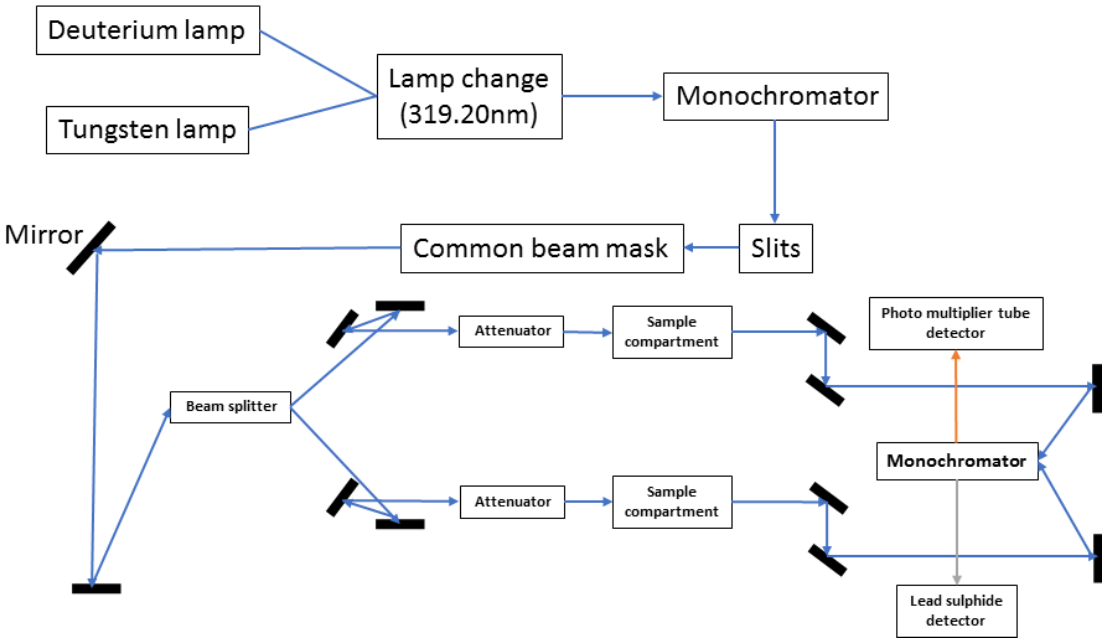

Figure 3.6: The inside layout of double beam absorption spectrometer (Faust, 1992).

The monochromator is used to filter the beam to emit a specific wavelength at a given time and the range measured in this experiment was in the near infra-red region i.e 1000-1800nm. Several attempts were made to measure the absorbance of the dopants in the samples due to low concentration of the rare earth dopants. However, transmittance of the thin films were measured (Faust, 1992).

3.3.2 Fluorescence spectroscopy

Fluorescence spectroscopy is a type of emission spectroscopy. When the fluorescent ion is supplied with energy more than the threshold energy, its electrons are transferred from the ground state to excited state. Whilst the electrons return from the excited state to the ground state it passes more than one energy level and it releases energy of specific wavelength. The spectrophotometer used in this research is FLS 920 fluorescence spectrometer from Edinburgh Instruments. The excitation wavelength used was 980 nm to obtain emission from Er^{3+} ions in the range of 1400 to 1700 nm (fig 1.3). The fluorescence lifetime is characteristic for each rare earth ion and it varies because of the resonant energy of the adjacent molecules. It is one of the most sensitive instruments as it has capability of single photon counting with effectively high resolution and remarkable stray light rejection capability. It has efficiency of peak count rate more than 750,000 cps. This technique is used to measure the fluorescence emission from the Er^{3+} ions.

Instrumentation

The spectrometer used for the measurement of fluorescence emission spectra and lifetime is described in figure 3.7. It consists of three monochromators all of which serve the purpose of separating a specific narrow bandwidth of light source or emission collected from the sample. The black dashed box in fig 3.7 were not used in the experiment however they are the part of spectrometer. The absorption wavelength for Er^{3+} ion is 980 nm, which involves absorption from ground state $^4I_{15/2}$ to $^4I_{11/2}$ energy level. While the rapid release of energy takes place when electron returns from $^4I_{11/2}$ to $4^4I_{13/2}$ with non radiative phonon emission. The longer wavelength with broad multi photon emission is observed at 1540 nm when electrons decay from $^4I_{13/2}$ to $^4I_{15/2}$ energy levels. In this case, 980 nm excitation

is required for optical transition thus the external source of 980nm class 3B laser was used in continuous form for emission spectroscopy and pulsed form in case of fluorescence lifetime measurements. Slits present in instrument are used to adjust the resolution of the scan. The instrument has UV-visible photomultiplier tube which measures from 200 nm to 850 nm and Near infra-red photomultiplier tube which measures from 850 to 1800 nm. NIR PMT is cooled by liquid nitrogen and maintained at -80 ^oC.

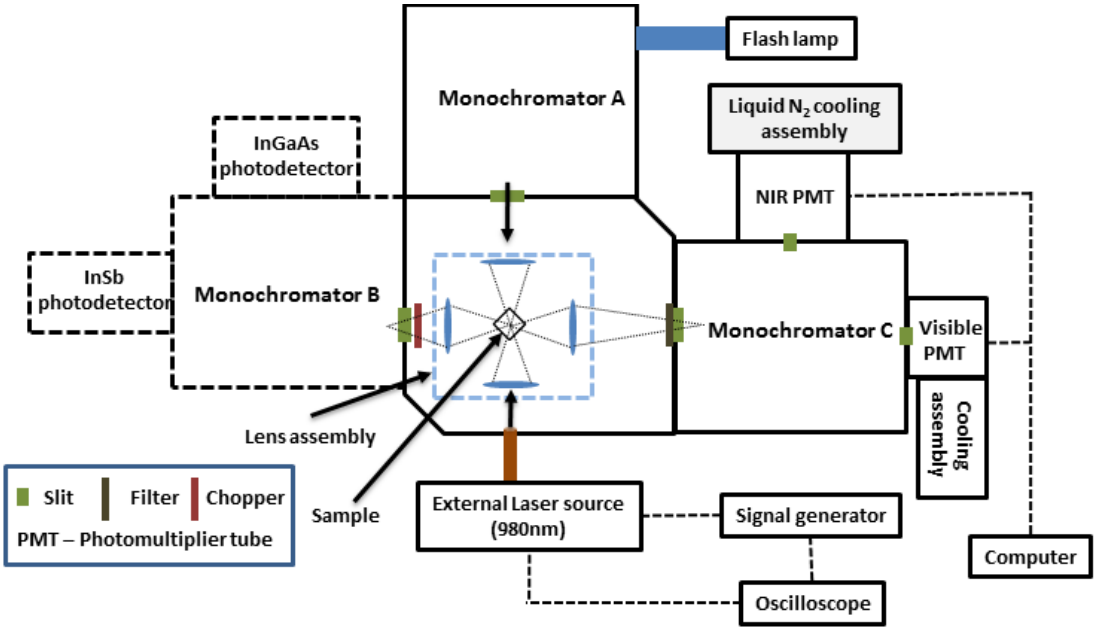

Figure 3.7: The inside layout of Edinburgh instruments FLS920 fluorescence spectrometer (Murray, 2013)

The signal generator is used to modulate a continuous wave diode laser and pulses ranging in the duration from 10 μs to 10 ms were used. An oscilloscope is used in conjugation with the signal generator to visually analyse the laser pulse. The sample is kept within the lens assembly and light is reflected perpendicularly to the monochromator through the slit. A silicon filter is placed at the slit to block the pump light from the monochromator and detector from wavelength below 1200 nm. The measurement is carried out from 1400 to 1700 nm which is emission bandwidth of Er^{3+} from the $^4I_{13/2}$ to $^4I_{15/2}$ energy levels (Murray, 2013).

3.3.3 Fluorescence lifetime spectroscopy

Fluorescence is the key parameter of the photonic chip which is being utilised in the sensing of glucose which has been discussed in detail in literature review. This parameter varies based on different parameters used in the fabrication of photonic chip. The fluorescence lifetime measurement were carried out with the same instrument mentioned in section 3.2.3. The pulse width of the 980 nm laser used for the fluorescent lifetime measurements is 100 μs. The fluorescence lifetime of the samples mentioned in table 2.2 and 2.3 were measured.

3.4 Results and discussion

3.4.1 Differential interface contrast (DIC) microscopy results

The DIC results give a gradient of the stress induced by the density or thickness of material implanted in the photonic chip. It is important to note that these images do not reveal the detail about thickness and the refractive index of the thin film. However, can be useful in assessing the homogeneity of refractive index of the thin films. All the Tseries photonic chip batch (table 2.3) were analysed using DIC however only four samples are shown in figure 3.8 to give a representation of the surface modification of thin films. The centres of the sample were analysed using a 50x objective lens. The denser regions which are darker in colour are observed on the surface of the photonic chip indicating the phase difference might be due to shear stress created on the surface as a result of fabrication. The key reason to understand the surface of the photonic chips is to optimise their optical performance. The stress introduced on the surface can cause the heterogeneous distribution of refractive index which might change the optical mode shapes of the waveguides (Huang, 2003). The samples were wiped with methanol and then dried with clean lint free lens tissue, finally dried with air duster to make sure no lint or methanol residue is left on the surface of the photonic chip.

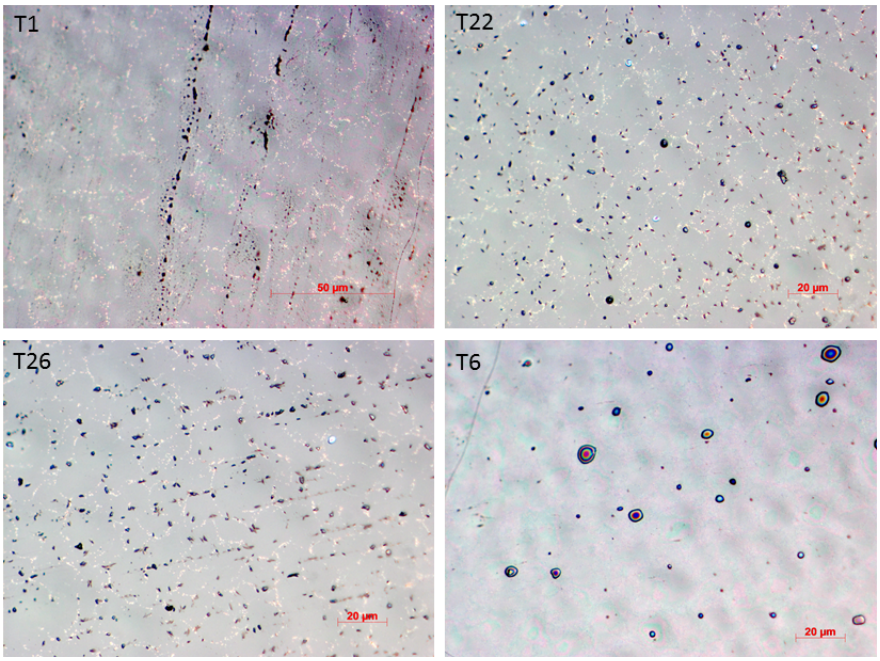

Figure 3.8: Comparison of the four photonic chips fabricated at deposition duration of 8 hours and at chamber pressure of 95mTorr with increasing concentration of Er^{3+} ions. (T1) 0.25 mol percent Er^{3+}, (T22) 0.25 mol percent Er^{3+} and 0.5 mol percent Yb^{3+} , (T26) 0.75 mol percent Er^{3+}, (T6) 0.75 mol percent Er^{3+} and 1.5 mol percent Yb^{3+}.

The photonic chip T1 (fig 3.8) shows no significant phase difference and dark regions indicating that the material implanted doesnt show notable shear stress. This is important because it reflects whether the polarization is isotropic or anisotropic. The clear phase difference can be observed in T6, whilst T1 appears to have more clear resolution of the image indicating the increased shear which can be because of more densely implanted ions in the thin film inducing larger stress in the film. T6 also has more peaks marked by darker contrasts, thus making the surface rougher than the T1. T22 also appear to be clearer than the T26 sample which might indicate the increase in density of the material in the thin film there is possible presence of anisotropy in refractive index which may effect the optical performance of the photonic chip. This phenomenon is known as photo-elastic effect (Sapriel, 1979; Xu & Stroud, 1992). This can be due to

changes in the local density of the optical states and also presence of excess silicon sensitizers in the doped layer causing high stress in the medium, thus can increase the amount of photons emitted from the doped layer (Cueff *et al.*, 2011).

3.4.2 3D Confocal Laser scanning microscopy (CLSM) results

3D microscopy was used for the topographical analysis of the photonic chip. It gives an estimation on how th surface alters as a result of fabrication. Four photonic chips were analysed using this method. As the microscope was only available for the demonstration for a short period more samples couldn't be analysed using this technique. However, these samples give an insight into the surface characteristics of the photonic chip. Spectrosil 2000 has surface quality of 60/40 which is considered as commercial quality. 60/40 standard is defined as the apparent width of the scratch is 60 μm and the allowed dig diameter is 0.4 mm. However, as defined in section 3.2.2 the parameters R_a, R_y, R_z were measured to assess the surface quality of the substrate doped with thin films. The sample doping parameters, deposition time and the chamber pressure of the samples measured is given in table 3.3 .

Table 3.3: Sample fabrication parameters of the photonic chips measured using 3D CLSM

Sample	Er^{3+} concentration (mol %)	Yb^{3+} concentration (mol %)	Deposition time (hours)	Chamber pressure (mTorr)
T2	0.25	0	8	95
T7	0.75	0	4	95
T15	0.25	0.5	4	95
T16	0.5	0.5	6	80
T29	0.5	0.5	6	80

The cross section of T2 photonic chip with fabrication parameters as mentioned in the table 3.3 was analysed. Using the silica substrate as the reference at a depth more than 10 μm from the surface a cross section image was obtained. The white region on the upper portion of the specimen indicates the implanted materials, based on the difference in refractive index of the material as compared with the fused silica as shown in figure 3.9. Though the stoichiometric description about implanted material cannot be obtained with this technique, it gives an idea about the depth of the layer implanted in the substrate and its refractive index.

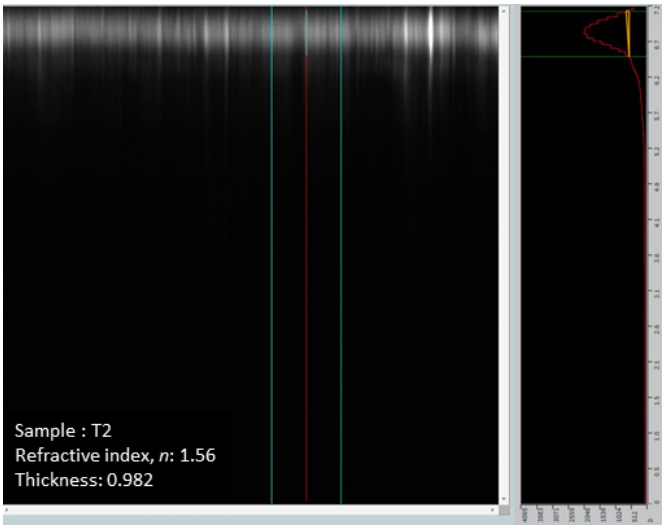

Figure 3.9: Cross section of T2 sample with white region depicting the implanted layer across the substrate

The thin film obtained through pulsed laser deposition is evenly distributed across z plane of the cross section (fig 3.9). The thickness obtained was 0.982 μm and refractive index is 1.56. Thorough analysis of thickness and refractive index has been done using prism coupler due to limitation of the availability of the microscope to measure other photonic chips.

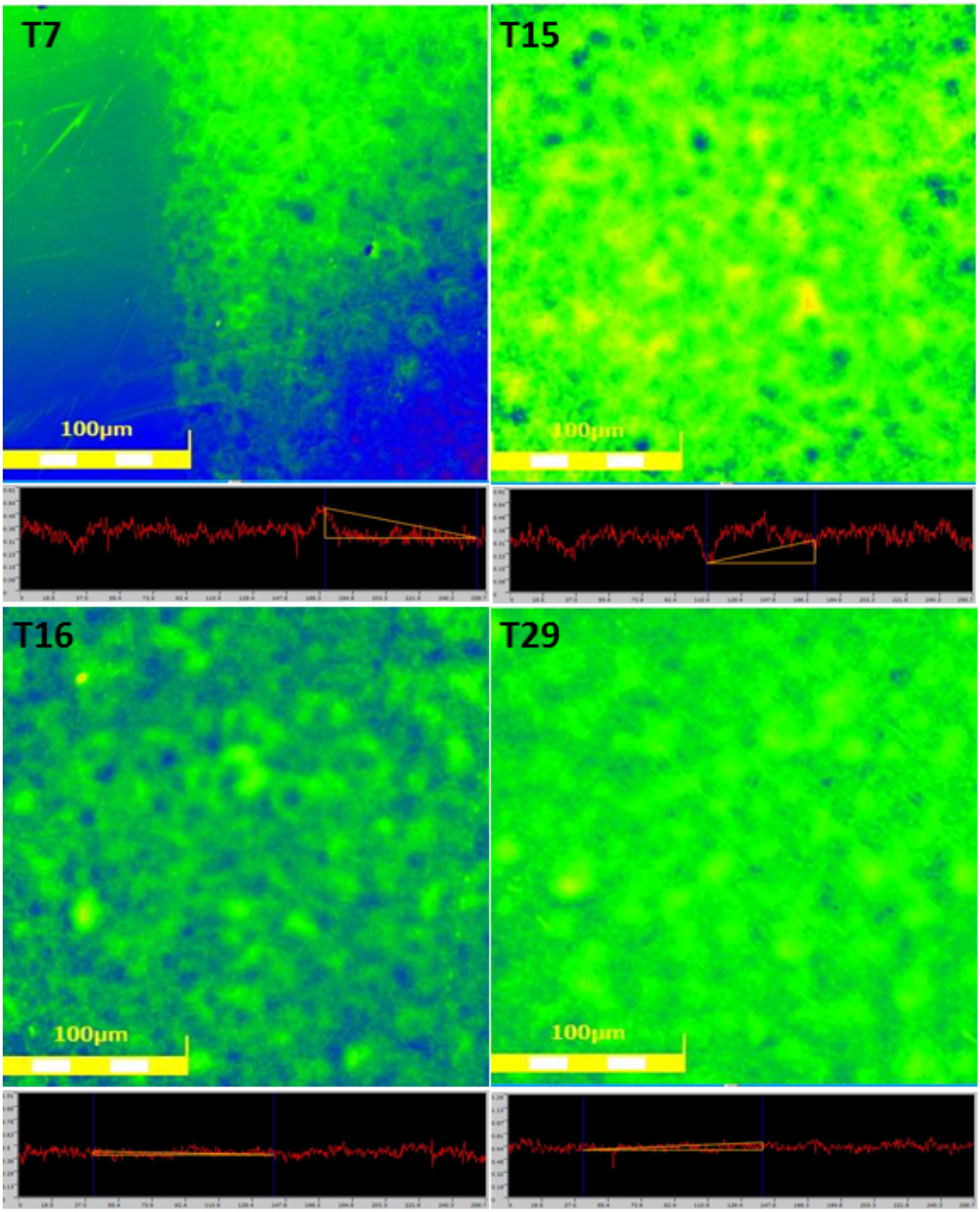

Figure 3.10: The part of sample photonic chips showing contour image depicting different heights on the surface and given below with each image is the surface profile of photonic chips

The surface characteristics of the four photonic chips as given in table 3.3 were analysed using 3D CLSM. In T7 the surface was analysed from one edge of the substrate(fig 3.10). The greenish blue region from the left side to the part where the green boundary starts is the pristine silica while the greener region is the implanted region. The clear distinction of the implanted layer shows that the doped material doesn't diffuse to side of the photonic chip which is covered in the substrate holder during PLD deposition process. The greenish colour in pristine silica is an optical background effect and should not be misinterpreted with the implanted region. A z axis scan of the same T7 image has an average surface roughness (R_a) $\approx 0.007\ \mu m$ indicating a fairly flat surface. It also indicates that the target material is implanted into the surface not as a coating on the top of the substrate as the surface graph below the T7 image show no visible increase in the peaks from the edge of the photonic to doped region. The maximum height, R_y of the surface is $0.034\ \mu m$ which is from the botton of the crater to top of the peak (table 3.4). This peak might be due to an existing scratch on the surface or possible release large particle of material released from the target which could not penetrate the surface as it doesn't show any fringe patterns or high shear stress on the surface of the chip.

Table 3.4: Surface roughness results of four photonic chips measured with 3D microscope

Sample	$R_a\ (\mu m)$	$R_y(\mu m)$	$R_z(\mu m)$
T7	0.007	0.034	0.044
T15	0.006	0.026	0.033
T16	0.006	0.026	0.035
T29	0.006	0.028	0.028

The T16 sample shows the maximum uneven surface compared to the other 3 samples indicating the higher shear stress in the surface. This could be related to the fabrication process as if the laser pulse duration is not stable enough the different femtosecond pulse durations can cause release of varied particle size from

the target material. The inhomogeneity in the particle sizes released from the target surface can cause an uneven implanted surface. The shear stress induced in the surface can cause an anisotropic distribution of refractive index (Huang, 2003). This causes incoherence in the emission of light from the thin film which follows in the direction of high refractive index region and also causes the uneven emission photons from the surface of thin film (Zhong *et al.*, 2013). T29 has a desirable surface due to homogeneous distribution of the implanted layer and less indication of stress produced in the surface due to implanted material, R_a = 0.006 μm and lowest absolute average height of 0.028 μm comparing to the other measured samples. T15 shows upward growth of material shown by more prominent yellow regions in the z plane. The height amplitude variations lead to phase fluctuations causing increased scattering from the surface (Harvey, 1976).

3.4.3 Scanning electron microscopy (SEM) results

The SEM micrograph of the Ge sample (table 2.2) was done before the FIB section to assess the surface of the photonic chip. Multiple craters can be observed on the surface of the substrate (figure 3.11). The diameters of the craters were measured and varied from 0.19 to 0.46 μm. The presence of the craters is unusual as no formation of craters has been reported on the substrate surface from pulsed layer deposition previously. The direct surface damage to fused silica from laser pulses has been reported in various articles (Couairon *et al.*, 2005; Sudrie *et al.*, 2002), however due to different impact and kinetics of laser compared to the plasma, it will not be relevant here.

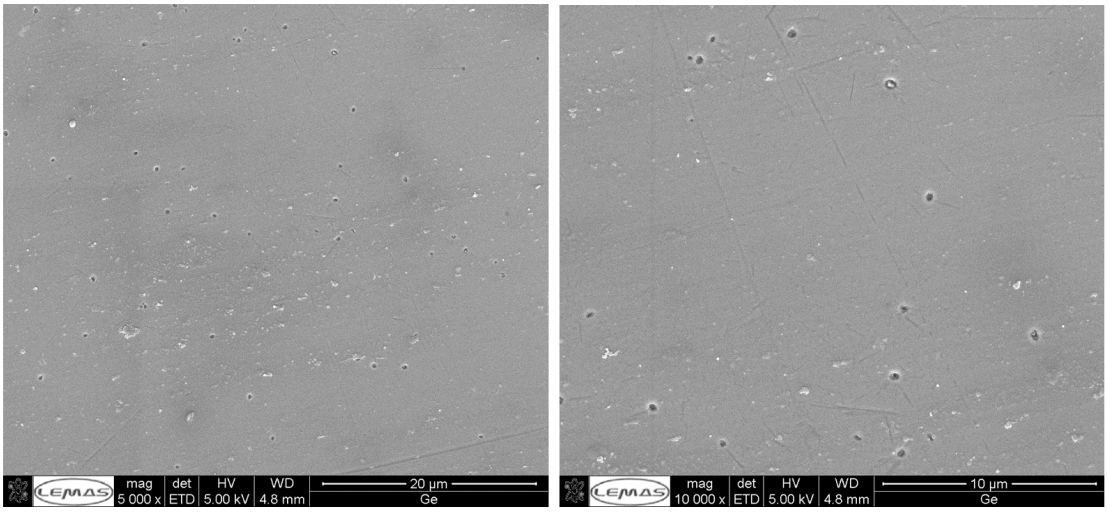

Figure 3.11: SEM micrograph of the amorphous silica substrate taken at 5 keV with magnification of 5000x (left) and 10000x (right).

3.4.4 Transmission electron microscopy (TEM) and energy dispersive x-ray (EDX) results

TEM micrograph of the surface of a photonic chip Ge, carried out at 5000x magnification shows the area from which FIB sectioning has been carried out as shown in figure 3.12 and the extracted cross section of the SiO_2 substrate with the implanted region. The top dark region of Ge cross section is the platinum layer which is used to inhibit any effect of Ga ions beam. The target materials used were in the ratio $79.5TeO_2 : 10ZnO : 10Na_2O : 0.5Er_2O_3$ mol percent, with 70 μJ of laser energy, 6 hours deposition time and 500 Hz frequency.

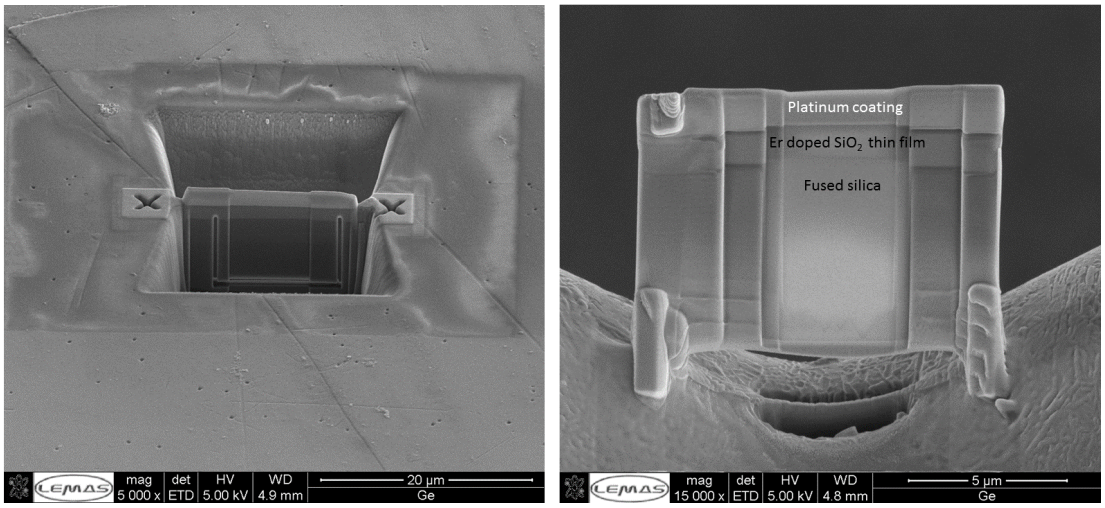

Figure 3.12: Drilled surface of Ge photonic chip (left) and FIB cross section showing different layers of the photonic chip (right) .

Fig 3.13 is the TEM micrograph of the cross section removed from the photonic chip. A distinctive layer sandwiched between the platinum layer and fused silica is visible. A distinctive boundary between the Er^{3+} doped silica layer and fused silica glass below is visible which is shown in higher magnification in fig 3.13 (right). This layer looks very similar to what has been reported in the literature (Chandrappan *et al.*, 2015) where a similar composition of the target material and substrate has been used. The thickness of the layer is 1.54 μm. Fig 3.13 (right) shows the homogeneous distribution of nano-material in the implanted region between the silica network.

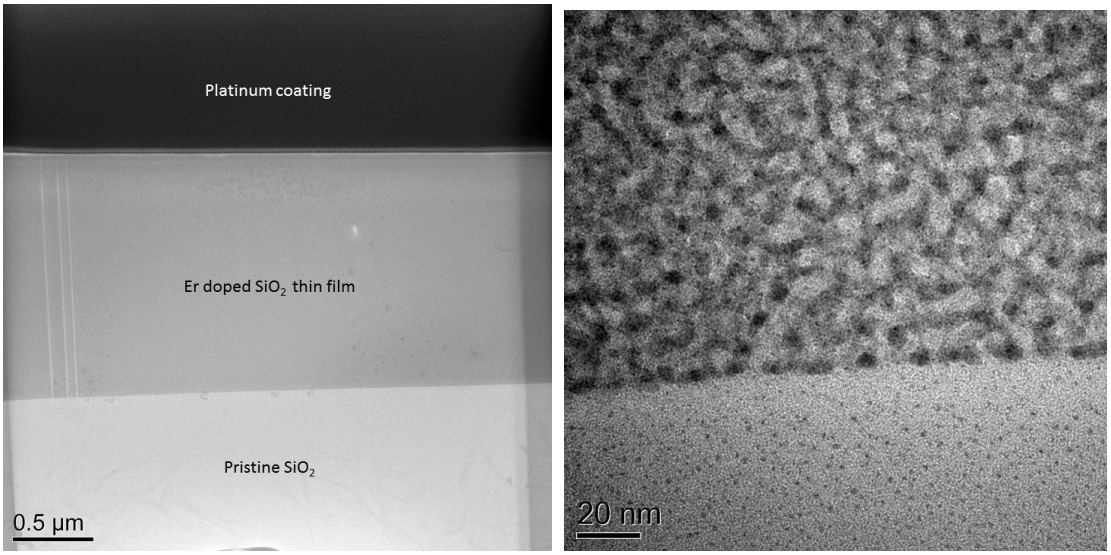

Figure 3.13: TEM micrograph of the Er^{3+} doped SiO_2 thin film which appear more darker than the pristine silica (left). The magnified TEM micrograph showing the distinctive boundary between pristine SiO_2 and doped thin film (right).

Furthermore, the EDX analysis was carried out to estimate the chemical composition of the material implanted in fused silica. The incorporation of $Te^{4+}$and Er^{3+} ions can be noted in the thin film as compared to the silica substrate. The rise in O^{2-} ions as shown in EDX spectra (fig 3.14 (bottom)) has been found previously to enhance the fluorescence intensity of Er^{3+} ions (Favennec *et al.*, 1990; Lourenço *et al.*, 2016). It is also noted that oxygen doping (due to fabrication of the photonic chip in oxygen environment) in silica with Er^{3+} ions cause an increase in the solubility of the Er^{3+} ions (Lourenço *et al.*, 2016; Matsuoka & Tohno, 1995). The tetrahedral structure of Er^{3+} surrounded by 6 O^{2-} atoms has been theoretically suggested as the ideal stable configuration thus an increased oxygen presence and decreased silicon concentration can be attributed to the spaces occupied by Er^{3+}-oxygen complex in silica network (Carey, 2002; Wan *et al.*, 1998). The presence of Cu element in silica has been reported in spectrosil but less than 0.01 ppm (Quarzglas, 2009) which shifts in the EDX of thin film indication change in Cu coordination in the silica environment due to the presence of Er^{3+} ions.

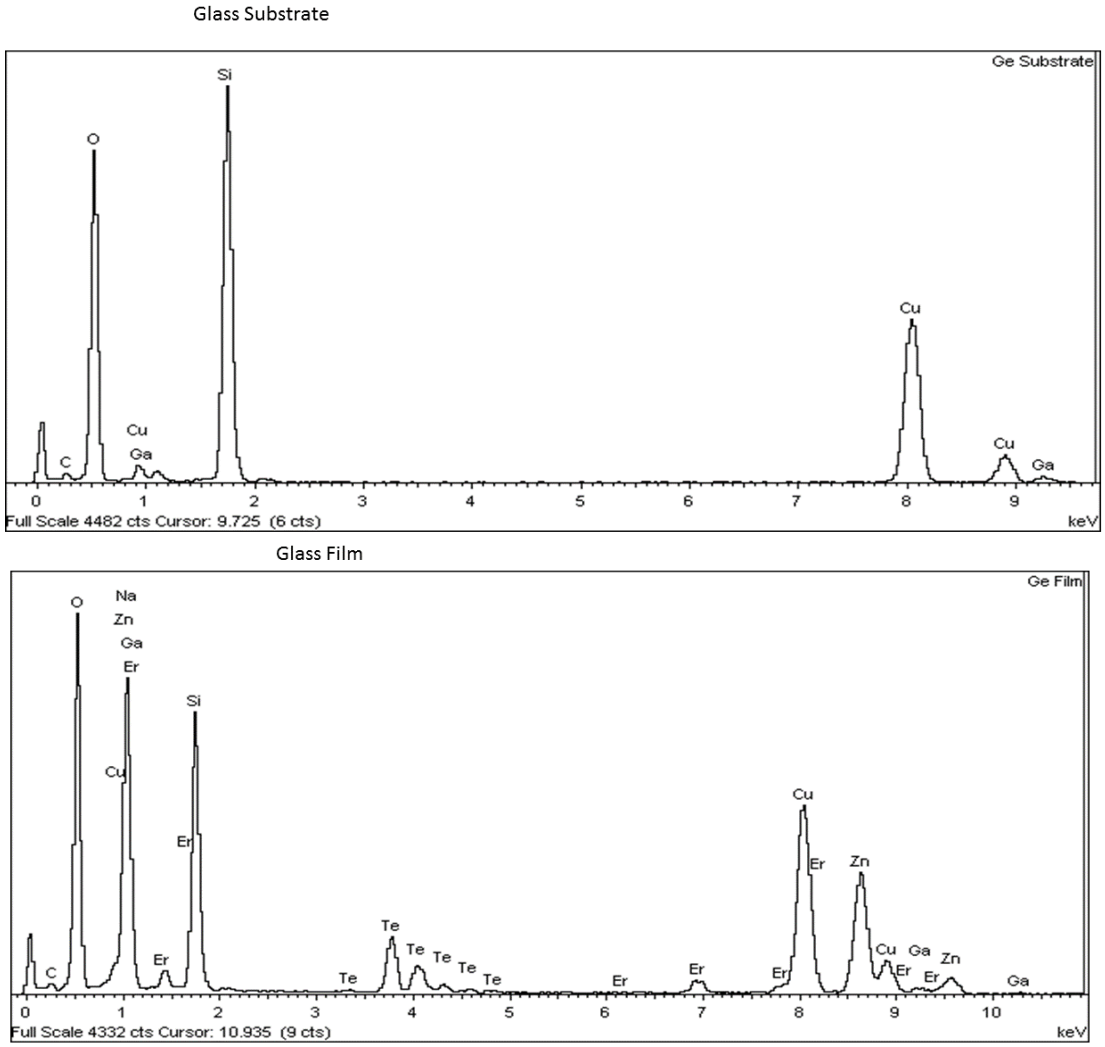

Figure 3.14: Energy Dispersive X ray graph shows the comparison between the thin film and glass substrate.

Increase in the Na^{+}, Zn^{+} and Te^{4+} ions is also evident from the EDX graph in fig 3.14 (bottom). The presence of Te^{4+} ions is less than the other ion whilst it has a higher concentration in Er/Yb doped TZN glass indicating lesser solubility in the silica glass. This might be related to the fact that the more volatile material during femtosecond laser ablation is lost when released from the surface of the target glass thus altering the stoichiometry of the thin film (Balling & Schou, 2013).

3.4.5 Prism coupler results

Prism coupler results were carried out on the G series and T series photonic chip batches using the Metricon model 2010 prism coupler. TE modes were measured at 633 nm while TM were measured only when one mode was found to measure thickness of the implanted layer. The photonic chip surface was cleaned with isopropanol and then air dusted to remove any dust particle from the surface. The thin film side of the chip was placed in contact with the prism. The mode from each samples were measured and then software calculated the thickness and refractive index based on the number of modes. The reference material was fused silica and the reference refractive index was set to 1.45. Figure 3.15 shows number of the modes obtained from different photonic chips. Sample from T24 to T3 are in the descending order of number of modes and for T3 sample TM polarization was also measured to calculate the thickness of the photonic chip.

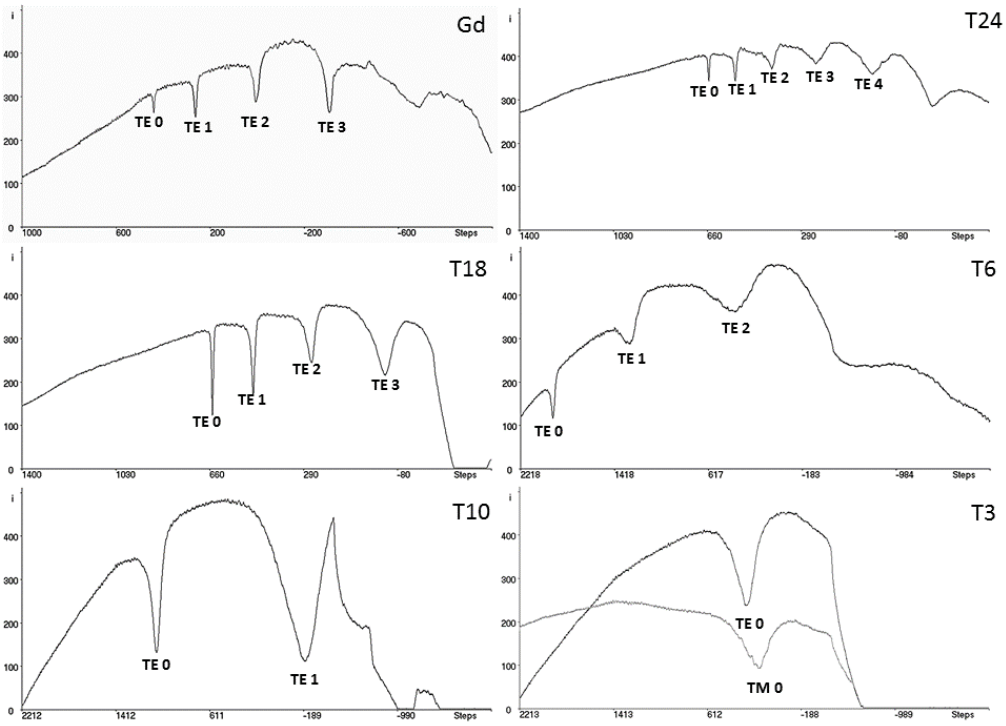

Figure 3.15: Example of prism coupler measurement of the different photonic chips showing different optical modes and refractive index

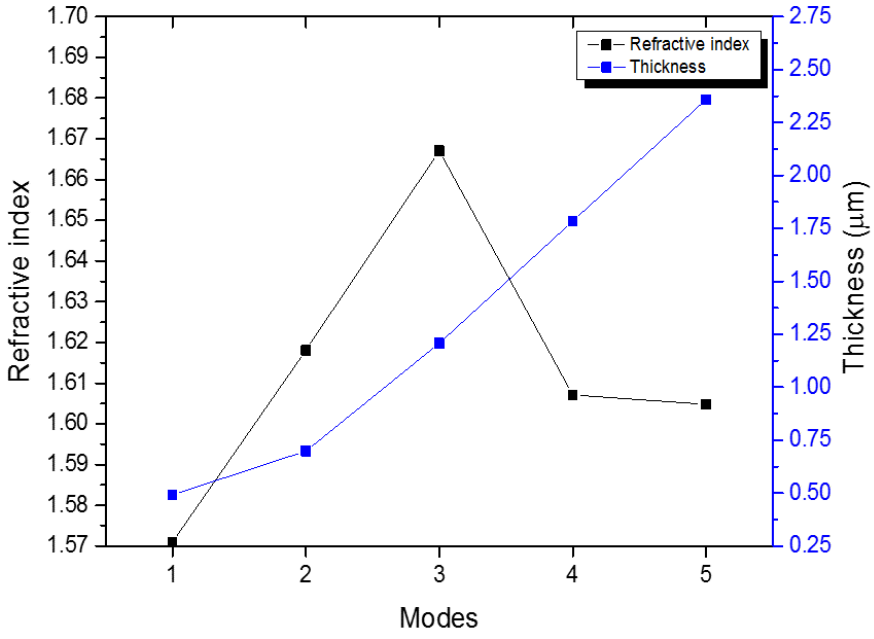

Figure 3.16: Comparison of the number of modes obtained in the photonic chip and the respective refractive index and thickness of the guiding layer measured at 633 nm

The modes present in the photonic chips are dependent on the thickness of the thin film implanted in the photonic chip as shown in figure 3.16 (Tong, 2014). The individual mode causes its own mode dispersion which causes the change in the propagation of spatial modes at different time intervals. The propagation from different modes in multi-mode planar waveguide causes wave mixing which leads to increase in error in measurement. Thus a single mode is more preferential than the multimode waveguide (Fischer-Hirchert, 2015; Ramaswami *et al.*, 2004). As shown in the Fig 3.16 the modes increase with the thickness of the photonic chip, thus the optimal case will be $\approx 1\ \mu m$ thickness of the photonic chip. However, the photonic chip should have high fluorescence intensity and longer lifetime.

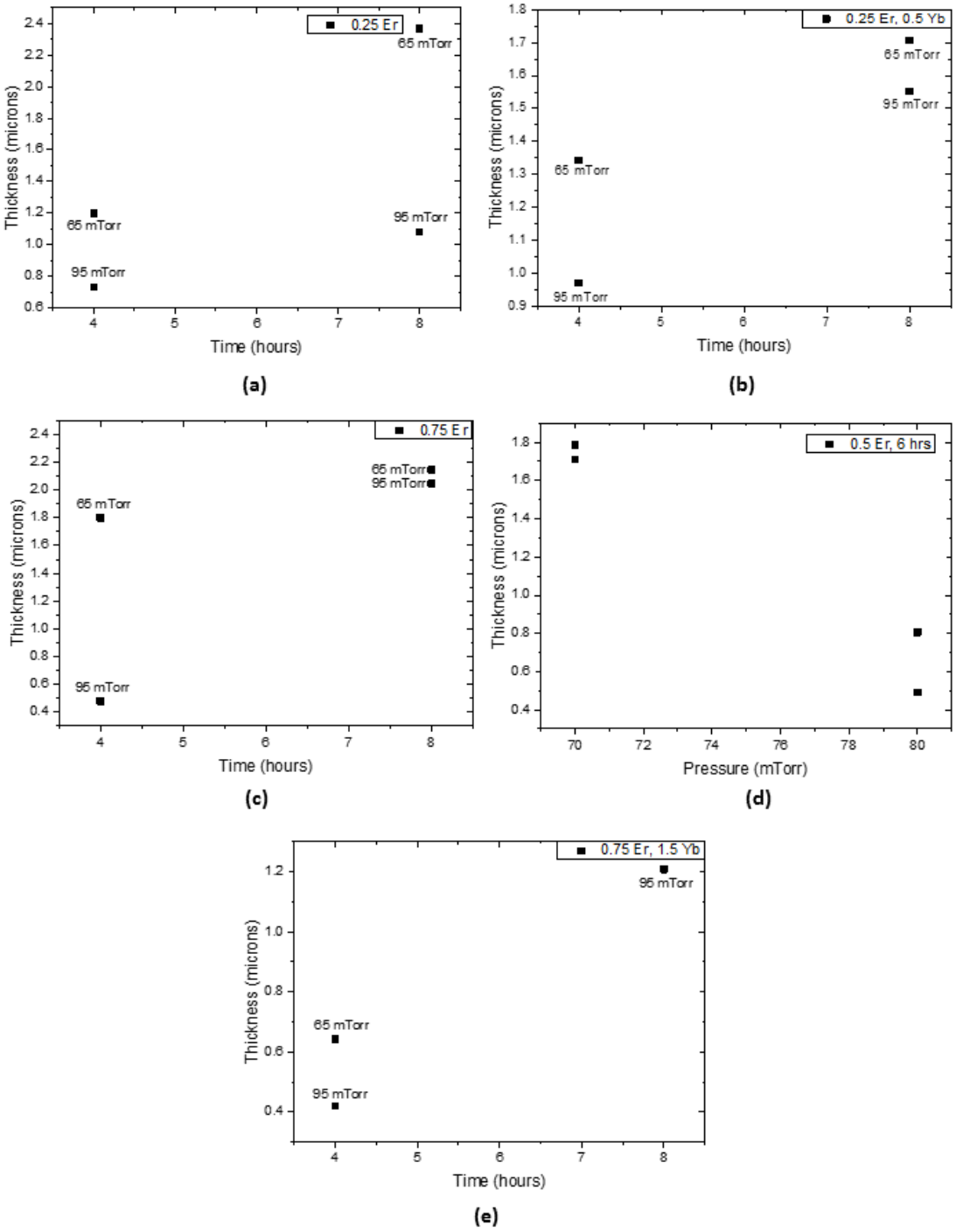

Figure 3.17: The comparison of the effect of pressure and temperature for the films fabricated with altering concentration of the Er^{3+} ions and Yb^{3+} ions on thickness of the thin film; (a) 0.25 mol percent Er^{3+} (b)0.25 mol percent Er^{3+} and 0.5 mol percent Yb^{3+} (c) 0.5 mol percent Er^{3+} (d)0.75 mol percent Er^{3+} (e)0.75 mol percent Er^{3+} and 1.5 mol percent Yb^{3+} ions.

The samples were prepared by altering the chamber pressure and the deposition time whilst keeping the concentration of the Er^{3+} and Yb^{3+} ions same for each group. The thickness and refractive index alter based on deposition time and the chamber pressure for fabrication of each photonic chip. Figure 3.17 compares the change in thickness of the photonic chip while figure 3.18 compares the refractive index of the photonic chip. Figure 3.17(a) shows the comparison of pressure and time for the photonic chip fabricated with target doped with 0.25 mol percent Er^{3+} ions. The thickness varies from 0.73 - 2.37 μm in photonic chip doped with 0.25 Er^{3+} ions. The highest thickness is obtained with lower chamber pressure and longer duration. The density of the plasma plume and the kinetic energy of the ions is known to be affected by the atmosphere in the chamber, the pressure of the chamber affects the plume expansion or deceleration (Ibrahim *et al.*, 2004b; Ojeda-GP *et al.*, 2017). Figure 3.17(b) shows the increase in the thickness of thin films by lowering the chamber oxygen pressure and longer deposition time which is similar in the case of photonic chip doped with the 0.5 mol percent Er^{3+} ions (Fig 3.17(d)), 0.75 mol percent Er^{3+} ions (Fig. 3.17(c)). However in the case of photonic chip doped with the 0.75 mol percent Er^{3+} and 1.5 mol percent ions thickness seems to be increasing but the result is inconclusive as the fabrication of photonic chip with latter concentration of the dopants at 65 mTorr oxygen pressure and 8 hours couldn't be fabricated due to closure of lab for BLM work.

The refractive index is an important parameter of the photonic chip as it determines the propagation of the light through the medium. For light to remain in the thin film of the photonic chip the refractive index needs to be higher than the substrate refractive index (Bloomfield, 2004). The smaller refractive index of thin film means that the absorption cross section will be less thus the net emission produced will be weaker. The advantage of the SiO_2 waveguide is that temperature dependence due to refractive index of the photonic chip is very low i.e. $(dn/dt = 1.1 + 10^{-5})$ thus light emitted varies less due to thermal drift (Fischer-Hirchert, 2015).

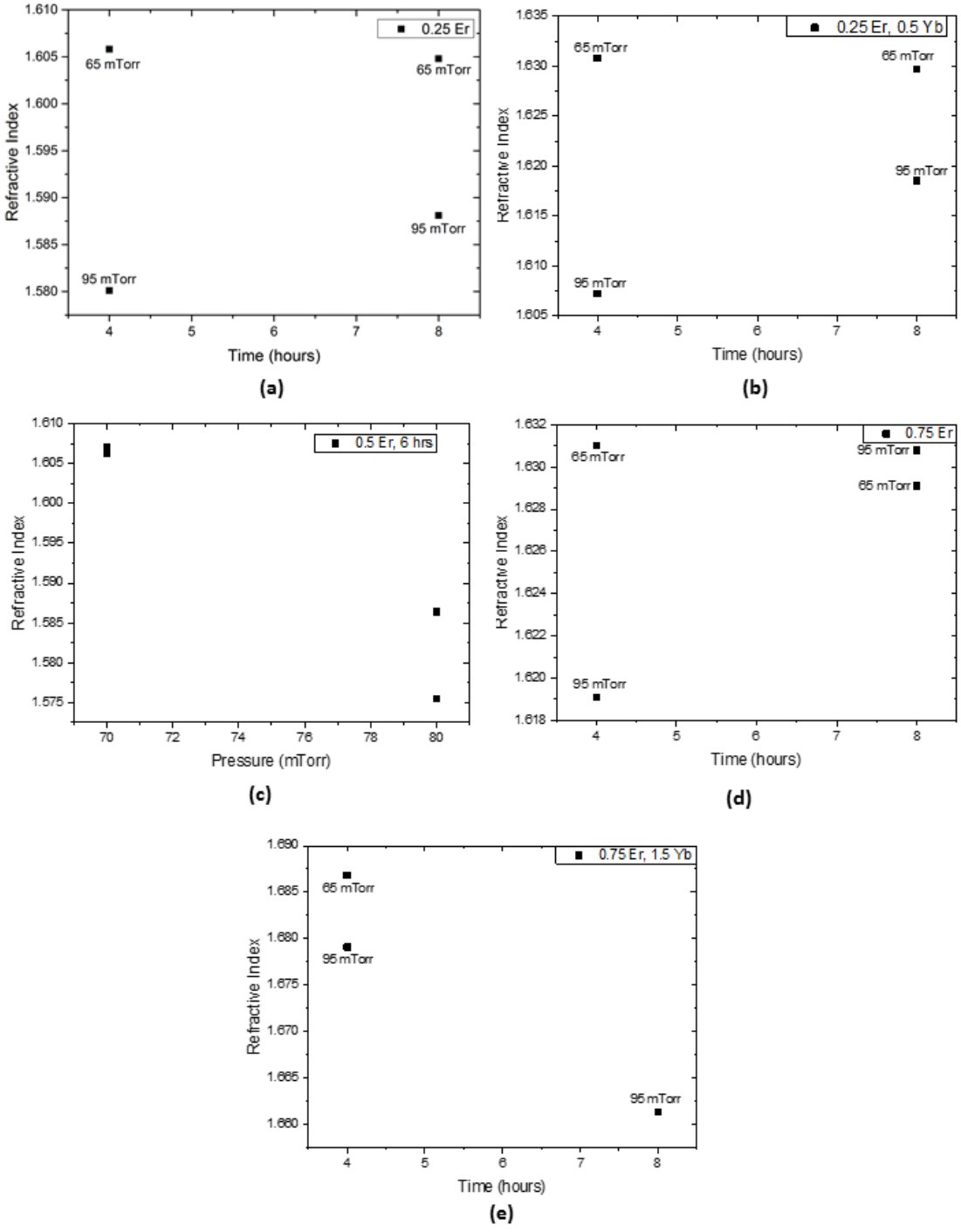

Figure 3.18: The comparison of the effect of pressure and temperature for the films fabricated with altering composition of the Er^{3+} and Yb^{3+} ions on refractive index of the thin film; (a) 0.25 mol percent Er^{3+} ions, (b)0.25 mol Er^{3+} and 0.5 mol percent Yb^{3+} ions, (c) 0.5 mol percent Er^{3+} ions, (d) 0.75 mol percent Er^{3+} ions (e)0.75 mol percent Er^{3+} and Yb^{3+} 1.5 mol percent ions.

The measured refractive index of the photonic chip was plotted against the oxygen chamber pressure and time of deposition. For the photonic chip doped with 0.25 mol percent Er^{3+} ions (Fig. 3.18(a)). The lower pressure and shorter deposition time seem to produce similar refractive index as the longer duration and lower chamber pressure. Fig 3.18 (e) shows the higher refractive index (1.696) of the photonic chip and while the refractive index is lower for the higher pressure. The refractive index varies from 1.58 to 1.69. Fig 3.18 (b) shows the refractive index of a co-doped photonic chip with 0.25 mol percent Er^{3+} and Yb^{3+} ions. Comparing with photonic chip doped with 0.25 mol percent Er^{3+} ions, the overall refractive index is higher and lower refractive index is produced with the higher oxygen chamber pressure. This indicates an increase in density of Er^{3+} and Yb^{3+} ions is observed mainly due to higher doped target material. However, the refractive index is decreasing with increasing chamber pressure indicating lesser density than photonic chip fabricated under lower oxygen pressure. Deposition time doesn't seem to affect the refractive index of the thin films. The photonic chip doped with 0.5 mol percent Er^{3+} ions also show similar trend i.e. refractive index decreases with the chamber pressure. This trend is also followed in the thin films doped with the 0.75 mol percent Er^{3+} ions and also in thin films 0.75 Er^{3+} & 1.5 mol percent Yb^{3+} ions. The increase in the concentration of Er^{3+} ion has been suggested with a change in morphology of the TeO_4 from tetrahedral structure to the TeO_3 triangular in the doped region of the substrate. Thus increasing the coordination number of the silica glass results in an increase in refractive index (Sidek *et al.*, 2009). This has been attributed to the fact that possible formation of the non bridging oxygen forms thus higher refractive index (Mohamed Kamari *et al.*, 2015; Rosmawati *et al.*, 2007) as it results more solubility of the Er^{3+} ions as explained in section 3.4.4. The photonic chip showing higher refractive index has higher solubility of Er^{3+} ions in the doped region.

3.4.6 Absorption spectroscopy results

The absorption of thin films couldn't be measured due to small optical path length of the doped regions and lower concentration of the Er^{3+} ions, the erbium

absorption peaks were not visible. The transmittance of the thin films were measured from 900 nm to 1800 nm at rate of 4.45 nm/sec. The optical transmission of thin film fabricated in the batch was between 90.7 to 92.6 percent over the measured NIR region. The pristine silica has transmittance around 93 percent. In fused silica, dip in transmission between 1350-1400 nm which is attributed to the OH content present in the system(Griscom, 1991).

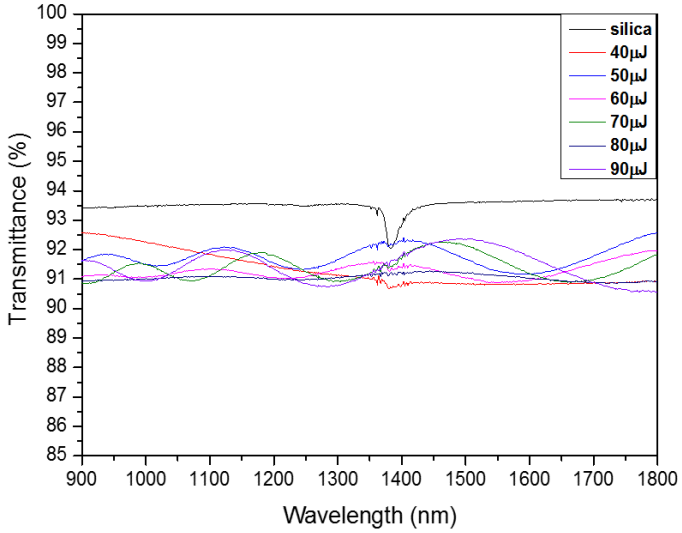

Figure 3.19: The above data shows the transmittance spectra of thin films of samples fabricated using 0.5 mole percent Er^{3+} ions with increasing laser energy from 40 μJ − 90 μJ as mentioned in table 2.2.

Fig 3.19 shows the transmittance spectra of the G series batch of samples where pristine silica has been compared to the doped samples. The absorption peak at ≈ 1380 nm with band width of 40 nm in pristine silica corresponds to the OH group which seems to disappear in the fabricated photonic chips. This is advantageous as the overtone of the non bonded OH group vibration overlaps with the energy gap of the Er^{3+} ions from the $^4I_{13/2}$ and $^4I_{15/2}$ levels (Feng *et al.*, 2001; Hayashi *et al.*, 2006). Overall transmittance of Er^{3+} doped photonic chip is lower than the pristine silica.

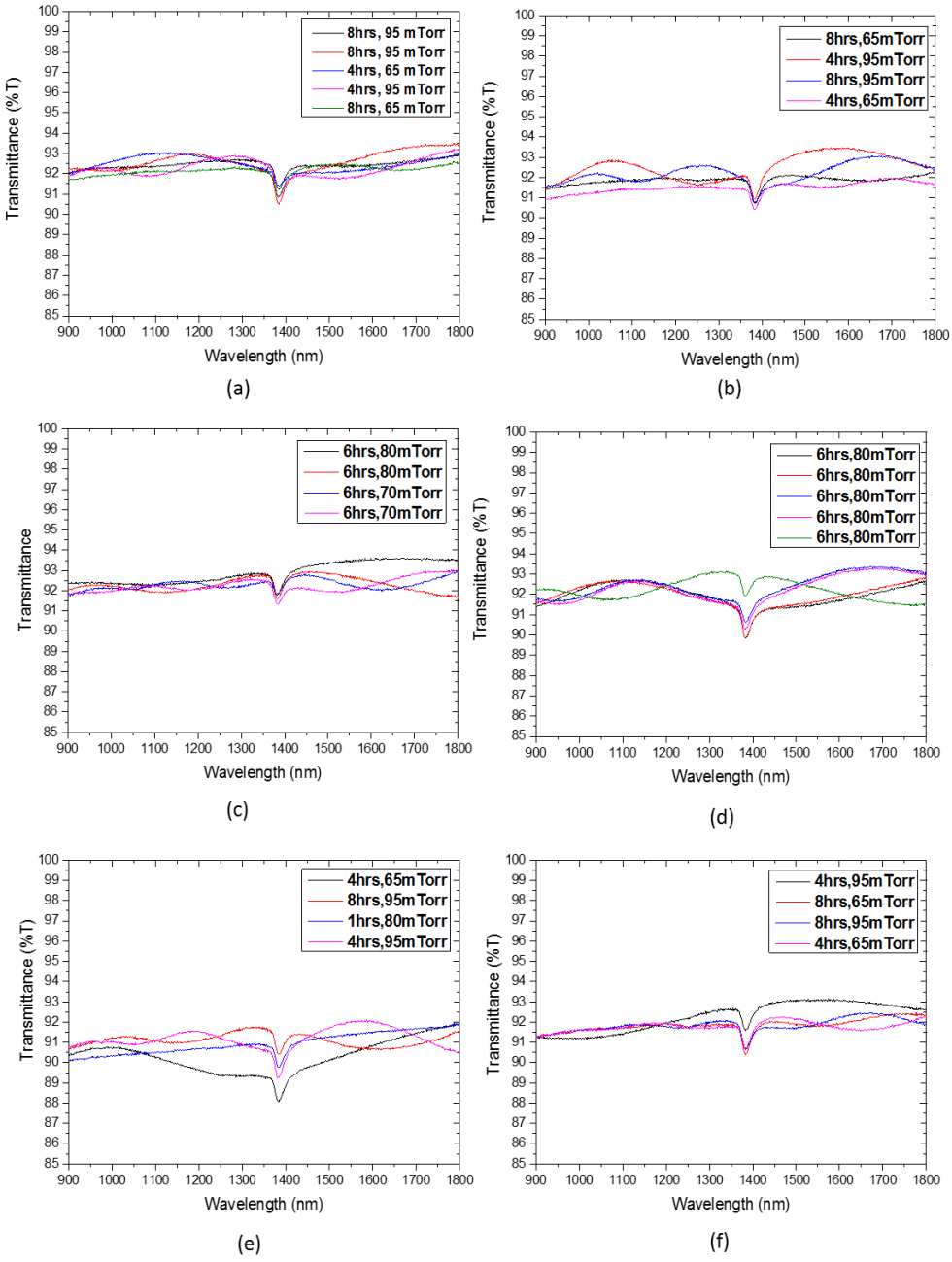

Figure 3.20: Transmittance data was collected according to the samples grouped in table 3.2. The transmittance spectra of samples fabricated with target glass with (a) 0.25 mol percent Er^{3+} ions, (b)0.25 mol percent Er^{3+}, 0.5 mol percent Yb^{3+} ions, (c) 0.5 mol percent Er^{3+} ions, (d) 0.5 mol percent Er^{3+} ions, 0.5 mol percent Yb^{3+} ions, (e) 0.75 mol percent Er^{3+} ions, (f)0.75 mol percent Er^{3+}, 1.5 mol percent Yb^{3+} ions.

Further analysis of the T series batch was carried out. The overall transparency of the photonic chip ranges from 90-93 percent. The OH content is visible in each graph shown in figure 3.20. The change in OH content can vary due to the fabrication of the fused silica glass as well. The decrease in concentration of OH^- is essential for a better optical performance of the photonic chip.

3.4.7 Fluorescence spectroscopy results

Erbium doped materials are of main importance in the field of photonic applications primarily due to Er^{3+} intra-$4f$ emission at 1535 nm which is the commercial optical communication wavelength. The Er^{3+} doped SiO_2 has now been well established in the field of optical amplifiers as it provides gain at 1535 nm (Fischer-Hirchert, 2015). SiO_2 as a substrate is important as it limits the emission of Er^{3+} to 1535 nm region (Ainslie, 1991). The fluorescence spectra of two batches of fabricated photonic chips i.e. G series and T series of photonic chips were analysed. A silicon filter was used to block all the light below 1200 nm going to the detector. Each measurement was made with 0.5 nm step, 0.4 seconds dwell time and maximum background noise of 100,000 counts per second. The Er^{3+} ions were excited with a 980 nm laser which excites the electrons from the $^4I_{15/2}$ ground state to the $^4I_{11/2}$ higher energy level. A decay of the electrons takes place from $^4I_{11/2}$ to $^4I_{13/2}$ with the release of non radiative energy and emission from Er^{3+} ions takes place from $^4I_{13/2}$ to $^4I_{15/2}$ level (Girard *et al.*, 2009; Savelii *et al.*, 2016). When the concentration of Er^{3+} ions increases, the space between the ions decreases causing the ion to ion energy transfer which leads to upconversion i.e. shorter wavelength is emitted. In this case the excited Er^{3+} ions releases energy which is transferred to corresponding energy levels of the other Er^{3+} ions. The excited electrons in Er^{3+} ions returns to the ground state whilst the electrons in receiver Er^{3+} ions is transferred to higher energy level. This phenomenon causes the fluorescence quenching at 1535 nm of Er^{3+} ions (Righini & Ferrari, 2005).

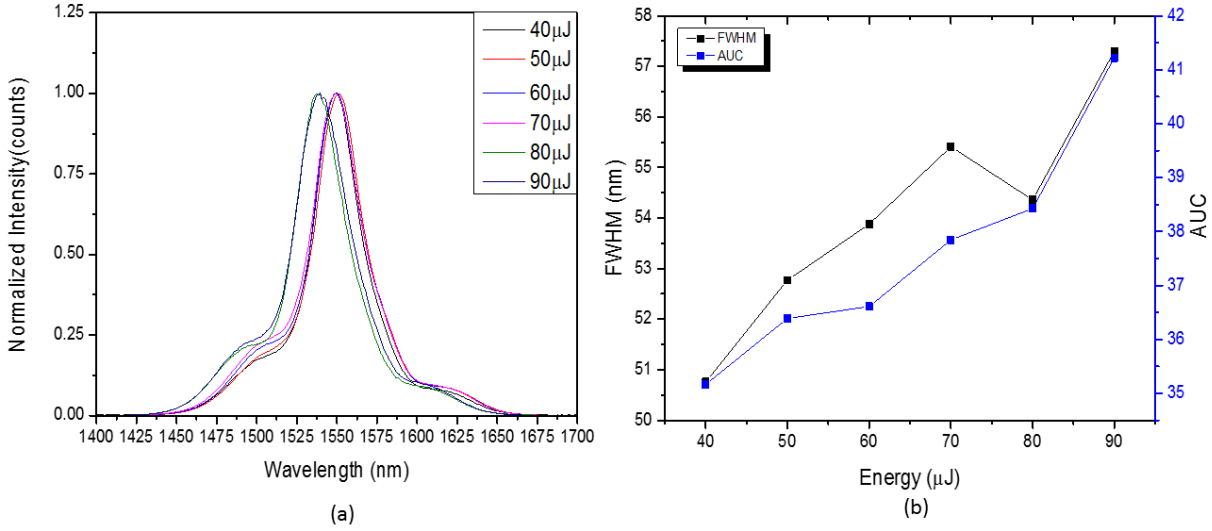

Figure 3.21: (a)Normalised fluorescence spectra results of photonic chip (G series) fabricated with 0.5 mol percent Er^{3+} oxide with increasing laser energy, 6 hours deposition, 70 mTorr oxygen pressure, (b) Full width half maximum(FWHM) and area under curve(AUC) of the emission spectra plotted against the laser energy used for deposition.

The fluorescence spectra shows an increase in intensity (fig 3.21) when the deposition laser energy was increased from 40 to 90 μJ with 10 μJ increase in each deposition. A total of 6 samples were fabricated. It has been discussed earlier in the fabrication chapter that an increasing laser energy causes the release of more ions from the target glass, thus more Er^{3+} ions will be deposited in the thin film. The full width half maximum(FWHM) varies from 36.2 to 41 nm and the area under curve varies from 50.5 to 57 which clearly show an increase in the overall emission indicating an increase in Er^{3+} concentration. This observation is in agreement with Righini & Chiappini (2014) which estimates high quantum efficiency at $\approx$ 41 nm FWHM bandwidth with a peak at 1535 nm. Chandrappan *et al.* (2015) observed that a narrower band width of the Er^{3+} fluorescence spectra is observed in silica glass compared to the broad emission of Er^{3+} ions doped in tellurite glass. The Fluorescence spectra show the shape dependence thus indicating the Stark levels of the $^4I_{13/2}$ levels are non-uniformly populated (Righini & Chiappini, 2014).

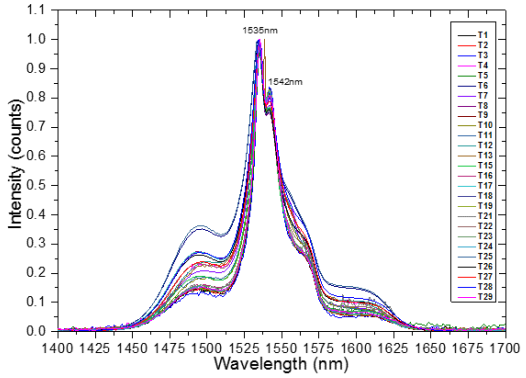

Figure 3.22: The fluorescence emission spectra of the T series batch in which the Er^{3+} ions concentration in the target glass varies from 0.25 mol percent to 0.75 mol percent and co-doped with Yb^{3+} at same concentration or double the concentration of Er^{3+} ions. It also includes spectra from single doped (Er^{3+}) photonic chips as well. The excitation wavelength used is 980 nm.

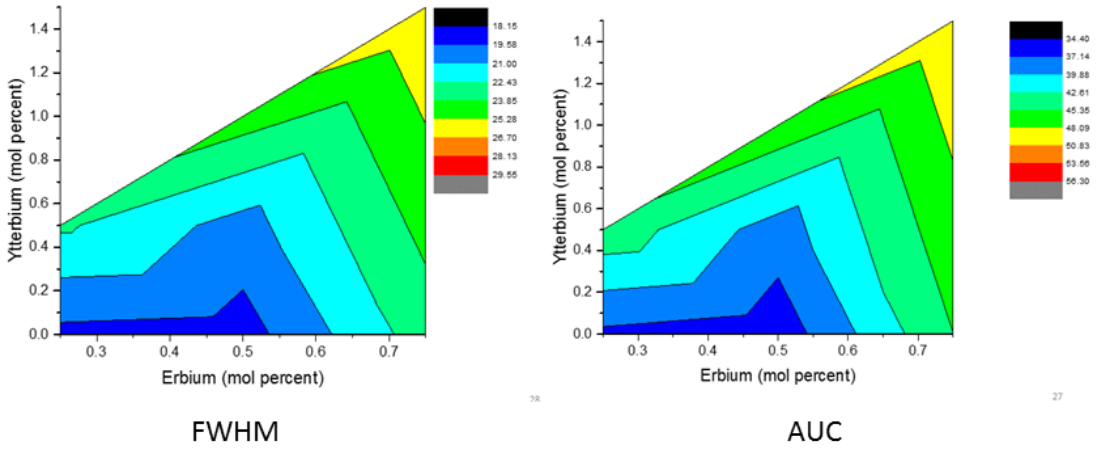

Figure 3.23: Contour plots comparing the effect of the altering concentration of and Er^{3+} ions with the FWHM and AUC of the fluorescence spectra plotted in figure 3.22.

The AUC and FWHM of the T series batch varies from the 34 to 55 and 18.2 to 28.37 nm respectively. The parameters altered in fabrication of T series batch were chamber oxygen pressure from 65 to 95 mTorr, deposition time from 4 to

8 hours, Er^{3+} and Yb^{3+} ions concentration. The laser energy used was 65 μJ and the substrate temperature was 700 ^oC. Clear differences can be observed in the fluorescence spectra of the photonic chips plotted in figure 3.22. The shortest AUC measured i.e. 34.2 was for the photonic chip fabricated with 0.5 mol percent Er^{3+} ions, 60 mTorr chamber oxygen pressure and 6 hours deposition time while the largest AUC reported i.e. 55.3 for photonic chip fabricated with 0.75 mol percent Er^{3+} and 1.5 mol percent Yb^{3+} ions, 95 mTorr chamber oxygen pressure, 8 hour deposition. As observed in fig 3.23 the bandwidth of the fluorescence emission from the thin films can be changed to the desired level based on data obtained. It is quite significant as the aim is to select the set of photonic chips which has high intensity, longest lifetime, large FWHM with lowest modes possible. In this subsection different groups of T series have been discussed in detail.

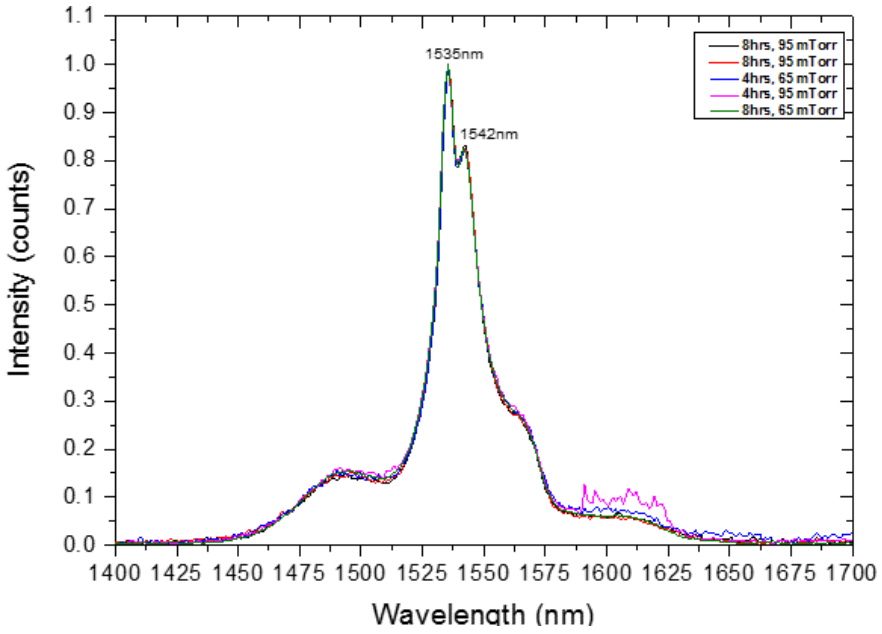

Figure 3.24: The fluorescence emission spectra of the photonic chips doped with 0.25 mol percent Er^{3+} ions when excited at wavelength 980 nm, fabricated with varying chamber oxygen pressure and deposition time.

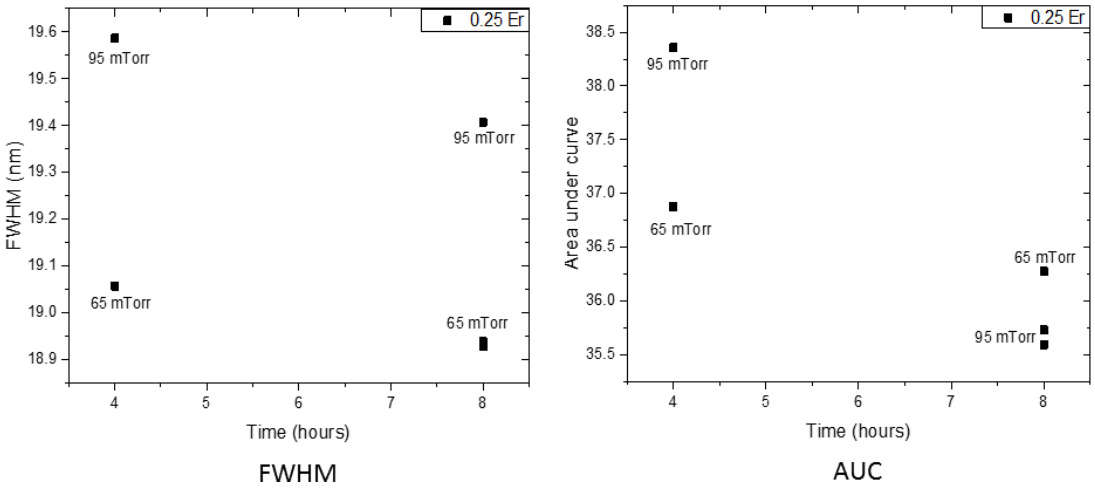

Figure 3.25: The graphical plots comparing the effect of altering chamber oxygen pressure and deposition time with the FWHM and AUC of the fluorescence spectra plotted in figure 3.24. The photonic chips were doped with 0.25 mol percent Er^{3+} ions.

Figure 3.24 compares the fluorescence emission spectra of the thin films fabricated with 0.25 mol percent Er^{3+} ions with altering chamber oxygen pressure and deposition time. There FWHM and AUC measured (fig 3.25) for the photonic chips varies over a narrow range of 18.9-19.6 nm and 35.6 to 38.6 respectively which is much higher drop in the FWHM from the G series batch. The changes in Stark levels can be characteristic of the phenomenon of fluorescence quenching by OH group (Yan *et al.*, 1995) which are clearly visible in the transmission spectra shown in figure 3.20. However, since the Er^{3+} ion concentration is low, it is expected to have more distance between each other within the silica network thus the quenching due to ion-ion interaction have a lesser possibility. It can also be noted that the FWHM and AUC of thin films fabricated at 65 mTorr is lower than the thin films fabricated at 95 mTorr.

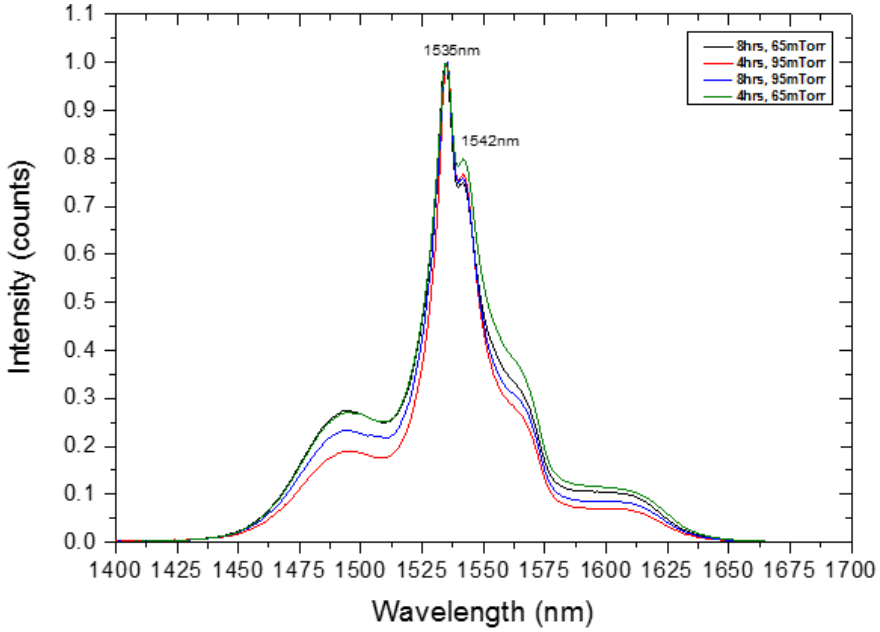

Figure 3.26: The fluorescence emission spectra of the photonic chips doped with 0.25 mol percent Er^{3+} and 0.5 mol percent Yb^{3+} ions, when excited at wavelength 980 nm, fabricated at altering chamber oxygen pressure and deposition time.

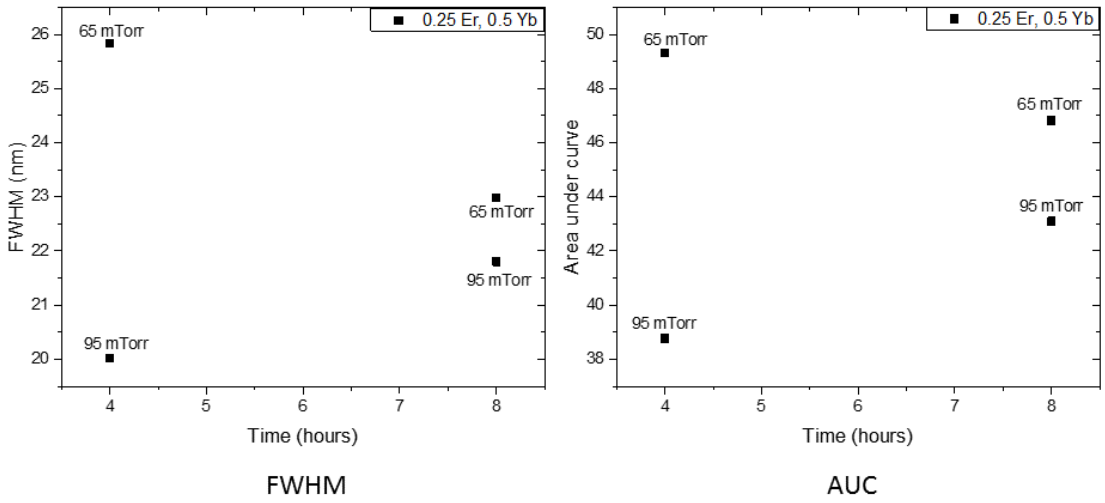

Figure 3.27: The graphical plots comparing the effect of altering chamber oxygen pressure and deposition time with the FWHM and AUC of the fluorescence spectra plotted in figure 3.26.The photonic chips were doped with 0.25 mol percent Er^{3+} and 0.5 mol percent Yb^{3+} ions.

To get more optical gain Yb^{3+} ions co-doping was done. The Yb^{3+} ions when excited at 980 nm, emits photons at 980-1001 nm. This is advantageous due to cooperative relaxation process, the transfer of energy takes place between the Yb^{3+} ions present within the proximity of the Er^{3+} ions thus the latter ions absorbs more pump energy. Another advantage of the Yb^{3+} ions is the reduction of the Er^{3+}-Er^{3+} ion interaction by increasing the mean atomic distance (Righini & Ferrari, 2005). The transfer of energy from $^2F_{5/2}$ to $^4I_{11/2}$ energy levels takes place and larger absorption cross-section is observed (Girard *et al.*, 2009). By adding 0.5 mol percent Yb^{3+} ions the FWHM has increased significantly from 18.93-19.41 nm to 20-25.83 nm, also the AUC shows the overall intensity increase from 35.6-38.4 to 38.8-49.32. The improvement in film thickness and refractive index in the silica (fig 3.17, 3.18) has also been observed for these samples. The more populated energy level at $^4I_{13/2}$ for 1535 nm peak emission can also be observed in figure 3.26. However, the decrease in FWHM and AUC is observed in the thin films fabricated with 95 mTorr chamber pressure.

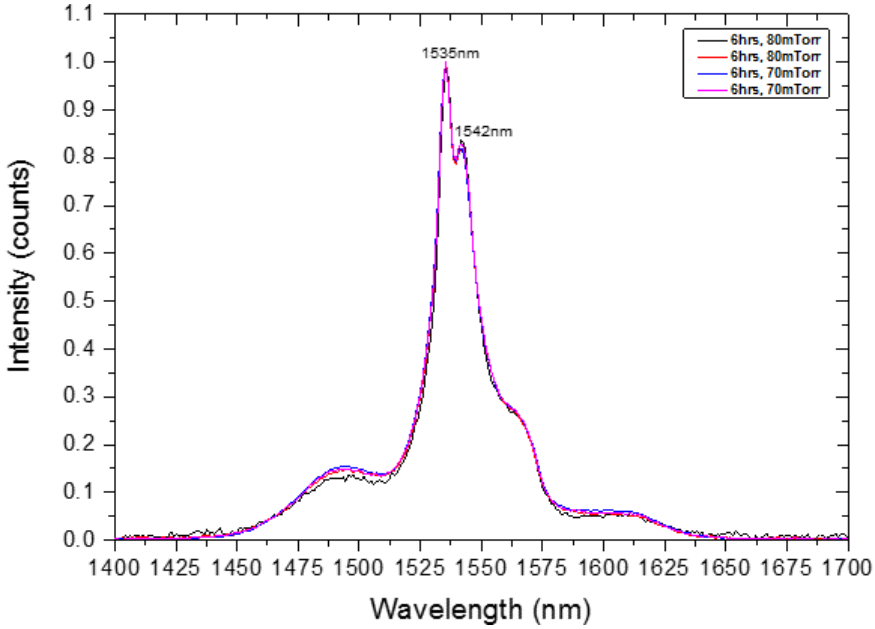

Figure 3.28: The fluorescence emission spectra of the photonic chips doped with 0.5 mol percent Er^{3+} ion concentration when excited at wavelength of 980 nm, fabricated by altering chamber oxygen pressure and deposition time.

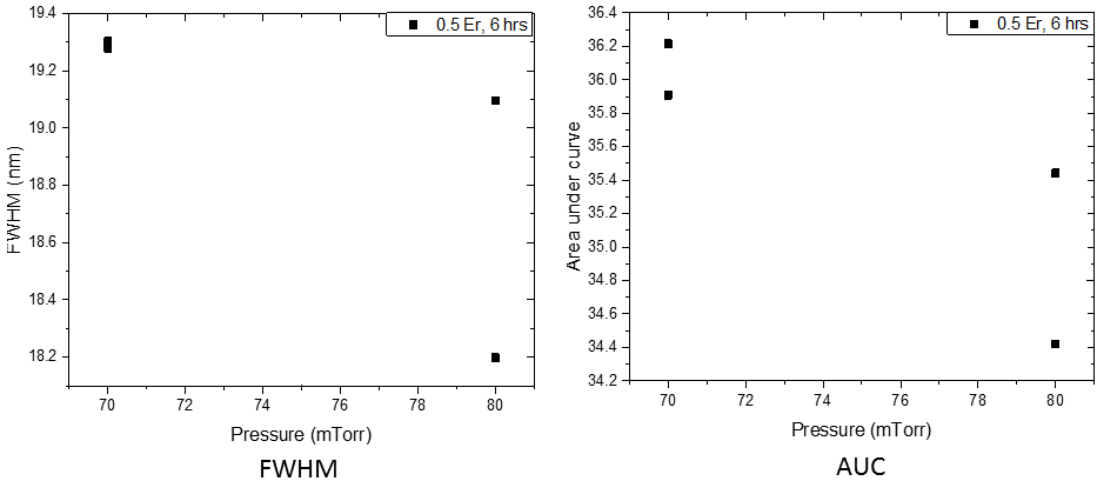

Figure 3.29: Plot of effect of altering chamber oxygen pressure with the FWHM and AUC of the fluorescence spectra plotted in figure 3.28. The photonic chips were doped with 0.5 mol percent Er^{3+} ions.

The 0.5 mol percent Er^{3+} ion deposition was the centre point of T batch series with the deposition time of 6 hours, and varying chamber oxygen pressure. The normalised intensity of fluorescence spectra (fig 3.28) shows similar intensity at $^4I_{13/2}$ energy level of 4 photonic chips in this batch. A small change in FWHM and AUC (fig 3.29) i.e. 18.20-19.3 nm and 34.42 to 36 respectively. It is important to note that although the concentration of Er^{3+} in target glass was increased from 0.25 to 0.5 mol percent there is no significant increase in the fluorescence intensity from thin films fabricated at 0.25 mol percent Er^{3+} and 0.5 mol percent Yb^{3+} ions thus the $^4I_{13/2}$ energy level is equally populated. This can be related to the fact that the thickness of the thin films fabricated with 0.25 mol percent Er^{3+} ions is high to the respective thin films fabricated at 0.5 mol percent Er^{3+} ions (fig 3.17). A small drop in FWHM and AUC can be observed with increasing the chamber oxygen pressure, however at 0.25 mol percent Er^{3+} level the increase in FWHM and AUC was observed.

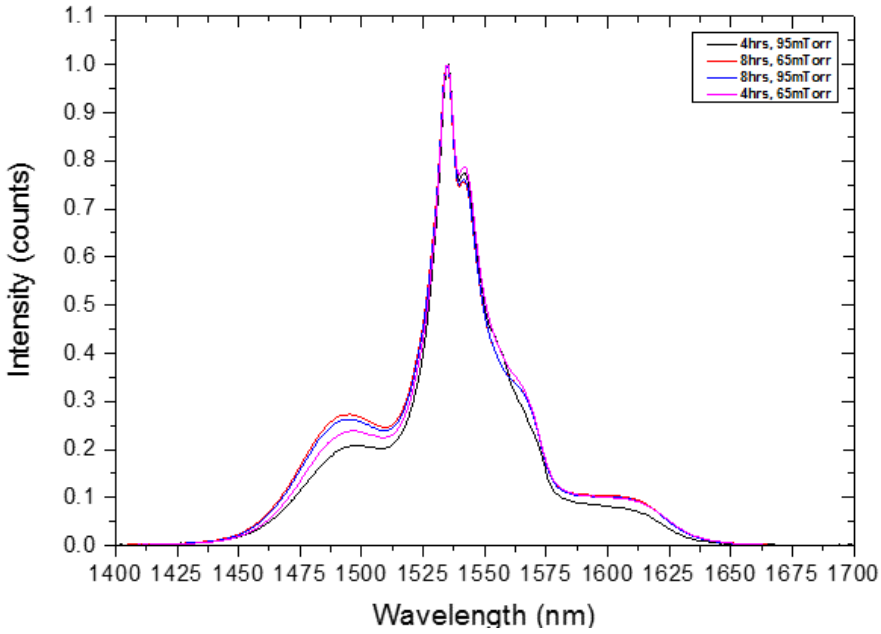

Figure 3.30: The fluorescence emission spectra of the photonic chips doped with 0.75 mol percent Er^{3+} ions concentration when excited at wavelength 980 nm, fabricated by altering chamber oxygen pressure and deposition time

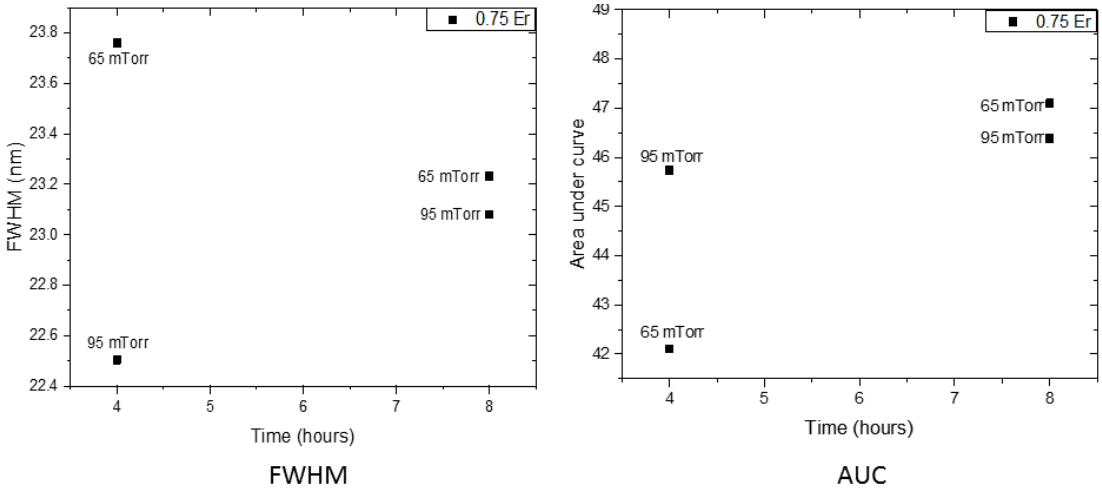

Figure 3.31: The graphical plot comparing the effect of altering chamber oxygen pressure and deposition time with the FWHM and AUC of the fluorescence spectra plotted in figure 3.31. The photonic chips were doped with 0.75 mol percent Er^{3+} ions.

The fluorescence spectra (fig 3.30) of the photonic chips fabricated with the 0.75 mol percent Er^{3+} ions show increase in the FWHM and AUC (fig 3.31) from photonic chips fabricated at 0.25 mol percent Er^{3+} ions i.e. from 18.2-19.3 nm and 34.4-36.2 range to 19.5-21.7 nm and 42.1-47.10 respectively. This indicates that Er^{3+} ions are closer to each other due to stoichiometric increase in the Er^{3+} ion concentration. This increases the absorption cross section thus increasing the intensity and populating more ${}^4I_{13/2}$ energy levels (fig 3.30). The highest FWHM is observed for the chip fabricated at the lower oxygen pressure and deposition time of 4 hours. While it decreases if either the oxygen pressure is increased or deposition time is increased. A similar observation can be found in the fig 3.27,3.29 while it is contradictory to the photonic chip fabricated at 0.25 mol percent Er^{3+} ions. It might be because initially Er^{3+} ions are far apart from each other in case lower Er^{3+} ions concentration compared to other photonic chips. At a concentration of Er^{3+} ions between 0.25 and 0.5 mol percent Er^{3+} ions, the absorption cross section is highest, without any fluorescence quenching produced due to ion-ion interactions. While the introduction of Yb^{3+} ions does increase the FWHM and AUC as observed in fig 3.26 the decrease in FWHM and AUC is observed as with either increases oxygen pressure and deposition time. This

indicated more ion-ion interaction whilst initiating the transfer of the photons to higher occupied molecular orbitals (HOMO) from ${}^4I_{13/2}$.

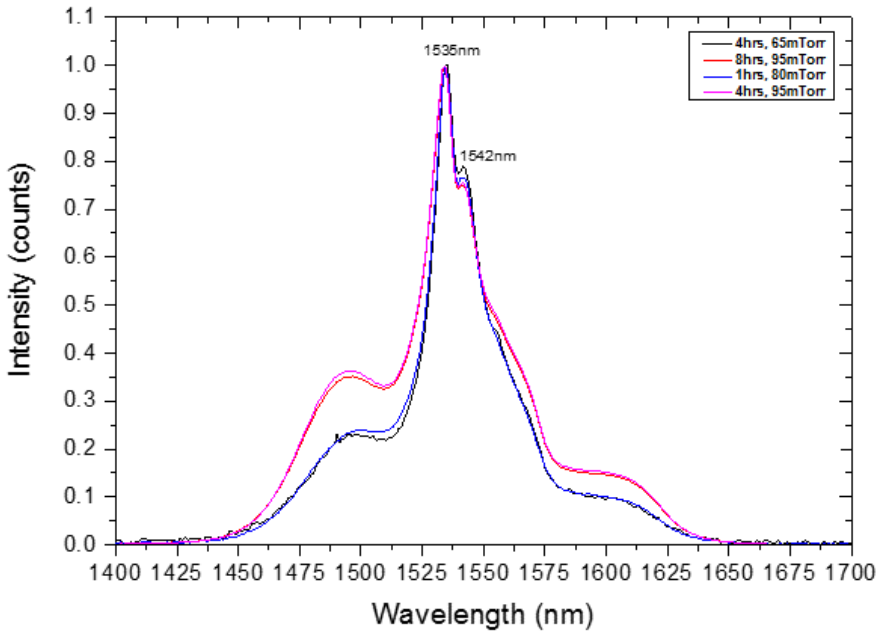

Figure 3.32: The fluorescence emission spectra of the photonic chips doped with 0.75 mol percent Er^{3+} ions and 1.5 mol percent Yb^{3+} ions, when excited at wavelength 980 nm and fabricated by altering chamber oxygen pressure and deposition time

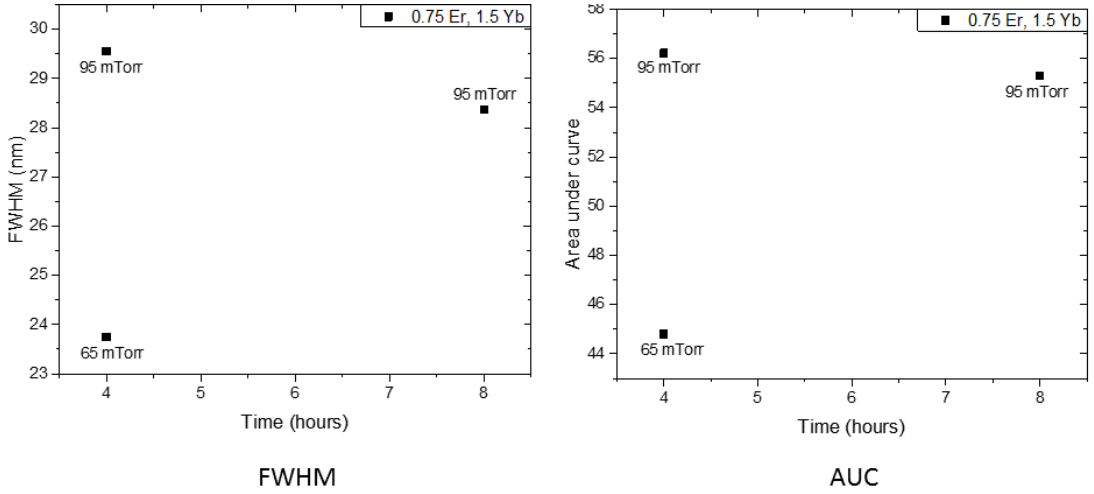

Figure 3.33: The graphical plots comparing the effect of altering chamber oxygen pressure and deposition time with the FWHM and AUC of the fluorescence spectra plotted in figure 3.33.The photonic chips were doped with 0.75 mol percent Er^{3+} and 1.5 mol percent Yb^{3+} ions.

The fluorescence emission spectra (fig 3.32) is the limit to which the Er^{3+} and Yb^{3+} ions have been implanted in this study. The FWHM has increased from 18.9 nm in photonic chip doped with 0.25 mol percent Er^{3+} to 29.55 nm while the AUC has increased from the 35.6 to 56.21. This is a significant increase as the bandwidth is broader and Er^{3+} and Yb^{3+} ions are in much closer vicinity to each other. The overall flux is increased due high density of Er^{3+} and Yb^{3+} ions but possible up-conversion can be present due to ion-ion interaction and cross coupling between identical ion can cause overall transfer of energy to higher occupied molecular orbitals (HOMO) (Yin *et al.*, 2012) which might be useful in other application but is possible problem for this study.

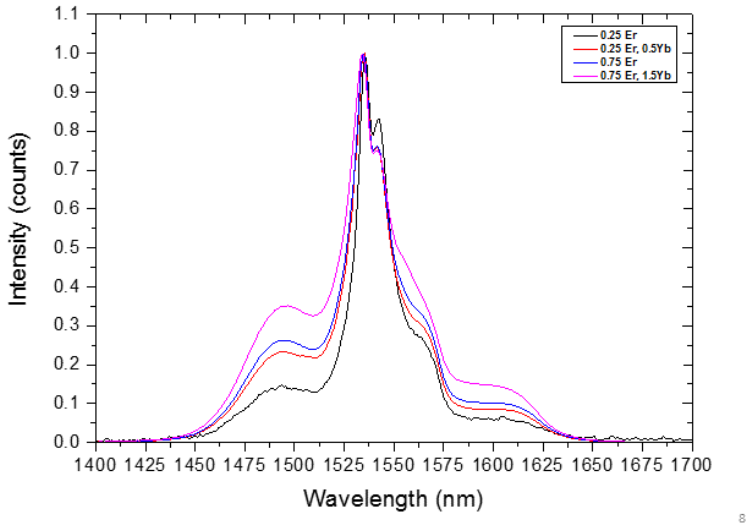

Figure 3.34: The fluorescence emission spectra of the photonic chips doped with increasing concentration of Er^{3+} and Yb^{3+} ions when excited at wavelength 980 nm and fabricated by 95 mTorr chamber oxygen pressure and 8 hours deposition time.

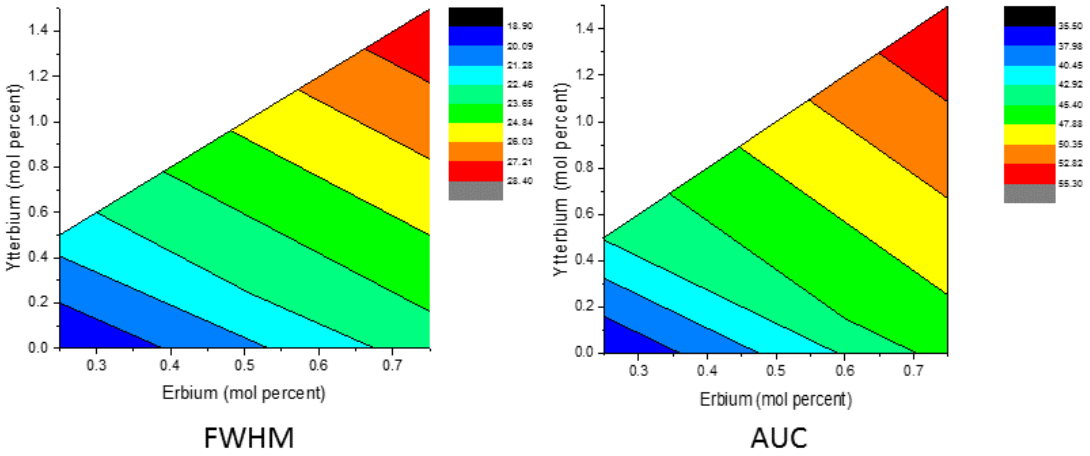

Figure 3.35: Contour plots comparing the effect of altering concentration Yb^{3+} and Er^{3+} ions with the FWHM and AUC of the fluorescence spectra plotted in figure 3.34.

Finally coming to the end of this subsection, comparison of the four photonic chips were which have altering target glass concentration as mentioned in the

graph plotted in the fig 3.34 whilst keeping the oxygen pressure and the deposition time same. The broadening of the peaks i.e. FWHM and AUC is observed. Fig 3.35 show the comparison of the FWHM and AUC of the fluorescence spectra of the photonic chips fig 3.34 plotted against increasing Yb^{3+} and Er^{3+} ions concentration. A linear response is observed i.e. higher the Er^{3+} and Yb^{3+} ions more flux is emitted by the photonic chip. While it should be kept in consideration the fluorescence quenching can be hindrance in obtaining more broader bandwidth of Er^{3+} ion emission at 1535nm (Righini & Ferrari, 2005).

3.4.8 Fluorescence lifetime spectroscopy results

The most common way to observe photoluminescence properties of the material is through the fluorescence lifetime time measurement. In this technique, the fluorescence intensity is measured as a function of time when it decays after a short period of excitation by a pump light source. The G series batch and T series batch were measured using this technique. The 980 nm pump laser with 100 μs pulse duration was used and the decay was measured over a period of 100 ms for G series batch and 200 ms for the T series batch. For each sample, 500 sweeps were carried out and summed to obtain one fluorescence decay measurement. In the G series samples, the fluorescence decay was measured from 1530 to 1590 nm, with an interval at 10 nm each while for the T series batch the fluorescence decay was measured at 1535 nm. Er^{3+} ions doped into the thin films in the silica exhibit the single exponential fluorescence decay which is a key characteristic of the low Er^{3+} doped silica (Zhang *et al.*, 1997). The longer lifetimes of Er^{3+} is mainly due to the self absorption also known as radiation trapping in which a photon is emitted by spontaneous emission, the released photon is reabsorbed by the Er^{3+} ions before it is released from the host medium, thus repopulating the $^4I_{13/2}$ energy level of Er^{3+} ions in close proximity. This process of emission and re-absorption occurs until the final photon is released from the silica glass thus increasing the overall lifetime (Nguyen, 2004). Radiation trapping has been noted as the key characteristic of the $^4I_{13/2}$ to $^4I_{15/2}$ only the case of erbium ions (Koughia & Kasap, 2008; Mattarelli *et al.*, 2005). The longer lifetime is essential

for the better optical gain and efficiency of the optical waveguides (Wu *et al.*, 2003).

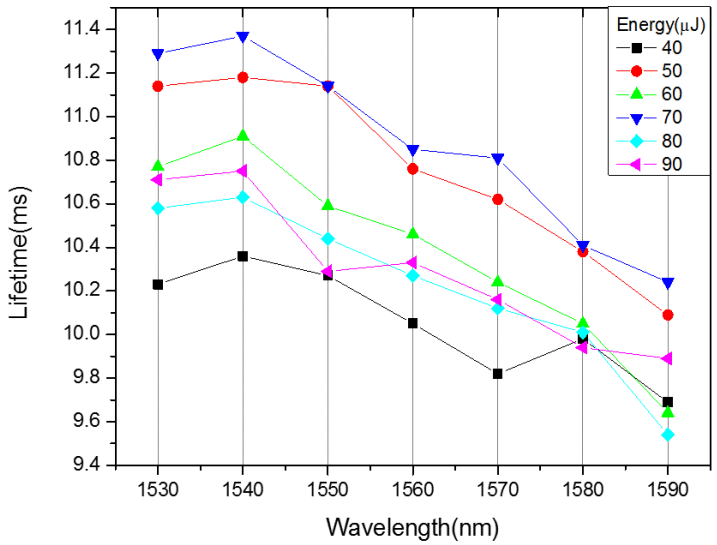

Figure 3.36: Measured fluorescence lifetime of thin films of samples fabricated using 0.5 mole percent Er^{3+} ions with increasing laser energy from 40 μJ − 90 μJ as mentioned in table 2.2

In G series samples, time resolved fluorescence decay measurements were carried out over the bandwidth of 60 nm of $^4I_{13/2}$ energy level after each 10 nm. The longest lifetime of 11.4 ms was observed for the sample fabricated at 70 μJ at 1540 nm. A non linear response in the fluorescence lifetime values is observed with the increasing laser ablation energy from 40 to 90 μJ. The aim of this part of the experiment was to determine the optimal laser ablation energy for the fabrication of next batch of the photonic chips also the emission wavelength at which the fluorescence lifetime of T series will be measured.

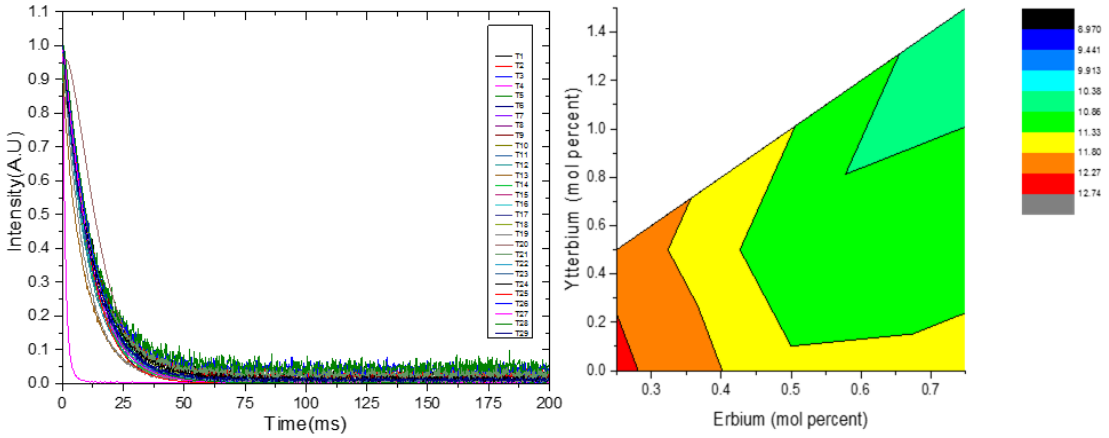

Figure 3.37: The fluorescence lifetime measurement (left) and contour plot (right) comparing the Yb^{3+} and Er^{3+} ions concentration of the photonic chip with lifetime of the T series batch. The Er^{3+} concentration of target glass varies from 0.25 mol percent to 0.75 mol percent and the Yb^{3+} ions as either co-doped with Er^{3+} at same concentration or double concentration of Er^{3+}. It also includes fluorescence lifetime of single doped (Er^{3+} ions) photonic chips as well. The excitation wavelength used is 980 nm.

The exponential decay curves of all the photonic chips fabricated in T series batch have been plotted in fig 3.37 (left) and the contour plot shows the effect of Yb^{3+} and Er^{3+} ions concentration on the fluorescence lifetime. The longest lifetime was reported for the 0.25 mol percent Er^{3+} ions doped photonic chip (4 hour deposition, 65 mTorr chamber oxygen pressure) which was 12.74 ms while the photonic chip doped with the 0.75 mol percent Er^{3+} and 1.5 mol percent Yb^{3+} ions (8 hours deposition, 95 mTorr) had the lowest lifetime of 10.45 ms which is longer than the fluorescence decay of Er^{3+} reported in literature for other glass (Grew *et al.*, 2006; Zhang *et al.*, 1997). The longer lifetime is a key characteristic of Er^{3+} doped into a SiO_2 environment (El Hamzaoui *et al.*, 2011; Kholodkov & Golant, 2005). The increasing concentration of the Er^{3+} and Yb^{3+} ions in the silica environment causes the fluorescence quenching due to possible up-conversion effect as reported (El Hamzaoui *et al.*, 2011; Righini & Ferrari, 2005). Thus as shown in fig 3.37 (right) the increasing Er/Yb concentration has the lower lifetime.

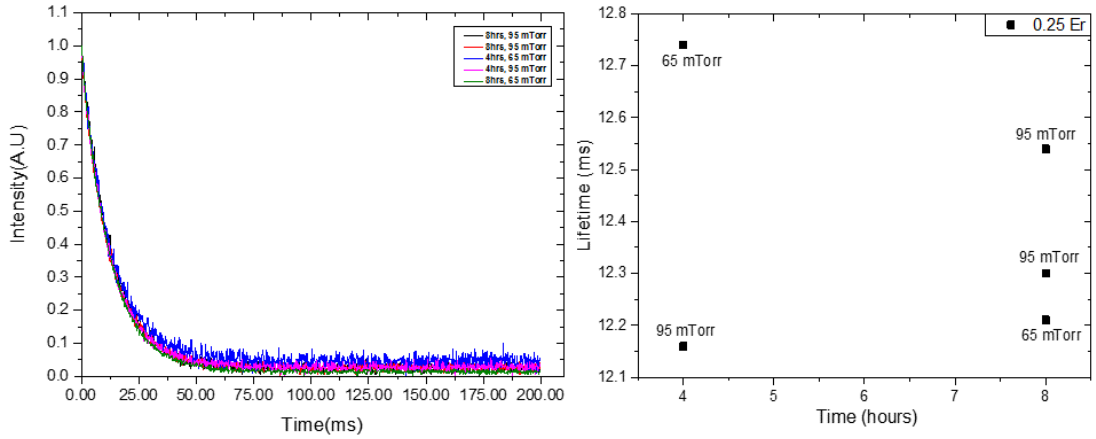

Figure 3.38: The fluorescence lifetime measurement(left) and x-y plot(right) comparing the chamber oxygen pressure and deposition time of the photonic chip with fluorescence lifetime. The photonic chips are doped with 0.25 mol percent Er^{3+} ions and the excitation wavelength is 980 nm. It is fabricated by altering chamber oxygen pressure and deposition time.

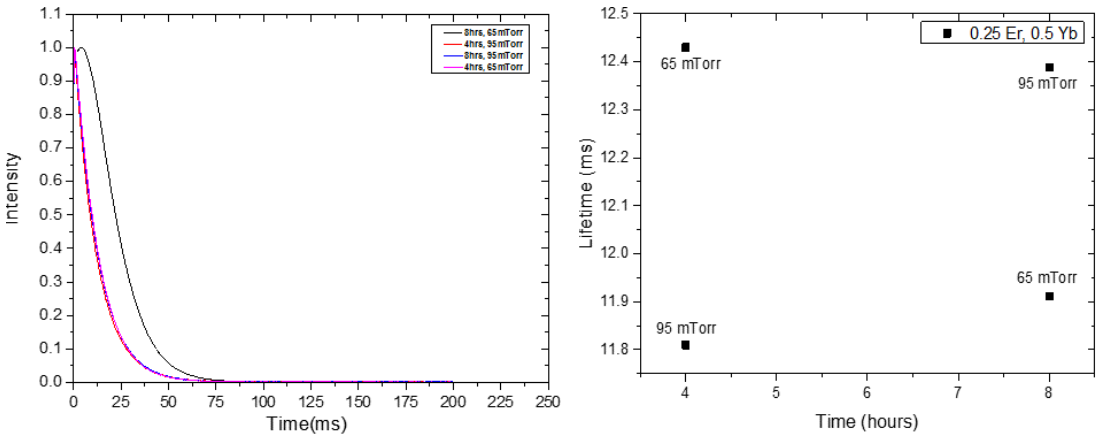

Figure 3.39: The fluorescence lifetime measurement (left) and x-y plot(right) comparing the chamber oxygen pressure and deposition time of the photonic chip with fluorescence lifetime. The photonic chips are doped with 0.25 mol percent Er^{3+} & 0.5 mol percent Yb^{3+} ions and the excitation wavelength is 980 nm. It is fabricated by altering chamber oxygen pressure and deposition time.

The fluorescence lifetime of the 0.25 mol percent Er^{3+} ions doped in photonic

chip varies from 12.16 to 12.74 ms (fig 3.38). The long lifetime value has been attributed to more distance between the Er^{3+} ions in silica network. The plot (fig 3.38(right)) shows that lower oxygen pressure shows the longer lifetime indicating a denser population of Er^{3+} ions in the photonic chips which decreases with increase in the pressure. The fluorescence lifetime is longer for samples deposited at 95 mTorr with same 8 hours deposition time this might be due to the larger emission cross-section due to increase in thickness more excitation light can be trapped in the silica network.

Fig 3.39 shows fluorescence lifetime of photonic chips doped with 0.25 mol percent Er^{3+} and 0.5 mol percent Yb^{3+} ions with altering chamber oxygen pressure and deposition time. The fluorescence lifetime measured was in the range 11.81 to 12.41 ms. The drop in the fluorescence decay is observed from the samples doped with 0.25 mol percent Er^{3+} ion. Two effects of change in lifetime due to changing pressure and deposition time can be observed: (1) lower oxygen chamber pressure results in a longer lifetime, indicating separated Er^{3+} ions, than higher oxygen pressure (2) thicker thin films have longer lifetimes which is similar to what is observed in fig 3.38 (right).

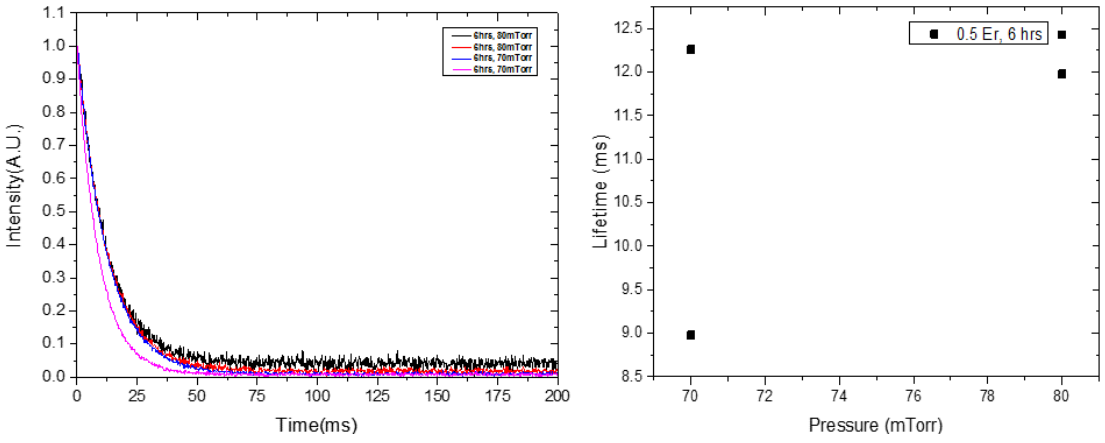

Figure 3.40: The fluorescence lifetime measurement(left) and contour plot(right) comparing the chamber oxygen pressure and deposition time of the photonic chip with fluorescence lifetime. The photonic chips are doped with 0.5 mol percent Er^{3+} ions and the excitation wavelength was 980 nm. It is fabricated by altering chamber oxygen pressure.

The photonic chips fabricated with 0.5 mol percent Er^{3+} ions exhibit fluorescence decay range from 11.98-12.26 ms with the deposition time of 6 hours. The fluorescence lifetime of the photonic chips has dropped to 8.98 ms indicating that Er^{3+} ion clustering centres in thin films might have been formed inside the photonic chip (fig 3.40). This might be due to some change in fabrication conditions. Another photonic chip fabricated with the same parameters has a decay of 12.26 ms which is more comparable with the other decay measured from the same set of photonic chips. Considering the 8.98 ms as an issue with fabrication there is no significant change in fluorescence lifetime by increasing chamber pressure from 70 mTorr to 80 mTorr while has fluorescence lifetime decreased from the sample fabricated with 0.25 mol percent Er^{3+} ions.

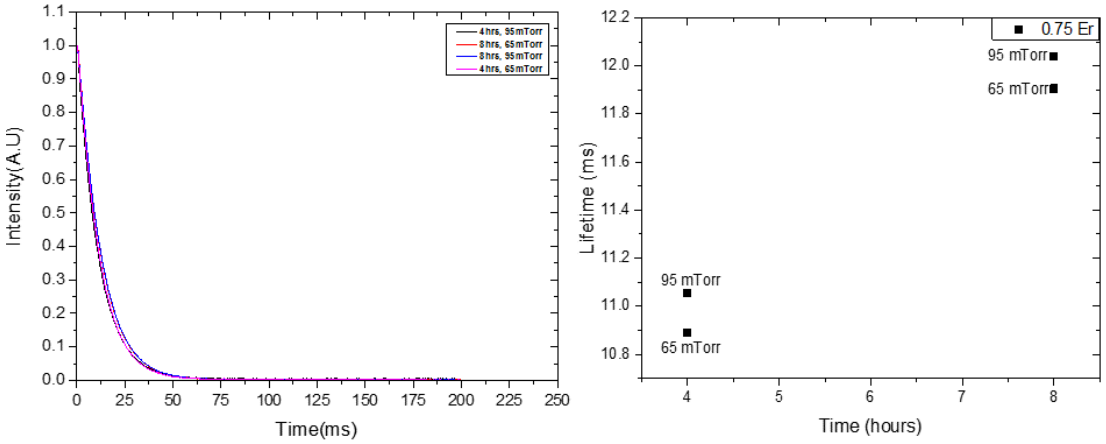

Figure 3.41: The fluorescence lifetime measurement (left) and x-y plot (right) comparing the chamber oxygen pressure and deposition time of the photonic chip with fluorescence lifetime. The photonic chips are doped with 0.75 mol percent Er^{3+} ions and the excitation wavelength is 980 nm. It is fabricated by altering chamber oxygen pressure and deposition time.

The photonic chips fabricated with the 0.75 mol percent Er^{3+} ions, has a fluorescence decay in range of 10.89 to 12.04 ms (fig 3.41). The fluorescence lifetime of this set of photonic chips seems to be independent of the oxygen chamber pressure between 65 mTorr and 95 mTorr while the longer deposition time shows longer lifetime which can only be due to increase in thickness of thin

films thus trapping more photons within the system. It is though consistent with the fact that increasing the Er^{3+} concentration causes the decrease in decay as reported in earlier findings (Chandrappan *et al.*, 2015).

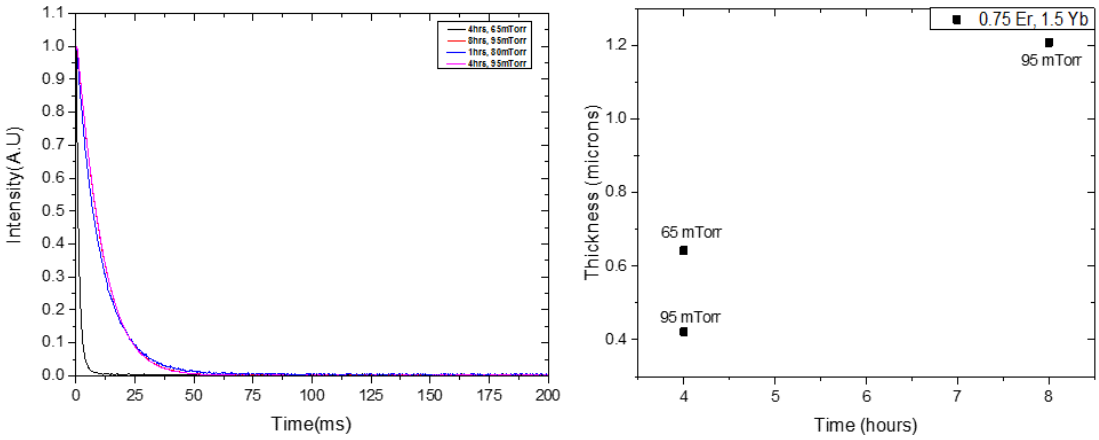

Figure 3.42: The fluorescence lifetime measurement (left) and x-y plot (right) comparing the chamber oxygen pressure and deposition time of the photonic chip with fluorescence lifetime. The photonic chips are doped with 0.75 mol percent Er^{3+} & 1.5 mol percent Yb^{3+} ions and the excitation wavelength is 980 nm. It is fabricated by altering chamber oxygen pressure and deposition time.

The fluorescence lifetime decay of the sample doped with 0.75 mol percent Er^{3+} and 1.5 mol percent Yb^{3+} ions has lowest overall lifetimes of the batch ranging from 10.13 to 11.17 ms. This is a significant drop in fluorescence lifetime from the sample doped with 0.25 mol percent of $\approx$ 1.3 ms thus suggesting change in Er^{3+} ions structural environment due to the presence of more Yb^{3+} ions. The up-conversion effect reported in the literature is likely to play a significant role in this case as the ion-ion interaction is likely to be larger than the low concentration of Er^{3+} doped thin films (Girard *et al.*, 2009; Savelii *et al.*, 2016).

3.5 Conclusion

The photonic chip doped with 0.25 mol percent Er^{3+} ion has given the longest lifetime compared to the other samples fabricated in this study. However, it can't

be the only single parameter essential for glucose sensing and the fluorescence intensity should be sufficient to penetrate the skin. The single mode photonic chip can provide an advantage over the multimode photonic chip as the propagation constant is different for each mode. Thus multimode photonic chip leads to wave mixing which can produce an error in the measurement. It is also clear from the results that FWHM and AUC are directly proportional to the concentration of the Er^{3+} and Yb^{3+} ions in the target glass used for the fabrication of the photonic chip (figure 3.23). However, the fluorescence lifetime is inversely proportional to the concentration of the Er^{3+} and Yb^{3+} ions in the target glass used for the fabrication of the photonic chip (figure 3.37). The ion-ion interaction and presence OH group seems to be playing a major role in the fluorescence quenching. The presence of Yb^{3+} ions has shown a significant impact on the FWHM and AUC of the Er^{3+} ions. The next chapter discusses the fabrication and IR sensing capabilities of the glass polymer (GP) superlattice fabricated using the nanosecond laser.

Chapter 4

Erbium doped Glass–polymer superlattice for integrated optics

4.1 Introduction

The objective of this part of the study was to demonstrate the feasibility of glass-polymer (GP) superlattice structures and biomimetic nanostructure fabrication by pulsed laser deposition (PLD) for transparent, reinforced and multi-functional materials. The hybrid structures were characterized by electron microscopy, optical spectroscopy, atomic force microscopy in this part of the study and some custom setups were built. The project was broadly classified into creating structures for two different applications areas:

1. Biomimetic nanolayers for strength enhancement
2. Tailoring of internal stress in a superlattice structure for infrared imaging/detection

4.2 Research methodology

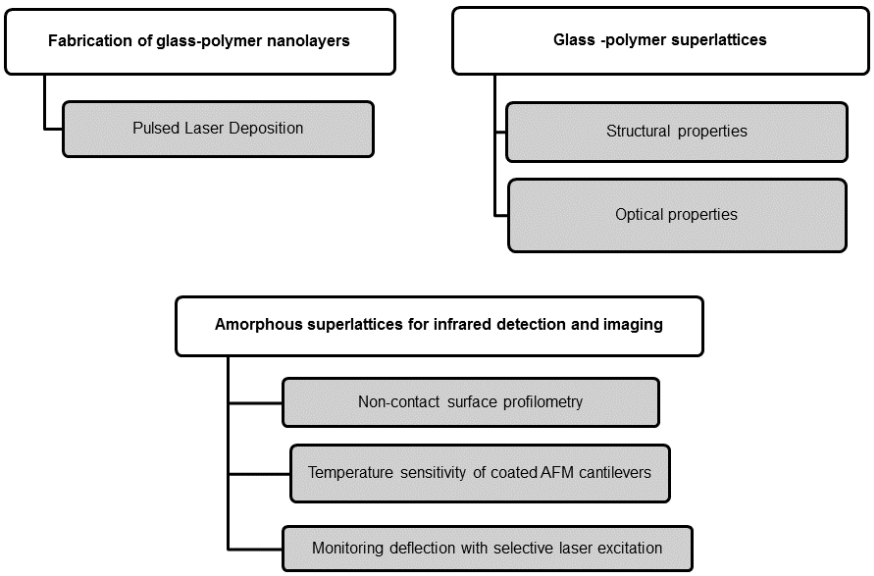

Figure 4.1: Research methodology adopted for fabrication and analysis of the glass polymer superlattice

The fabrication of glass-polymer superlattice was carried out by multi-target nanosecond pulsed laser deposition which has been proven to be the most suitable technique for nano-level structural fabrication (Eason, 2007). This technique is useful in creating nanocoatings over the substrate i.e. silicon in this part of the study. The key aim was to induce the stress in hybrid thin films, thus require a mismatch in thermal expansion coefficients. The thermal expansion coefficient of poly-dimethyl siloxane (PDMS) is -3.1 x 10^{-4} $^oC^{-1}$ whilst tellurite glass has coefficient of $\approx$ 20 x 10^{-6} $^oC^{-1}$ (El-Mallawany, 1999; Wiederhorn, 1969). The tellurite glass gives an advantage in offering wide tunability of wavelength absorption based on the element doped in the glass (Zhao *et al.*, 2012). The structural properties and optical properties of the GP superlattice has been discussed in this chapter. The modified AFM is used to analyse the temperature sensing of superlattice on laser excitation.

4.3 Fabrication of glass polymer superlattice

The primary component in the research methodology was the fabrication for glass-polymer superlattice structures. The differing thermo-mechanical properties of the glass and polymer makes such structures difficult to fabricate using conventional methods like chemical vapour deposition (CVD) or radiofrequency sputtering (Craciun *et al.*, 1995; Seshan, 2012). We used a pulsed laser deposition system equipped with multiple target holding capability. The system used is shown in Figure 4.2. It is composed of a nanosecond (ns) pulsed excimer laser with wavelength 193 nm and a vacuum chamber. The pulse repetition rate of the laser is 20 Hz and the maximum energy available in the chamber is 150 μJ.

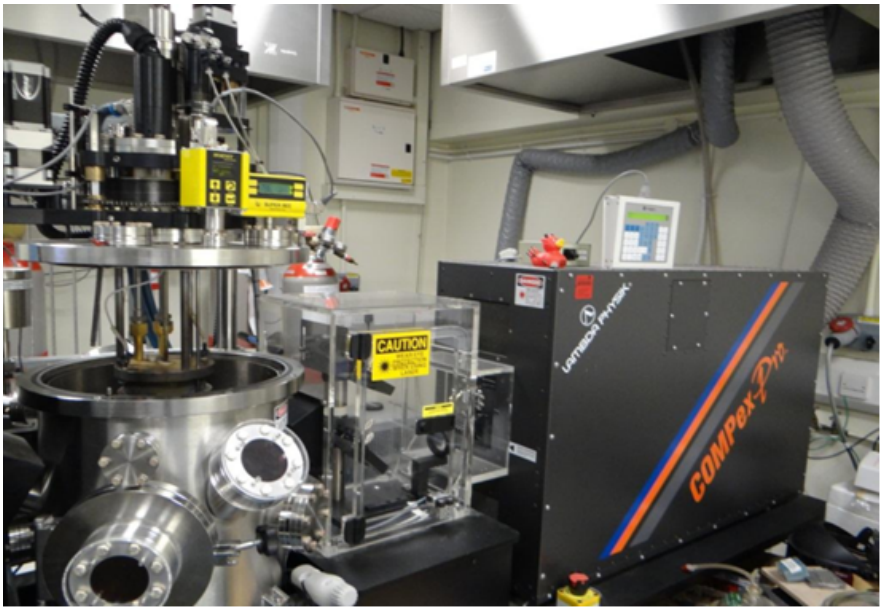

Figure 4.2: Excimer PLD setup

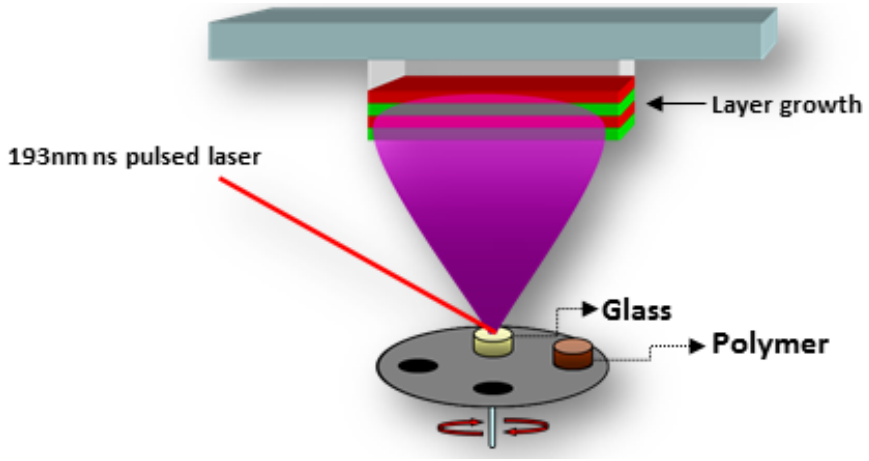

Figure 4.3: The mutli target nanosecond excimer PLD deposition process of PT glass and Sylgard polymer.

Deposition starts with the laser ablation of target material under reactive gas ambient which leads to the formation of plasma plume. This expanding plasma contains the ions evaporated from the target material which are then

deposited over the substrate surface. The volume and energy of laser ablated ions and particles depend on the laser parameters such as wavelength, energy per pulse and repetition rate as well the process parameters such as ambient gas and gas pressure, substrate temperature, target materials and, target to substrate distance. So in process like growth superlattice structures from two amorphous target materials like Er^{3+} doped PT glass and polymer, the above parameters have to be optimised for each target materials separately. This is particularly important when target materials have largely varying properties as shown in Table 4.1. Table 4.2 report the nearly optimum parameters that we used in this study for growing superlattice structure of glass and polymer. The PDMS target material was fabricated by mixing the base and cure polymers in a ratio of 10:1 Sylgard 184. The phospho-tellurite (PT) target glass was fabricated with composition of $46.5TeO_2$-$20Na_2O$-$20P_2O_5$-$10ZnF_2$-$1.1Er_2O_3$-$1.5Yb_2O_3$-$0.9CeO_2$. The deposition was carried out in vacuum chamber filled with 96% O_2 and 4 % He by volume maintained at 5 mTorr pressure. The pulsed laser deposition was carried out at pulse duration of 20 ns, 20 Hz repetition rate, 193 nm nanosecond excimer laser, and laser fluence of $\approx$ 0.4 J/cm^2. The temperature of the substrate was kept at 100 ^oC. The substrate to target height was kept at 55 cm.

Table 4.1: Properties of the target materials used for superlattice formation (El-Mallawany, 1999; Wiederhorn, 1969)

	Polymer	Glass
Sample type	PDMS, Dow Corning sylgard 184	Erbium doped phosphotellurite
Surface energy	21 mJ/m^2	One order higher
Thermal expansion coefficient	$310 \times 10^{-6}/^oC$	$20 \times 10^{-6}/\ ^oC$

Table 4.2: Process parameters used for superlattice fabrication

Parameter	Value
Laser wavelength	193 nm
Pulse duration	20 ns
Laser repetition rate	20 Hz
Target to substrate distance	55 mm
Substrate temperature	100^oC
Ambient gas	$96\%O_2 + 4\%He$
Ambient pressure	5 mTorr
Substrate	Silicon

4.4 Glass polymer superlattice

4.4.1 Structural properties

Figure 4.5 shows the formation of almost perfect superlattice of glass and polymer fabricated using PLD. Optimum deposition conditions for both polymer and glass allow the growth of such layers with minimum disruption. The thickness of the layers can be varied by varying the deposition time for each layer. It is possible to grow layers as thin as 2 nm (Zhao *et al.*, 2012) (see Fig 4.5b) by controlling deposition time and it is important considering the complexities involved in amorphous superlattice growth. The TEM Micrograph were obtained from a cross-section lamina as thin as 100nm produced by focused ion beam (FIB) etching (fig 4.5(b)). The thickness of each polymer layer obtained is 8.8 nm and that of the glass layer is 4.4 nm for the D3 sample. Figure 4.4 shows a sample prepared by FIB under scanning electron microscope (SEM). Further to investigate the interlayer uniformity we studied them using X-ray reflectometry (XRR). Figure 4.6(a) shows the results of XRR investigation done on same material by (Zhao *et al.*, 2012). Table 4.3 reports the density of superlattice obtained by XRR measurements (Zhao, 2012).

Table 4.3: Densities of the materials used for superlattice structure growth and the density of the resulting superlattice (Zhao, 2012; Zhao *et al.*, 2012)

	PDMS polymer	Phosphotellurite glass	Superlattice
Density	1 g/cm^3	5-6 g/cm^3	3.5 g/cm^3

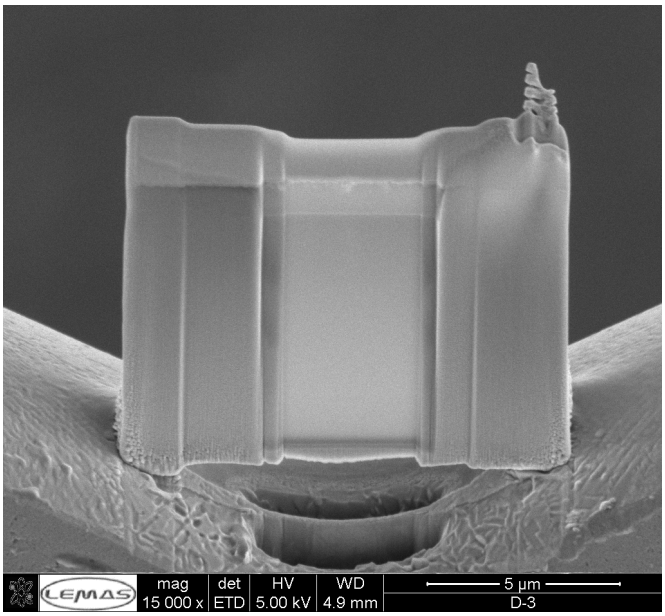

Figure 4.4: SEM of the sample prepared by FIB for TEM analysis. The layer below the top platinum layer is the superlattice thin film. The platinum is deposited to assist the FIB etching and sample detachment.

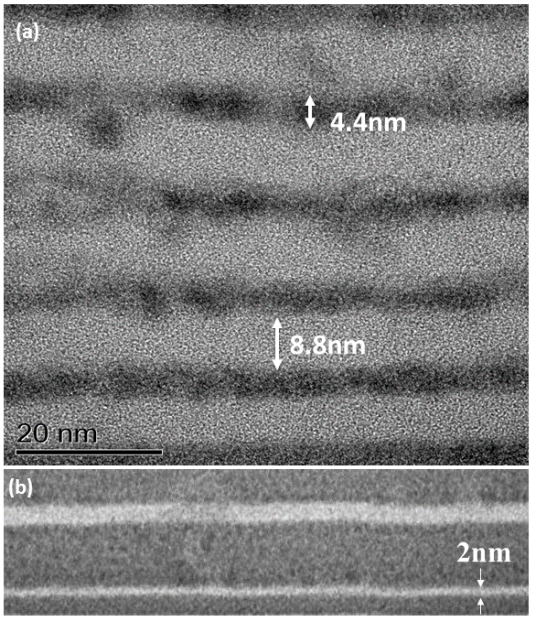

Figure 4.5: (a) TEM micrograph of amorphous superlattice of glass and polymer of D3 samples, b) TEM micrograph of the thin film with 2nm polymer layer (Zhao *et al.*, 2012).

Table 4.4: Details of glass-polymer superlattice deposited on silicon substrates

Sample ID	Top layer	Bottom layer	Layer ratio	Total thickness	Refractive index
D1	GLASS	POLYMER	2:1	0.9 μm	1.629
D2	GLASS	POLYMER	1:1	1.3 μm	1.634
D3	GLASS	POLYMER	1:2	1.6 μm	1.637

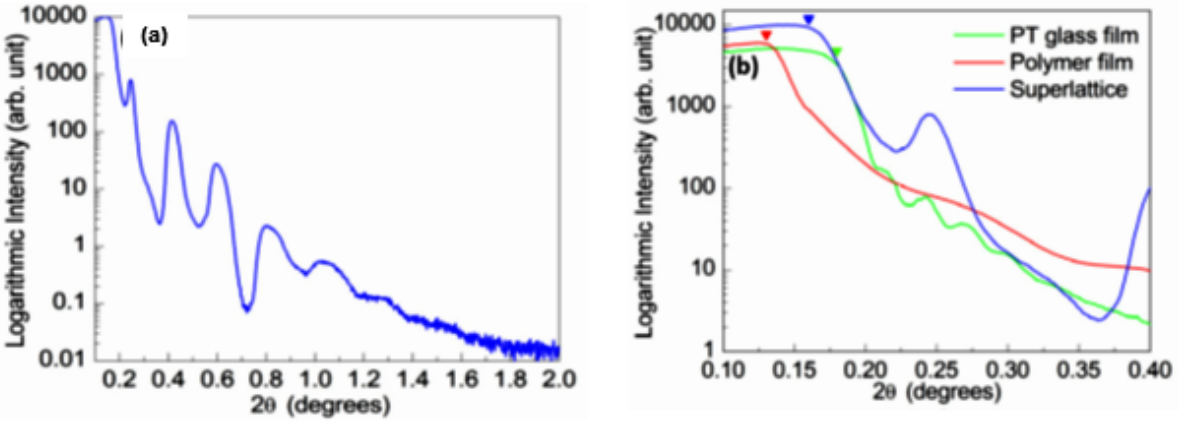

Figure 4.6: a) Shows the interference fringes obtained for glass-polymer superlattice period 10, almost 8 fringes are visible in the XRR plot. b) Comparison of the cut-off edge for individual glass and polymer films with the glass-polymer superlattice structure. The densities of the thin film materials were estimated from the cut-off edge position (Zhao *et al.*, 2012).

4.4.2 Optical properties

Figure 4.7 (a) shows the transmittance spectrum of the superlattice compared with that of a glass only thin film having equal thickness. The superlattice has higher transmittance extending to longer wavelengths however the transmittance of glass only film drops sharply above 2200 nm (Zhao *et al.*, 2012). Prism coupling method was used to measure the refractive index of the superlattice of all three samples by measuring the waveguiding modes at 1321 nm (Figure 4.8). The refractive index of the superlattice was obtained as 1.635 close to the glass refractive index (table 4.4).

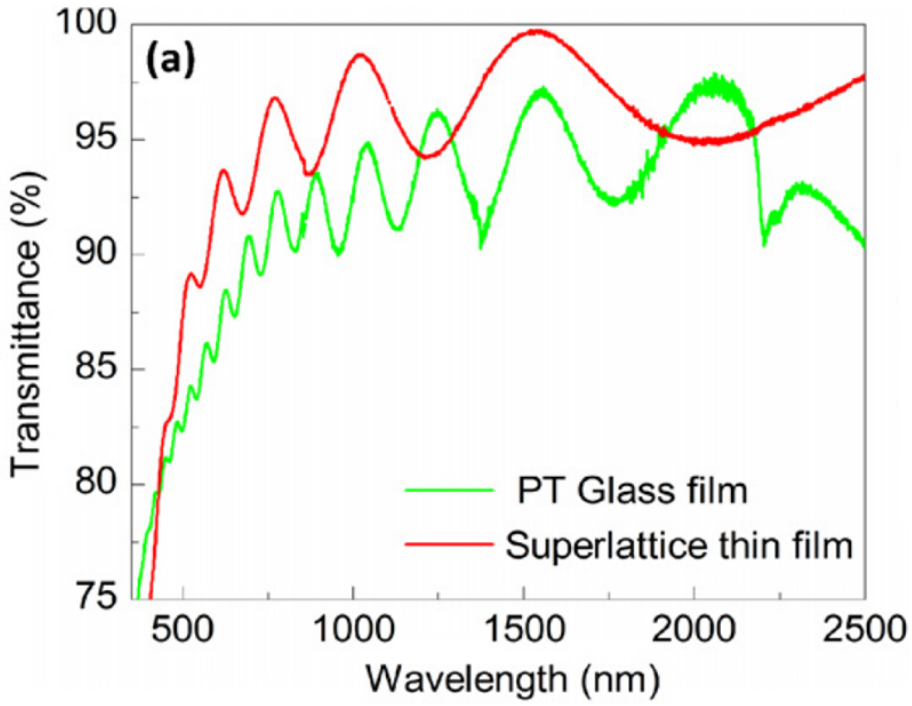

Figure 4.7: Transmittance spectrum of the glass only and superlattice structures (Zhao *et al.*, 2012)

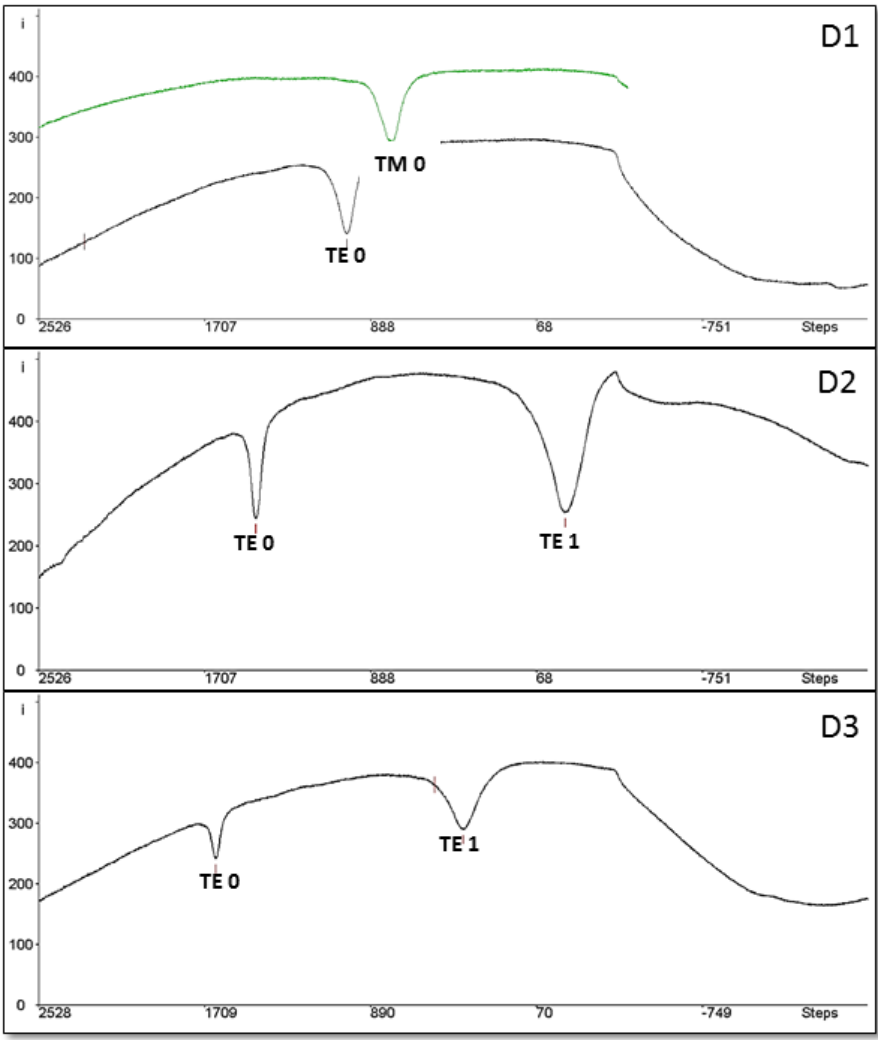

Figure 4.8: Prism coupling measurement data (633 nm) showing the position of guided modes indicating refractive index used to calculate the total effective refractive index of the films. In both measurements nanostructures in the superlattice are invisible to the laser used to measure and the material acts as a glass-polymer composite.

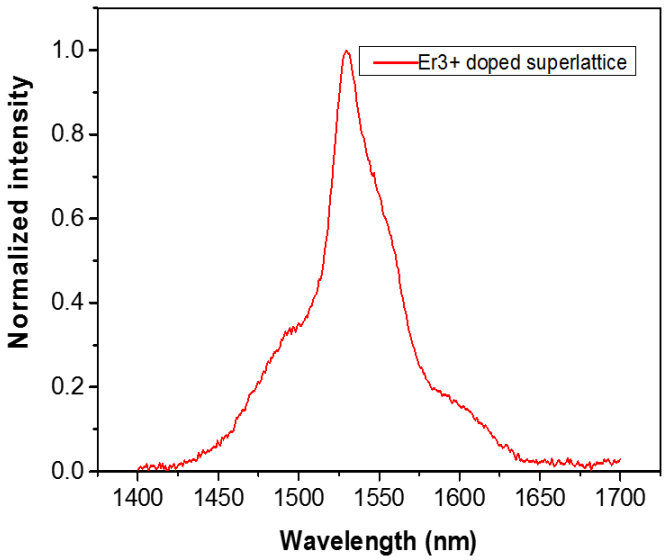

Figure 4.9: Fluorescence spectrum of Er^{3+} doped superlattice obtained under 980 nm laser diode excitation.The emission is peaked at 1533nm..

The fluorescence spectrum of erbium doped glass polymer superlattice was measured using 980 nm laser excitation and the emission peak at 1535 nm that is related to the transition from $^4I_{13/2}$ to $^4I_{15/2}$ energy level is shown fig 4.9. A broader peak is observed with bandwidth of 200 nm. This peak similar to a broad emission peak of PT glass reported in Zhao *et al.* (2012) paper.

4.5 Amorphous superlattices for infrared detection and imaging

As a new approach to utilise the nanofabrication we proposed the application of superlattice for development of uncooled mid-IR imaging devices. This is a new direction we explored as the project evolved. The basic principle of sensing of heat from a distant source was found observing the Jewel Beetle (fire Beetle) and has been reported before. The deflection of their receptors with respect to the small variations in heat radiation is considered to be the underlying physical mechanism allowing the beetle to detect forest fires from several kilometres

(Klocke *et al.*, 2011; Schmitz *et al.*, 2009). As a proof of concept we looked at the internal stress control in a GP superlattice coated on silicon and silicon AFM cantilevers fig 4.13 (tipless). The temperature dependent and specific wavelength irradiation effects on the stress and resultant bending due to differing thermal expansion coefficients of this silicon-GP superlattice bimorphs are investigated. The samples were fabricated using PLD described previously but we used crystalline silicon substrates in this instance. Table 4.4 reports details of the samples prepared using 3x2cm silicon substrate prepared from a silicon wafer of thickness 150 μm. Samples were prepared by varying the order and thickness of the glass and polymer as reported in the table 4.4. In the case of AFM cantilevers, we mounted them on silicon substrates for deposition and characterization.

4.5.1 Non-contact surface profilometry

To evaluate the stress induced in the superlattice thin films, the radius of curvature (Ra) of the 3 samples listed in Table 4.4 was measured using a non-contacting surface profiler Wyko NT3300S (see Fig 4.10). The instrument uses white light interferometer instead of a stylus to measure the surface profile. Its key advantage of this technique is that it doesn't damage the surface as no physical contact is made to assess the sample surface features (Olszak, 2000).

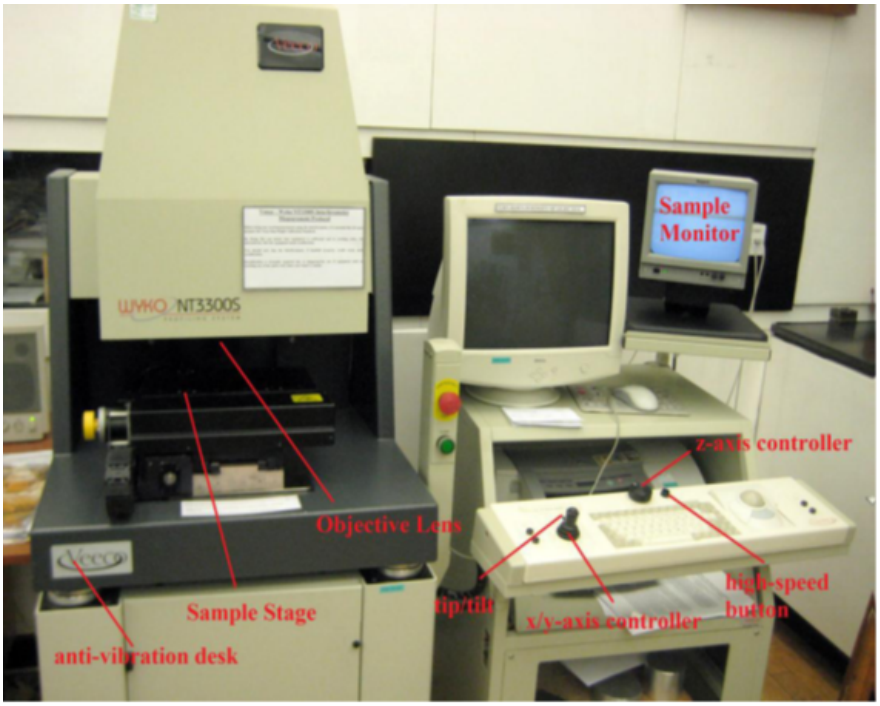

Figure 4.10: Wyko NT3300S Non contacting surface profiler

WykoNT3300S surface profiler record data from specimen either by phase shift interferometry technique or vertical scanning interferometry technique which has an accuracy of 1 nm and 30 nm respectively. The deposited super-lattice thin films can have either of two types of stress i.e. tensile stress and compressive stress which is due to the mismatch in thermal expansion coefficient of substrate and super-lattice thin film (fig 4.12) (Waters, 2008).

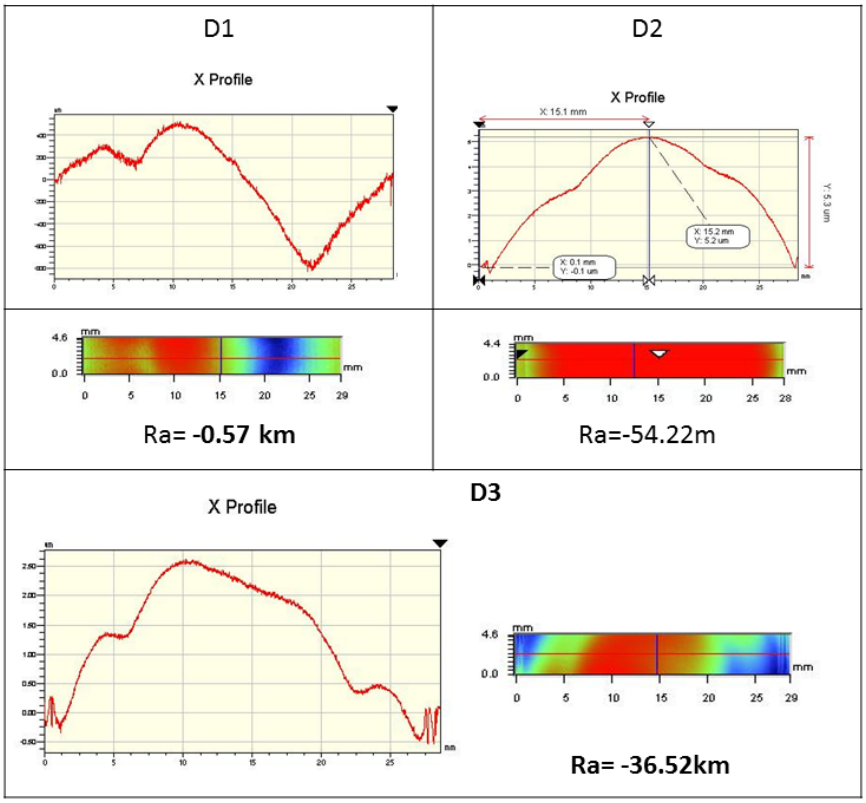

Figure 4.11: 2D surface profile for three samples D1, D2 and D3. Radius of curvature for each sample is also given.

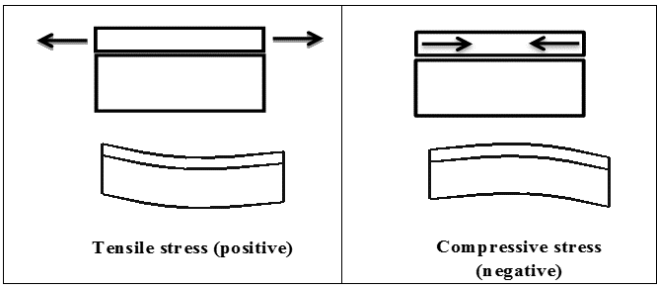

Figure 4.12: Stress induced in a biomorph structure, it could be either tensile of compressive stress depending on the combination of materials used. A tensile stress gives a positive radius of curvature in profilometry while compressive stress results in negative radius of curvature (Waters, 2008).

Figure 4.12 compares the effect of tensile and compressive stress in a biomorph structure of dissimilar materials and defines their mechanical effects. The non-contact profilometry results show a compressive stress in the film as indicated by the negative radius of curvature (fig 4.12). The inward bending of the structure increases with increase in film thickness and is highest for D3 with 1.6 μm thickness. It is observed that this internal compressive stress is enhanced in samples with polymer-glass ratio 2:1 and therefore thinner films can be used.

4.5.2 Temperature sensitivity of coated AFM cantilevers

In order to study the bending, we prepared a set of tipless AFM cantilevers with the coating parameters same as that of D3. Figure 4.13 shows the photograph of a cantilever coated with superlattice thin film. Specifications of the silicon AFM cantilever used in this study are reported in Table 4.5.

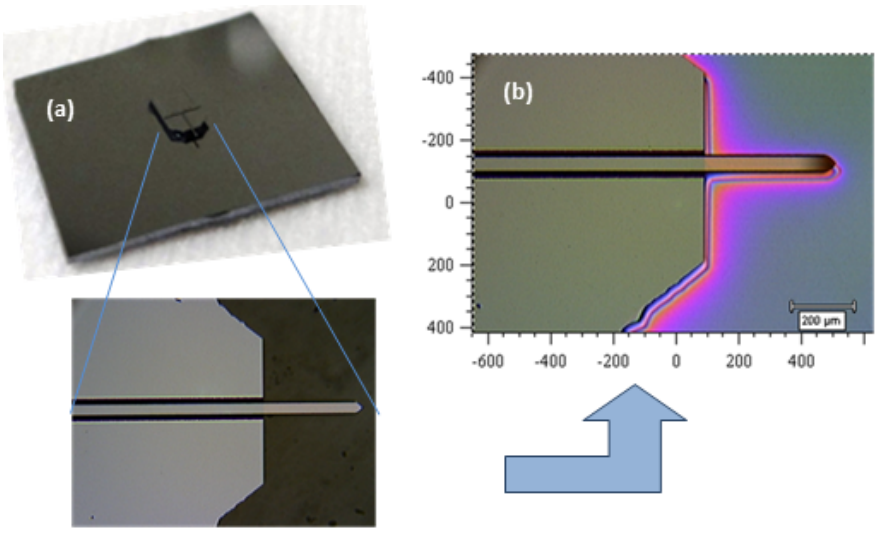

Figure 4.13: a) Tipless AFM cantilever resting on silicon base and its magnified view b) Glass Polymer superlattice coated AFM cantilever.

Table 4.5: Specifications of silicon AFM cantilever

Parameters	Nominal value	Specified range
Thickness(μm)	2	1-3
Width (μm)	50	42.5-57.5
Length(μm)	450	440-460
Force (N/m)	2	0.02-0.77
Resonance frequency (kHz)	13	6-21

Figure 4.14 shows the SEM micrograph of a cantilever after deposition of superlattice thin film. The angle and deflection of the bent tip can be measured using this method. As described before by the profilometry, the stress in this case is compressive leading to a downward bending that can be measured accurately to nanometre level. This characterization step was carried out to the measure the dimension of the cantilever tip and radius of curvature due to glass polymer superlattice. The measured data can be used to calculate the internal stress in the film.

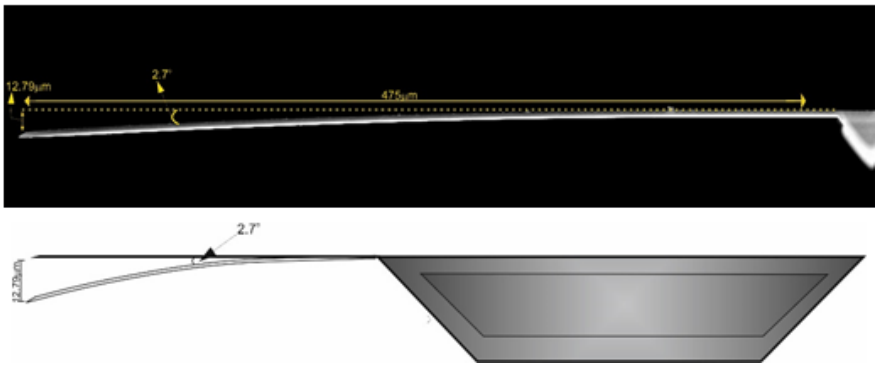

Figure 4.14: SEM of the GP superlattice coated AFM cantilever showing the bending due to the bimorph structure.

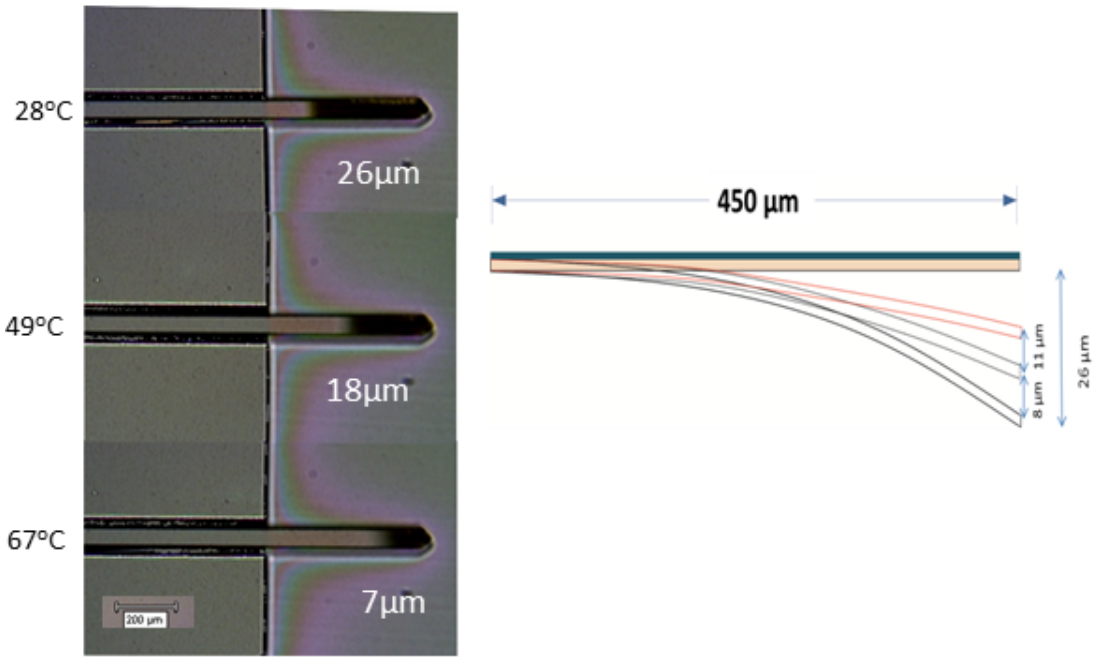

Figure 4.15: Optical microscope image of the bend cantilever at different temperatures. The angle of deflection decreases with increase in temperature.

Qualitative assessment of the cantilever bending can be observed in an optical microscope while monitoring its temperature. We used a custom microscope setup to record the bending at different temperatures. Figure 4.15 shows the image of the cantilever at different temperature while keeping the focal position unchanged.

4.5.3 Monitoring deflection with selective laser excitation

In order to monitor the nanoscale deflection under moderate temperature change we used an AFM. We have modified the setup by removing the original cantilever from the AFM and mounted the GP superlattice coated cantilever directly on the sample stage. We used erbium doping in the glass layer of the superlattice which will absorb light at 980 nm also the silicon absorbs 980 nm laser. Therefore by using 980 nm laser focused at the cantilever it is possible to heat it continuously (fig 4.17). As the Er^3+ ions in the GP superlattice absorbs 980 nm wavelength

it heats the superllatice due to non radiative emission of Er^{3+} ion from $^4I_{11/2}$ to $^4I_{13/2}$ energy level. As shown in fig 4.11, a D3 film has internal compressive stress due to which cantilever bends downwards at room temperature (see fig 4.13(b)). The cantilever deflects upwards with the increasing temperature as shown in fig 4.15. The continuous heating of the cantilever was done for different time periods of 10 mins, 20 mins until 60 mins. A low power 633 nm continuous wave laser was focussed on the cantilever and reflected to AFM detector to note the bending direction (see fig 4.17). The change in the cantilever position due to increase in temperature was analysed from AFM and optical microscopy data. The calibrated data comparing cantilever deflection in degrees and temperature change was plotted. The slope of the linear fit was 0.5 nm/mK (fig 4.18(right)). This superlattice can be modified comparing to what is reported in the literature for only polymers and a biomorph with controlled internal stress can be fabricated (LeMieux *et al.*, 2006).

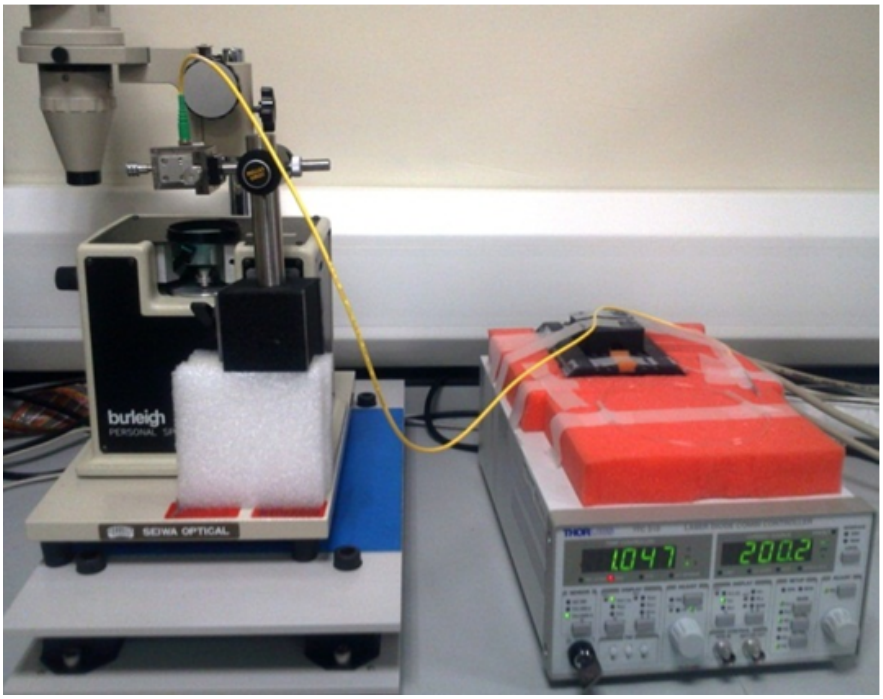

Figure 4.16: AFM microscope with laser assembly.

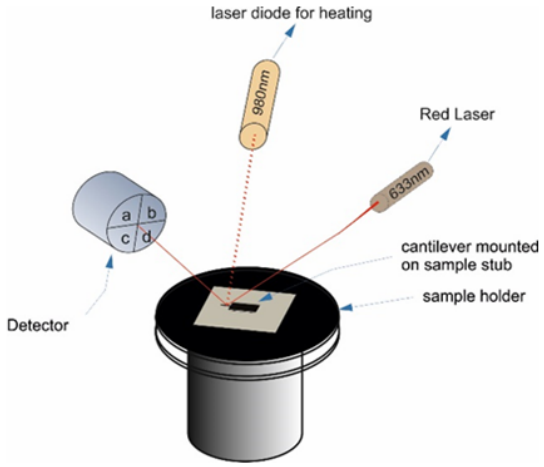

Figure 4.17: Schematic illustration of AFM assembled so as to measure the change in bending in cantilever tip.

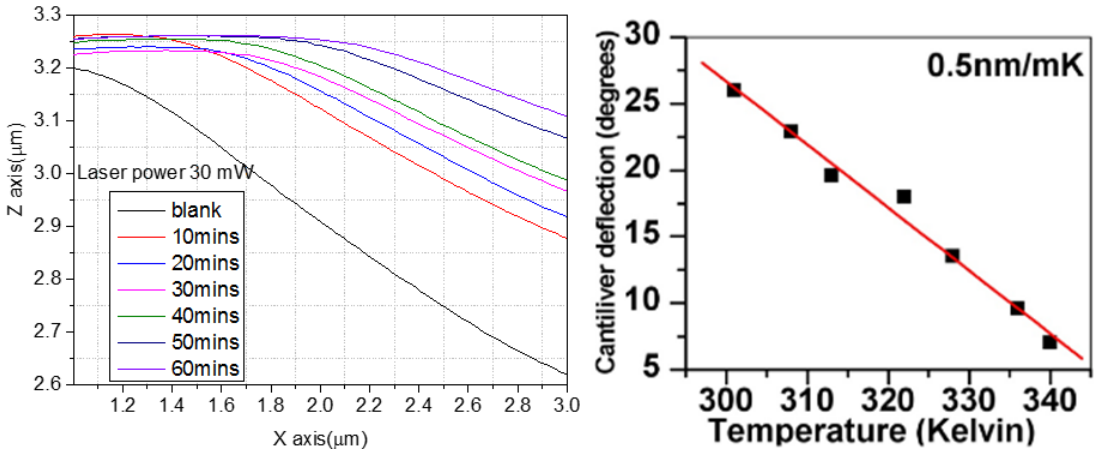

Figure 4.18: Bending curvature of cantilever tip, Graph of GP superlattice coated microcantilever deflection with increasing temperature

4.5.4 Conclusion

Application of GP superlattice structure for long wavelength (IR) detection and imaging is investigated.The internal stress in superlattice thin films on silicon is studied using non-contact profilometry, further studies are required to investigate

the effect of layer thickness variation on internal stress. Such studies will allow new bimorph design for application in IR imaging devices.The temperature dependence of the deflection in a AFM cantilever is investigated and demonstrated the feasibility for IR imaging with such micro-nano structures.A functional cantilever surface was prepared by doping the glass layer in the superlattice with the rare earth ion Er^{3+} and a preliminary investigation of its response with 980 nm laser irradiation is carried out. Further research and device development required to use the micro-cantilever approach to be translated for IR imaging applications. Based on the laser fabrication process as the high value fabrication could benefit the commercialization.

Chapter 5

Bio-compatibility of photonic Chip

5.1 Introduction

The biosensor requires cyto-toxicity testing to check whether the thin films are safe to use in medical diagnostics according to guidelines given in ISO-10993. This evaluation is based on the type of contact sensor makes with body, duration of contact, area of contact. The compatibility of biosensor will determine whether or not the chemical properties of the sensor will cause any static/dynamic effect on the morphology of the host system (Anderson & Shive, 2012; Shim *et al.*, 2002; Shukla *et al.*, 2005). The biosensor has to go through a rigorous testing before they are safe to use on human body as described in International Organization of Standardization(ISO). The two ISO documents that have been followed here are ISO 10993-5, biological evaluation of medical devices: tests for in-vitro cytotoxicity and 10993-12, Sample preparation and reference materials (ISO, 2008, 2009). Studies performed on the silica nano particles in the past have found that smaller particle size of silica seems to be less toxic than the larger particle size (Kim *et al.*, 2015; Yu *et al.*, 2011). Also the crystalline silica is noted to cause the congestive obstructive pulmonary disease and silicosis (Hnizdo & Vallyathan, 2003). However, surface modification characteristic of silica as well biodegradability makes it useful in biomedical applications (Pasqua *et al.*, 2009). The thin films will be used for sensing glucose by keeping the surface of glass in the contact of the skin. It is important to know how safe the device will be in regular use. The commercially available glucose monitor falls under in vitro medical devices and requires IVDMDD(98/79/EC) (Directive, 1998) directive to be followed due to the examination of a specimen derived from the human body. Since no specimen is extracted for the measurement of the glucose and the device is in contact with the human body, the non-invasive finger touch glucose monitor(NFTGM) falls under the Medical Device Directive 93/42/EEC as a Class IIa or IIb device, according to rule 10 of the Directive. *"Rule 10 is defined as an active device for diagnosis, intended to supply energy for direct diagnosis or for monitoring of vital physiological processes as Class IIa device. If the device is specifically intended to monitor vital physiological parameters where variations could result in immediate danger then the device is classified as a Class IIb device"* (Directive, 1993). It also states that biological risk related to the device should be assessed prior to the use

of a device according to standards set in BS ISO 10993-1. The aim of this chapter is to use three assays i.e. MTT, XTT and neutral red assay to assess the level of cytotoxicity of the thin films and their individual chemicals. The test samples used in this part of the study has been described in Table 5.1 and 5.2. The individual chemicals were added based on the ISO-10993-12 requirements which state that test sample is chosen according to the maximum concentration used in the study, thus the concentration of 0.75 mol percent Er^{3+} and 1.5 mol percent Yb^{3+} ion in target glass was used for cytotoxicity of individual constituents. To test cytotoxicity of the thin films five photonic chips were tested based on Er^{3+} and Yb^{3+} ions concentrations in target glass that are used to fabricate thin films (Table 5.2).

Table 5.1: The concentration of each mixture made according to the target glass concentration for cyto-toxicity assay.

Sample	**Weight (mg)**	**Mol percent**
TeO_2	4.29	77.75
ZnO	0.27	10
Er_2O_3	0.09	0.75
Yb_2O_3	0.18	1.5
Na_2O	0.36	10

Table 5.2: The concentration of the each individual chemical made according to the target glass concentration for cyto-toxicity assay.

Sample ID	**Er^{3+}**	**Yb**
T1	0.25	0
T6	0.75	1.5
T8	0.25	0.5
T16	0.5	0.5
T17	0.75	0

5.2 Cell culture

5.2.1 L929 cell culture

The fibroblast mouse cells L929 were obtained from European collection of cell cultures, Salisbury,UK. The cell culture of L929 cells was done up to 4 passages to create a stock before the assay was carried out as follows:

1. The cells are stored in dimethyl sulfoxide which do not allow the formation of ice crystals during freezing which can be detrimental to the cell lines.
2. The growth medium used in the study was eagle minimum essential medium (MEM) supplemented with 10 % (v/v) of foetal calf serum (FCS), 4 mM of L glutamine, 100 IU/ml of penicillin, and 100 μg of streptomycin.
3. The prepared medium was used only for two weeks and stored at 4 ^oC. The MEM for culture is warmed at 37 ^oC.
4. The 5 ml of warm MEM medium was transferred to the 15 ml sterile falcon tube.
5. The frozen cells were then thawed inside the incubator for $\approx$ 3-4 mins.
6. The cells were then transferred into the falcon tube containing the warm medium. The cryovials which hold the cells was then washed with 1 ml of medium to take any remaining cells in the vial.
7. Total volume was then made up to 10 ml of cells in MEM and transferred to the T75 flask for cell culture and then incubated at 37 ^oC in 5 % CO_2 in humidifier incubator.
8. Half of the growth medium was changed next day to remove excess DMSO from the culture.

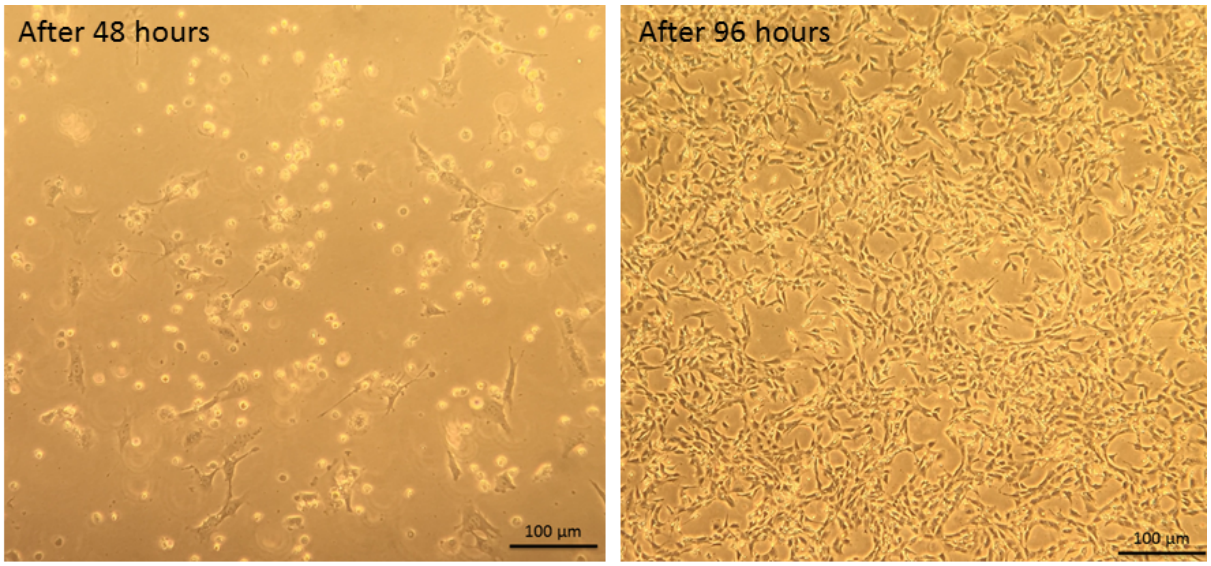

Figure 5.1: L929 cells seeded in T75 flask observed under optical microscope with 10x magnification at different times of cell culture.

9. The monolayer growth of cells was observed under the microscope after every 24 hours to check whether the cells are confluent or not. The monolayer analysed after 48 hours of seeding showed half confluence and almost 80 % confluent after 96 hours. MEM was also changed after 72 hours of seeding the cell as well.

10. When the cells reached 80 % confluence, they were split for the next passage.

11. For splitting cells, sterile phosphate buffer saline(PBS) and trypsin were warmed to 37 ^oC. The medium from the cells was drained and cells were washed with 3 ml PBS for 2 mins to remove any leftover growth medium.

12. PBS was removed and 3 ml of 0.25% trypsin/EDTA solution was added to the cell flask and then kept in an incubator at 37 ^oC and 5 % CO_2. The cell splitting was observed under microscope every 5 mins untill all the cells have been removed from the surface of T75 flask (see figure 5.2). The cells were incubated for $\approx$ 20 mins until all cells were suspended in the solution. A gentle tapping of flask was also done to suspend the cells.

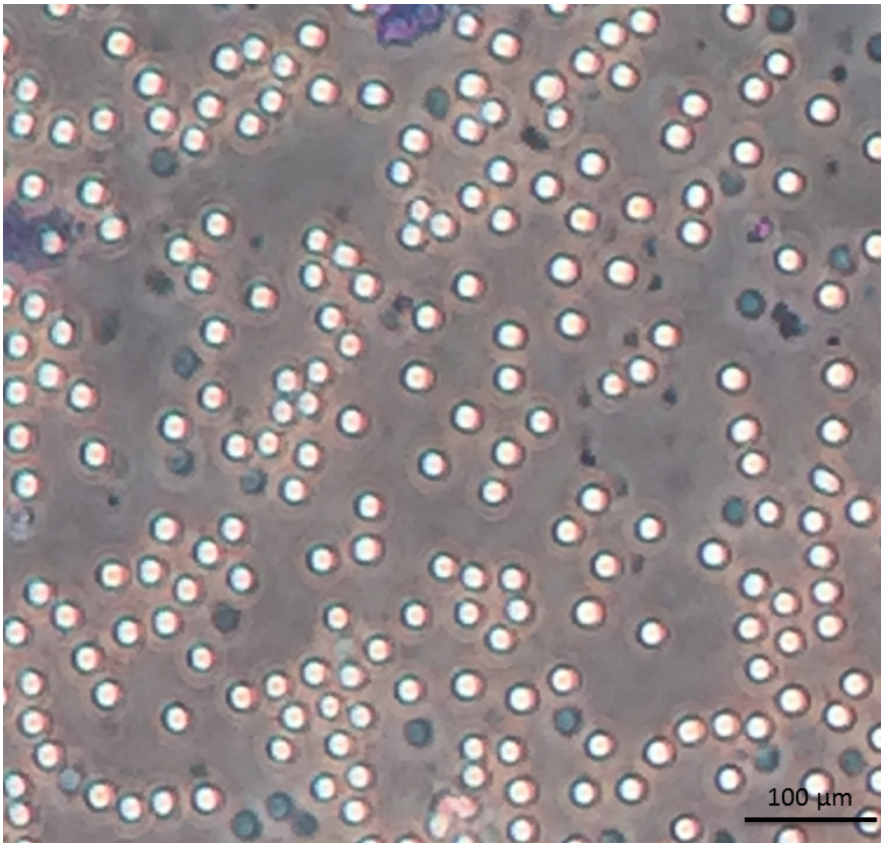

Figure 5.2: L929 cells suspended in 0.25% trypsin/EDTA solution after 12 mins of incubation observed under optical microscope with 10x magnification.

13. 5 ml of the growth medium i.e. MEM was added to the cells and then mixed with the 10 ml pipette. This was done to inhibit the cell splitting action of trypsin. The cells were collected in the sterile 15 ml centrifugal tube and then centrifuged for 4 mins at 1300 rpm, 26 ^oC.

14. A pellet of the cells at the bottom of the tube was formed. The remaining solution in the tube was thrown away and then aspirated with 1 ml MEM using micropipette and counted. The counting technique is common for both cell cultures used in this study and has been described in detail in section 5.2.2.

15. The cells are then used for either to passage more cells / for assay/ for freezing the cells in liquid nitrogen as a stock.

Freezing the cells

1. For freezing the cells, a solution of 20 % foetal calf serum (FCS) and 10 % by volume DMSO was mixed in MEM medium to prepare a cryopreservation solution.

2. The cells from the previous passage were counted and adjusted to 1 x 10^6 cell/ml using cryopreservation solution.

3. 1 ml of cells suspended in cryopreservation solution is then filled into cryovials which are able to withstand -196 ^oC temperature when stored in liquid nitrogen.

4. The cryovials were then stored in Frosty Freezing Container. The container was then transferred to -80 ^oC freezer and stored for 12 hours before it is transferred finally into the liquid nitrogen dewar.

5.2.2 Cell counting

The cell suspensions were stained using trypan blue dye and only the living cells are stained by this dye. It is important that cells do not overlap each other on the cell counter and are evenly distributed. While counting the cells there should be minimum 50 cells per large square, if cells are less than that then lesser dilution of trypan blue to cell containing medium was used. The cells were counted using hemocytometer (see fig 5.3) which has grids on two side of 3 mm each. Each grid has four large squares on each corner of one side of the plate and each large squares is divided into 12 mini squares (fig 5.4). Hemocytometer and cover slips were cleaned with the alcohol before using it. The cover slip was kept over the grid in the hemocytometer (fig 5.1) and the trypan blue solution mixed with the cell suspended medium was introduced from each side of plate using pasteur pipette. The cell suspended layer forms a thickness of 0.1 mm in the plate (Diego, 2017).

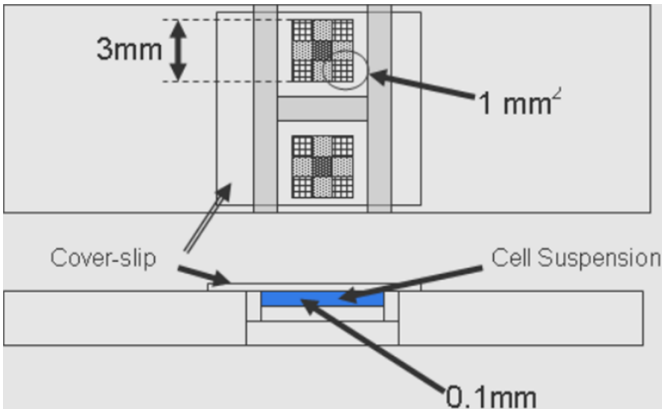

Figure 5.3: Arrangement of Hemocytometer and dimensions of the grid (phe-culture collections, 2011).

Procedure

1. The hemocytometer and cover slip were cleaned with ethanol and left to dry. Thereafter the cover slip was placed on the hemocytometer.

2. From the cell medium suspension which were prepared after centrifugation in previous section, 0.2 ml of the cell suspension was pipetted out into an Eppendorf tube. The Eppendorf tube was swirled to suspend the cells and then 100 μl of the cell was pipetted out into new Eppendorf tube and 100 μl of the 0.4 % by volume of trypan blue was added which makes the final concentration to *approx* 0.32 % by volume trypan blue and mixed with pipette. Dilution factor was 1:2.

3. 50 μl of the stained solution was then drawn and gently spread into the grid by pipette. Due to capillary action the solution easily spread into space between the top of the plate and cover slip (fig 5.3).

4. The plate was then observed under 10x magnification under optical microscope and the viable cells present in the 4 larger squares on each side of the plates are counted with hand tally counter.

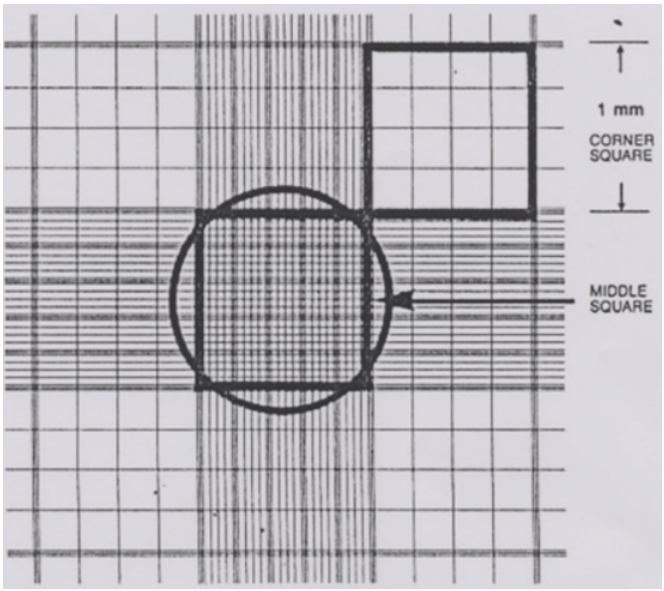

Figure 5.4: The scaling of the hemocytometer as visible under optical microscope (phe-culture collections, 2011).

5. The count was done only of the live cells within the 16 mini square present of each large squares shown in fig 5.5. The cells present on the two edge of the large squares were counted and also from the cells present within large squares. The live cells were counted from each large squares (fig 5.6) and total count of lives was done and added from eight large squares and averaged. Total cells present per ml of the solution was calculated from following formulae:

   Total number of live cells per ml = average count per square x dilution factor(1:2) x 10^4 (conversion factor)

6. One large square is 1 mm^2 and height of sample is 0.1 mm. The total volume is 0.1 mm^3 or 10^{-4} cm^3 or 10^{-4} ml. Thus the conversion factor, 10^4 is used to calculate total number of cells based on total volume of each large square i.e. 0.1 mm^3 or 10^{-4} cm^3.

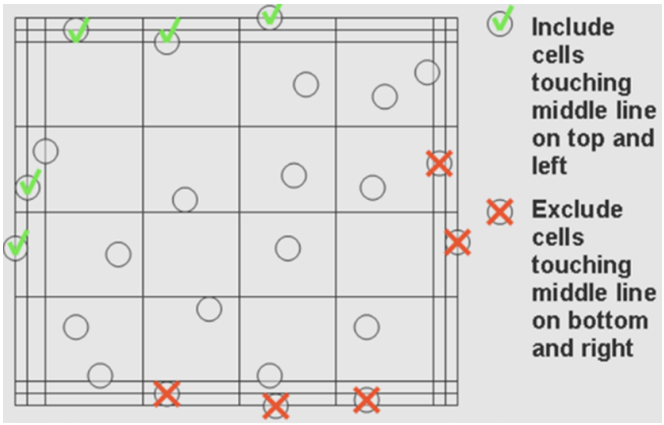

Figure 5.5: The cell counting technique using the plate to ensure consistency in results. Cell from only two side of the large is counted as well from the mini squares present within the boundary of large squares (phe-culture collections, 2011).

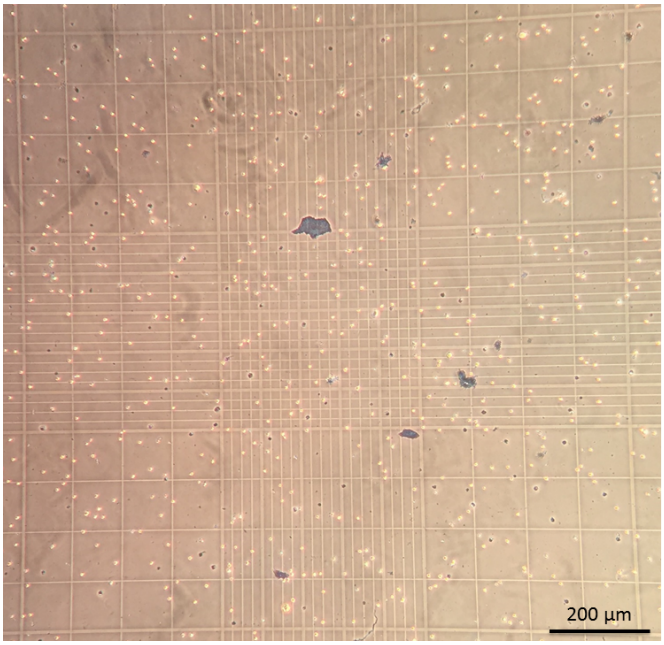

Figure 5.6: L929 live cells stained with trypan blue under 10x magnification in optical microscope

7. Final step was to add more volume of MEM in to falcon tube to make

cell count of 1 x 10^6/ml in case of next passage or freezing the cells or 1 x 10^4/100 μl MEM cell culture medium in case of test samples (Abcam, 2017).

5.2.3 BALB 3T3 cell culture

The fibroblast mouse BALB 3T3 cells were obtained from European collection of cell cultures, Salisbury,UK. The cell culture of L929 cells was done up to 4 passage create a stock before the assay was carried out as follows:

1. The growth medium used in the study was Dulbecco's modification of eagle's minimum essential medium (DMEM) and 10 % (v/v) of new born calf serum (NBCS), 4 mM of L glutamine, 100 IU/ml of penicillin,100 μg of streptomycin, 20 mM of HEPES buffer was added.

2. The prepared medium was used only for two weeks and stored at 4 ^oC. The MEM for culture is warmed at 37 ^oC.

3. 5 ml of warm DMEM medium was then transferred to the 15 ml sterile falcon tube.

4. The frozen cells were then thawed inside the incubator for $\approx$ 3-4 mins. The cells are stored in dimethyl sulfoxide which do not allow the formation of ice crystals during freezing which can be detrimental to the cell lines.

5. The cells were then transferred into the falcon tube containing the warm medium. The cryovials which hold the cells was then washed with 1 ml of medium to take any remaining cells in the vial.

6. Total volume was then made up to 10ml of cells in DMEM and transferred to the T75 flask for cell culture and then incubated at 37 ^oC and 5 % CO_2.

7. Half of the growth medium is changed next day to remove excess DMSO from the culture.

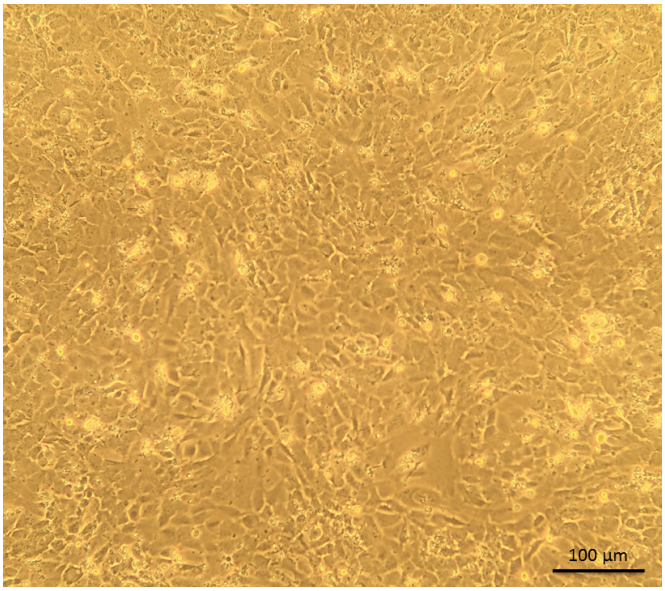

Figure 5.7: Confluent mono-layer of 3T3 cells seeded in T75 flask observed under optical microscope with 10x magnification.

8. The growth of cell monolayer was observed under the microscope after every 24 hours to check where the cells were confluent or not. DMEM was also changed after 72 hours of seeding the cell as well.

9. When the cells reached 80 % confluence, the cells were split for the next passage (fig 5.7).

10. For splitting the cells, the same procedure for L929 cells was used.

11. 5 ml of the growth medium i.e. DMEM was added to the cells and then mixed with the 10 ml pipette. This was done to inhibit the cell splitting action of trypsin. The cells were then collected in the sterile 15 ml centrifugal tube and then centrifuged for 4 mins at 1300 rpm, 26 ^oC.

12. A pellet of the cells at the bottom of the tube was formed. The remaining solution in the tube was thrown away and then aspirated with 1 ml DMEM solution using micropipette and counted.

13. The cell were then used for either to passage more cells or for assay or for freezing the cells in liquid nitrogen as a stock.

5.3 Experimental setup

For the assay to be carried out, the cells were cultured up to passage 4 and frozen at -196 ^oC for later use. The samples to be tested for cytotoxicity were stored in the extraction medium i.e. respective growth medium without serum according to the manufacturing instruction for each cell line for 24 hours in 6 well plates and the plates were kept in an incubator at 37 ^oC for 24 hours with 5 % CO_2. The sample that were kept in the extraction medium were placed according to table 5.1 and 5.2. The thin films were kept according to 0.1 g/ml of the extraction medium (ISO, 2008). The thin films were cut to required size by using the cutting machine specialised for glass cutting and the sterilized using the 70 % ethanol in a ultrasonic cleaner then stored in a sterile tube containing 70 % ethanol during transfer of samples from engineering to medicine department. The thin films were then again rinsed thoroughly with 70 % ethanol and immediately stored in the new sterile tube. It was ensured that external contact was not possible for the thin films to avoid any contamination thereafter. The sterile thin films were then transferred under sterile conditions in laminar air flow to the 6 well plate containing extraction mediums for each assay as discussed further in this section. The extraction medium should contain polar and non polar solvents which is required according to ISO (2009) for leaching (if any) from the test samples. The extraction medium contained chemical released from the surface of thin films (if any). It is important know the cytotoxicity of individual chemicals present in the thin films to assess how the cell viability is changing according to each chemical. Thus a potential toxic material can be identified and if in case of thin films show less cell viability, we can understand possible reagent/reagents causing cytotoxicity. The cell lines were cultured in the 96 well tissue culture microtitre plates on day 1. On day 2, the cell culture medium was removed from each well and the extraction medium was added according to their respective samples as shown in fig 5.8 and 5.9 for each assay. On day 3, the test solution according to each assay is added and the optical density of each well was measured for each

assay. The experiment was repeated three times and then obtained optical density was averaged and plotted as percent cell viability (mean ± sd) for each assay using a spectrophotometer. The significance of the results was tested according $p < 0.05$. Asterisk in each bar graph is marked to show the results which have p value < 0.05.

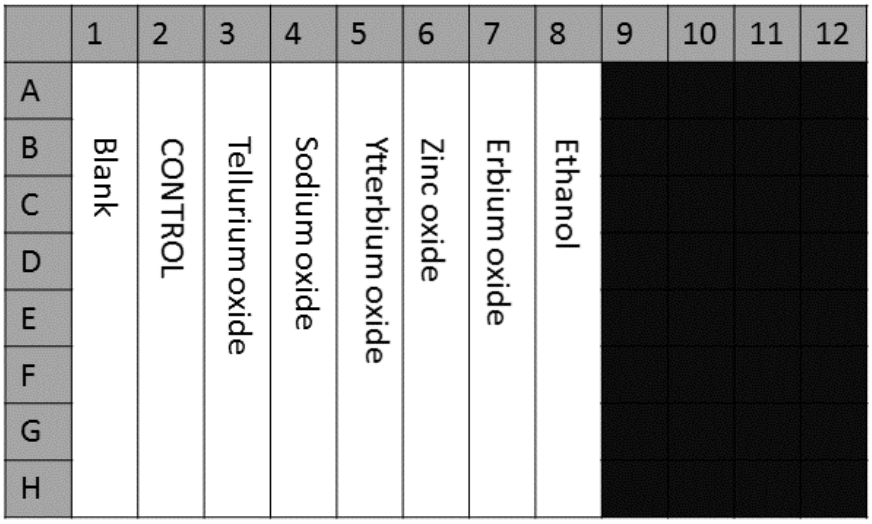

Figure 5.8: The arrangement of the test samples in which the extraction medium containing individual chemicals were used to grow the cells in the 96 well plates for MTT/XTT/Neutral red assay according to table 5.1.

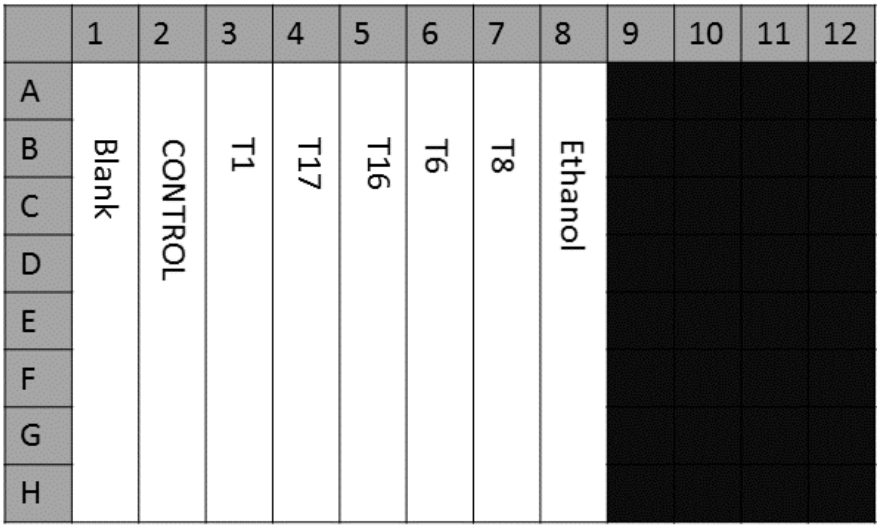

Figure 5.9: The arrangement of the test samples in which the treatment medium containing extract from each thin film used in this part of study were used to grow the cells in the 96 well plates for MTT/XTT/Neutral red assay according to table 5.2.

5.3.1 MTT assay

The cell viability was measured using this technique by assessing the response of external factor to the cell lines cultured in this study. It is a standard assay in which tetrazolium MTT (3-(4,5-dimethylthiazolyl-2)-2,5-diphenyltetrazolium bromide) is reduced in living animal cells by dehydrogenase enzymes forming a byproduct i.e. formazan crystals which were then dissolved in the isopropanol and measured using a spectrophotometer at 570 nm. It evaluates the overall mitochondrial activity in the viable cells. The optical density of formazan crystals is directly proportional to the number of living cells in the culture (van Meerloo *et al.*, 2011). MTT solution was prepared in MEM without supplements and phenol red at 1 mg/ml concentration. The growth medium used for L929 cells in assay was same as the one used of routine cell culture (ISO, 2009).

Test method

1. **Step 1** : The cells were cultured from the L929 cells (passage 2) by using cell splitting method from the cell monolayer from each T75 flask. The

cells were then suspended in the growth medium and counted according to section 5.2.2 and then adjusted to density of 1 x 10 ^{5} cells/ml and 100 μl of the adjusted cell suspension was added to each well in the 96 well plate. One column of the 96 well plate was filled with MEM for blank measurement. The 96 well plate was then incubated for 24 hrs in an incubator maintained at 37 ^oC and 5 % CO_2. The plate was observed under an optical microscope every 24 hours until cells reached half confluency in each well.

2. **Step 2** : When the cells had reached half confluency, the growth medium was removed from each well and the respective extraction medium (according to fig 5.8 and 5.9) was added to each well. The 96 well plate is again kept in the incubator for 24 hours at 37 ^oC in 5 % CO_2.

3. **Step 3** : The cell line was observed on the final day for any contamination or seeding errors under optical microscope. The extraction medium from each well was removed and 50 μl of the prepared MTT solution was added to each well and incubated for 3 hours at 37 ^oC and 5 % CO_2. At the end of three hours, MTT solution was removed and 100 μl of iso-propanol was added to each well. The 96 well plate was then shaken for 20 mins to dissolve formazan crystals obtained as by product of MTT. The optical density was recorded from each well at 570 nm with a reference wavelength of 670 nm using iMark microplate absorbance reader (ISO, 2009).

5.3.2 Neutral red (NR) assay

The neutral red uptake cytotoxicity assay was carried using BALB 3T3 mouse fibroblasts obtained from European collection of cell cultures (Salisbury, UK). This assay is used widely in testing cytotoxicity of materials used in biomedical applications (Babich & Borenfreund, 1990; Borenfreund & Puerner, 1985; Clothier, 1990; Repetto & Sanz, 1993). It is used to assess the cytopathogenicity of the test material. It was first developed at Rockefeller University as to check the chemical sensitivity of the test material on the 3T3 cells (Borenfreund & Puerner, 1985). It is based on the principle that live cell absorbs the neutral red dye and concentrates in the lysososme present in each viable cell. It chemically integrates

with the non polar bonds of the phosphate groups present in the matrix of lysosomes (Nemes *et al.*, 1979; Winckler, 1974). The dye is taken out of the live cells by using ethanol-acetic acid solution and then quantified by measuring absorbance at 540 nm using spectrophotometer (Repetto *et al.*, 2008). The growth medium used for this assay is DMEM with 5 % NCBS, 4 mM glutamine, 1 % penicillin/streptomycin solution, and 20 % HEPES buffer. 0.4 g of neutral dye was mixed with 100 ml sterile water to make a stock solution of the neutral red medium. Then 1 ml of NR stock solution was added to 79 ml of DMEM and incubated for 12 hours at 37 ^oC. The solution was then filtered using sterile millipore filters to remove any undissolved neutral red crystals. The Neutral red medium was warmed at 37 ^oC before using it for assay. The ethanol-acetic acid solution was prepared by mixing 1 % glacial acetic acid medium into 50 % ethanol and 49 % sterile water which was used to extract NR crystals from the viable cells. The test extracts were prepared in accordance with ISO-10993-12 (ISO, 2008).

Test procedure

1. **Step 1** : The cells were cultured from the monolayer of 3T3 cells (passage 2) by using cell splitting method from each T75 flask. The cells were then suspended in growth medium and counted according to section 5.2.2 and then adjusted to a density of 1 x 10 ^{5} cells/ml. 100 μl of the adjusted cell suspension was added to each well in the 96 well plate. One column of the 96 well plate was filled with untreated neutral red medium as blank to check the quality of the assay. The 96 well plate was then incubated for 24 hrs at 37 ^oC in 5 % CO_2. The 96 well plates were observed under optical microscope every 24 hours until cells reached half confluency in each well.

2. **Step 2** : When the cells have reached half confluency, the growth medium was removed from each well and the respective extraction medium (according to fig 5.8 and 5.9) was added to each well. The 96 well plate was again kept in the incubator for 24 hours at 37 ^oC in 5 % CO_2.

3. **Step 3** : The cell line was observed on the final day for any contamination or seeding errors under an optical microscope. The extraction medium from

each well was removed and cells were washed with 150 μl of PBS (warmed at 37 ^oC). The PBS was then removed from each well and 100 μl of neutral red medium was added and then incubated for 3 hours at 37 ^oC and 5 % CO_2. The NR medium was then removed from each well and cells were again washed with the 150 μl PBS and then decanted. Thereafter 150 μl of prepared ethanol-glacial acetic acid solution was added to each well. The 96 well plate was then shaked for 10 mins to extract NR from the viable cells. The optical density was recorded from each well at 540 nm using Thermofischer Microplate Absorbance Reader (ISO, 2009).

5.3.3 XTT assay

The cell viability of L929 cells was also assessed using XTT Assay. It is another form of tetrazolium reagent, 2,3-bis(2-methoxy-4-nitro-5-sulfophenyl)-S-[(phenylamino)carbonyl]-2//-tetrazolium hydroxide (XTT). Its mechanism of action is similar to MTT, that XTT is reduced by the dehyrogenase enzyme to produce formazan salt. The phenazine methosulfate (PMS) was added to the XTT to markedly increase the reduction process to form formazan salt (Scudiero *et al.*, 1988). The XTT solution was made by adding 1 mg/ml into MEM (without phenol red) and heated to 56 to 60 ^oC. The solution was then passed through milipore sterile filter to remove any contaminants. 5 mM PMS solution was prepared in sterile PBS buffer and also passed through a sterile filter to remove any contaminants. The PMS solution was mixed with XTT just before the assay to make a final concentration of 25 μM of PMS in XTT by adding 5 μl of 5 mM PMS in 1 ml of XTT solution (ISO, 2009). The optical density was measured at 450 nm with a reference wavelength of 630 nm.

Test procedure

The step 1 and step 2 of the XTT assay is same as test protocol of MTT assay (section 5.3.1). In the final step, 50 μl of the XTT/PMS solution was pipetted into each well making up the overall volume of each well to 150 μl and 96 well plates hlwere incubated at 37 ^oC and 5 % CO_2 for 5 hours. Thereafter, the XTT/PMS solution with the treatment medium was transferred to new 96 well

plate and then optical density of each well was measured at 450 nm using iMark microplate absorbance Reader.

5.4 Results and discussion

During the cell toxicity trials, the L929 cells prepared in one of the 96 well plates for MTT assay were found contaminated with bacteria and experiment was repeated. The optical density of the test samples was converted to percent cell viability by following formulae:

$$Viab, \% = \frac{100 \times OD_{450e}}{OD_{450b}} \tag{5.1}$$

where

OD_{450e} represent the average value of the optical density of the test samples

OD_{450b} represent the average value of the optical density of the control (Bharate *et al.*, 2015)

The cell viability < 70 % of the control sample is considered to have a high risk of causing cytotoxicity The extract prepared from half the concentration of the 100% test sample i.e. highest concentration must have larger cell viability, else the experiment is not considered significant (ISO, 2009). It is important to note that samples in question are thin films and assay of individual chemicals has been done to assess which chemicals have more cytotoxic potential. The results from the three assay have been discussed below. Each assay was repeated three times and overall percent cell viability has been plotted as mean $\pm$ sd. P value less than 0.05 was test for every treatment medium. The negative control was used to assess the appropriateness of the test procedure, whether the assay was able to produce accurate results. The negative control used here is 75 % ethanol.

5.4.1 MTT assay

The MTT assay of thin films and individual chemicals are shown in fig 5.10. The x-axis shows the cell viability of the control and photonic chips are arranged in descending order of the Er^{3+} ion concentration from left to right of the bar

graph (left). Two thin films which are T6 with 0.75 mol percent Er^{3+} & Yb^{3+} ion concentration and T17 with 0.75 mol percent Er^{3+} ion concentration failed the cell viability test. The asterisk sign over the bar graph shows the results of these sample as passed p value (<0.05) test. The T1 show higher cell viability than the control but since it doesn't pass the p value test mean that results is not significant enough. Overall there is a linear increase in cell viability with decrease in the Er^{3+} and Yb^{3+} ion concentration.

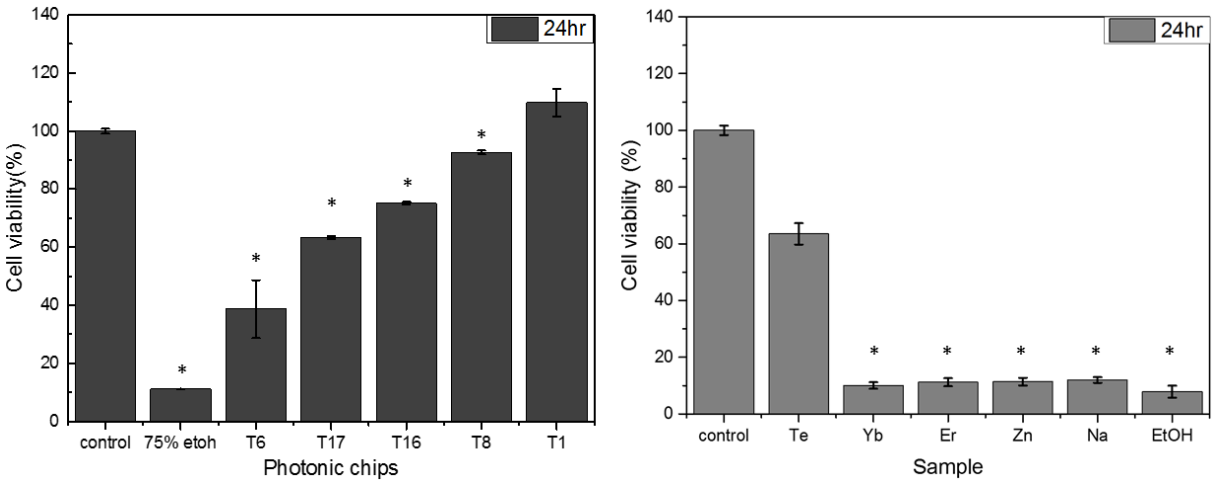

Figure 5.10: Cell viability of the thin films (left) and invidual chemicals (right) using MTT assay with 75 % ethanol used as negative control. Result data has been plotted as mean±sd and asterisk sign representing the data which shows p value < 0.05.

The bar graph (right) in fig 5.10 shows the cytotoxicity of the individual chemicals which have been implanted in the thin films. Each chemical shows cytotoxicity except Te^{4+} which might be due to precipitation of Te^{4+} ion while it was mixed with MEM solution thus overall Te^{4+} ions present in the MEM solution must have been lesser than required. The Te^{4+} has both antioxidant (Ba *et al.*, 2010) and cytotoxic effect which depends on the final integration of Te^{4+} ions in the biological medium. Organo-tellurite compounds has been known to increase toxicity in the kidney and liver in mouse (Maciel *et al.*, 2000). However cytotoxicity of Te^{4+} ions to the fibroblast such as L929 or BALB 3T3 mouse cells has not been reported. Yb^{3+} ions has a cytotoxicity potential as reported

in the literature and also shown to cause cytotoxic effect on cell lines, while cytotoxicity of erbium has not been investigated in detail previously (Rim *et al.*, 2013). Zn^2+ ion shows the cytotoxicity by generating the oxygen free radicals causing inflammation and cell death (Song *et al.*, 2010). The toxicity of sodium oxide has not been reported in the literature while other chemical form such as sodium fluoride reduces the protein synthesis and causes defect in DNA in mucosa fibroblasts (Jeng *et al.*, 1998). Sodium oxide does show significant cell death of L929 cells in the MTT assay.

5.4.2 Neutral red upatake assay

The Neutral red assay of thin film (left) and individual chemicals (right) is shown in figure 5.11. The cell viability of the thin films was higher than 70 % indicating they are potentially safe to use, however all the results have p value > 0.05 thus indicating results are insignificant. Although negative control does have p value < 0.05 implying that there is a less chance of effect of an unknown variable. The cytotoxicity of individual chemicals shows high toxicity with sodium oxide showing most cell death of 3T3 mouse cells.

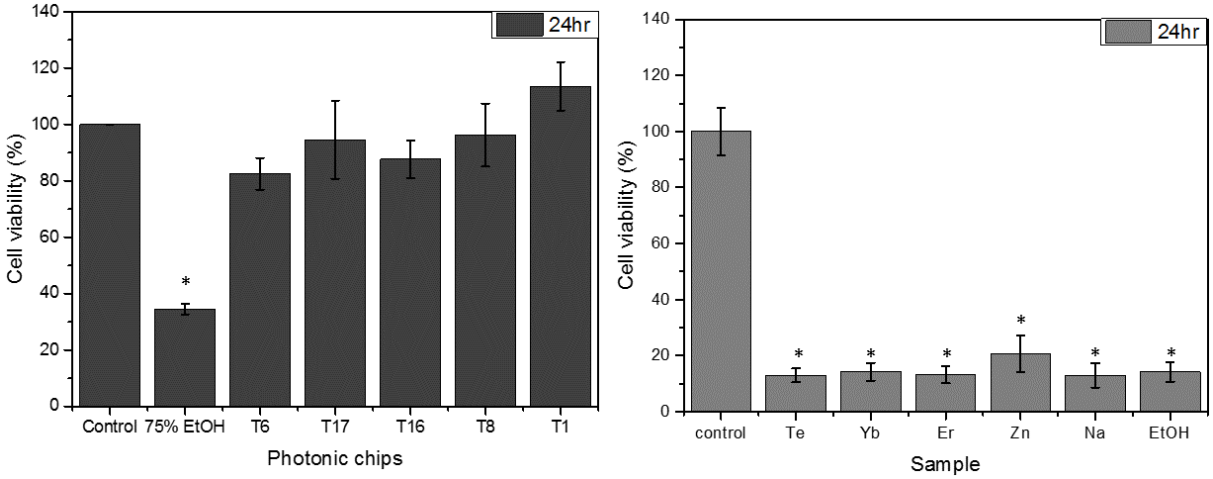

Figure 5.11: Cell viability of the thin films (left) and invidual chemicals (right) assessed using NR uptake assay with 75 % ethanol used as negative control. Result data has been plotted as mean ± sd and asterisk sign representing the data which shows p value < 0.05.

5.4.3 XTT assay

XTT assay shows the similar linear response in the cytotoxicity of thin films (see fig 5.12 (left)) with most of the thin films except T8 and T1 has p value $<$ 0.05. The thin films T6 show 64 % cell viability thus it fails the cell viability test while T17 show near safe cell viability of 70.4 %. Other thin films do not show significant cytotoxic effect. Whilst the individual chemicals show high chemical toxicity. The Te^{+4} and Zn^{+} show less cytotoxicity than other ions.

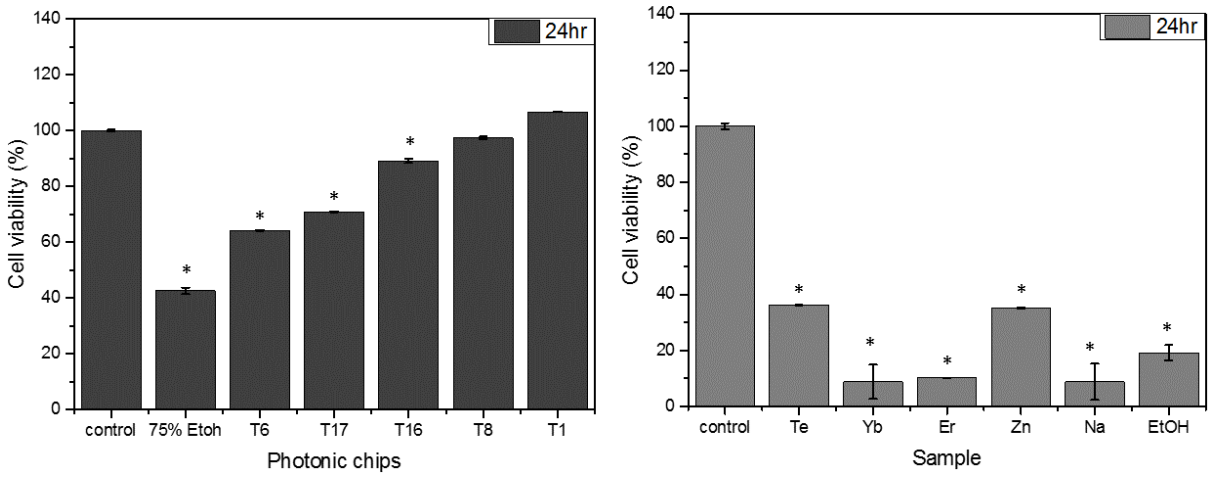

Figure 5.12: Cell viability of the thin films (left) and invidual chemicals(right) extracts using XTT assay with 75 % ethanol used as negative control. Result data have been plotted as mean±sd and asterisk sign representing the data which shows p value $<$ 0.05.

5.5 Conclusion

All the test were carried out with extracts prepared at 24 hr at 37 ^oC and 5 % CO_2. The materials present in the thin films does show high cytotoxicity, however, the cytotoxicity of these ions is reduced significantly while doped in the fused silica substrate. T6 photonic chip fails the cell viability test. It has implanted layer thickness of 1.2 μm and 1.66 refractive index. This sample was fabricated at 95 mTorr oxygen pressure and 8 hours deposition. The phase contrast images of the photonic chips is shown in figure 5.13. The T17 chip does show clear chipping

and cracks on the surface which can expose the material causing the release of materials from the surface while T6 show high waviness on the surface indicating more presence of the material on the surface of the photonic chip which can be responsible for decreased cell viability.

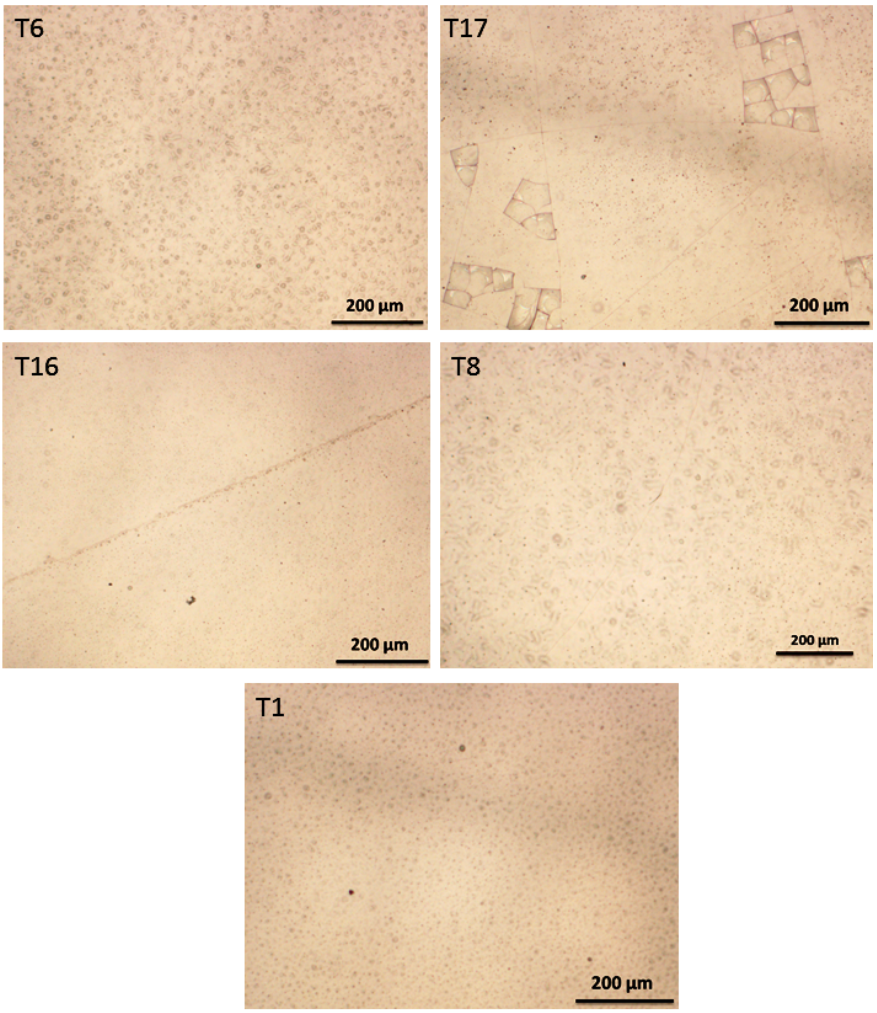

Figure 5.13: The surface of the photonic chips used in this part of the study observed at 5x magnification using optical microscope.

Chapter 6

In-vitro Sensing of Glucose

6.1 Introduction

The Er^{3+} ions doped in thin films in silica glass with an emission in the range of 1450-1650 nm and the absorption band of glucose falls in the similar spectrum (Amerov *et al.*, 2004). The skin has 30 % transmittance in the near infrared region from 1480 nm - 1600 nm (Cohen, 1977). The glucose is also known to alter the optical scattering of the medium by changing the refractive index (Maier *et al.*, 1994). Thus we investigated the photonic chip for glucose sensing. It senses the glucose levels through the skin in the near infrared region and its specificity toward glucose is the key advantage. Since the erbium is implanted into the silica network it offers a high level of transparency. The Er^{3+} ions present in the system have specific absorption line at 980nm. The light travelling through different mediums have to come across different refractive index e.g. refractive index of silica glass is 1.45, the planar waveguide is $\approx$ 1.59, air is 1, skin is 1.325-1.40 (Maier *et al.*, 1994). This causes more scattering of the light. This is based on the random scattering phenomenon. It states that when flux of light is applied to the active region, the emission from the erbium ions cause multiple scattering due to which the overall fluorescence is altered. The waveguide acts as a random laser, when the light travels through the medium the direction is changed randomly. The particle which cause that bending in light is called as scattering centre. When the light hits another erbium ion (scattering centre) it changes direction again. The planar waveguide is made up of multiple scattering centres causing a state known as "random walk". The multiple scattering causes the increase in the path length (Cao & Sheehan, 2013; Wiersma, 2008). Since the erbium ions are also emitting light thus the overall optical gain of is amplified. This is the key reason of high sensitivity of the device. The photonic chip is excited at 980 nm from the one edge of the waveguide, the light travels through the waveguide causing emission from erbium ion between 1450-1650nm. The fluorescence emission is scattered on the surface giving a large area of emission. Scattered fluorescence travel over and below the surface of the photonic chip. The detector used in the system is the avalanche photodiode which collects the signal produced after the excitation. The fluorescence lifetime is measured over the time period when the electron from higher energy levels decays to the level

when $\tau = 1/k$ (Berezin & Achilefu, 2010). The avalanche photodiode detector measures the number of photon striking the surface of the detector which is then converted to the fluorescence lifetime using a multi-scale photon counter card. Single exponential decay is measured from the spontaneous emission of the Er^{3+} ions in the region 1500-1600 nm.

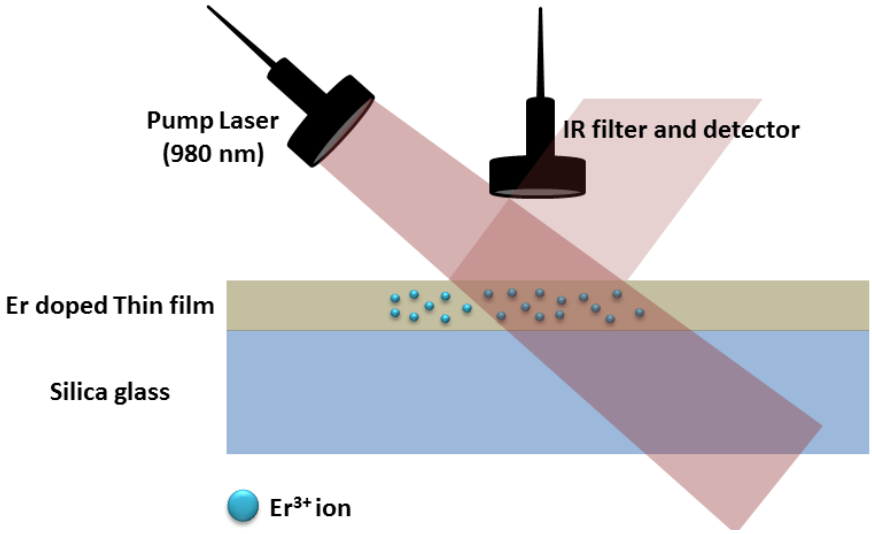

Figure 6.1: The optical setup of the device where the pump laser is used to excite the Er^{3+} ions for 100 μs and theoretical direction of laser excitation at 980 nm.

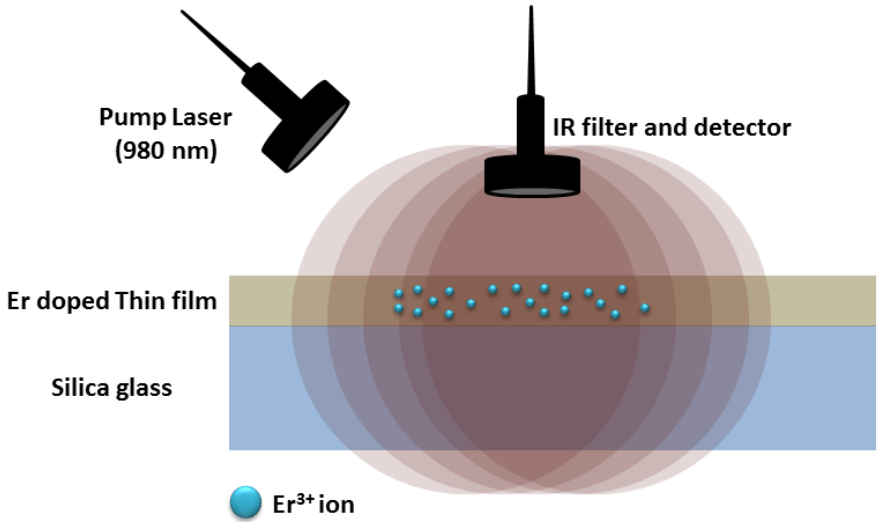

Figure 6.2: The emission from the Er^{3+} ions in the region of 1470-1650 nm when excited by the 980 nm pump laser

The near infra red sensing of the glucose has been described in detail in section 1.2.15. The optical fibre of the 980 nm pump laser is connected with fibre collimator and is directed at the laser from either the edge of the photonic chip or incident at 45^o to the surface of the thin film (see figure 6.1). The photo-detector is placed parallel to the surface of the thin film. The fluorescence emitted from the Er^{3+} ions is isotropic in nature (Chen & Chi, 1993; Thyagarajan, 2002) thus the emitted light travels to every direction. The analyte sample can be placed on either side of the photonic chip. The sample is required have scattering centres so that light can radiate back to the detector. The sample measured here is the glucose molecules which have an absorption spectrum in range of 1500-1800nm (Amerov *et al.*, 2004).

6.2 Experimental setup

The 980 nm pulsed laser is used for the excitation of the photonic chip. The photonic chip is excited for 100 μs and then signal collected up to 100 ms. 500 sweeps of the lifetime is measured and then summed to get final lifetime. It takes about 30 seconds to finish one measurement. Since the molar absorptivity of

glucose is higher than other biomolecules present in the biological medium in the region 1500-1600 nm the light is absorbed more by the glucose (Amerov *et al.*, 2004). The overall change in fluorescence is due to the absorption and scattering phenomenon which causes the change in the fluorescence signal.

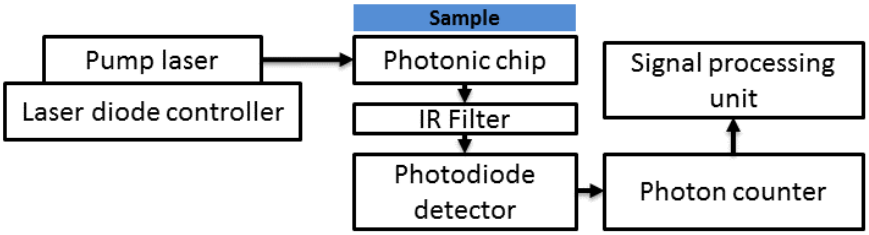

Figure 6.3: Basic optical setup for invitro sensing of glucose

The fluorescence lifetime measurements were done to check the glucose sensing by Er^{3+} ions doped thin films in an optical setup as described in fig 6.3. The 980 nm laser diode is modulated by the Thorlab's laser diode controller. In the first setup, excitation of Er^{3+} ions was done from the edge of the photonic chip. The sample was placed on the thin film side of the photonic chip and the detector was placed on the other side of the photonic chip. Between the detector and the photonic chip, a band pass 1500- 1600 nm filter is placed to block the light flux from the pump laser. The lifetime of fluorescence emission with a peak at 1535 nm is measured using photodetector.

6.3 In-vitro sensing of glucose in different biological mediums

The glucose concentration in intralipids, deionized water, human blood were prepared. The concentrations were prepared such that it covers the glucose range from hypoglycaemic region to hyperglycaemic region. The photonic chip which had the longest fluorescence lifetime from G series batch was used i.e. Ge and all the T series batch chips were used in in-vitro glucose sensing. The glucose concentrations were measured using YSI analyser which is the gold standard for

glucose measurements. The 2 % intralipids has been recognised as a fair tissue simulating optical phantoms. 2 % intralipids has a good correlation to optical properties of skin over the infrared region (Troy & Thennadil, 2001). The pooled human blood samples were obtained from the NHS pathology lab, LGI hospital, Leeds. All the samples were checked for any clumps formation due to agglomeration of blood cells. Initially blood cells were settled at the bottom of the tube. The cells were re-suspended using 300 rpm stirrer.

6.4 Result and discussion

6.4.1 Glucose measurements with α unit

Aq glucose measurements

The first glucose measurement was made using the optical setup given in fig 6.4. This setup was developed under guidance of Dr Billy Richards who is research fellow in the same research group. The initial testing was done for the stability of the lifetime measurements from the device. The different concentration of glucose were made from 1 mM to 25 mM of glucose in water. The YSI analyser was not available in the lab when these measurements were done. So actual glucose concentration could not be measured by a gold standard. However, since the glucose was dissolved in deionized water, variation in glucose concentration can only be attributed to human error. The 10 μl of glucose solution of each concentration was placed in silicone chamber attached to the top surface of the photonic chip and the cover-slip was placed immediately after filling the silicon chamber. Four infrared filters were used in the measurement, details are given in the table 6.1. The top layer of the photonic chip was rinsed with water after every measurement and then dried with lens tissue and laboratory grade air duster.

Table 6.1: The four infrared filters used in the aqueous glucose measurements

IR filter	Center wavelength (nm)	Bandwidth (nm)	Peak trasnmittance (%)	Blocking wavelength (nm)
FB 1500	1500 (edge pass filter)	700nm	95	200-1500
FB 1530-12	1530	12	60	200-1524,1536-1850
FB 1550-12	1550	12	60	200-1544,1556-1850
FB 1580-12	1580	12	70	200-1574,1586-1850

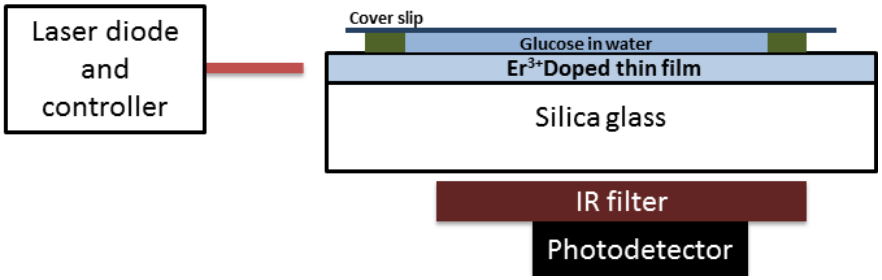

Figure 6.4: The optical device setup for aqueous glucose measurements

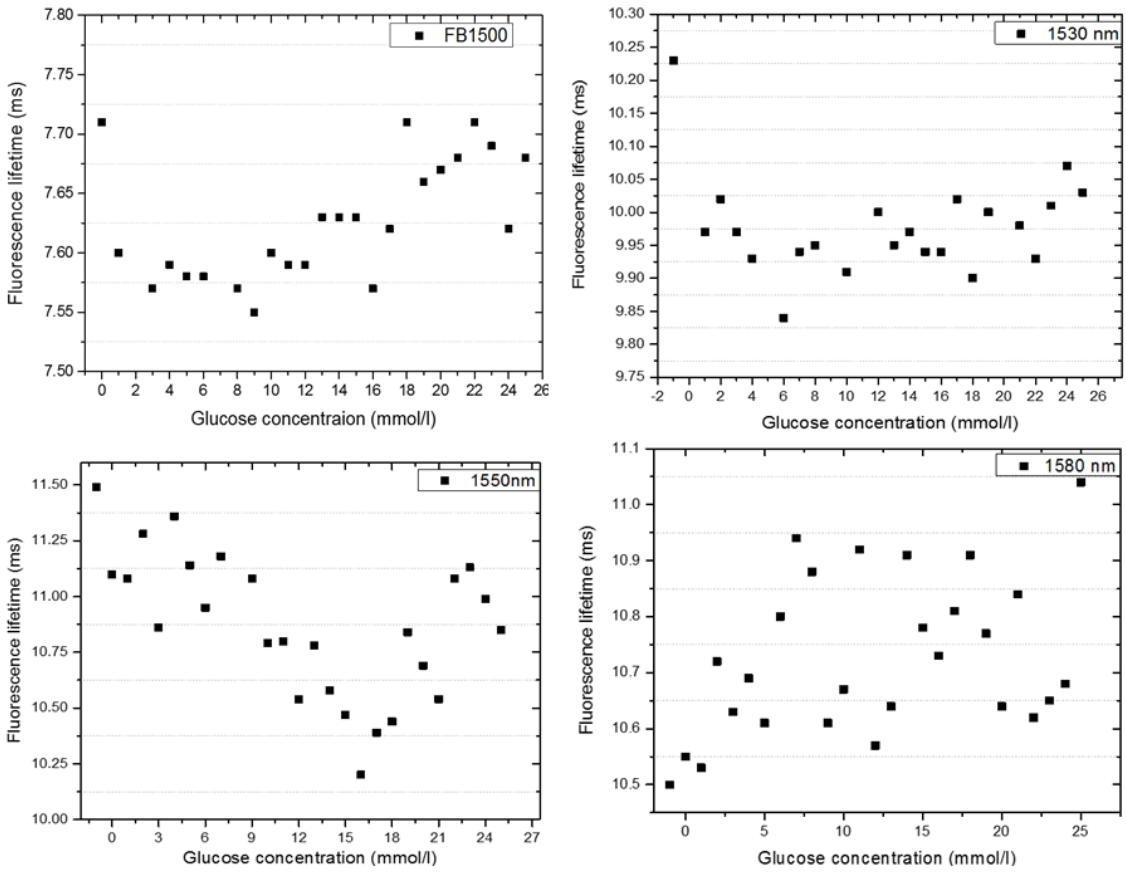

Figure 6.5: The fluorescence lifetime of photonic chip Ge measured with different concentration of the glucose using four different infra-red filters mentioned in table 6.1 .

The photonic chip used in this measurement is Ge doped with 0.5 mol percent Er^{3+} ion, with 1.5 μm thickness with 11.3 ms lifetime measured in fluorescence spectrometer at 1535nm. The aqueous glucose measurement using FB 1500 edge pass filter shows the lifetime of 7.6 ms of the blank sample. The lifetime decrease slightly with increasing glucose concentration then after 12 mM glucose it starts rising again. More sensitivity in the hyperglycaemic region is observed. The measurements carried out using the 1530 nm short pass filter show the blank lifetime of 10.22 ms. The increasing glucose concentration doesn't change linearly with the lifetime. The 1530 nm filter has net transmittance of 35 % at 1535 which

means most of the signal going to the detector has been blocked. A slight change in lifetime is observed but the spread of lifetime values is random. With 1550 nm, the linear decrease in fluorescence lifetime with an increase in glucose concentration is observed until 17 mM glucose which rises thereafter while with 1580 nm a random spread of fluorescence lifetime measured is observed. The aqueous water doesn't offer scattering centres most of the fluorescence is lost. Thus a medium was required which gives a better scattering of fluorescence emission than de ionized water.

Blood glucose measurement

In the next stage of measurements pooled human blood samples were obtained from NHS pathology lab, LGI, Leeds. The blood groups and other details of the donor were anonymised before the samples were collected. Only non infectious blood samples were used in the study. The glucose value of each blood sample was measured using YSI analyzer. The glucose concentration in the blood samples drops linearly with time due to respiration by blood cells. More glucose was added in blood samples to increase the concentration and glucose measurement was carried out using YSI analyser for each blood sample just before the lifetime measurement of the same concentration. 10 μl of the blood sample was kept in the silicone chamber as shown in fig 6.7. In these measurements, the Semrock 1064 nm razor edge long pass filter was used. The setup for this measurement was assembled by EG technology consultants, Cambridge, UK. The picoscope was used in this measurement instead of multi scale photon counter card to develop a more portable device. The analysis software for the lifetime measurements was developed by Thomas Mann (PhD student (SCAPE, University of Leeds) with Prof.Gin Jose as an academic supervisor) to ease the data analysis process. I carried out the blood glucose measurements vs fluorescence lifetime in the T series.

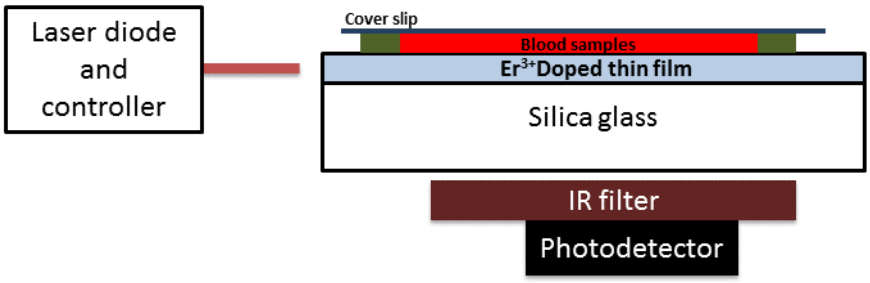

Figure 6.6: The optical device setup for blood glucose measurements

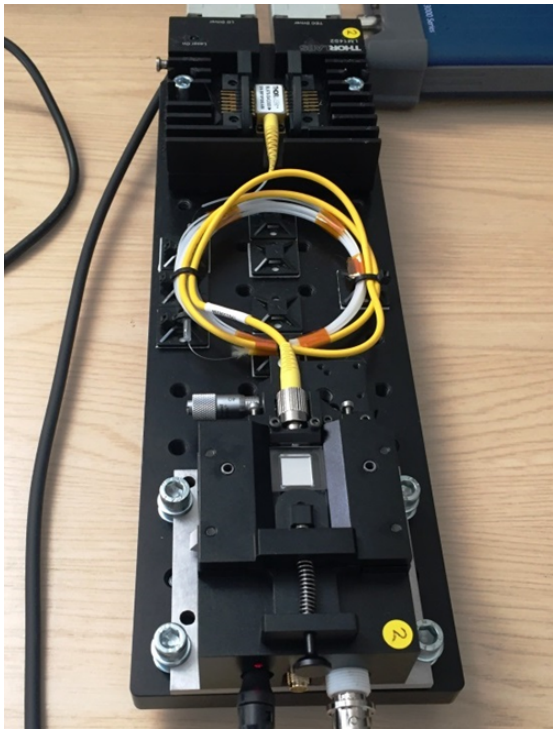

Figure 6.7: α optical device for glucose measurements

In this part of the study, the fluorescence lifetime of the photonic chip was measured with increasing glucose concentrations in pooled human blood samples. 7 photonic chips have shown the change in fluorescence lifetime of photonic chips with increasing glucose concentrations. The measured parameters of these photonic chips are mentioned in table 6.2. Also, the plot of the lifetime against

glucose concentration is shown in figure 6.8. The photonic chips doped with 0.25 mol percent Er^{3+} ions which are T2, T21, T24, have depicted the change in the lifetime with increasing glucose concentrations. The lifetime decreases with increase in glucose concentration. Another promising candidates are the chip fabricated with 0.5 mol % Er^{3+} and 0.5 mol % Yb ions, T11, T23, T29. The trend is reversed in the T23 where the fluorescence lifetime increase with increasing glucose concentrations. One candidate from the chip doped with 0.75 mol % Er^{3+} ions has shown a decrease in fluorescence lifetime with increasing glucose concentration. However, the range of fluorescence lifetime variation is higher in the latter photonic chip. The overall lifetime change with glucose does vary for each candidate. The photonic chip doped with 0.25 and 0.5 Er^{3+} ion have more chips showing a correlation between changing fluorescence lifetime and glucose concentrations.

Table 6.2: The measured parameters of the photonic chip in T batch which has illustrated correlation between increasing glucose concentration and fluorescence lifetime in part of the study

Sample Id	Er^{3+} (mol %)	Yb^{3+} (mol %)	Film Thickness (μm)	Refractive index	FWHM (nm)
T2	0.25	0	1.08	1.59	18.93
T11	0.5	0.5	0.68	1.62	21.69
T21	0.25	0	1.2	1.61	19.59
T23	0.5	0.5	1.08	1.61	19.84
T24	0.25	0	2.37	1.6	19.41
T27	0.75	0	1.8	1.63	23.76
T29	0.5	0.5	0.84	1.6	19.48

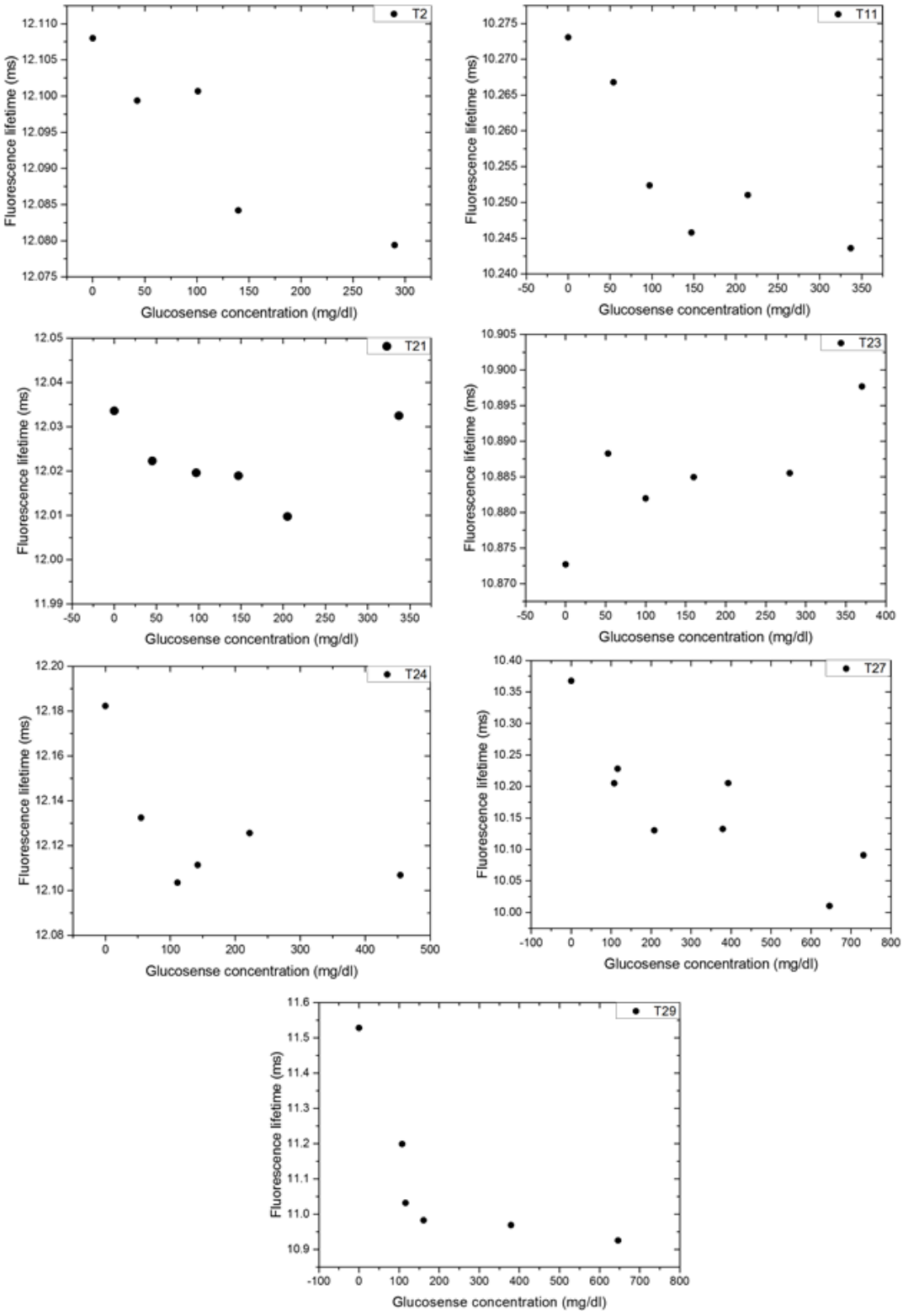

Figure 6.8: The blood glucose measurements of the photonic chips from T series batch which showed change in lifetime with changing glucose concentrations.

6.4.2 Glucose measurements with the flow cell

The biological medium used here are 2 % intralipids and human blood. The human blood was obtained from Seralab, UK. The initial glucose concentration in blood was 0.3 mM which might be due consumption of glucose by blood cells over the period of transportation. The glucose was added to each blood sample and measured using YSI analyser.The rate of blood flow in human finger is 1-4 ml/min in veins and 3 ml to 26 ml in arteries (Klarhöfer *et al.*, 2001). The flow rate of venous blood in fingers is taken in account as veins are more superficial than the arteries in finger. The flow rate assumed in this part of study is 2ml/min. The flow cell setup was developed under guidance of Prof Nik Kapur, Faculty of Mechanical engineering, University of Leeds. The setup has been modified from α unit where edge coupling was used to excite the Er^{3+} ion in the photonic chip to front illumination, where the pump laser is connected with fibre collimator and the laser beam is directed at 45^o angle (fig 6.9, 6.10). Since the emitted fluorescence is isotropic in nature the light will interact with both the biological medium containing glucose and photo-detector. FB1500 nm edge pass filter was used to block the light emitted by the laser.

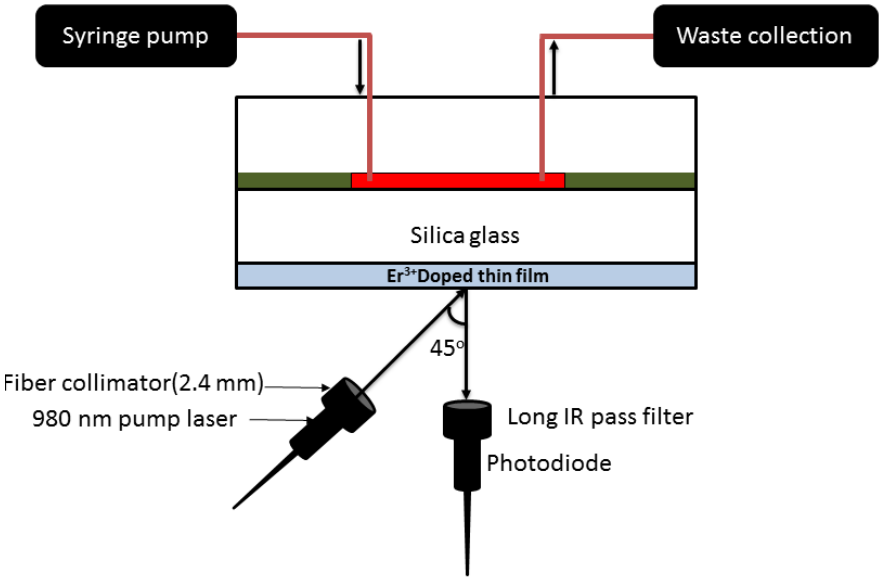

Figure 6.9: The optical setup encompassing photonic chip in a flow cell connected with syringe pump.

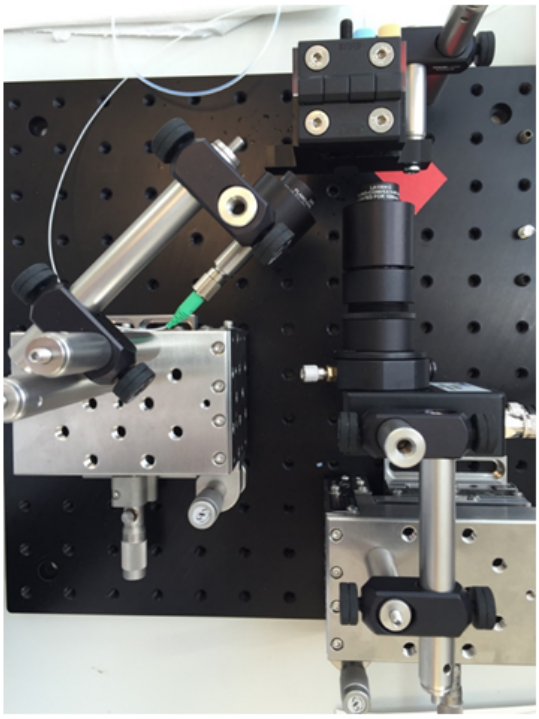

Figure 6.10: Laboratory flow cell setup for glucose sensing.

The 2% intralipids solution was prepared and glucose was added similar to the concentrations used in human blood. The glucose concentration was measured before the lifetime measurement of each sample. The temperature of the biological medium was maintained at 37 ^oC and constantly monitored with the thermocouple. In this setup, a chamber was fabricated using 3D printing which holds the blood/intralipids sample and connected with PVC tubes. The syringe pump is used to maintain the flow of blood/intralipids. The blank lifetime was measured before the start of every blood/intralipids solution measurement and then the blood/intralipids solution was filled in the chamber with a constant flow. Once the sample had been analysed, it was discarded according to standard protocol followed in LICAMM laboratories All the photonic chips in T series were analysed using this setup. After every measurement, the photonic chip was cleaned by running deionized water for 2 mins, and and then a quick flush of air.

Glucose measurements using intralipids

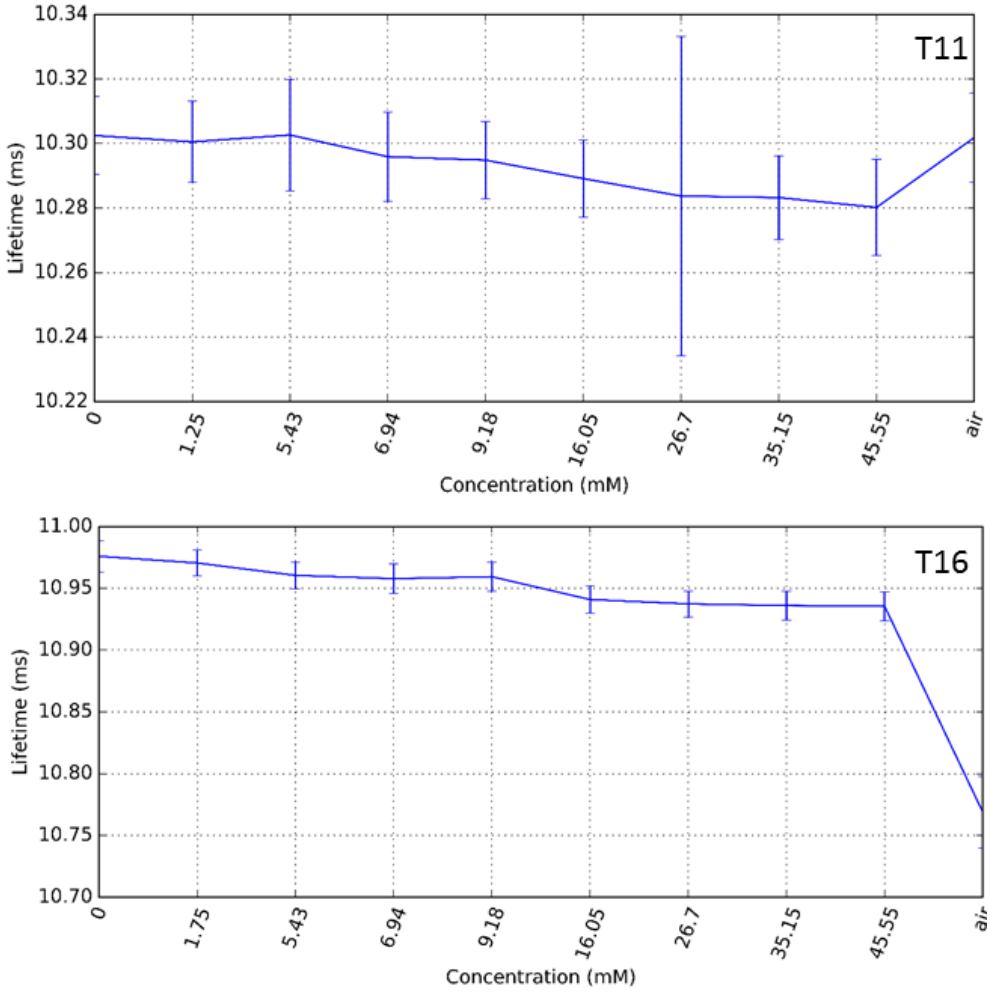

Figure 6.11: The intralipids-glucose of T11, T16 photonic chips showing change in lifetime with changing glucose concentrations.

In the *in-vitro* glucose sensing using 2 % intralipids, the measurement was repeated 3 times and the mean fluorescence lifetime ± standard deviation was plotted for each photonic chip (fig 6.11, 6.12). The photonic chips i.e T11, T16, T21 and T29 show change in fluorescence lifetime with increasing glucose concentrations. The fluorescence lifetime decreases with increase in glucose concentrations for T11, T16, while T21, T29 shows a non-linear response. These results

are similar to what is obtained in glucose measurements using α units. The fluorescence lifetime change with increasing glucose concentration in intralipids was inconclusive for other photonic chips. The sensitivity of photonic chip is varying with the setup and type of biological medium used as the light scattering will be different. Also, no correlation could be established on which parameter or parameters measured dictates the sensitivity of photonic chips.

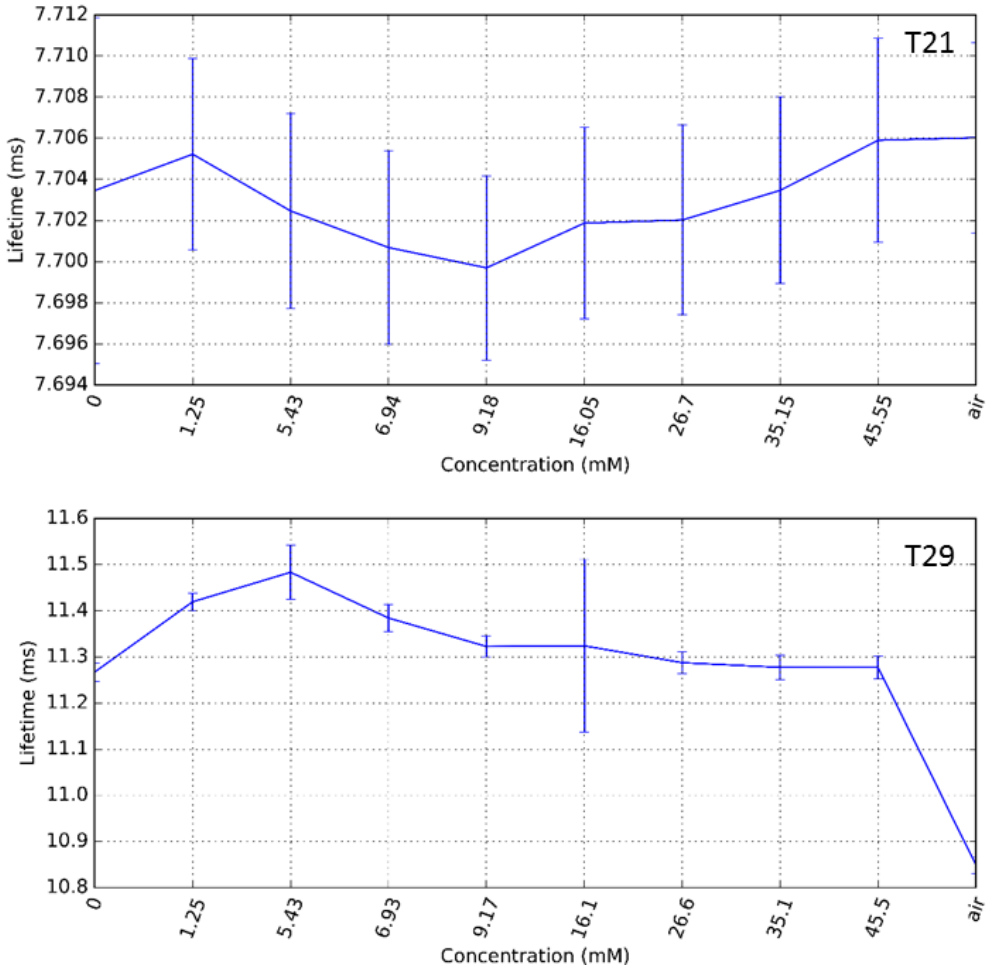

Figure 6.12: The intralipids-glucose of T21, T29 photonic chips showing change in lifetime with changing glucose concentrations.

Glucose measurements using Human blood

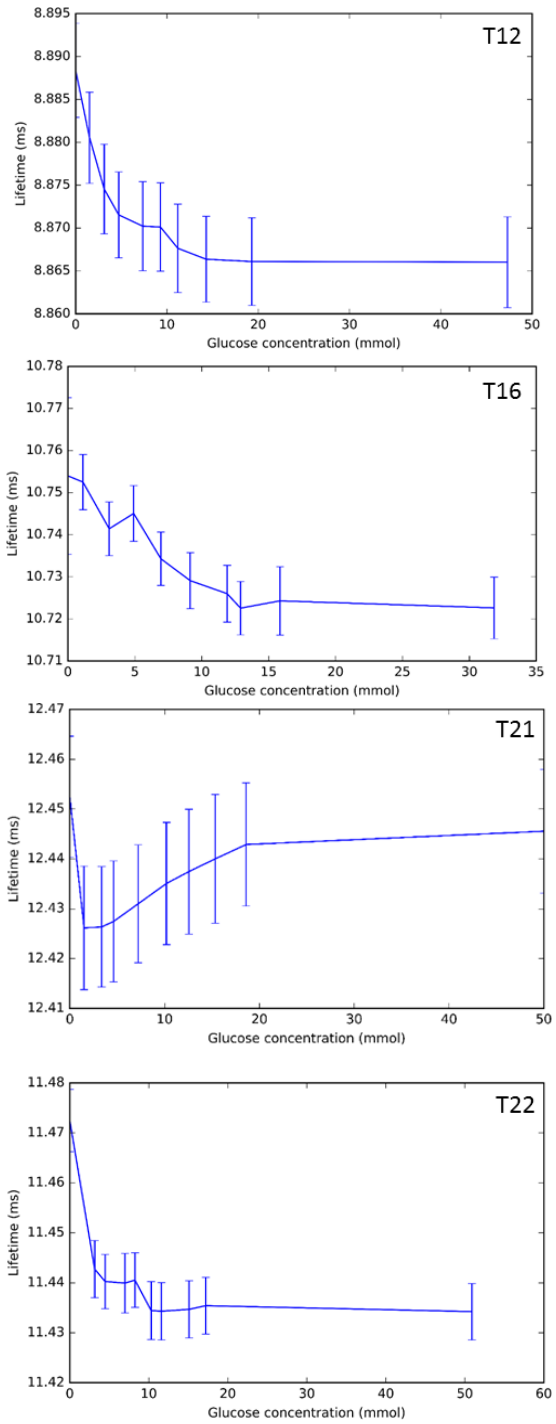

Figure 6.13: The blood glucose measurements of four photonic chips showing change in lifetime with changing glucose concentrations.

Table 6.3: The measured parameters of the photonic chip in T batch which has illustrated correlation between increasing glucose concentration and fluorescence lifetime in flow cell setup

Sample Id	Er^{3+} (mol %)	Yb^{3+} (mol %)	Film Thickness (μm)	Refractive index	FWHM (nm)
T12	0.75	1.5	0.57	1.56	24.17
T16	0.5	0.5	1.05	1.61	19.85
T21	0.25	0	1.2	1.61	19.59
T22	0.25	0.5	1.55	1.62	21.81

In the in-vitro sensing of blood glucose by photonic chips, the lifetime measurement was repeated 3 times and the mean fluorescence lifetime ± standard deviation was plotted for each photonic chip. The photonic chips T12, T16, T21,T29 depicted significant response with increase in glucose concentrations (see fig 6.13). T21 showed an increase in the fluorescence lifetime with increasing glucose concentrations while other three photonic chips shows a decrease in fluorescence lifetime with increase in glucose concentrations The measured parameters for these photonic chips are given in table 6.3.

6.5 Conclusion

The out of all the T series batch analysed, few candidate are identified which had potential to sense glucose. The glucose does change with changing fluorescence lifetime of the the samples doped with 0.25 % and 0.5 % Er^{3+} ions. Therefore these samples have more chance of sensing glucose than the photonic chip doped with higher concentration of Er^{3+} ions. The drawback of this part of the study is that the blood is kept either static or flowing at certain rate. Thus all the blood cells will be settling down or due to pressure applied during the flow, they stack themselves in a manner which changes the overall optical scattering (Sakota & Takatani, 2012). Thus the scattering medium is not similar. However since it contains all biomolecules at certain unknown concentrations, it does provide relevant information about glucose sensing intended in this part of the study.

The key barrier i.e. optical properties of the skin is still not considered in this part of the study which does play a significant role in light scattering, transmittance, absorption, reflectance of the fluorescence emission. So the glucose trend with lifetime observed in in-vitro sensing can be different from the glucose trend observed in lifetime in in-vivo sensing of photonic chips.

Chapter 7

Invivo Sensing of glucose

7.1 Introduction

The glucose laser sensor has been developed in Institute for Materials Research, University of Leeds, with the design of sensor head and prototyping was completed by LDT design. In this device a low power 980 nm laser is pulsed on the edge of the photonic chip. The fluorescence lifetime of the photonic chip is measured which is altered by the glucose ions present in blood and thus we can measure the change in concentration of glucose in capillary blood. The low power laser based sensor interacts optically with the skin surface to provide direct information about the glucose concentration in interstitial fluid or blood. We have developed a laboratory prototype of this sensor for clinically investigating the new measurement concept. This device is proposed as an alternate for finger prick handled meter which will be advantageous to people with diabetes requiring insulin treatment. The clinical trials were designed to assess the performance of the non-invasive finger touch glucose monitor (NFTGM) sensor. In NFTGM sensor, measured glucose values were compared with corresponding reference glucose value from continuous glucose meter and finger prick glucose meter. The clinical trials were carried out in Leeds institute for cardiovascular and metabolic medicine (LICAMM formerly LIGHT), Faculty of medicine, University of Leeds under the supervision of research nurse.

7.1.1 Device design

The current laboratory based non-invasive glucose sensing platform consists of the sensor head, diode laser with controller, PCI interface box, and laptop (fig 7.1). The sensor head hosts the detector, photonic chip and optical fibre holder. The optical fibre is coupled from the laser diode to the polished edge of the photonic chip. The detector is connected to the PCI interface box containing multi-scale photon counter. Laser diode controller activates the 980 nm pump laser and Er^{3+} ion doped in the photonic chip are excited to $^4I_{11/2}$ from $^4I_{15/2}$ energy levels. A radiative emission from $^4I_{13/2}$ to $^4I_{15/2}$ energy levels is released. The fluorescence lifetime from the broadband emission of 1500-1600 nm is measured with photodiode detector. During the clinical trials, prior to recording the signal from the fingertip, a blank signal is recorded from the sensor. The glucose value is recorded

from the SMBG meter and subcutaneous ICGM at the same time in parallel to the fluorescence lifetime value obtained from NFTGM from the fingertip. The blood glucose reading is recorded every 1 hour from SMBG meter and NFTGM sensor I. In every 10 minutes, both invasive continuous glucose monitor (ICGM) and NFTGM sensor I record data concurrently.

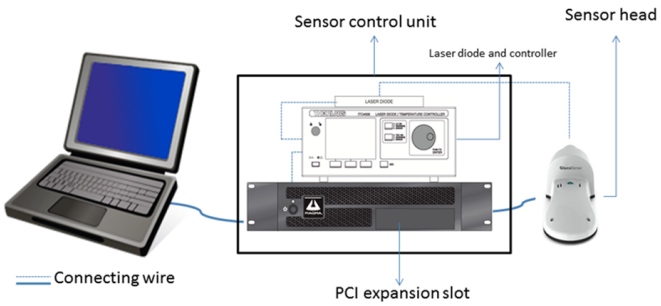

Figure 7.1: Device design for NFTGM sensor I

Algorithm used in NFTGM sensor 1

The algorithm used to calculate the glucose value from the signal generated from the NFTGM sensor I. The pulse generator generates the laser pulse of 1 millisecond from the laser diode controller with a pulse width of 100 ms. Emitted signal is averaged over 250 sweeps and then plotted as exponential decay. The data is then correlated with calibrated data to generate the final glucose value.

7.1.2 Demographic selection

Inclusion criteria

1. Subjects with Type 1 diabetes
2. Age 18 to 40 years
3. Able to give written informed consent
4. Subjects with white skin. This is because darker pigmentation in skin may bring additional parameters for the data analysis which is beyond scope of this small pilot study.

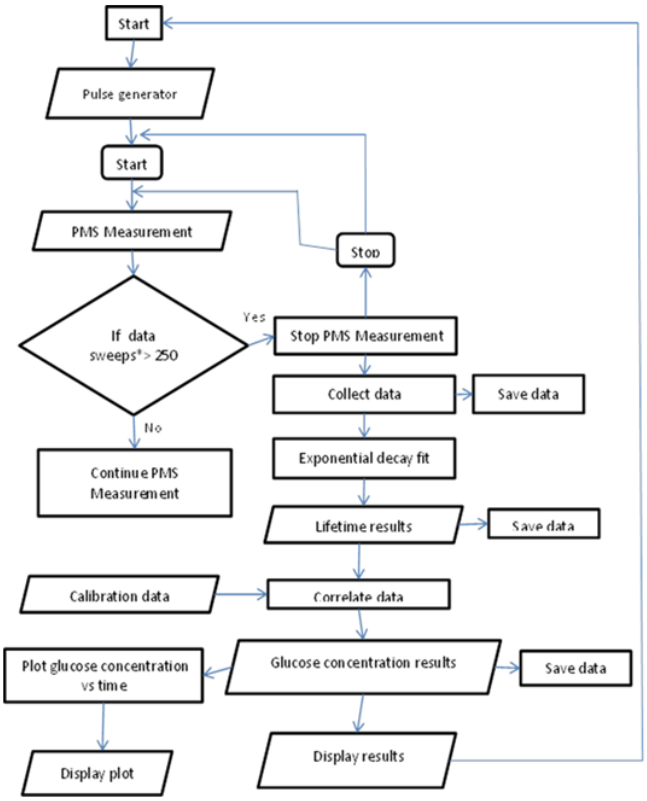

Figure 7.2: Algorithm for NFTGM sensor I

Exclusion criteria

1. Skin conditions causing irritation e.g., eczema, psoriasis.

2. Pregnant women or women intending to become pregnant or not using adequate contraception e.g. OCP, or condoms + IUD.

7.1.3 Trial design

This was a single-centre, prospective, randomised, controlled, within-patient study of the photonic chip as glucose sensors for subjects with diabetes mellitus. There was a minimal deviation from the subjects' normal diabetes management practice. The study has been designed to assess biosensing capability of NFTGM

for monitoring glucose levels in a small population specific to patients with Type I diabetes. Photonic chip was short-listed on the basis of a longer lifetime and reasonable intensity (Ge) was tested to determine early stage ability to measure glucose. Data from each subject was assessed on an ongoing basis during the study and total 13 candidates over 2 days(each trail of 8 hours) each were recruited during the clinical trials.

1. 12 subjects with Type 1 diabetes participated in the study over 2 separate days (one day each for phases 1&2) .Written informed consent was taken(refer appendix) in this regard and they were informed that this is research study and the device used is non CE marked.

2. Preparation of the bench-top device clinic for the Phase 1 study with electrical and laser safety checks was done.

3. Participants used to arrive at 8 am, they were fitted with the standard continuous glucose monitor, (Abbot Freestyle Navigator).

4. Glucose measurements were collected continuously using the NFTGM sensor and standard continuous glucose monitoring equipment after every 10 mins. The participant will also be asked to check their blood glucose hourly using their own handheld glucose meters.

5. The measurements were concluded after 8 hours (between 1600 and 1700hrs).

6. NFTGM sensor calibration was redesigned/adapted based on the phase 1 results and steps d,e,f will be repeated for each subject in Phase 2.

7. Data from phase 2 will be analysed and results from the NFTGM sensor were compared to those obtained using current standard methods (continuous monitor and hand held meter).

7.2 Calibration

At the day of the trial the capillary blood glucose value from the finger prick glucose meter were obtained every hour for total 8 hours. The ICGM values

were measured using Abbott freestyle navigator every 10 mins. The fluorescence lifetime measurement from NFTGM was done parallel to the ICGM measurement and also when the capillary blood glucose reading was taken. The calibration of the NFTGM was done using the fluorescence lifetime values measured and plotting them against the corresponding measured capillary blood glucose values. Out of 8 values obtained 4 capillary blood glucose values were used for calibration which covers the maximum concentration range of the glucose. These four values were plotted against the corresponding fluorescence lifetime value measured from NFTGM. The fluorescence lifetime value was obtained by keeping the tip of the finger in contact of the top surface of the sensor while the pump laser is switched on.

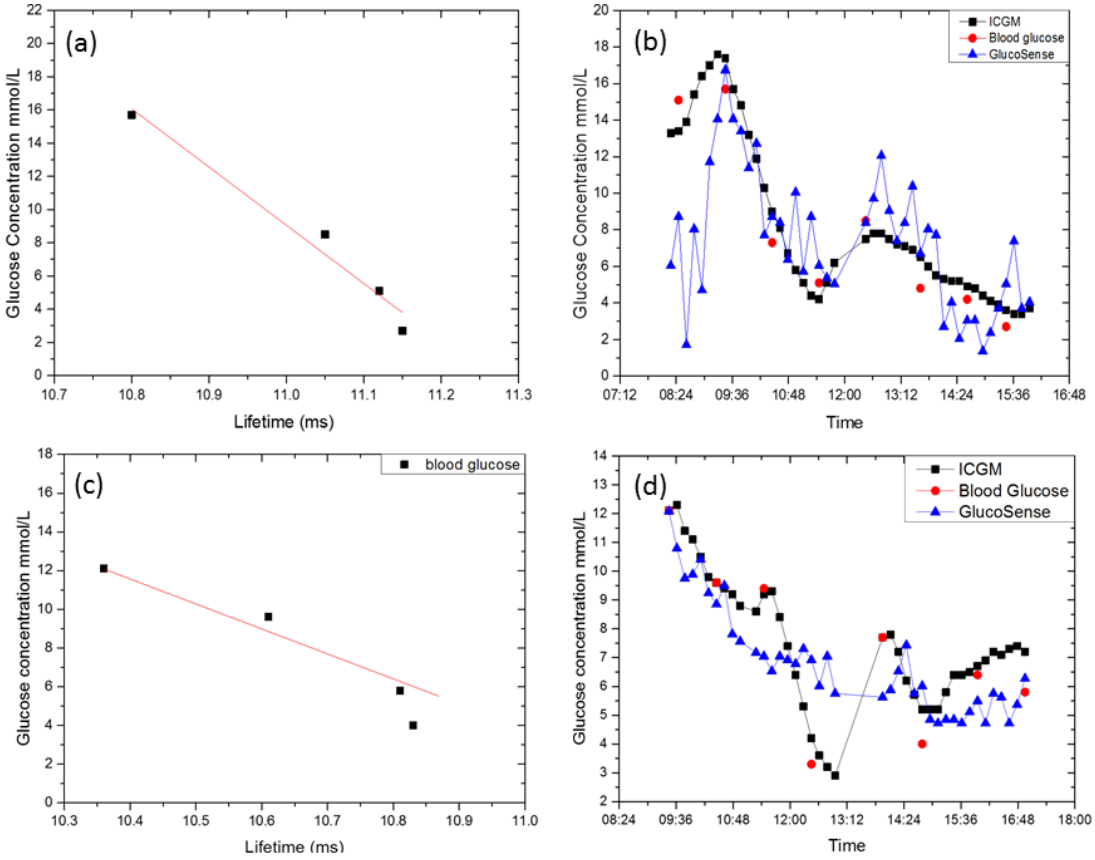

Figure 7.3: (a),(b) The capillary blood glucose values obtained from the finger prick measurement plotted against the corresponding glucose lifetime values. (c),(d) example of the glucose values of the candidate obtained over ≈ 8 hours from NFTGM, ICGM and finger prick glucose meter.

The linear fitting equation was used to measure the slope and intercept of the line in the graph (see figure 7(a), (c)) . The linear equation used here is:

$$Y = a + bx \tag{7.1}$$

where

a = intercept b = slope x = measured lifetime value y = calulated glucose value from NFTGM corresponding to measured lifetime value

For each measured lifetime value its corresponding glucose value was obtained. All these values were used to plot Clarke error grids which represent the clinical

performance of the device. In fig 7 (c), (d) measured glucose values were plotted against the ICGM and blood glucose values. It gives a representation on how device measured against the ICGM and finger prick blood glucose monitor

7.3 Statistical design

So as to evaluate the clinical accuracy of the glucose device various methods were used for the examining the data obtained in clinical trials. These standard models offer analysis of key parameters and thus help to define the overall performance of the device. The methods used in the study are explained below:

7.3.1 Clarke error grid analysis

This is a linear regression model which was built in 1970 by William Clarke so as to provide a clear picture of the accuracy and possible clinical risk/failure of the device (Clarke, 2005; Clarke *et al.*, 1987). The glucose value are analysed in from 0-400 mg/dl which cover the hypoglycaemic, euglycemic, and hyperglycaemic regions. The error grid analysis compares the glucose values obtained from the device under analysis and thereby compared with the corresponding reference glucose value. The reference glucose values are on the x-axis and the predicted glucose values are on the y-axis.

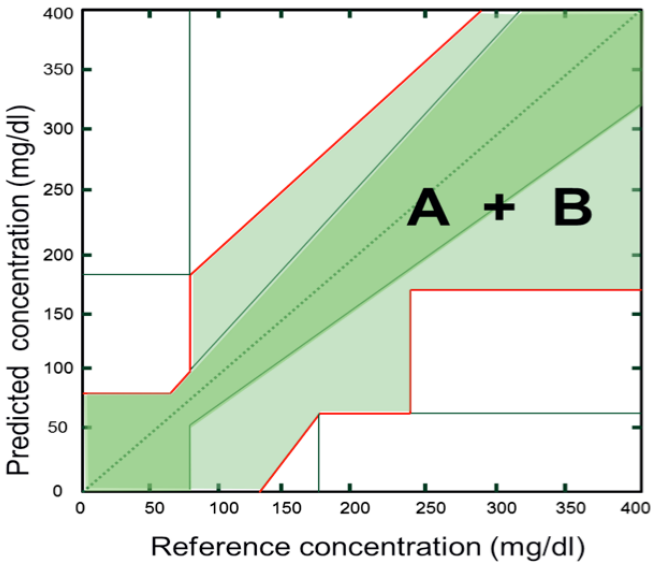

Figure 7.4: Clarke error grid model

A region shown brighter green corresponds to a clinical accurate region and B region which is light green corresponds to clinically benign values region. Both components added together provides the clinical accuracy of the system.

The Clarke error grid is divided into 5 different region which have their own significance.

A region represent the glucose values which are closer to central linear regression line and thus these value are accurate to reference glucose value and can be used to make a clinical decision. The value in A region should have less than 20 percent variability with respect to reference glucose values.

B region these value are neither harmful nor useful for making the clinical decision. These have more than 20 percent variability than reference glucose values. However it should lie within the limiting range defined in the graph.

C region predicts that if the data present in this region are used to make a clinical decision may result in overcorrection of blood glucose value. Thus it may cause extreme fall and rise in blood glucose values.

D region depicts that these data points are dangerous for the even detecting the glucose value and clinical decision cannot be made from these for the treatment purpose.

E region signifies the flawed glucose value from the device. The value obtained in this region are opposite to the reference value thus treatment taken on based on these data point can results in fatal outcomes.

7.3.2 Bland Altman plot

The limits of agreement method also known as Bland Altman method is used to evaluate levels of acceptability between the reference glucose values and corresponding glucose values. The key advantage of this technique is to assess how the device will perform in an actual scenario and also whether the accurate glucose values are reproducible or not. It estimates 95 percent limits of agreement of the glucose values and to obtain this difference of the measurement of two methods is calculated. Thereafter the mean and standard deviation from the values obtained is calculated. The graph is plotted which has a difference of glucose values on y axis and the average of glucose values on x axis. The 95 percent limit of agreement are kept between mean minus 1.96 standard deviation and mean plus 1.96 standard deviation (Bland & Altman, 2007).

7.3.3 Mean absolute relative difference

The glucose monitor performance is evaluated by the identifying the mean absolute relative difference to check the performance of the device during swings of blood glucose can be assessed. It is the most common statistical method and absolute relative difference is defined as

$$ARD = 100\frac{(yCGM - yRGB)}{yRGB} \tag{7.2}$$

yCGM = reference blood glucose concentration yRGB = predicted glucose concebtraion

The mean of the individual ARD's obtained from the system is then calculated therefore highlighting the overall picture of the device performance. The study design is the key to the accuracy of the device. MARD defines how much significantly device will show the change in glucose while the glucose fluctuation are going on in the body. According to ISO 15197:20131 classifies the device

based percent of MARD. Lesser the MARD better is the device performance (Obermaier *et al.*, 2013).

7.4 Clinical outcome

During the clinical trials, NFTGM sensor was compared with the handheld glucose monitor and invasive continuous glucose monitor (ICGM). Total 192 points were obtained in comparison with finger prick hand held monitor and 1,008 points were obtained in comparison with the continuous glucose monitor from a total of 24 session.

7.4.1 Clarke error grid analysis results

In order to get better picture of the data obtained from clinical trial of 12 Type-1 subjects in total 24 sessions of 8 hrs Clarke error grid (CEG) analysis was used to check the correlation of capillary blood glucose measurement using finger prick handheld glucose meter with non-invasive finger touch glucose meter i.e. NFTGM sensor I. Total 96 calibrated paired glucose points were obtained from 24 sessions with candidates following their regular meal and insulin regimen (fig 7.5). A simple linear fitting was used to calibrate the data and no data corrections were applied. Region A marks for the less than 20 percent deviation from BG data and signifies that data measured in this region is clinically accurate and can be used for diagnosing and treatment.

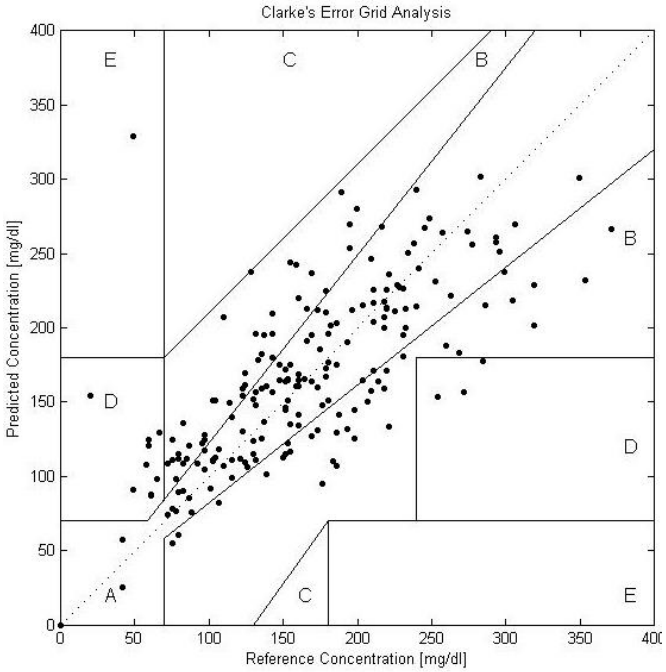

Figure 7.5: Calibration Clarke error grid (CEG) in which the calibrated glucose value were compared to the reference blood glucose value from the photonic chip.

NFTGM have 77 % data in A region which ranges from 2.5 mmol/l to 18mmol/l of blood glucose (fig 7.5). Region B depicts that the measured data has a deviation more than 20% of the BG data and data of this region will not be considered for treatment. NFTGM sensor has measured 19.5% of the data in this region do not have any effect on the clinical outcome. C region specifies that there is an issue in the calibration and thus this data is incorrect. Following these data can probably deliver incorrect treatment. NFTGM sensor I, has no data in this region signifying its accuracy. D region in the CEG analysis illustrates the clinical risk of the sensor and possible failure for the device to work. NFTGM calibration data shows 3.5% clinical risk of our sensor which might be in the hypoglycaemic region. A key reason for this risk factor shorter glucose range obtained in some candidates which is to obtain a linear fit of the data form NFTGM. The Clarke error grid was plotted to compare the glucose values obtained from NFTGM sensor with the glucose values obtained from the invasive continuous glucose monitor (ICGM).

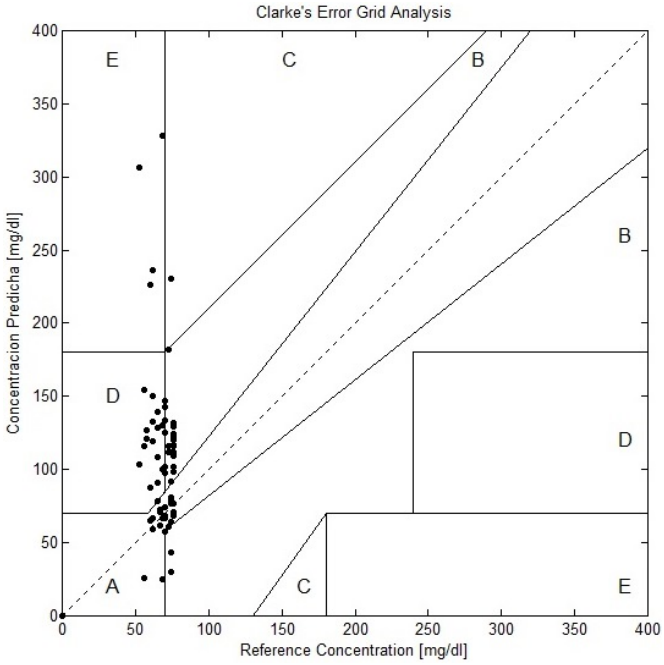

Figure 7.6: Hypoglycaemic region CEG analysis comparing NFTGM sensor with the reference glucose values from ICGM

The hypoglycaemic clinical accuracy of the NFTGM compared to ICGM was observed to be 77.3, which shows an efficient sensitivity of the device in measuring lower blood glucose levels (fig 7.6). However, the clinical risk of the device producing a false negative or false positive value is 11.1%. Overall, the clinical acceptability was 89 %.

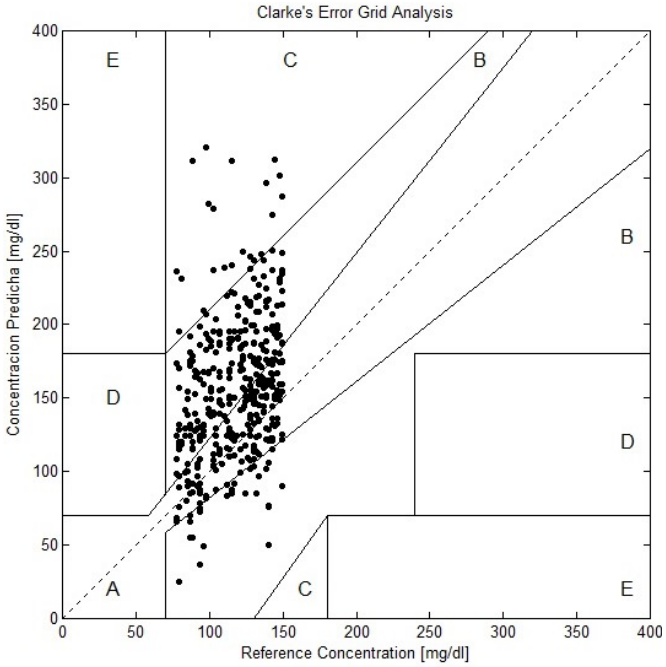

Figure 7.7: Euglycaemic region CEG analysis comparing NFTGM sensor with the reference glucose values from ICGM

The euglycaemic clinical accuracy of the NFTGM compared to ICGM was observed to be 36%, which shows an poor sensitivity of the device in measuring normal blood glucose levels (fig 7.7). Possible reason for this poor result might be due to linear fitting of the fluorescence lifetime while it originally shows a nonlinear trend. However the clinical risk of device producing a false negative or false positive value in this region is 5.7%. Overall, the clinical acceptability was 96%.

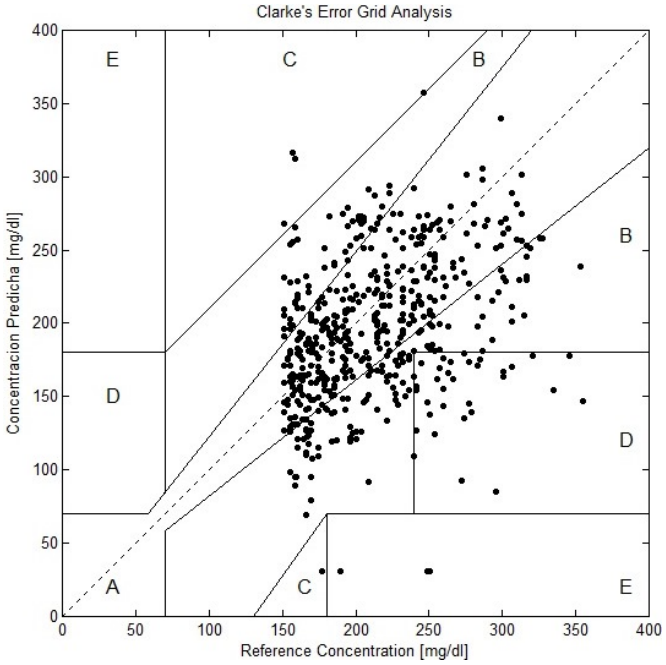

Figure 7.8: Hyperglycaemic region CEG analysis comparing NFTGM with the reference glucose values from ICGM

The hyperglycaemic clinical accuracy of the NFTGM sensor compared to ICGM was observed to be 59.1%, which shows fair sensitivity of the device in measuring higher blood glucose levels (fig 7.8). However the clinical risk of device producing a false negative or false positive value in this region is 7.7%. Overall, the clinical acceptability was found to be 92.3%.

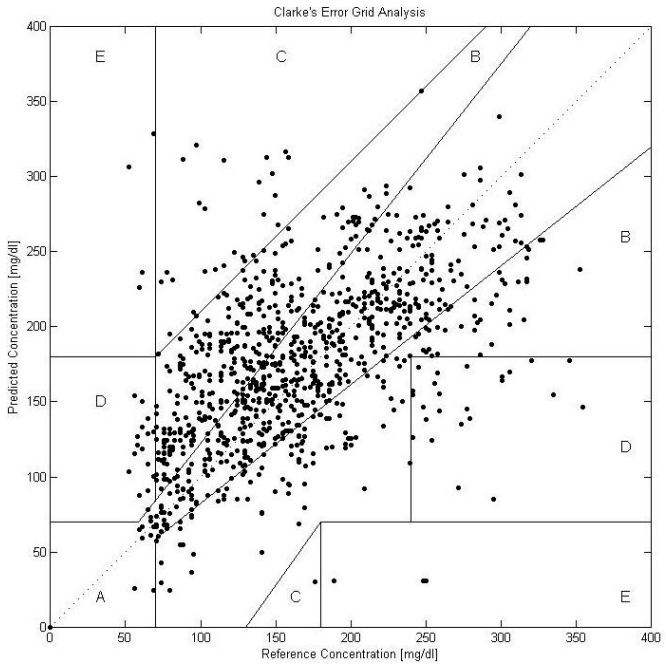

Figure 7.9: CEG analysis comparing glucose values obtained from NFTGM with the reference glucose values from ICGM

Table 7.1: The clarke error grid data obtained by comparing the glucose values obtained from the NFTGM with corresponding glucose values obtained from the ICGM

Error grid	A	A+B	C	D	E
NFTGM sensor-invasiveCGM error grid	53.7	92.4	2.7	4.2	0.6
Hypoglycaemic error grid	77.3	89	1	8.1	2
Euglycaemic error grid	36	94	5.7	0	0
Hyperglycaemic error grid	59.1	92.3	1	6.1	0.6

The CEG value of different comparing NFTGM sensor value with ICGM values. In comparison with other invasive continuous glucose monitors the device has depicted a very competitive performance. The three devices compared with NFTGM sensor are Abbott's freestyle navigator, Dexcom's Seven plus ICGM, Medtronic's Guardian ICGM. All these devices are currently in the market and

are invasive in nature. Comparing Clarke error gird of the NFTGM sensor with the shows a relative trend in the data similar to invasive glucose monitors. The overall clinical accuracy of these meters ranges between 50% to 81% i.e. Zone A of Clarke error grid. The NFTGM was also compared with Glucotrack which is non invasive glucose monitor (in development) shoon in table 7.2 (Gal *et al.*, 2011). Since the clinical accuracy of the NFTGM sensor is also in this region it can ascertained that the novel concept of sensing of glucose is significant (Damiano *et al.*, 2013; Kovatchev *et al.*, 2008).

Table 7.2: The statistical results obtained from NFTGM compared with current commercially available ICGMs (Damiano *et al.*, 2013; Kovatchev *et al.*, 2008) and also other non invasive glucose technique (in development) (Gal *et al.*, 2011) .

Numerical and clinical accuracy of NFTGM sensor and CGMs (in percent)			
	MARD	Error grid Zone(A)	Error grid zone (A+B)
Calibration error grid	28.7	77	96.5
NFTGM sensor-ICGM error grid	33.6	53.7	92.4
Glucotrack (non invasive)	30.6	42	97
Dexcom	18.75	49	90
Medtronic	17.32	61.7	96
Abbot free style navigator	12.8	81.7	98.4

The mean absolute relative difference i.e. the mean change in glucose value above or below the reference glucose was found to be 28.7% and 33.6% in calibration CEG and CEG with IGM respectively. Comparing the CEG results with the current glucose monitor i.e. leading competent in NGM technique which is GlucoTrack and three market leading IGM brands, the clinical accuracy of the NFTGM sensor was found to be better than GlucoTrack.

7.4.2 Bland altman plot

Most of the measured data point obtained from NFTGM sensor is in the limits of agreement of glucose handheld meter, mainly from 50-200mg. The limits of agreement are between 92.9mg/dl to -97.3 dl with the blood glucose handheld monitor. 5.7% of the point was outside the limits of agreement which assess the clinical risk for the device. The measurements were not made in hypoglycaemic region and as controlled glycemic clamp study is required for the conducting that type of experiment. Thus with more data points in the hypoglycaemic region the overall accuracy of the device can be improved.

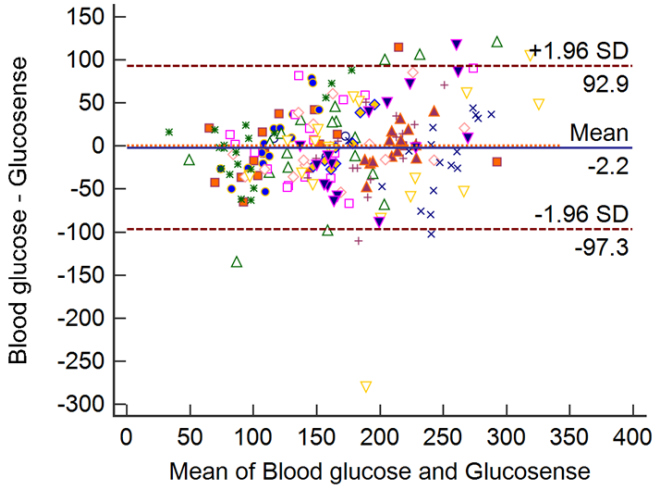

Figure 7.10: Bland Altman plot - comparison between NFTGM sensor and BG monitor.

Chapter 8

Future work

8.1 Next stage of development

8.1.1 IR detection

The aim of this research was to develop IR detectors which can work at room temperatures. The GP superlattice coated AFM cantilevers does show an innate stress in the films which change with an increase in temperature. This evident from the bending in tip of the cantilever. The Er^{3+} ions doped GP superlattice doped with glass:polymer::1:2 layers has maximum sensitivity to the temperature change. In the next stage of the study, more rare earth metals should be doped in the GP superlattice. In this study NIR range of 950 to 1010 nm and 1450 to 1650 nm has been assessed using Er^{3+} ions. So as to cover the whole range of the IR spectrum, the doping of more rare earth metals should be used such as Praseodymium (Pr^{3+}), Dysprosium Dy^{3+}, Terbium Tb^{3+} rare earth metals which covers mid IR range of 3-12 μm (Shaw *et al.*, 2001). Another approach can be using a lower thickness of the cantilever and also different ratio of glass polymer superlattice such as 1:3::Glass:polymer. This an early stage research for Er^{3+} ions doped GP superlattice. More analysis in required to check the density of the erbium ions doped in the GP superlattice. Doping with different erbium ion concentration can suggest which formulation will more accuracy in sensing temperature changes.

8.1.2 Glucose sensing

An earlier laboratory bench prototype of the device has previously been tested in the clinical proof-of-concept study involving 12 patients with Type I diabetes at the Leeds Institute for Cardiovascular and Metabolic Medicine (LICAMM formerly LIGHT), Faculty of Medicine, University of Leeds. This first laboratory prototype of non-invasive glucose monitor was compared with finger prick method and with a continuous glucose meter. A Clarke error grid analysis showed 96 % clinical acceptability and 92 % clinical accuracy with reference to conventional finger prick testing. However, only one composition of the photonic chip was previously tested. Different compositions of photonic chips may improve the signal and calibration curve of the glucose sensor. In-vitro testing has been carried

out to test photonic chips with different compositions. Photonic chips with 0.25 and 0.5 mol % concentration of Er^{3+} ions has shown sensitivity in measuring glucose concentrations. These photonic chips can be tested in the clinical study as clinical trials are representative of how photonic chips will perform once in contact with the skin. A similar laboratory bench prototype which was used in previous study of the non-invasive device with more stable lifetime can be used to test photonic chips in a broader study population. The study design is generally very similar to the previous clinical proof of concept study.

8.1.3 Proposed clinical study

1. Identify the optimum composition of the photonic chip for measurement of glucose in tissue;
2. Evaluate the effect of operational variables related to the patient skin type on the glucose measurement;
3. Assess the consistency and stability of the device calibration;
4. Correlate the physical characteristics of the photonic chip with clinical performance;
5. Determine whether further chip optimisation is required.

The clinical study should be a single-centre, prospective, randomised, controlled, within-patient study of photonic chips as glucose sensors for subjects with diabetes mellitus. There will be minimal deviation from the subjects' normal diabetes management practice. The study should allow a comparison of the performance of several different photonic chips for monitoring glucose levels in a broad population including Type I and insulin treated Type II diabetes. Baseline measurements should be recorded, including height, weight, BMI, body fat percentage, fingertip skin thickness, and blood analysis for haematocrit, glycated haemoglobin (HbA1c), lipid profile (including triglycerides), sodium, potassium and urea. Laboratory blood glucose levels must be measured every 30 minutes for 4 hours using a YSI glucose analyser (accepted gold standard reference value) and

an established, commercially available, self-monitoring blood glucose device (finger strip analysis). Subjects with Type I diabetes and insulin dependent Type II diabetes must be included because they can experience wide variation in glucose levels. Insulin dependent Type II diabetes is generally prevalent only in older subjects, so the effect of age on ability to measure glucose levels will be examined in Type I diabetes only as this condition is prevalent across all age groups.

Inclusion criteria

1. Subjects with Type I diabetes or insulin dependent Type II diabetes
2. Age 18 to 70 years
3. Able to give written informed consent
4. Age and ethnicity meet the study population and sample size requirements

Exclusion criteria

1. Skin conditions causing irritation e.g., eczema, psoriasis.
2. Pregnant women or women intending to become pregnant or not using adequate contraception e.g. OCP, or condoms + IUD.
3. Gestational diabetes
4. Liver function failure within the last 12 months: ALT elevation by more than 2 fold upper end of normal range
5. Impaired renal function within the last 12 months: eGFR <60 mls/min/1.73 m^2
6. Retinopathy other than background changes, microalbuminuria
7. Cardiac or cerebral ischaemic event within 6 months of enrolment
8. Currently participating in another clinical trial
9. Allergy to Elastoplast

The performance of the photonic chips shall be compared through evaluation of the calibration curves obtained by plotting the change in the fluorescent lifetime against the glucose value using the YSI instrument. Repeated measures regression analysis on the response change in fluorescent lifetime, with covariates for chip composition, glucose concentration, age, ethnicity, period, and interaction between chip composition and glucose concentration; also an assessment of the interaction between age and ethnicity with chip composition and glucose concentration. Non-linear terms for glucose concentration may also be assessed. Standard Clarke Error Grid (CEG) analysis for each chip composition.

The preferred photonic chip should be selected based on:

- A linear relationship between fluorescence lifetime and glucose levels over the widest range
- The steepest slope in linear region
- Best fit of data to calibration curve

The calibration curves between patients shall be compared and the feasibility of applying a universal calibration model will be assessed through standard statistical approaches for measuring goodness of fit. Clinical performance measures can be compared with physical properties of the photonic chip and previously collected in vitro data in order to establish a model that correlates glucose monitoring capability with photonic chip composition. Device and chip performance can be assessed by plotting the predicted glucose level from the photonic sensor device against glucose levels obtained with the YSI laboratory analysis at contemporaneous time points.

References

Abcam (2017). Counting cells using a hemocytometer — abcam. http://www.abcam.com/protocols/counting-cells-using-a-haemocytometer, (Accessed on 12/08/2017). 145

Adams, A., Schinke, D. & Capio, C. (1979). An evaluation of the prism coupler for measuring the thickness and refractive index of dielectric films on silicon substrates. *Journal of The Electrochemical Society*, **126**, 1539–1543. 67

Adler, A.I., Stratton, I.M., Neil, H.A.W., Yudkin, J.S., Matthews, D.R., Cull, C.A., Wright, A.D., Turner, R.C. & Holman, R.R. (2000). Association of systolic blood pressure with macrovascular and microvascular complications of type 2 diabetes (ukpds 36): prospective observational study. *Bmj*, **321**, 412–419. 24

Ainslie, B.J. (1991). A review of the fabrication and properties of erbium-doped fibers for optical amplifiers. *Journal of Lightwave Technology*, **9**, 220–227. 93

Albani, J.R. (2008). *Principles and applications of fluorescence spectroscopy*. John Wiley & Sons. xv, xxvii, 15, 16, 17, 18, 19

Alexeeva, N.V. (2011). *Characterization of skin tissue heterogeneity with near-infrared microspectroscopy and its effects on noninvasive measurements of glucose*. The University of Iowa. 26

Allen, R. & David, G. (1969). The zeiss-nomarski differential interference equipment for transmitted-light microscopy. *Zeitschrift fur wissenschaftliche Mikroskopie und mikroskopische Technik*, **69**, 193–221. 61

Amerov, A.K., Chen, J. & Arnold, M.A. (2004). Molar absorptivities of glucose and other biological molecules in aqueous solutions over the first overtone and combination regions of the near-infrared spectrum. *Applied spectroscopy*, **58**, 1195–1204. xvi, 28, 30, 31, 159, 161, 162

Anderson, J.M. & Shive, M.S. (2012). Biodegradation and biocompatibility of pla and plga microspheres. *Advanced drug delivery reviews*, **64**, 72–82. 136

Anderson, R.R. & Parrish, J.A. (1981). The optics of human skin. *Journal of investigative dermatology*, **77**, 13–19. xvi, 30, 32

Astles, J.R., Sedor, F.A. & Toffaletti, J.G. (1996). Evaluation of the ysi 2300 glucose analyzer: algorithm-corrected results are accurate and specific. *Clinical biochemistry*, **29**, 27–31. 24

Ba, L.A., Döring, M., Jamier, V. & Jacob, C. (2010). Tellurium: an element with great biological potency and potential. *Organic & biomolecular chemistry*, **8**, 4203–4216. 154

Babich, H. & Borenfreund, E. (1990). Applications of the neutral red cytotoxicity assay to in vitro toxicology. *Alternatives to laboratory animals: ATLA*. 150

Balling, P. & Schou, J. (2013). Femtosecond-laser ablation dynamics of dielectrics: basics and applications for thin films. *Reports on Progress in Physics*, **76**, 036502. 84

Banks, P., Dinh, L., Stuart, B., Feit, M., Komashko, A., Rubenchik, A., Perry, M. & McLean, W. (1999). Short-pulse laser deposition of diamond-like carbon thin films. *Applied Physics A*, **69**, S347–S353. 38

Beletic, J.W., Blank, R., Gulbransen, D., Lee, D., Loose, M., Piquette, E.C., Sprafke, T., Tennant, W.E., Zandian, M. & Zino, J. (2008). Teledyne imaging sensors: Infrared imaging technologies for astronomy & civil space. In *Proc. SPIE*, vol. 7021. 9

Berezin, M.Y. & Achilefu, S. (2010). Fluorescence lifetime measurements and biological imaging. *Chemical reviews*, **110**, 2641–2684. 160

Berneschi, S., Nunzi Conti, G., Bányász, I., Watterich, A., Khanh, N., Fried, M., Pászti, F., Brenci, M., Pelli, S. & Righini, G. (2007). Ion beam irradiated channel waveguides in er 3+-doped tellurite glass. *Applied physics letters*, **90**, 121136. 47

Bharate, J.B., Batarseh, Y.S., Wani, A., Sharma, S., Vishwakarma, R.A., Kaddoumi, A., Kumar, A. & Bharate, S.B. (2015). Synthesis and p-glycoprotein induction activity of colupulone analogs. *Organic & biomolecular chemistry*, **13**, 5488–5496. 153

Bistrian, B.R. (2001). Hyperglycemia and infection: which is the chicken and which is the egg? *Journal of Parenteral and Enteral Nutrition*, **25**, 180–181. 20

Bland, J.M. & Altman, D.G. (2007). Agreement between methods of measurement with multiple observations per individual. *Journal of biopharmaceutical statistics*, **17**, 571–582. 187

Bloomfield, P. (2004). *Fourier analysis of time series: an introduction*. John Wiley & Sons. 88

Borenfreund, E. & Puerner, J.A. (1985). A simple quantitative procedure using monolayer cultures for cytotoxicity assays (htd/nr-90). *Methods in Cell Science*, **9**, 7–9. 150

Bradley, J.D. (2017). Rare earth doped light emitting thin film materials for silicon photonics. In *Meeting Abstracts*, 17, 1013–1013, The Electrochemical Society. 5

Briscoe, V.J. & Davis, S.N. (2006). Hypoglycemia in type 1 and type 2 diabetes: physiology, pathophysiology, and management. *Clinical Diabetes*, **24**, 115–121. 20

Brückner, R. (1970). Properties and structure of vitreous silica. i. *Journal of non-crystalline solids*, **5**, 123–175. 13

Bulgakova, N., Stoian, R., Rosenfeld, A., Hertel, I. & Campbell, E. (2004). Electronic transport and consequences for material removal in ultrafast pulsed laser ablation of materials. *Physical Review B*, **69**, 054102. 44

Cao, H. & Sheehan, S.W. (2013). Applied physics: A cascade laser's random walk. *Nature*, **503**, 200–201. 159

Carey, J. (2002). Structure of multi-oxygen-related defects in erbium-implanted silicon. *Journal of Physics: Condensed Matter*, **14**, 8537. 83

Chandrappan, J., Murray, M., Kakkar, T., Petrik, P., Agocs, E., Zolnai, Z., Steenson, D., Jha, A. & Jose, G. (2015). Target dependent femtosecond laser plasma implantation dynamics in enabling silica for high density erbium doping. *Scientific reports*, **5**, 14037. 82, 94, 112

Chen, C.Y. & Chi, S. (1993). Attenuation and fluorescence characteristics of optical signals propagating in an erbium-doped fiber. *IEEE photonics technology letters*, **5**, 1020–1022. 161

Cheney, B. (2007). Introduction to scanning electron microscopy. *Materials Engineering department San Jose State University*. 65

Chrisey, D.B. & Hubler, G.K. (1994). Pulsed laser deposition of thin films. 12, 36

Ciminelli, C., Campanella, C.M., Dell'Olio, F., Campanella, C.E. & Armenise, M.N. (2013). Label-free optical resonant sensors for biochemical applications. *Progress in Quantum Electronics*, **37**, 51–107. 7

Clark, L.C. & Lyons, C. (1962). Electrode systems for continuous monitoring in cardiovascular surgery. *Annals of the New York Academy of sciences*, **102**, 29–45. 6

Clarke, W.L. (2005). The original clarke error grid analysis (ega). *Diabetes technology & therapeutics*, **7**, 776–779. 185

Clarke, W.L., Cox, D., Gonder-Frederick, L.A., Carter, W. & Pohl, S.L. (1987). Evaluating clinical accuracy of systems for self-monitoring of blood glucose. *Diabetes care*, **10**, 622–628. 185

Claxton, N.S., Fellers, T.J. & Davidson, M.W. (2006). Laser scanning confocal microscopy. *Department of Optical Microscopy and Digital Imaging, Florida State University, Tallahassee, http://www. olympusconfocal. com/theory/LSCMIntro. pdf*. 62

Clothier, R. (1990). The frame modified neutral red uptake cytotoxicity test. *Invittox protocol*. 150

Cohen, M.L. (1977). Measurement of the thermal properties of human skin. a review. *Journal of investigative dermatology*, **69**, 333–338. 159

Corporation, M. (2017a). Model 2010/m overview. 69

Corporation, N. (2017b). Shear amount in differential interference. xvi, 61

Corsi, C. (2010). History highlights and future trends of infrared sensors. *Journal of modern optics*, **57**, 1663–1686. 9

Couairon, A., Sudrie, L., Franco, M., Prade, B. & Mysyrowicz, A. (2005). Filamentation and damage in fused silica induced by tightly focused femtosecond laser pulses. *Physical Review B*, **71**, 125435. 80

Craciun, V., Amirhaghi, S., Craciun, D., Elders, J., Gardeniers, J.G. & Boyd, I.W. (1995). Effects of laser wavelength and fluence on the growth of zno thin films by pulsed laser deposition. *Applied surface science*, **86**, 99–106. 116

Cryer, P.E., Davis, S.N. & Shamoon, H. (2003). Hypoglycemia in diabetes. *Diabetes care*, **26**, 1902–1912. 20

Cueff, S., Labbé, C., Jambois, O., Garrido, B., Portier, X. & Rizk, R. (2011). Thickness-dependent optimization of er3+ light emission from silicon-rich silicon oxide thin films. *Nanoscale research letters*, **6**, 395. 76

Damiano, E.R., El-Khatib, F.H., Zheng, H., Nathan, D.M. & Russell, S.J. (2013). A comparative effectiveness analysis of three continuous glucose monitors. *Diabetes Care*, **36**, 251–259. xxviii, 194

Davis, K., Agarwal, A., Tomozawa, M. & Hirao, K. (1996). Quantitative infrared spectroscopic measurement of hydroxyl concentrations in silica glass. *Journal of non-crystalline solids*, **203**, 27–36. 13

DeFronzo, R.A. (1988). The triumvirate: β-cell, muscle, liver. a collusion responsible for niddm. *Diabetes*, **37**, 667–687. 20

DeFronzo, R.A. (1997). Pathogenesis of type2 daiabetes: metabolic and molecular implications for identhfying diabetes genes. *Diabetes reviews*, **5**, 177–269. 20, 23

Diego, S. (2017). Hemocytometer cell counting protocol. 141

Directive, C. (1993). 93/42/eec of 14 june 1993 concerning medical devices. 136

Directive, I.V.D. (1998). 98/79/ec. *Vitro Diagnostic Medical Device Directive*. 136

Douglas, A. & Teaney, D. (1988). Hand-held glucose monitor and recorder. In *Engineering in Medicine and Biology Society, 1988. Proceedings of the Annual International Conference of the IEEE*, 747–748, IEEE. 24

Du, D., Liu, X., Korn, G., Squier, J. & Mourou, G. (1994). Laser-induced breakdown by impact ionization in sio2 with pulse widths from 7 ns to 150 fs. *Applied physics letters*, **64**, 3071–3073. 44

Eason, R. (2007). *Pulsed laser deposition of thin films: applications-led growth of functional materials*. John Wiley & Sons. 12, 36, 37, 46, 116

Egerton, R.F. (2005). *Physical principles of electron microscopy*. Springer. 67

El Hamzaoui, H., Bigot, L., Bouwmans, G., Razdobreev, I., Bouazaoui, M. & Capoen, B. (2011). From molecular precursors in solution to microstructured optical fiber: a sol-gel polymeric route. *Optical Materials Express*, **1**, 234–242. 108

El-Mallawany, R. (1999). Tellurite glasses: Part 2. anelastic, phase separation, debye temperature and thermal properties. *Materials chemistry and physics*, **60**, 103–131. xxvii, 116, 118

Estevez, M.C., Otte, M.A., Sepulveda, B. & Lechuga, L.M. (2014). Trends and challenges of refractometric nanoplasmonic biosensors: a review. *Analytica chimica acta*, **806**, 55–73. 7

Fan, X., White, I.M., Shopova, S.I., Zhu, H., Suter, J.D. & Sun, Y. (2008). Sensitive optical biosensors for unlabeled targets: A review. *analytica chimica acta*, **620**, 8–26. xv, 7, 8

Faust, C.B. (1992). *Modern chemical techniques*. Royal Soc. of Chemistry, Educ. Divn. xvii, 71, 72

Favennec, P., l'Haridon, H., Moutonnet, D., Salvi, M. & Gauneau, M. (1990). Optical activation of er3+ implanted in silicon by oxygen impurities. *Japanese Journal of Applied Physics*, **29**, L524. 83

Feng, X., Tanabe, S. & Hanada, T. (2001). Hydroxyl groups in erbium-doped germanotellurite glasses. *Journal of non-crystalline solids*, **281**, 48–54. 91

Fischer-Hirchert, U.H. (2015). *Photonic Packaging Sourcebook: Fiber-Chip Coupling for Optical Components, Basic Calculations, Modules*. Springer. 86, 88, 93

Fox, S.I. (2009). *Fundamentals of human physiology*. McGraw-Hill. xv, 21

Gadelmawla, E., Koura, M., Maksoud, T., Elewa, I. & Soliman, H. (2002). Roughness parameters. *Journal of materials processing technology*, **123**, 133–145. xvi, xvii, 63, 64, 65

Gal, A., Harman-Boehm, I., Naidis, E., Mayzel, Y. & Trieman, L. (2011). Validity of glucotrack®, a non-invasive glucose monitor, for variety of diabetics. *Age*, **1**, 61. xxviii, 194

Gamaly, E.G., Rode, A.V. & Luther-Davies, B. (1999). Ultrafast ablation with high-pulse-rate lasers. part i: Theoretical considerations. *Journal of Applied Physics*, **85**, 4213–4221. 37

Gamaly, E.G., Rode, A.V., Luther-Davies, B. & Tikhonchuk, V.T. (2002). Ablation of solids by femtosecond lasers: Ablation mechanism and ablation thresholds for metals and dielectrics. *Physics of Plasmas (1994-present)*, **9**, 949–957. 12, 36, 37

Gamaly, E.G., Rode, A.V., Uteza, O., Kolev, V., Luther-Davies, B., Bauer, T., Koch, J., Korte, F. & Chichkov, B. (2004). Control over a phase state of the laser plume ablated by femtosecond laser: Spatial pulse shaping. *Journal of Applied Physics*, **95**, 2250–2257. 37

Gehrz, R., Becklin, E., De Pater, I., Lester, D., Roellig, T. & Woodward, C. (2009). A new window on the cosmos: The stratospheric observatory for infrared astronomy (sofia). *Advances in Space Research*, **44**, 413–432. 9

Gepts, W. (1965). Pathologic anatomy of the pancreas in juvenile diabetes mellitus. *Diabetes*, **14**, 619–633. 22

Giannuzzi, L.A. *et al.* (2006). *Introduction to focused ion beams: instrumentation, theory, techniques and practice*. Springer Science & Business Media. 66

Gierak, J., Mailly, D., Faini, G., Pelouard, J., Denk, P., Pardo, F., Marzin, J., Septier, A., Schmid, G., Ferré, J. *et al.* (2001). Nanofabrication with focused ion beams. *Microelectronic Engineering*, **57**, 865–875. 66

Girard, S., Ouerdane, Y., Tortech, B., Marcandella, C., Robin, T., Cadier, B., Baggio, J., Paillet, P., Ferlet-Cavrois, V., Boukenter, A. *et al.* (2009). Radiation effects on ytterbium-and ytterbium/erbium-doped double-clad optical fibers. *IEEE Transactions on Nuclear Science*, **56**, 3293–3299. 93, 99, 112

Gonen, B., Rochman, H., Rubenstein, A., Tanega, S. & Horwitz, D. (1977). Haemoglobin a1: an indicator of the metabolic control of diabetic patients. *The Lancet*, **310**, 734–737. 20

Grew, R.S., Ebendorff-Heidepriem, H., Veitch, P.J. & Monro, T.M. (2006). Concentration effects in erbium doped tellurite glass. In *Optoelectronic and Microelectronic Materials and Devices, 2006 Conference on*, 196–199, IEEE. 108

Griscom, D.L. (1991). Optical properties and structure of defects in silica glass. *Journal of the Ceramic Society of Japan*, **99**, 923–942. 91

Group, D.R.S.R. *et al.* (1978). Photocoagulation treatment of proliferative diabetic retinopathy: the second report of diabetic retinopathy study findings. *Ophthalmology*, **85**, 82–106. 23

Group, U.P.D.S. *et al.* (1988). Prospective diabetes study iv. characteristics of newly presenting type 2 diabetic patients: male preponderance and obesity at different ages. multicenter study. *Diabetic Medicine*, **5**, 154–159. 24

Guo, J., Keathley, P.D. & Hastings, J. (2008). Dual-mode surface-plasmon-resonance sensors using angular interrogation. *Optics letters*, **33**, 512–514. 8

Haglund, R.F., Miller, J.C., Lucatorto, T. & De Graef, M. (1997). *Laser Ablation and Desorption*, vol. 30. Academic Press. 12

Harman-Boehm, I., Gal, A., Raykhman, A.M., Zahn, J.D., Naidis, E. & Mayzel, Y. (2009). Noninvasive glucose monitoring: a novel approach. 26

Hart, G. (1927). The nomenclature of silica. *American Mineralogist*, **12**, 383–395. 12

Harvey, J.E. (1976). Light-scattering characteristics of optical surfaces. 80

Hayashi, H., Sugimoto, N., Tanabe, S. & Ohara, S. (2006). Effect of hydroxyl groups on erbium-doped bismuth-oxide-based glasses for fiber amplifiers. *Journal of applied physics*, **99**, 093105. 91

Hayashi, S. (1990). Differential interference microscope. US Patent 4,964,707. 61

Hetherington, G., Jack, K. & Ramsay, M. (1965). High-temperature electrolysis of vitreous silica. i. oxidation ultra-violet induced fluorescence and irradiation colour. *Physics and Chemistry of Glasses*, **6**, 6–+. 13

Hillier, T.A., Abbott, R.D. & Barrett, E.J. (1999). Hyponatremia: evaluating the correction factor for hyperglycemia. *The American journal of medicine*, **106**, 399–403. 28

Hnizdo, E. & Vallyathan, V. (2003). Chronic obstructive pulmonary disease due to occupational exposure to silica dust: a review of epidemiological and pathological evidence. *Occupational and Environmental Medicine*, **60**, 237–243. 136

Holman, R. & Turner, R. (1979). Maintenance of basal plasma glucose and insulin concentrations in maturity-onset diabetes. *Diabetes*, **28**, 227–230. 20

Homola, J. (2008). Surface plasmon resonance sensors for detection of chemical and biological species. *Chemical reviews*, **108**, 462–493. 7

Huang, M. (2003). Stress effects on the performance of optical waveguides. *International Journal of Solids and Structures*, **40**, 1615–1632. 62, 74, 80

Ibrahim, M.H., Kassim, N.M., Mohammad, A.B. & Gang, S.Y. (2004a). Modelling of rib optical waveguide structure using effective index method. *Jurnal Elektrika*, **6**, 43–49. 69

Ibrahim, M.H., Kassim, N.M., Mohammad, A.B. & Chin, M.K. (2006). Prism coupling measurement of benzocyclobutene (bcb 4024-40) polymer for optical devices application. *Elektrika Journal of Electrical Engineering*, **8**, 13–16. xvii, 68, 69

Ibrahim, Y.M., Alsharaeh, E.H. & El-Shall, M.S. (2004b). Evidence for penning ionization in the generation of electronically excited states of transition metal cations by laser vaporization. *The Journal of Physical Chemistry B*, **108**, 3959–3962. 88

ISO, E. (2008). 10993-12: 2008–biological evaluation of medical devices–part 12: Sample preparation and reference materials (iso 10993-12: 2007). *German version: DIN EN ISO*, 10993–10912. 136, 147, 151

ISO, I. (2009). 10993–5: 2009 biological evaluation of medical devices–part 5: Tests for in vitro cytotoxicity. *International Organization for Standardization, Geneva*. 136, 147, 149, 150, 152, 153

Jeng, J.H., Hsieh, C., Lan, W., Chang, M., Lin, S., Hahn, L. & Kuo, M. (1998). Cytotoxicity of sodium fluoride on human oral mucosal fibroblasts and its mechanisms. *Cell biology and toxicology*, **14**, 383–389. 155

Jorgenson, R. & Yee, S. (1993). A fiber-optic chemical sensor based on surface plasmon resonance. *Sensors and Actuators B: Chemical*, **12**, 213–220. 8

Karim, A. & Andersson, J.Y. (2013). Infrared detectors: Advances, challenges and new technologies. In *IOP Conference Series: Materials Science and Engineering*, vol. 51, 012001, IOP Publishing. 9, 10

Keiser, G. (2003). *Optical fiber communications*. Wiley Online Library. 13

Kersten, R.T. (1975). A new method for measuring refractive index and thickness of liquid and deposited solid thin films. *Optics Communications*, **13**, 327–329. 67

Kholodkov, A. & Golant, K. (2005). Er 3+ ions luminescence in non-fused silicate glasses fabricated by spcvd. *Optical materials*, **27**, 1178–1186. 108

Kik, P.G. (2001). *Energy transfer in erbium doped optical waveguides based on silicon*. Ph.D. thesis. 12, 15

Kim, I.Y., Joachim, E., Choi, H. & Kim, K. (2015). Toxicity of silica nanoparticles depends on size, dose, and cell type. *Nanomedicine: Nanotechnology, Biology and Medicine*, **11**, 1407–1416. 136

Kitamura, R., Pilon, L. & Jonasz, M. (2007). Optical constants of silica glass from extreme ultraviolet to far infrared at near room temperature. *Applied optics*, **46**, 8118–8133. 12

Klarhöfer, M., Csapo, B., Balassy, C., Szeles, J. & Moser, E. (2001). High-resolution blood flow velocity measurements in the human finger. *Magnetic resonance in medicine*, **45**, 716–719. 170

Klocke, D., Schmitz, A., Soltner, H., Bousack, H. & Schmitz, H. (2011). Infrared receptors in pyrophilous ("fire loving") insects as model for new un-cooled infrared sensors. *Beilstein journal of nanotechnology*, **2**, 186. 126

Koughia, C. & Kasap, S.O. (2008). Excitation diffusion in gegase and gegas glasses heavily doped with er 3+. *Optics express*, **16**, 7709–7714. 106

Kovatchev, B., Anderson, S., Heinemann, L. & Clarke, W. (2008). Comparison of the numerical and clinical accuracy of four continuous glucose monitors. *Diabetes care*, **31**, 1160–1164. xxviii, 194

Landau, L.D., Bell, J., Kearsley, M., Pitaevskii, L., Lifshitz, E. & Sykes, J. (2013). *Electrodynamics of continuous media*, vol. 8. elsevier. 41

Lang, W. (1982). *Nomarski differential interference-contrast microscopy*. Oberkochen, Carl Zeiss. 61

Latif, A. (2000). *Nanofabrication using focused ion beam*. Ph.D. thesis, University of Cambridge. 66

Lawson, W., Nielsen, S., Putley, E. & Young, A. (1959). Preparation and properties of hgte and mixed crystals of hgte-cdte. *Journal of Physics and Chemistry of Solids*, **9**, 325–329. 9

LeMieux, M.C., McConney, M.E., Lin, Y.H., Singamaneni, S., Jiang, H., Bunning, T.J. & Tsukruk, V.V. (2006). Polymeric nanolayers as actuators for ultrasensitive thermal bimorphs. *Nano letters*, **6**, 730–734. 132

Liedberg, B., Nylander, C. & Lunström, I. (1983). Surface plasmon resonance for gas detection and biosensing. *Sensors and actuators*, **4**, 299–304. 8

Liu, Y., Lü, C., Li, M., Zhang, L. & Yang, B. (2008). High refractive index organic–inorganic hybrid coatings with tio 2 nanocrystals. *Colloids and Surfaces A: Physicochemical and Engineering Aspects*, **328**, 67–72. 67

Lorazo, P., Lewis, L.J. & Meunier, M. (2003). Short-pulse laser ablation of solids: from phase explosion to fragmentation. *Physical review letters*, **91**, 225502. 40

Lourenço, M., Milošević, M., Gorin, A., Gwilliam, R. & Homewood, K. (2016). Super-enhancement of 1.54 μm emission from erbium codoped with oxygen in silicon-on-insulator. *Scientific reports*, **5**. 83

Luther-Davies, B. & Gamaliĭ (????). Matter in ultrastrong laser fields. 41

Ma, H., Shieh, K.J., Qiao, T.X. & Cherng, S. (2006). Transmission electron microscopy (tem) and scanning electron microscopy (sem). *Nature and Science*, 14. 67

Maciel, E., Bolzan, R., Braga, A. & Rocha, J. (2000). Diphenyl diselenide and diphenyl ditelluride differentially affect δ-aminolevulinate dehydratase from liver, kidney, and brain of mice. *Journal of Biochemical and Molecular Toxicology*, **14**, 310–319. 154

Maier, J.S., Walker, S.A., Fantini, S., Franceschini, M.A. & Gratton, E. (1994). Possible correlation between blood glucose concentration and the reduced scattering coefficient of tissues in the near infrared. *Optics letters*, **19**, 2062–2064. 29, 33, 159

Mailis, S., Zergioti, I., Koundourakis, G., Ikiades, A., Patentalaki, A., Papakonstantinou, P., Vainos, N.A. & Fotakis, C. (1999). Etching and printing of diffractive optical microstructures by a femtosecond excimer laser. *Applied optics*, **38**, 2301–2308. 38

Maine, P., Strickland, D., Bado, P., Pessot, M. & Mourou, G. (1988). Generation of ultrahigh peak power pulses by chirped pulse amplification. *IEEE Journal of Quantum electronics*, **24**, 398–403. 49

Matsuoka, M. & Tohno, S.i. (1995). 1.54 μm photoluminescence of in situ erbium-oxygen co-doped silicon films grown by ion-beam epitaxy. *Journal of applied physics*, **78**, 2751–2757. 83

Mattarelli, M., Montagna, M., Zampedri, L., Chiasera, A., Ferrari, M., Righini, G., Fortes, L., Gonçalves, M., Santos, L. & Almeida, R. (2005). Self-absorption and radiation trapping in er3+-doped teo2-based glasses. *EPL (Europhysics Letters)*, **71**, 394. 106

McAulay, V., Deary, I. & Frier, B. (2001). Symptoms of hypoglycaemia in people with diabetes. *Diabetic Medicine*, **18**, 690–705. 20

McCance, D.R., Ritchie, C.M. & Kennedy, L. (1988). Is hba1 measurement superfluous in niddm? *Diabetes Care*, **11**, 512–514. 20

McCowen, K.C., Malhotra, A. & Bistrian, B.R. (2001). Stress-induced hyperglycemia. *Critical care clinics*, **17**, 107–124. 20

McMahon, M.M. & Bistrian, B.R. (1995). Host defenses and susceptibility to infection in patients with diabetes mellitus. *Infectious disease clinics of North America*, **9**, 1–9. 20

Mendes, R., Ramos, M. & Stoneham, A. (1998). Mesoscopic modelling of laser ablation. *Thermophysics & Aeromechanics*, **5**, 223–223. 42

Miller, J.C. (1998). *Laser ablation and desorption*. Academic Press. 36

Miller, S.E. (1969). Integrated optics: An introduction. *Bell Labs Technical Journal*, **48**, 2059–2069. 10

Millon, E., Perrière, J., Defourneau, R., Defourneau, D., Albert, O. & Etchepare, J. (2003). Femtosecond pulsed-laser deposition of batio3. *Applied Physics A*, **77**, 73–80. 38

Mohamed Kamari, H., Azlan, M. & Shafinas, S. (2015). Optical properties of erbium doped borotellurite glass system. In *Advanced Materials Research*, vol. 1112, 7–10, Trans Tech Publ. 90

Mohan, H. (2005). *The Skin, Textbook of pathology*. Jaypee brothers medical publishers New Delhi. xvi, 30, 31

Müller, U., Mertes, B., Fischbacher, C., Jageman, K. & Danzer, K. (1997). Non-invasive blood glucose monitoring by means of near infrared spectroscopy: methods for improving the reliability of the calibration models. *The International journal of artificial organs*, **20**, 285–290. 25

Murray, M. (2013). *Femtosecond pulsed laser deposition as a novel route for nanocomposite photonic materials on silicon*. University of Leeds. xvii, 65, 73

Nathan, D.M. (1993). Long-term complications of diabetes mellitus. *New England Journal of Medicine*, **328**, 1676–1685. 23

Nemes, Z., Dietz, R., Lüth, J., Gomba, S., Hackenthal, E. & Gross, F. (1979). The pharmacological relevance of vital staining with neutral red. *Experientia*, **35**, 1475–1476. 151

Neuman, M.R., Buck, R.P., Cosofret, V.V., Lindner, E. & Liu, C. (1994). Fabricating biomedical sensors with thin-film technology. *IEEE Engineering in Medicine and Biology Magazine*, **13**, 409–419. 9

Newman, J.D. & Turner, A.P. (2005). Home blood glucose biosensors: a commercial perspective. *Biosensors and Bioelectronics*, **20**, 2435–2453. 25

Nguyen, T.B. (2004). *Determining rare earth dopant concentrations in optical fibres and waveguides*. Ph.D. thesis, Victoria University of Technology. 106

Nolan, C.J., Damm, P. & Prentki, M. (2011). Type 2 diabetes across generations: from pathophysiology to prevention and management. *The Lancet*, **378**, 169–181. 19

Obermaier, K., Schmelzeisen-Redeker, G., Schoemaker, M., Klötzer, H.M., Kirchsteiger, H., Eikmeier, H. & del Re, L. (2013). Performance evaluations of continuous glucose monitoring systems: precision absolute relative deviation is part of the assessment. 188

Ojeda-GP, A., Schneider, C.W., Döbeli, M., Lippert, T. & Wokaun, A. (2017). Plasma plume dynamics, rebound, and recoating of the ablation target in pulsed laser deposition. *Journal of Applied Physics*, **121**, 135306. 88

Okoshi, M., Higashikawa, K. & Hanabusa, M. (2000). Pulsed laser deposition of zno thin films using a femtosecond laser. *Applied Surface Science*, **154**, 424–427. 38

Olszak, A. (2000). Lateral scanning white-light interferometer. *Applied optics*, **39**, 3906–3913. 126

Pasqua, L., Cundari, S., Ceresa, C. & Cavaletti, G. (2009). Recent development, applications, and perspectives of mesoporous silica particles in medicine and biotechnology. *Current medicinal chemistry*, **16**, 3054–3063. 136

Pawley, J.B. (2006). Fundamental limits in confocal microscopy. In *Handbook of biological confocal microscopy*, 20–42, Springer. 62

Perriere, J., Millon, E., Seiler, W., Boulmer-Leborgne, C., Craciun, V., Albert, O., Loulergue, J. & Etchepare, J. (2002). Comparison between zno films grown by femtosecond and nanosecond laser ablation. *Journal of Applied Physics*, **91**, 690–696. 38

Perry, M., Stuart, B., Banks, P., Feit, M., Yanovsky, V. & Rubenchik, A. (1999). Ultrashort-pulse laser machining of dielectric materials. *Journal of applied physics*, **85**, 6803–6810. 12, 37, 39

phe-culture collections (2011). Culture collections. https://www.phe-culturecollections.org.uk/technical/ccp/cellcounting.aspx, (Accessed on 12/08/2017). xxiii, xxiv, 142, 143, 144

Phipps, C. (2007). *Laser ablation and its applications*, vol. 129. Springer. 38

Pickup, J.C. & Williams, G. (1997). *Textbook of diabetes. Vol. 2*. Blackwell Science. 22, 23

Piliarik, M., Homola, J., Manikovà, Z. & Čtyrokỳ, J. (2003). Surface plasmon resonance sensor based on a single-mode polarization-maintaining optical fiber. *Sensors and Actuators B: Chemical*, **90**, 236–242. 8

Potts, R.O., A Tamada, J. & J Tierney, M. (2002). Glucose monitoring by reverse iontophoresis. *Diabetes/metabolism research and reviews*, **18**. 27

Prasad, P.N. (2004). *Introduction to biophotonics*. John Wiley & Sons. 5

Pronko, P. & Pan, X. (2001). Ultrafast-laser ablation creates new thin films. *Laser focus world*, **37**, 103–105. 38

Pronko, P., VanRompay, P., Horvath, C., Loesel, F., Juhasz, T., Liu, X. & Mourou, G. (1998). Avalanche ionization and dielectric breakdown in silicon with ultrafast laser pulses. *Physical Review B*, **58**, 2387. 44

Pronko, P., VanRompay, P., Zhang, Z. & Nees, J. (1999). Isotope enrichment in laser-ablation plumes and commensurately deposited thin films. *Physical review letters*, **83**, 2596. 38

Quarzglas, H. (2009). Base materials. 83

Ramaswami, R., Sivarajan, K. & Sasaki, G. (2004). *Optical networks: a practical perspective*. Academic press, San Diego. 86

Razavi, M. & Shapiro, J.H. (2003). Wireless optical communications via diversity reception and optical preamplification. In *Communications, 2003. ICC'03. IEEE International Conference on*, vol. 3, 2262–2266, IEEE. xv, 14

Repetto, G. & Sanz, P. (1993). Neutral red uptake, cellular growth and lysosomal function: in vitro effects of 24 metals. *Alternatives to laboratory animals: ATLA*. 150

Repetto, G., Del Peso, A. & Zurita, J.L. (2008). Neutral red uptake assay for the estimation of cell viability/cytotoxicity. *Nature protocols*, **3**, 1125. 151

Righini, G.C. & Chiappini, A. (2014). Glass optical waveguides: a review of fabrication techniques. *Optical Engineering*, **53**, 071819–071819. xv, 10, 11, 94

Righini, G.C. & Ferrari, M. (2005). Photoluminescence of rare-earth-doped glasses. *Rivista del Nuovo Cimento*, **28**, 1–53. 93, 99, 106, 108

Rim, K.T., Koo, K.H. & Park, J.S. (2013). Toxicological evaluations of rare earths and their health impacts to workers: a literature review. *Safety and health at work*, **4**, 12–26. 155

Ristoscu, C., Mihailescu, I.N., Velegrakis, M., Massaouti, M., Klini, A. & Fotakis, C. (2003). Optical emission spectroscopy and time-of-flight investigations of plasmas generated from aln targets in cases of pulsed laser deposition with sub-ps and ns ultraviolet laser pulses. *Journal of applied physics*, **93**, 2244–2250. 38

Rivera, V., Rodriguez, E., Chillcce, E., Cesar, C. & Barbosa, L. (2007). Waveguide produced by fiber on glass method using er 3+-doped tellurite glass. *Journal of non-crystalline solids*, **353**, 339–343. 47

Rode, A.V., Luther-Davies, B. & Gamaly, E.G. (1999). Ultrafast ablation with high-pulse-rate lasers. part ii: Experiments on laser deposition of amorphous carbon films. *Journal of Applied Physics*, **85**, 4222–4230. 12, 37

Rosmawati, S., Sidek, H., Zainal, A. & Zobir, H.M. (2007). Ir and uv spectral studies of zinc tellurite glasses. *Journal of Applied Sciences*, **7**, 3051–3056. 90

Rozmus, W. & Tikhonchuk, V. (1990). Skin effect and interaction of short laser pulses with dense plasmas. *Physical Review A*, **42**, 7401. 41

Saha, S., Arya, S.K., Singh, S., Sreenivas, K., Malhotra, B. & Gupta, V. (2009). Nanoporous cerium oxide thin film for glucose biosensor. *Biosensors and Bioelectronics*, **24**, 2040–2045. 38

Sakota, D. & Takatani, S. (2012). Quantitative analysis of optical properties of flowing blood using a photon-cell interactive monte carlo code: effects of red blood cells' orientation on light scattering. *Journal of biomedical optics*, **17**, 0570071–05700712. 176

Sapriel, J. (1979). *Acousto-optics*. Wiley New York. 75

Sato, T., Funamori, N. & Yagi, T. (2011). Helium penetrates into silica glass and reduces its compressibility. *Nature communications*, **2**, 345. 54

Sauer, M., Hofkens, J. *et al.* (2010). *Handbook of fluorescence spectroscopy and imaging: from ensemble to single molecules*. John Wiley & Sons. xv, 16

Savelii, I., El Hamzaoui, H., Bigot, L., Bouwmans, G., Fsaifes, I., Capoen, B. & Bouazaoui, M. (2016). Nanostructuring an erbium local environment inside sol–gel silica glasses: toward efficient erbium optical fiber lasers. *Laser Physics Letters*, **13**, 025108. 93, 112

Scheen, A. (2003). Pathophysiology of type 2 diabetes. *Acta Clinica Belgica*, **58**, 335–341. 22

Scheen, A. & Lefebvre, P. (1992). Assessment of insulin resistance in vivo: application to the study of type 2 diabetes. *Hormone Research in Paediatrics*, **38**, 19–27. 22

Schmitz, H., Norkus, V., Hess, N. & Bousack, H. (2009). The infrared sensilla in the beetle melanophila acuminata as model for new infrared sensors. In *Proc. SPIE, Bioeng. Bioinspired Syst. IV*, vol. 7365, 73650A–73650A. 126

Scudiero, D.A., Shoemaker, R.H., Paull, K.D., Monks, A., Tierney, S., Nofziger, T.H., Currens, M.J., Seniff, D. & Boyd, M.R. (1988). Evaluation of a soluble tetrazolium/formazan assay for cell growth and drug sensitivity in culture using human and other tumor cell lines. *Cancer research*, **48**, 4827–4833. 152

Senior, J.M. & Jamro, M.Y. (2009). *Optical fiber communications: principles and practice*. Pearson Education. 13

Seshan, K. (2012). *Handbook of thin film deposition*. William Andrew. 116

Shaw, L., Cole, B., Thielen, P., Sanghera, J. & Aggarwal, I. (2001). Mid-wave ir and long-wave ir laser potential of rare-earth doped chalcogenide glass fiber. *IEEE Journal of Quantum Electronics*, **37**, 1127–1137. 197

Shen, S., Richards, B. & Jha, A. (2006). Enhancement in pump inversion efficiency at 980 nm in er3+, er3+/eu3+ and er3+/ce3+ doped tellurite glass fibers. *Opt. Express*, **14**, 5050–5054. 47

Shim, M., Shi Kam, N.W., Chen, R.J., Li, Y. & Dai, H. (2002). Functionalization of carbon nanotubes for biocompatibility and biomolecular recognition. *Nano Letters*, **2**, 285–288. 136

Shukla, R., Bansal, V., Chaudhary, M., Basu, A., Bhonde, R.R. & Sastry, M. (2005). Biocompatibility of gold nanoparticles and their endocytotic fate inside the cellular compartment: a microscopic overview. *Langmuir*, **21**, 10644–10654. 136

Sidek, H., Rosmawati, S., Talib, Z., Halimah, M. & Daud, W. (2009). Synthesis and optical properties of zno-teo 2 glass system. *American Journal of Applied Sciences*, **6**, 1489. 90

Sokolowski-Tinten, K., Bialkowski, J., Cavalleri, A., von der Linde, D., Oparin, A., Meyer-ter Vehn, J. & Anisimov, S. (1998). Transient states of matter during short pulse laser ablation. *Physical Review Letters*, **81**, 224. 40

Solehmainen, K., Kapulainen, M., Heimala, P. & Polamo, K. (2004). Erbium-doped waveguides fabricated with atomic layer deposition method. *IEEE Photonics Technology Letters*, **16**, 194–196. 62

Song, W., Zhang, J., Guo, J., Zhang, J., Ding, F., Li, L. & Sun, Z. (2010). Role of the dissolved zinc ion and reactive oxygen species in cytotoxicity of zno nanoparticles. *Toxicology letters*, **199**, 389–397. 155

Sosman, R.B. (1965). Phases of silica. 12

Stelzer, E.H. (2000). Practical limits to resolution in fluorescence light microscopy. In *Imaging Neurons*, CSH Laboratory Press, New York. 62

Strickler, S. & Berg, R.A. (1962). Relationship between absorption intensity and fluorescence lifetime of molecules. *The Journal of chemical physics*, **37**, 814–822. 29

Stuart, B.C., Feit, M.D., Herman, S., Rubenchik, A., Shore, B. & Perry, M. (1996). Nanosecond-to-femtosecond laser-induced breakdown in dielectrics. *Physical review B*, **53**, 1749. 43

Sudrie, L., Couairon, A., Franco, M., Lamouroux, B., Prade, B., Tzortzakis, S. & Mysyrowicz, A. (2002). Femtosecond laser-induced damage and filamentary propagation in fused silica. *Physical Review Letters*, **89**, 186601. 80

Thyagarajan, K. (2002). Linear and nonlinear propagation effects in optical fibers. In *Optical Solitons*, 33–70, Springer. 161

Tien, P. (1971). Light waves in thin films and integrated optics. *Applied optics*, **10**, 2395–2413. 69

Tierney, M.J., Tamada, J.A., Potts, R.O., Eastman, R.C., Pitzer, K., Ackerman, N.R. & Fermi, S.J. (2000). The glucowatch® biographer: a frequent, automatic and noninvasive glucose monitor. 28

Tong, X.C. (2014). Characterization methodologies of optical waveguides. In *Advanced Materials for Integrated Optical Waveguides*, 53–102, Springer. 86

Troy, T.L. & Thennadil, S.N. (2001). Optical properties of human skin in the near infrared wavelength range of 1000 to 2200 nm. *Journal of biomedical optics*, **6**, 167–176. 163

Turner, A.P. (2013). Biosensors: sense and sensibility. *Chemical Society Reviews*, **42**, 3184–3196. 6

Ulrich, R. & Torge, R. (1973). Measurement of thin film parameters with a prism coupler. *Applied Optics*, **12**, 2901–2908. 69

Van Grieken, R. & Markowicz, A. (2001). *Handbook of X-ray Spectrometry*. CRC Press. 67

van Meerloo, J., Kaspers, G.J. & Cloos, J. (2011). Cell sensitivity assays: the mtt assay. *Cancer cell culture: methods and protocols*, 237–245. 149

Vashist, S.K. (2012). Non-invasive glucose monitoring technology in diabetes management: A review. *Analytica chimica acta*, **750**, 16–27. 26, 27

Vernon-Parry, K. (2000). Scanning electron microscopy: an introduction. *III-Vs Review*, **13**, 40 – 44. 65

Vidhya, K., Sudhir, R. & Mohan, V. (2004). Continuous glucose monitoring system–useful but expensive tool in management of diabetes. *The Journal of the Association of Physicians of India*, **52**, 587–90. 24

Von der Linde, D. & Schüler, H. (1996). Breakdown threshold and plasma formation in femtosecond laser–solid interaction. *JOSA B*, **13**, 216–222. 40

Von der Linde, D. & Sokolowski-Tinten, K. (2000). The physical mechanisms of short-pulse laser ablation. *Applied Surface Science*, **154**, 1–10. 38

Waldron-Lynch, F. & Herold, K.C. (2011). Immunomodulatory therapy to preserve pancreatic β-cell function in type 1 diabetes. *Nature reviews Drug discovery*, **10**, 439–452. xv, 22

Wan, J., Ling, Y., Sun, Q. & Wang, X. (1998). Role of codopant oxygen in erbium-doped silicon. *Physical Review B*, **58**, 10415. 83

Wang, J. (2008). Electrochemical glucose biosensors. *Chemical reviews*, **108**, 814–825. 25

Waters, P. (2008). *Stress analysis and mechanical characterization of thin films for microelectronics and MEMS applications*. University of South Florida. xxiii, 127, 128

Wentholt, I., Hoekstra, J., Zwart, A. & DeVries, J. (2005). Pendra goes dutch: lessons for the ce mark in europe. *Diabetologia*, **48**, 1055–1058. 28

Wiederhorn, S.M. (1969). Fracture surface energy of glass. *Journal of the American Ceramic Society*, **52**, 99–105. xxvii, 116, 118

Wiersma, D.S. (2008). The physics and applications of random lasers. *Nature physics*, **4**, 359. 159

Winckler, J. (1974). Vital staining of lysosomes and other cell organelles of the rat with neutral red (author's transl). *Progress in histochemistry and cytochemistry*, **6**, 1. 151

Wu, R., Myers, J.D., Myers, M.J. & Rapp, C. (2003). Fluorescence lifetime and 980 nm pump energy transfer dynamics in erbium and ytterbium co-doped phosphate laser glasses. In *Proceedings of SPIE*, vol. 4968, 11–17. xxvii, 58, 107

Xu, J. & Stroud, R. (1992). *Acousto-optic devices: principles, design, and applications*, vol. 12. Wiley-Interscience. 75

Yan, Y., Faber, A.J. & De Waal, H. (1995). Luminescence quenching by oh groups in highly er-doped phosphate glasses. *Journal of Non-Crystalline Solids*, **181**, 283–290. 97

Yin, L., Ning, H., Turkdogan, S., Liu, Z., Nichols, P.L. & Ning, C. (2012). Long lifetime, high density single-crystal erbium compound nanowires as a high optical gain material. *Applied Physics Letters*, **100**, 241905. 104

Yki-Järvinen, H. (1994). Pathogenesis of non-insulin-dependent diabetes mellitus. *The Lancet*, **343**, 91–95. 20

Yu, T., Malugin, A. & Ghandehari, H. (2011). Impact of silica nanoparticle design on cellular toxicity and hemolytic activity. *ACS nano*, **5**, 5717–5728. 136

Zammitt, N.N. & Frier, B.M. (2005). Hypoglycemia in type 2 diabetes. *Diabetes care*, **28**, 2948–2961. 20

Zergioti, I., Mailis, S., Vainos, N., Ikiades, A., Grigoropoulos, C. & Fotakis, C. (1999). Microprinting and microetching of diffractive structures using ultrashort laser pulses. *Applied surface science*, **138**, 82–86. 38

Zergioti, I., Papazoglou, D., Karaiskou, A., Fotakis, C., Gamaly, E. & Rode, A. (2003). A comparative schlieren imaging study between ns and sub-ps laser forward transfer of cr. *Applied Surface Science*, **208**, 177–180. 38

Zhang, Z., Grattan, K., Palmer, A., Meggitt, B. & Sun, T. (1997). Fluorescence decay-time characteristics of erbium-doped optical fiber at elevated temperatures. *Review of scientific instruments*, **68**, 2764–2766. 106, 108

Zhang, Z., VanRompay, P., Nees, J., Clarke, R., Pan, X. & Pronko, P. (2000). Nitride film deposition by femtosecond and nanosecond laser ablation in low-pressure nitrogen discharge gas. *Applied surface science*, **154**, 165–171. 38

Zhao, Z. (2012). *Pulsed laser deposition and characterisation of rare earth doped glass-polymer optical materials*. University of Leeds. xxviii, 119, 120

Zhao, Z., Jose, G., Steenson, P., Bamiedakis, N., Penty, R.V., White, I.H. & Jha, A. (2011). Tellurite glass thin films on silica and polymer using uv (193 nm) pulsed laser ablation. *Journal of Physics D: Applied Physics*, **44**, 095501. 47

Zhao, Z., Jose, G., Fernandez, T.T., Comyn, T.P., Irannejad, M., Steenson, P., Harrington, J.P., Ward, M., Bamiedakis, N., Penty, R.V. *et al.* (2012). Active glass–polymer superlattice structure for photonic integration. *Nanotechnology*, **23**, 225302. xxii, xxviii, 116, 119, 120, 121, 122, 123, 125

Zhong, N., Zhu, X., Liao, Q., Wang, Y., Chen, R. & Sun, Y. (2013). Effects of surface roughness on optical properties and sensitivity of fiber-optic evanescent wave sensors. *Applied optics*, **52**, 3937–3945. 80